UNIVERSITA' DEGLI STUDI DI PADOVA

DIPARTIMENTO DI INGEGNERIA INDUSTRIALE
DIPARTIMENTO DI TECNICA E GESTIONE DEI SISTEMI INDUSTRIALI
CORSO DI LAUREA MAGISTRALE IN INGEGNERIA DEI MATERIALI

Tesi di laurea magistrale in
Ingegneria dei Materiali

INFLUENCE OF THE STRESS RATIO ON THE MULTIAXIAL FATIGUE BEHAVIOR OF COMPOSITE MATERIALS

Relatore: Ch.mo Prof. Quaresimin Marino

Correlatore: Ing. Carraro Paolo Andrea

Laureando: Lucio Maragoni

Matricola: 1012878

ANNO ACCADEMICO 2012-2013

A mamma Gioia

e papà Mauro

Index

Introduction

Thanks to their outstanding specific strength and stiffness, fiber reinforced plastics (FRP) are being widely utilized in various fields (aerospace, automotive, marine, civil infrastructure, wind turbines…) and their usage is constantly increasing. In many of their structural applications, FRP are often subjected to multiaxial fatigue loading. For this reason, the study of the fatigue life is a matter of primary importance for this kind of materials. In particular, the development of safe and reliable fatigue design criterions, that is independent on structure and loading mod, would be of great help in reducing the time and the cost of extensive experimental testing.

If the behavior of FRP under uniaxial cyclic stress state has been extensively investigated (although not fully developed yet), their behiaviour under multiaxial fatigue loading has been much less analyzed, despite the importance it has in structural design: because of the material anisotropy, in fact, even a uniaxial load applied on a multidirectional laminate induces in its individual laminae multiaxial states of stress.

The damage evolution of a composite laminate during fatigue life is characterized by the formation of cracks in the off-axis layers, that multiply until saturation, followed by delamination between layers, up to the cracking of the fibers of the on-axis layers, that controls the final fracture of the laminate. In order to fully characterize the behavior of a composite materials under fatigue loading is then necessary to understand how the damage develops during cycling (in particular the evolution of the crack density, that causes stiffness degradation) and to predict the final failure under general multiaxial loading conditions. The tools needed for this are a multixiality criterion, that can avoid the carrying out of experiments under different multiaxiality conditions, and an analytical description of the damage evolution. Both of these tools have to take into account the effect of various parameters, such as the laminate lay-up, the thickness of the individual laminae, the sequence effect and the stress ratio.

These topics are currently investigated by an international research network, in which participate the University of Padova (Italy), Texas A&M University (TAMU), University of Risoe – DTU (Denmark), University of Lulea (Sweden), and Uppsala University (Sweden). In particular, the research team of the University of Padova is working on the development of a multiaxiality criterion based on damage mechanisms, it worked in closed contact with TAMU for the creation of a model that can predict the evolution of the crack density under in-plane loading conditions, and it

developed an analytical model for correlating the crack density to the stiffness degradation of a composite laminate.

In the present work, the effect of the stress ratio on the fatigue life of composite materials under multiaxial loading conditions is investigated, with the aim of synthesizing and modeling it. As mentioned above, this is necessary for the multiaxiality criterion and the damage evolution description to be as general as possible. In particular, what is of interest here is how this parameter influences the matrix dominated behavior of composite materials that undergo fatigue loading.

The present work is structured as follows: Chapter 1 is a brief introduction to the multiaxial fatigue behavior of composite materials, in order to give the basic knowledge needed for the comprehension of the following chapters. In Chapter 2 the experimental results found in literature concerning the effect of stress ratio are reported, as well as the attempts made to take the effect of this parameter into account in the formulation of fatigue life-predicting models. Chapter 3 is dedicated to the materials used and the testing procedures followed in the experimental campaign that was conducted. Chapters 4 and 5 contains, respectively, the results of the quasi-static tests and the fatigue tests. In Chapter 6 some of the models found in literature are validated against the experimental data, and in Chapter 7 the conclusions are made together with possible future developments. In addition, in the Appendix can be found the instructions for the use of a Matlab® program in which is implemented the analytical model, mentioned above, that correlates the stiffness degradation to the crack density.

Chapter 1

Generalities of the multiaxial fatigue behavior of composite materials

The multiaxial fatigue behavior of composite materials is a very complex phenomenon, which makes its full comprehension complicated. This chapter provides a summary of the main aspects of this problem, referring in particular to the aspects needed to understand the current research carried out by the research team of the Department of Management and Engineering of the University of Padova.

1.1 – Generalities of the fatigue phenomenon of composite materials

The heterogeneity and the anisotropy of composite materials makes their fatigue behavior a very complex phenomenon, even more difficult to fully understand than the one of traditional materials: if in metals the fatigue damage evolution consists of nucleation and propagation of a dominant crack, in composite materials the damage process involves multiple matrix cracking, fiber-matrix debonding, delaminations and fiber breakage, so that the damage is dispread into a much wider area than the tip of a single crack. Moreover, the damage process causes, in a cumulative way, a gradual degradation of the mechanical properties of the individual layers of a laminate, and therefore a continuous redistribution of the stresses. The complexity of this multi-damage mechanism, together with the inherent difficulties of fatigue, have delayed the establishment of a general fatigue criterion for composite materials.

1.2 – A model based on damage mechanisms

Not many life-predicting models can be found in literature concerning the multiaxial fatigue behavior of composite materials. In a recent review [1] some of these models were analyzed and compared with a large amount of experimental data. In spite of their rather simple formulations,

which make them attractive in design, they revealed to be in some cases inaccurate and non-conservative, showing the lack of a reliable general fatigue life criterion and in particular the unreliability of empirical models. In order to develop a general fatigue criterion, it is necessary to fully comprehend and describe the damage mechanisms that occur during fatigue life, and their dependence on loading parameters.

1.2.1 – A description of damage mechanisms

At a qualitative level, damage processes in composite materials, subjected to any type of loading, can be divided in two main classes: *primary* and *secondary damage mechanisms. Primary damage mechanisms* are the ones that involve fibers breakage and they control the final failure (i.e. separation) of a laminate, hence the term *primary*. *Secondary damage mechanisms* are instead all those processes that occur before the final failure of a laminate, and they include matrix cracking, fiber-matrix debonding and delaminations. In spite of the term *secondary*, these processes are fundamental in both influencing the *primary mechanisms* and in producing a progressive degradation of the mechanical properties of a laminate.

As stated above, damage evolution may vary depending on the multiaxiality conditions: in the case of sufficiently high tensile stress along fibers, three damage regions can be individuated [2], reported in Figures 1.1 and 1.2. The presence of transverse and shear stresses will narrow the scatter band relative to fiber breakage and make it assume a downward slope, it will increase the fiber/matrix debonding and reduce the strain needed in order to initiate the damage.

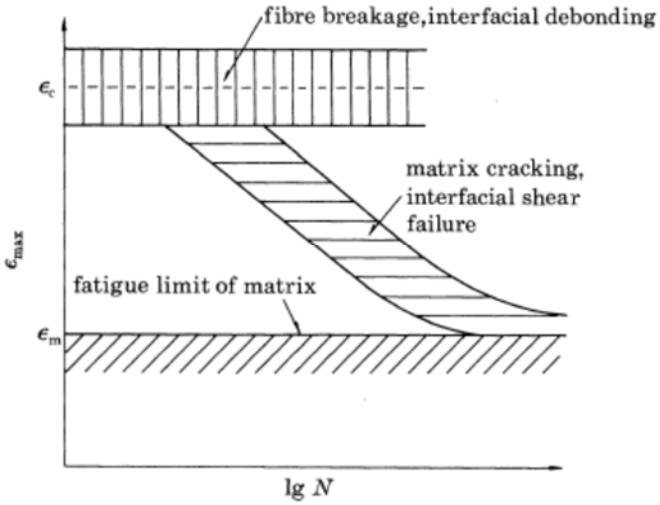

Figure 1.1 – Damage regions in the case of high tensile stress along fibers (taken from [2]).

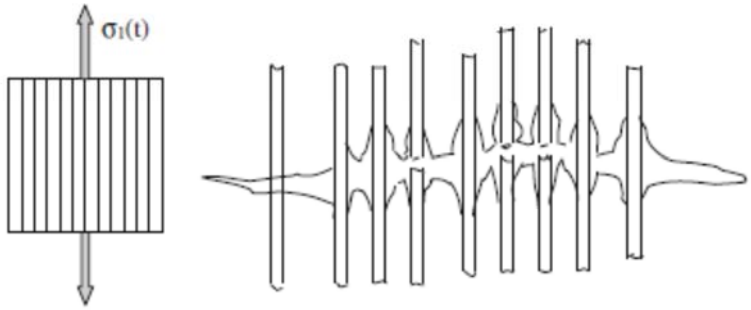

Figure 1.2 – Fiber-bridged matrix cracking, characteristic of the second damage region in the case of high tensile stress along fibers (taken from [1]).

If, instead, the tensile stress along fibers is relatively low, the dominant damage mechanisms are matrix cracking and fiber/matrix debonding, that are both driven by transverse and in plane-shear stresses and therefore directly influenced by multiaxial parameters.

When the tension along fibers is compressive, then microbuckling becomes the failure-controlling damage mechanism. In such case, both in plane shear and transverse tensile stresses will contribute to enhance this phenomenon.

A compressive transverse stress alone does not lead to fatigue failure, unless it is applied at very high levels. Anyway, combined with tensile loading along fibers, it increases the axial strain in the fibers via Poisson's effect.

At present, it is still missing a quantitative description of the nucleation and evolution until final failure of all these different damage mechanisms, in particular as functions of multiaxiality conditions. In a laminate, the first damage mechanism to occur usually is the nucleation of multiple cracks in the matrix in the off-axis laminae. This means that in order to establish a fatigue criterion based on damage mechanisms for a generic laminate, it is necessary to study first the behavior of a single lamina, in particular under loading conditions that involve only transverse and in plane shear stresses so as to understand the matrix and fiber-matrix interface controlled failure mechanisms. The research that is being currently carried out by the research team of the Department of Management and Engineering of the University of Padova is focused right on the study of the *secondary damage mechanisms* under different multiaxial conditions, through experimental campaigns and modeling activity [3].

1.3 – Design parameters influencing the multiaxial fatigue behavior of composites.

An analysis conducted by Quaresimin and Susmel [4] showed that the most important parameters in the design of composite materials under multiaxial loading conditions are the following:

- off-axis angle (lay-up in the case of laminates)
- biaxiality ratios (see paragraph 1.5)
- degree of non-proportionality of the applied stress field (out-of-phase stresses)
- stress intensity factors (if any)
- stress ratio
- frequency

For what concerns the biaxiality ratios, of major importance are the ones in the material frame of reference ($\lambda_1 = \sigma_{2,a} / \sigma_{1,a}, \lambda_2 = \sigma_{6,a} / \sigma_{1,a}, \lambda_{12} = \sigma_{6,a} / \sigma_{2,a}$), since it is the local stress state that governs the fatigue strength.

In their extensive analysis of literature data, Quaresimin, Susmel and Talreja [1] pointed out that the influence of λ_1 on the fatigue strength of composite materials is minimal, whereas much larger is the effect of λ_2: an increase of the shear component induces indeed a drop of the fatigue life that is much more dramatic than the addition of a stress component normal to the fibers (σ_2). In the same work, the authors hypothesize that the combination of a shear stress and a compressive stress could cause an even more dangerous condition for the material.

From an experimental point of view, the problem in dealing with all the above parameters is that it is sometimes difficult to uncouple the effects of every single one on the global fatigue strength, and this implies the need to conduct dedicated experimental programs for identifying the effect of each of them.

1.4 – External multiaxiality and inherent multiaxiality

Multiaxiality loading conditions, in the case of composite materials, can be induced in two different ways: one is by testing conditions that involves an opportune combination of external loads (“global” or “external” multiaxiality), the other is induced by the material itself due to its intrinsic anisotropy (“local”, or “inherent” multiaxiality). An example of the latter condition is an unidirectional laminates having off-axis angle larger than zero and subjected to uniaxial fatigue loading. As deeply investigated in [5] and confirmed in [4], there is no reason for hypothesizing that

the effect on the fatigue damage are different in the case of external or inherent multiaxiality, therefore it can be stated that the fatigue damage is expected to be the same independently of the type of source of multiaxiality, as long as the local stress fields remain the same.

1.5 – Preliminary definitions

In order to make more understandable all the following discussion on the theme of multiaxial fatigue behavior of composite materials, all the quantities involved in stress analysis are defined in the following. Consider the specimen geometry represented in Figure 1.3, that is the one that was used in the experimental campaign. The frame of reference denoted by the x,y,z axes is defined as the "geometrical (structure) coordinate system", whereas the one denoted by the 1,2,3 is the "material coordinate system", and they are both centered at the same point O. θ, the angle between the x direction and the 1 direction is generally referred to as the "off-axis angle".

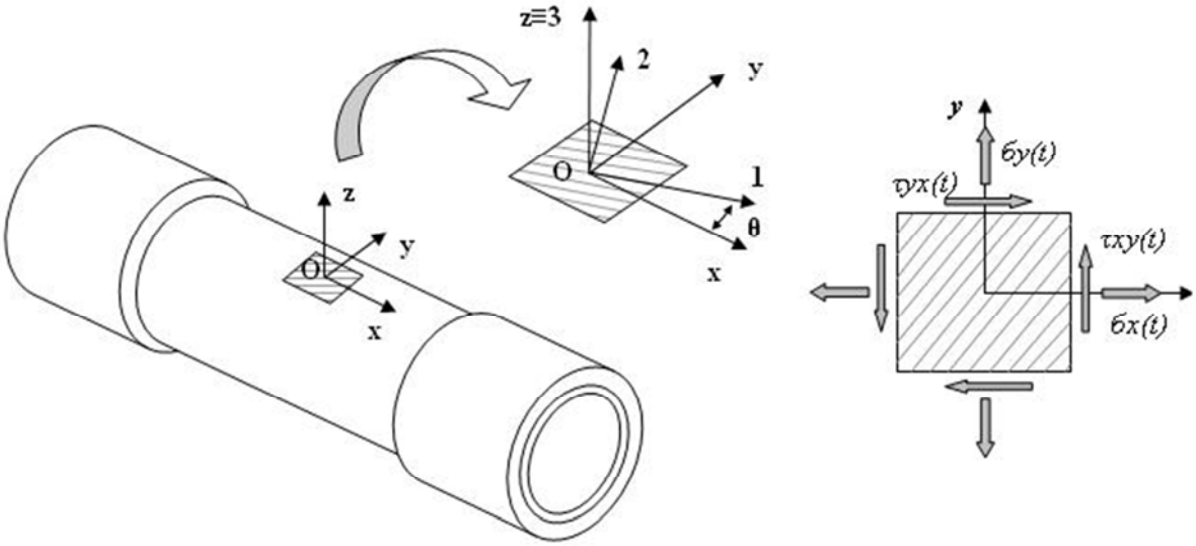

Figure 1.3 – Description of the adopted frames of reference in the specimen geometry used in the experimental campaign.

The external loading conditions are considered to induce a plain stress state in the material, reported always in Figure 1.3. The "geometrical" stress components are $\sigma_x(t), \sigma_y(t), \tau_{xy}(t)$ with $t \in \mathrm{T}$ (T is the period of the applied cyclic load). According to [1], the degree of multiaxiality can be measured in terms of biaxiality ratios, that for the geometrical stress components are defined as:

$$\lambda_C = \frac{\sigma_{y,a}}{\sigma_{x,a}} \tag{1.1}$$

$$\lambda_T = \frac{\tau_{xy,a}}{\sigma_{x,a}} \tag{1.2}$$

in which the subscript a denotes the stress amplitude. Anyway, it is more convenient to study cyclic loading conditions in the material coordinate system (1,2,3), because the geometrical stresses do not give the real degree of multiaxiality of the local stress fields. For cyclic plain stress state, the relationship between material and geometrical stresses is the following:

$$\begin{aligned}
\sigma_1(t) &= m^2\sigma_x(t) + n^2\sigma_y(t) + 2mn\tau_{xy}(t) \\
\sigma_2(t) &= n^2\sigma_x(t) + m^2\sigma_y(t) - 2mn\tau_{xy}(t) \\
\sigma_6(t) &= -mn\sigma_x(t) + mn\sigma_y(t) + (m^2 - n^2)\tau_{xy}(t)
\end{aligned} \tag{1.3}$$

where $m = \cos(\theta)$ and $n = \sin(\theta)$. The degree of multiaxiality can therefore be quantified by the following stress ratios:

$$\lambda_1 = \frac{\sigma_{2,a}}{\sigma_{1,a}} \tag{1.4}$$

$$\lambda_2 = \frac{\sigma_{6,a}}{\sigma_{1,a}} \tag{1.5}$$

$$\lambda_{12} = \frac{\sigma_{6,a}}{\sigma_{2,a}} \tag{1.6}$$

In a general multiaxial loading condition, it is possible that the stress components are not all in phase respect to each other. Therefore, making the assumption that the geometrical stress components are sinusoidal, the expression of the general loading condition is:

$$\begin{aligned}
\sigma_x(t) &= \sigma_{x,m}(t) + \sigma_{x,a}\sin(\omega t) \\
\sigma_y(t) &= \sigma_{y,m}(t) + \sigma_{y,a}\sin(\omega t - \delta_{y,x}) \\
\tau_{xy}(t) &= \tau_{xy,m}(t) + \tau_{xy,a}\sin(\omega t - \delta_{xy,x})
\end{aligned} \tag{1.7}$$

where ω is the angular velocity, $\delta_{y,x}$ and $\delta_{xy,x}$ the phase shifts between $\sigma_y(t)$ and $\sigma_x(t)$, and between $\tau_{xy}(t)$ and $\sigma_x(t)$, respectively, and the subscript *m* denotes mean stresses. The stresses in the material coordinate system can therefore be written:

$$\begin{aligned}\sigma_1(t) &= \sigma_{1,m}(t) + \sigma_{1,a}\sin(\omega t)\\ \sigma_2(t) &= \sigma_{2,m}(t) + \sigma_{2,a}\sin(\omega t - \delta_{2,1})\\ \sigma_6(t) &= \sigma_{6,m}(t) + \sigma_{6,a}\sin(\omega t - \delta_{6,1})\end{aligned} \qquad (1.8)$$

where the meaning of the symbols are analogous to the ones of the equations (1.7).

It can be noticed that multiaxiality of the local stress state can be induced either by the external loading conditions or by the local orientation of the fibers respect to the loading direction (or even, of course, by both of them), as discussed in paragraph 1.4.

As a reference, the meaning of all the symbols used here and in the following chapters are reported in Table 1.1 (in brackets there are the models in which they are used).

E_1, E_2, G_{12}	elastic moduli	O_{xyz}	geometrical (structure) frame of reference
O_{123}	material frame of reference	θ	off-axis angle
$\sigma_x, \sigma_y, \sigma_z$	geometrical normal stresses	$\tau_{xy}, \tau_{xz}, \tau_{yz}$	geometrical shear stresses
$\varepsilon_x, \varepsilon_y, \varepsilon_z$	normal stresses calculated in the material frame of reference	$\gamma_{xy}, \gamma_{xz}, \gamma_{yz}$	shear stresses calculated in the material frame of reference
$\sigma_1, \sigma_2, \sigma_3$	normal stresses calculated in the material frame of reference	$\sigma_4, \sigma_5, \sigma_6$	shear stresses calculated in the material frame of reference
$\varepsilon_1, \varepsilon_2, \varepsilon_3$	normal strains calculated in the material frame of reference	$\varepsilon_4, \varepsilon_5, \varepsilon_6$	shear strains calculated in the material frame of reference
λ_C	$\lambda_C = \sigma_{y,a}/\sigma_{x,a}$	λ_T	$\lambda_T = \tau_{xy,a}/\sigma_{x,a}$
λ_1	$\lambda_2 = \sigma_{2,a}/\sigma_{1,a}$	λ_2	$\lambda_2 = \sigma_{6,a}/\sigma_{1,a}$
λ_{12}	$\lambda_2 = \sigma_{6,a}/\sigma_{2,a}$	$\sigma_{i,\max}$	fatigue maximum stress, (i = 1,2,...,6)
$\sigma_{i,\min}$	fatigue maximum stress (i = 1,2,...,6)	$\sigma_{i,m}$	fatigue mean stress, (i = 1,2,...,6)
$\sigma_{i,a}$, $\Delta\sigma_i$	fatigue stress amplitude (i = 1,2,...,6)	$\varepsilon_{i,\max}$	fatigue maximum strain, (i = 1,2,...,6)
$\varepsilon_{i,\min}$	fatigue maximum strain (i = 1,2,...,6)	$\varepsilon_{i,m}$	fatigue mean strain, (i = 1,2,...,6)
$\varepsilon_{i,a}$, $\Delta\varepsilon_i$	fatigue strain amplitude (i = 1,2,...,6)	R	stress ratio, $R = \sigma_{i,\min}/\sigma_{i,\max}$ (i = 1,2,...,6)
N	number of cycles	N_f	number of cycles to failure
t	time	T	period of the applied cyclic load
ω	angular velocity	$\delta_{y,x}$	phase shift between $\sigma_y(t)$ and $\sigma_x(t)$
$\delta_{xy,x}$	phase between $\tau_{xy}(t)$ and $\sigma_x(t)$	$\delta_{2,1}$	phase shift between $\sigma_2(t)$ and $\sigma_1(t)$
$\delta_{6,1}$	phase shift between $\sigma_6(t)$ and $\sigma_1(t)$	dW_{damage}	Damage accumulation (El Kadi-Ellyin)

dW_{supplied}	Stored Energy (El Kadi-Ellyin)	dQ	Heat loss (El Kadi-Ellyin)
$dW_{\text{recoverable}}$	Recoverable part of stored energy (El Kadi-Ellyin)	ΔW^{+}	Strain energy for positive stress in fatigue cycles (El Kadi-Ellyin)
ΔW^{-}	Strain energy for negative stress in fatigue cycles (El Kadi-Ellyin)	W_f^{+}	Maximum monotonic strain energy under tensile load (El Kadi-Ellyin)
W_f^{-}	Maximum monotonic strain energy under compressive load (El Kadi-Ellyin)	Ψ^{+}	Normalized strain energy for positive stress in fatigue cycles (El Kadi-Ellyin)
Ψ^{-}	Normalized strain energy for negative stress in fatigue cycles (El Kadi-Ellyin)	Ψ	Total strain energy in fatigue cycles (El Kadi-Ellyin)
$k(\theta)$	Intercept of the fatigue curve (El Kadi-Ellyin)	$\alpha(\theta)$	Exponent of the fatigue curve (El Kadi-Ellyin)
S_r	Tension of the reference curve (Fawaz-Ellyin)	m_r	Slope of the reference curve (Fawaz-Ellyin)
b_r	Intercept of the reference curve (Fawaz-Ellyin)	R_r	Stress ratio of the reference curve (Fawaz-Ellyin)
P_N	Smith-Wattson-Topper parameter, $P_N = \sigma_{\max}\Delta\varepsilon$ (Plumtree-Cheng)	$\sigma_{22,\max}$	Maximum fatigue normal stress at in the fracture plane (Plumtree-Cheng)
$\tau_{12,\max}$	Maximum fatigue shear stress at the fracture plane (Plumtree-Cheng)	$\varepsilon_{22,\max}$	Maximum fatigue normal strain at in the fracture plane (Plumtree-Cheng)
$\gamma_{12,\max}$	Maximum fatigue shear strain at in the fracture plane (Plumtree-Cheng)	ΔW_1^{*}	Modified SWT parameter for normal stress (Plumtree-Cheng)
ΔW_2^{*}	Modified SWT parameter for shear stress (Plumtree-Cheng)	ΔW_{tot}^{*}	Total modified SWT parameter (Plumtree-Cheng)
f	Frequency (Miyano et al.)	T	Temperature (Miyano et al.)
$\sigma_{f:R}$	Failure stress for the stress ratio R (Miyano et al.)	W_1^{*}	Normal component of the fatigue parameter (Petermann-Plumtree)
W_2^{*}	Shear component of the fatigue parameter (Petermann-Plumtree)	W_{tot}^{*}	Unified fatigue parameter (Petermann-Plumtree)
ω	Damage variable (Kawai-Suda)	K	Material's constant (Kawai-Suda)
k	Material's constant (Kawai-Suda)	Φ	Fatigue strength parameter, $\Phi = \sigma_{\max}^{*}$ (Kawai-Suda)
$\sigma_{\max}^{*}$	Non-dimensional effective stress (Kawai-Suda)	$X,\ Y,\ S$	Longitudinal, transverse and shear strengths (Kawai-Suda)
n(R)	Exponent of the fatigue curve (Kawai-Suda)	ψ	Fatigue strength ratio (Kawai)
Ψ	Modified fatigue strength ratio (Kawai)	σ_B	Experimental static strength (Kawai)
$\sigma_{B,pred}$	Predicted static strength (Kawai)	Σ^{*}	Modified non-dimensional effective stress (Kawai)
n^{*}	Exponent of the fatigue curve, material's constant (Kawai)	ult	Ultimate (Shokrieh-Taheri Behrooz)
ΔW_I^{*}	Contribution to the fatigue parameter given by longitudinal stress (Shokrieh-Taheri Behrooz)	ΔW_{II}^{*}	Contribution to the fatigue parameter given by normal stress (Shokrieh-Taheri Behrooz)
ΔW_{III}^{*}	Contribution to the fatigue parameter given by shear stress (Shokrieh-Taheri Behrooz)	ΔW_{STB}^{*}	Fatigue parameter (Shokrieh-Taheri Behrooz)
ΔW_I	Contribution to the fatigue parameter given by matrix cracking (Varvani Farahani et al.)	ΔW_{II}	Contribution to the fatigue parameter given by matrix-fibers debonding (Varvani Farahani et al.)
ΔW_{III}	Contribution to the fatigue parameter given by fibers cracking (Varvani Farahani et al.)	ΔW	Fatigue parameter (Varvani Farahani et al.)
D	Damage during fatigue cycling (Chen-Whang)	F_r, F_R, F_f	Corrective functions (Chen-Whang)
a, c	Experimental parameters (Chen-	σ_C	Static compressive strength (Kawai-

	Whang)		Teranuma)
σ_T	Static tensile strength (Kawai-Teranuma)	χ	Critical stress ratio (Kawai-Teranuma)
ψ_χ	Fatigue strength ratio associated with χ (Kawai-Teranuma)	K_χ, n, a, b, $\psi_{\chi(L)}$	Fitting parameters (Kawai-Teranuma)
χ_L, χ_R	Auxiliary stress ratios	k_T, k_C	Shape change rate adjusting parameters (Kawai-Teranuma)
X_f, Y_f, S_f	Principal fatigue strength for longitudinal, normal and shear stress (Kawai-Teranuma)	μ_L	Parameter accounting for the different effect of shear in tension and compression (Kawai-Teranuma)

Table 1.1 – Meaning of the symbols used in the present work.

Chapter 2

Previous works on the effect of stress ratio on the matrix-dominated fatigue behavior of composite materials

In this section a review is made of several works found in literature concerning the effect of the stress ratio ($R = \sigma_{min} / \sigma_{max}$) on the matrix-dominated fatigue behavior of composite materials, focusing on two main aspects: the experimental effect of different stress ratios, in terms of S–N curves, and the way in which authors account for this effect in their fatigue life-predicting model of composite materials.

2.1 – Experimental data on unidirectional laminae

Only a few authors in literature conduced experimental tests in order to observe the effect of the stress ratio (R) on the fatigue behavior of composite materials. In particular, only two satisfying investigations were found concerning unidirectional laminae, made respectively by El Kadi and Ellyin [6] and by Kawai and Suda [11]. In this section, their results are reported in different forms (fatigue curves at constant R, fatigue curves at constant θ, and $\sigma_{2,max}$- $\sigma_{2,m}$ and $\sigma_{2,a}$- $\sigma_{2,m}$ diagrams) and commented.

2.1.1 – Experimental data by El Kadi and Ellyin (1994)

El Kadi and Ellyin [6] tested flat specimens of the E-glass/epoxy system "Schotchply Reinforced Plastic type 1003" (a 3M product), under R = 0.5, 0, -1, for fibers angles $\theta = 0,\ 19,\ 45,\ 71,\ 90°$ and at a frequency of 3.3 Hz. For $\theta = 0°$, an anti-buckling guide was used for R = -1, since the specimens were thinner for this fibers angle. The experimental results are shown in Figures 2.1 to 2.17 (x indicates the load direction). In the present work the interest is

focused on the matrix dominated behavior of composites, hence the data for $\theta = 0°$ are not reported.

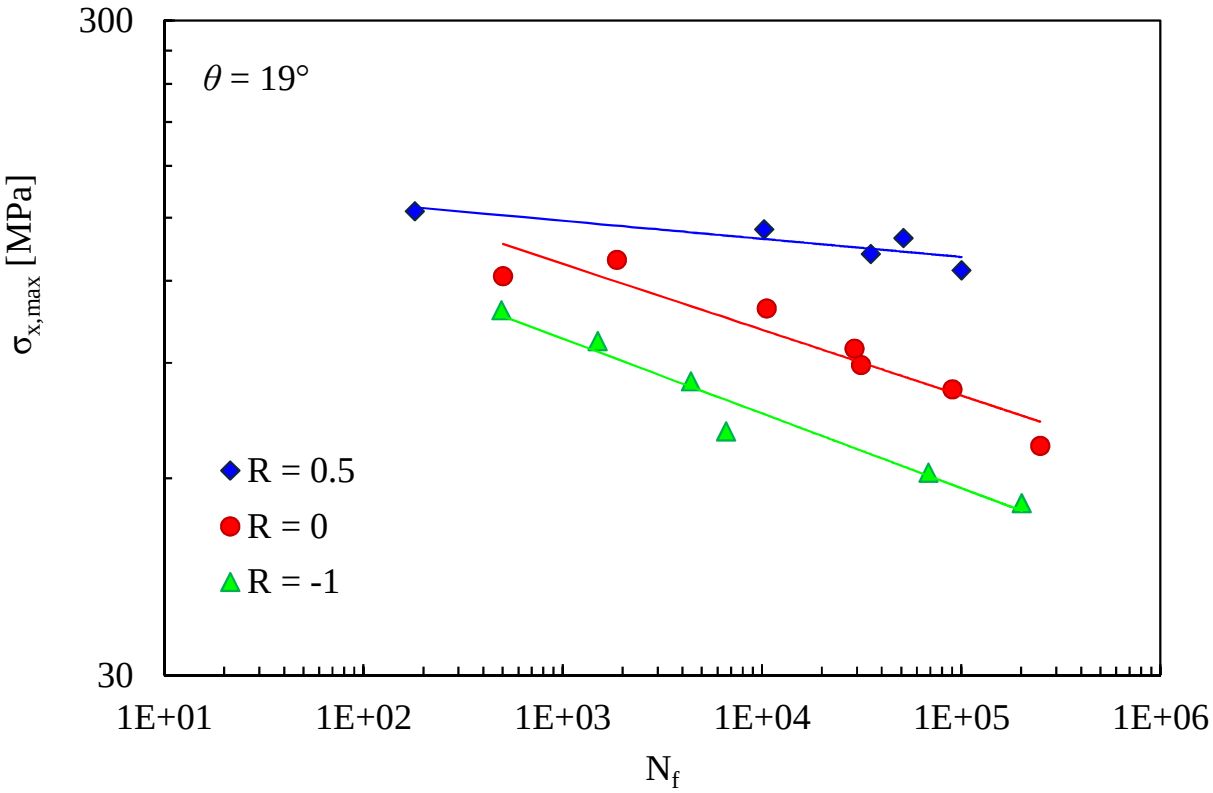

Figure 2.1 – Experimental data by El Kadi and Ellyin for $\theta = 19°$ at R = 0.5, 0, -1.

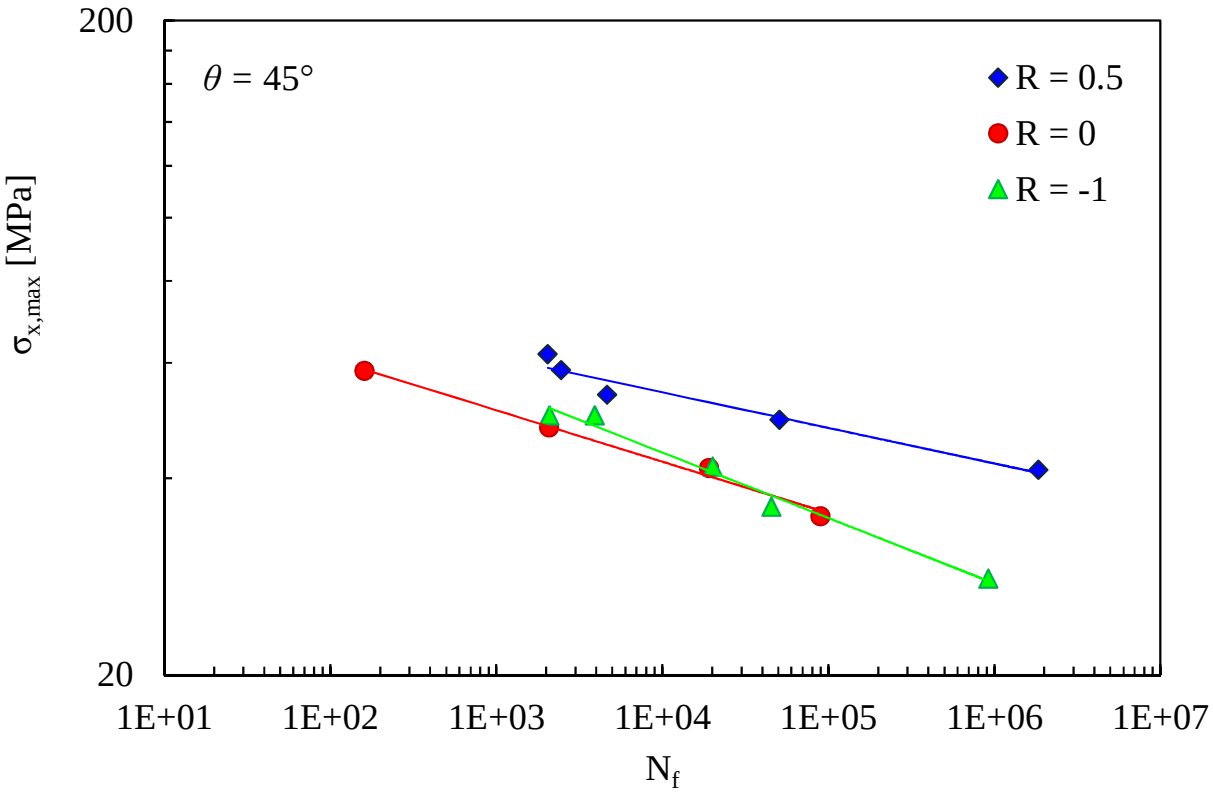

Figure 2.2 – Experimental data by El Kadi and Ellyin for $\theta = 45°$ at R = 0.5, 0, -1.

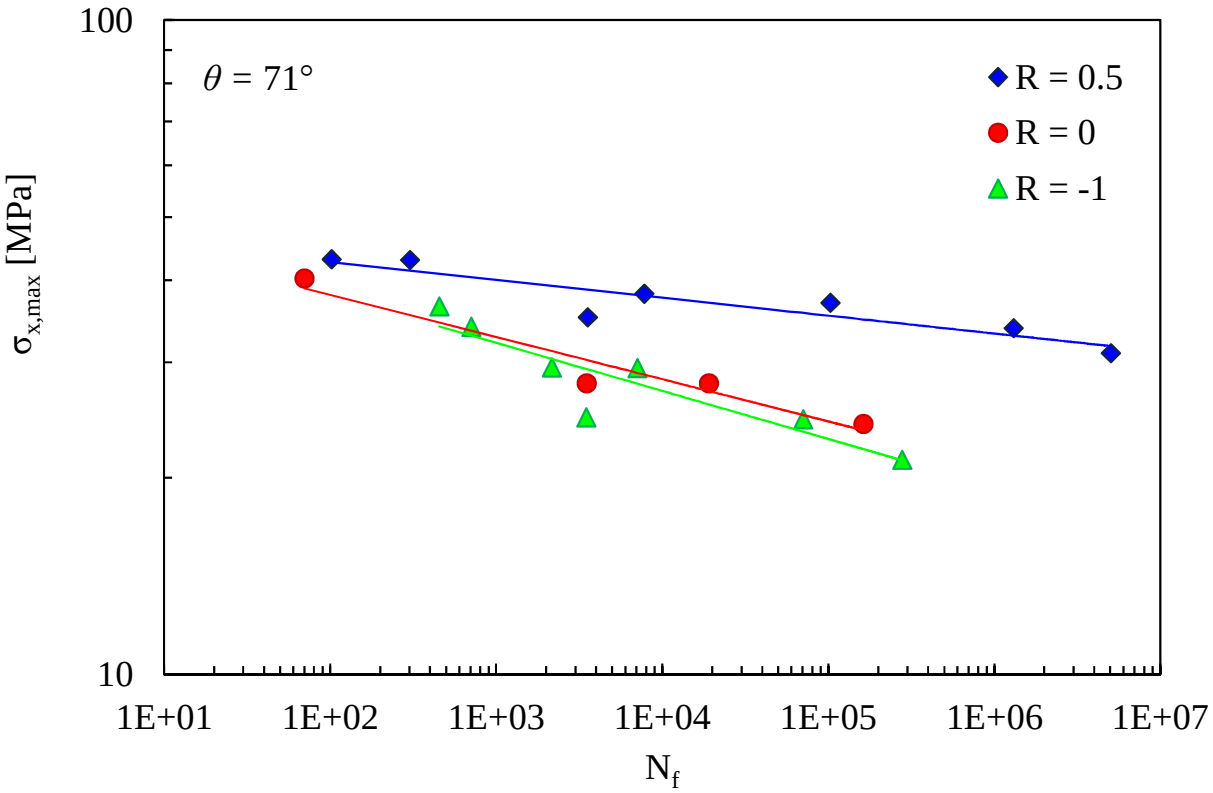

Figure 2.3 – Experimental data by El Kadi and Ellyin for $\theta = 71°$ at R = 0.5, 0, -1.

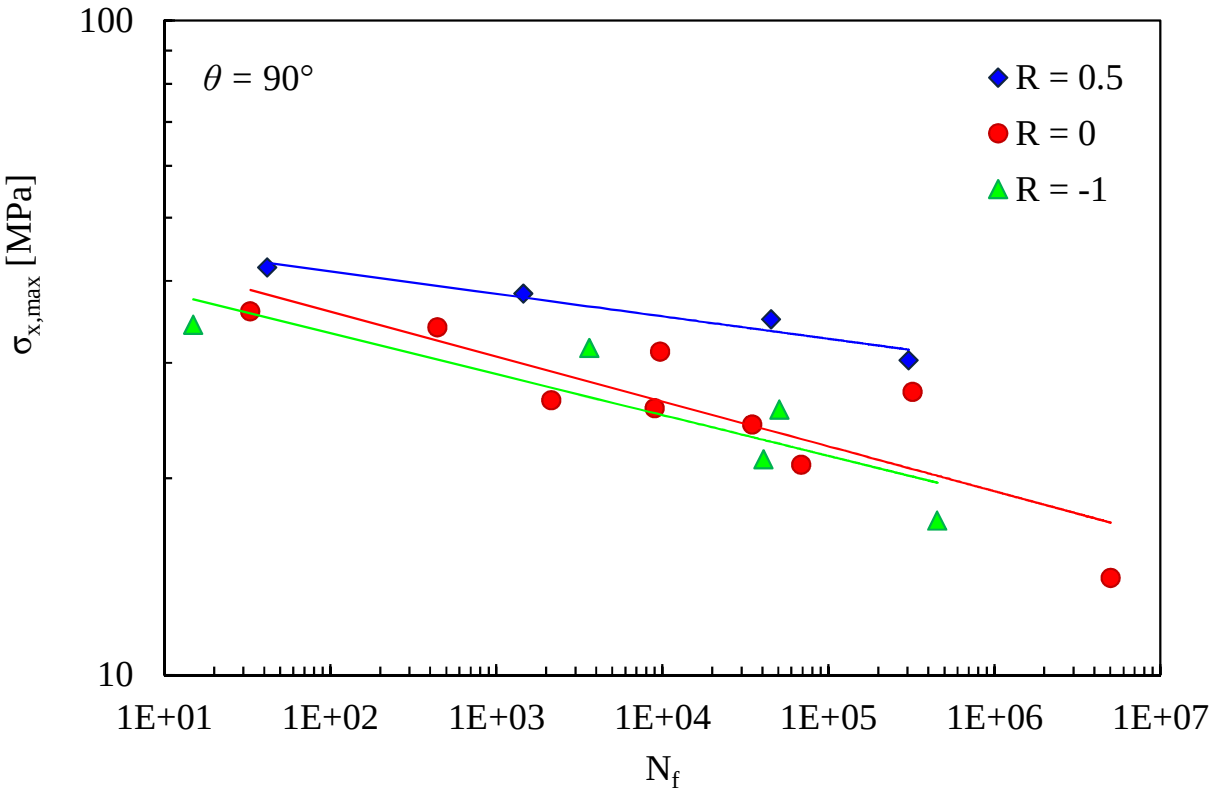

Figure 2.4 – Experimental data by El Kadi and Ellyin for $\theta = 90°$ at R = 0.5, 0, -1.

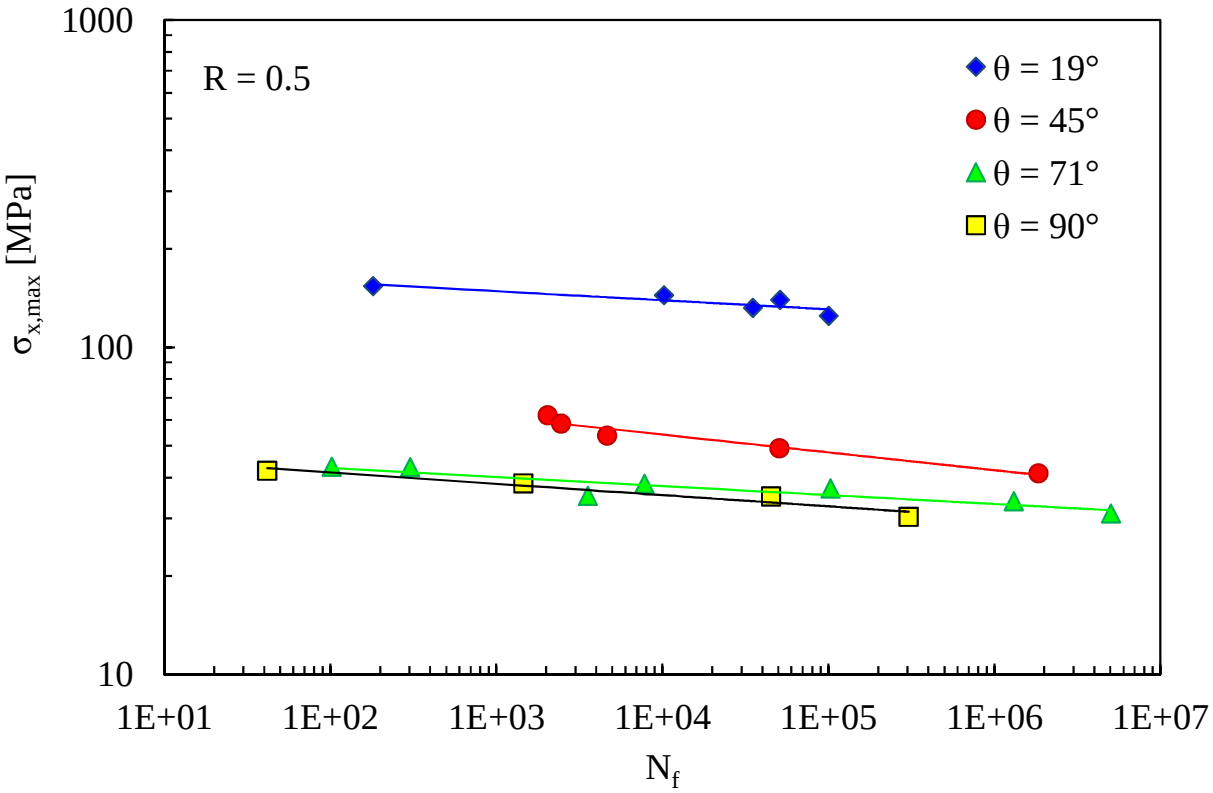

Figure 2.5 – Experimental data by El Kadi and Ellyin at R = 0.5 for $\theta = 19,\ 45,\ 71,\ 90°$.

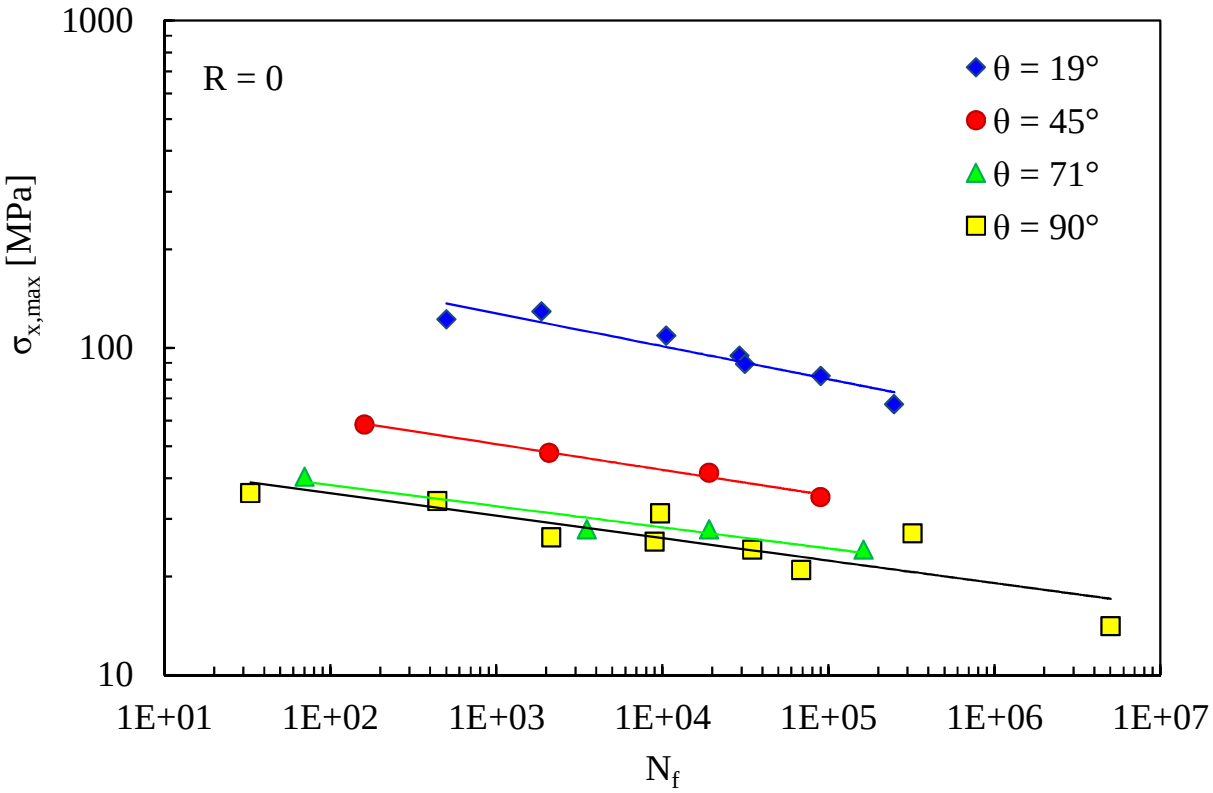

Figure 2.6 – Experimental data by El Kadi and Ellyin at R = 0 for $\theta = 19,\ 45,\ 71,\ 90°$.

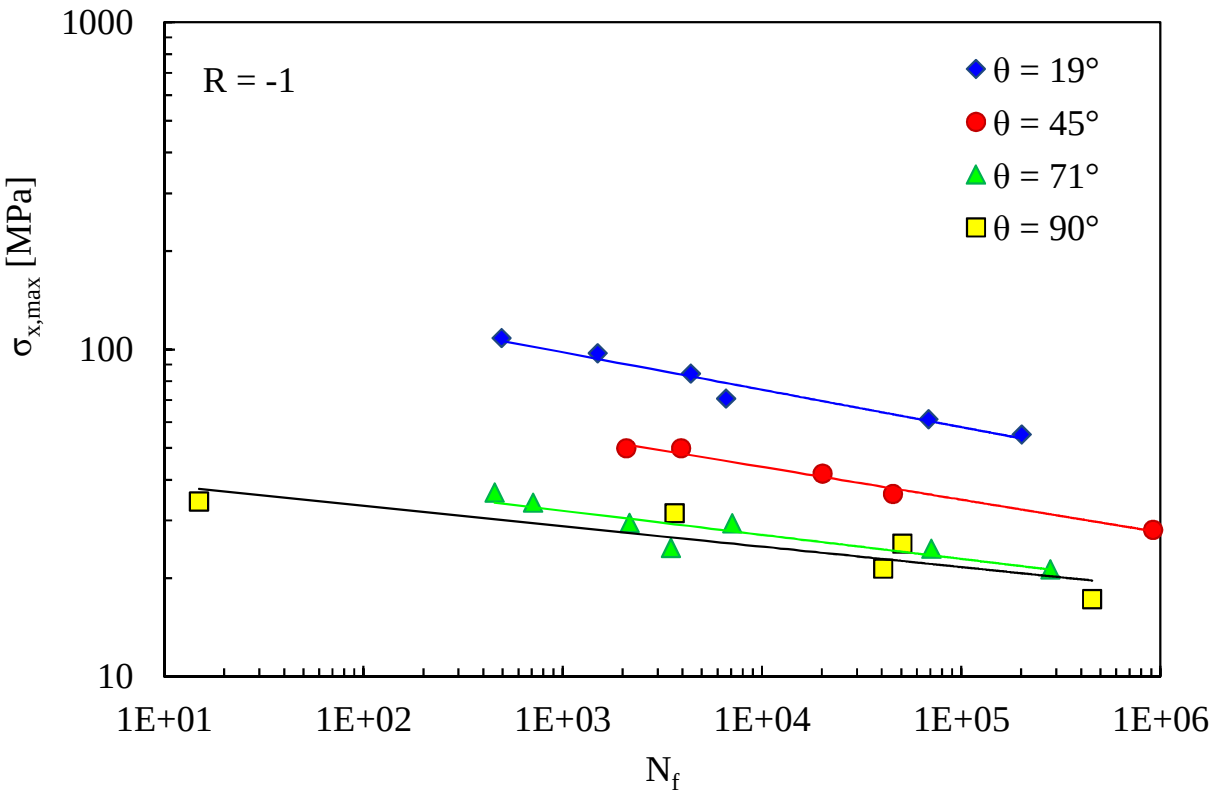

Figure 2.7 – Experimental data by El Kadi and Ellyin at R = -1 for $\theta = 19,\ 45,\ 71,\ 90°$.

From Figures 2.1, 2.2, 2.3 and 2.4 it is possible to observe that, as a general trend, the higher the stress ratio is, the higher the fatigue life. This behavior is shown also by metallic materials. However, if this trend is evident for $\theta = 19°$, the others fibers angles exhibit fatigue curves at R = 0 and R = -1 that are very similar, sometimes even overlapped, while the fatigue curves at R = 0.5 remain separated. The slope of the fatigue curves appears to become steeper at lower stress ratios, with the exception of $\theta = 90°$, that may be caused anyway by the statistical data scattering. From this observation, it is possible to state that the effect of different stress ratios is larger at lower loads (higher number of cycles to failure).

Figures 2.5, 2.6 and 2.7 show that the fatigue life shortens as the off-axis angle grows. Only marginal variations of the slope is observed, compatible with statistical data scattering.

Figures 2.8 to 2.12 report the experimental data by El Kadi and Ellyin in terms of stress amplitude versus mean stress ($\sigma_{2,a}$- $\sigma_{2,m}$, Haigh-type or "constant fatigue life" diagrams), for all the tested fibers angles and also for N = 10^6. It is possible to observe that for all fibers orientations (with the exception of $\theta = 45°$), at a macroscopic level and for a fixed number of cycles to failure, a lower stress ratio enables to bear higher stress amplitudes. All the curves appear to converge to the point representing the static strength in x direction. From the constant fatigue life diagram for N = 10^6 (Figure 2.12), it is possible to observe that, at a qualitative level, the trend of the allowable stress amplitude seems not to change respect to the off-axis angle.

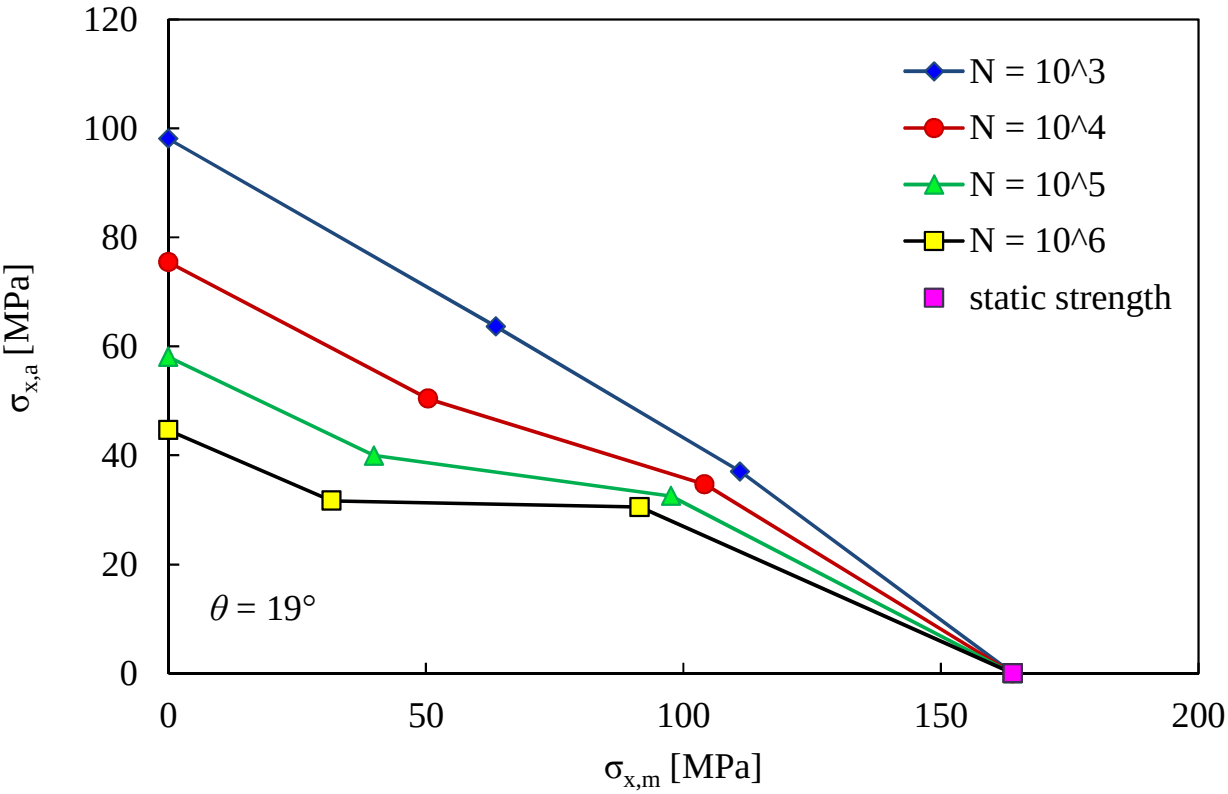

Figure 2.8 – $\sigma_{2,a}$- $\sigma_{2,m}$ diagram for experimental data by El Kadi and Ellyin, $\theta = 19°$.

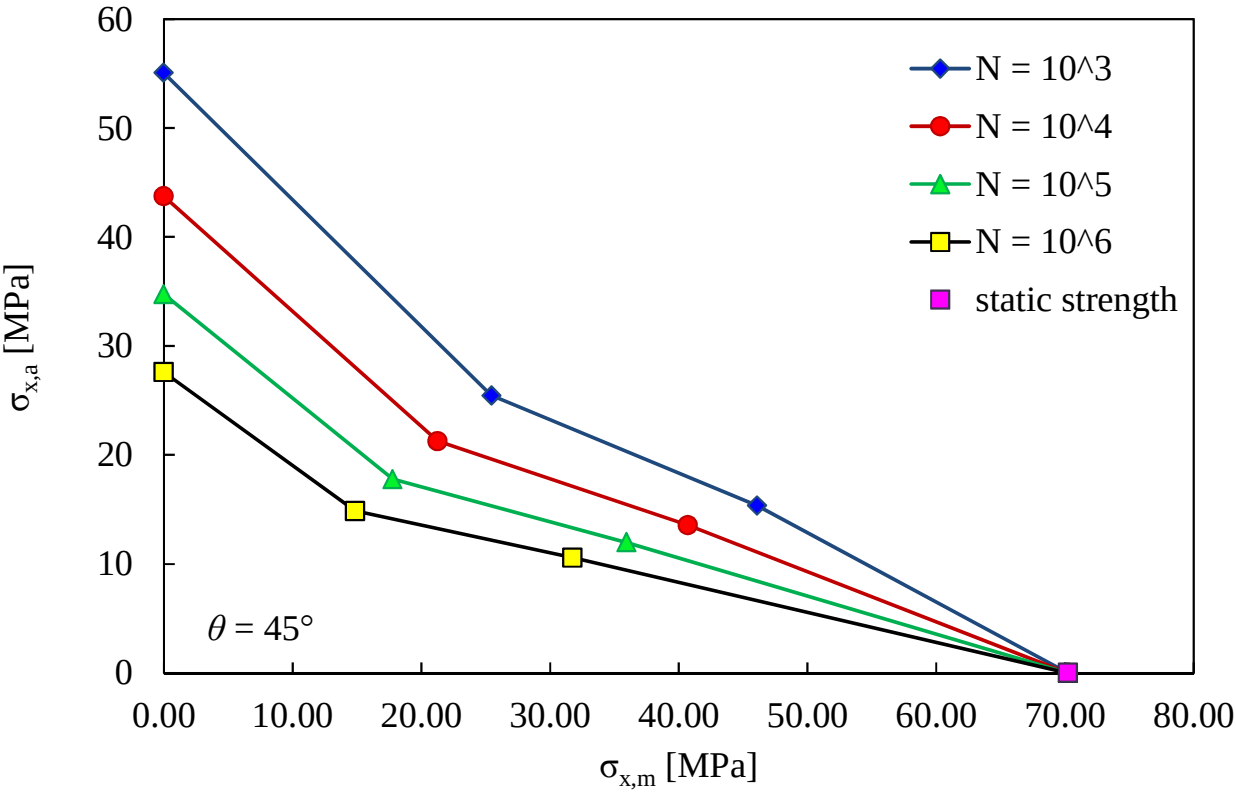

Figure 2.9 – $\sigma_{2,a}$- $\sigma_{2,m}$ diagram for experimental data by El Kadi and Ellyin, $\theta = 45°$.

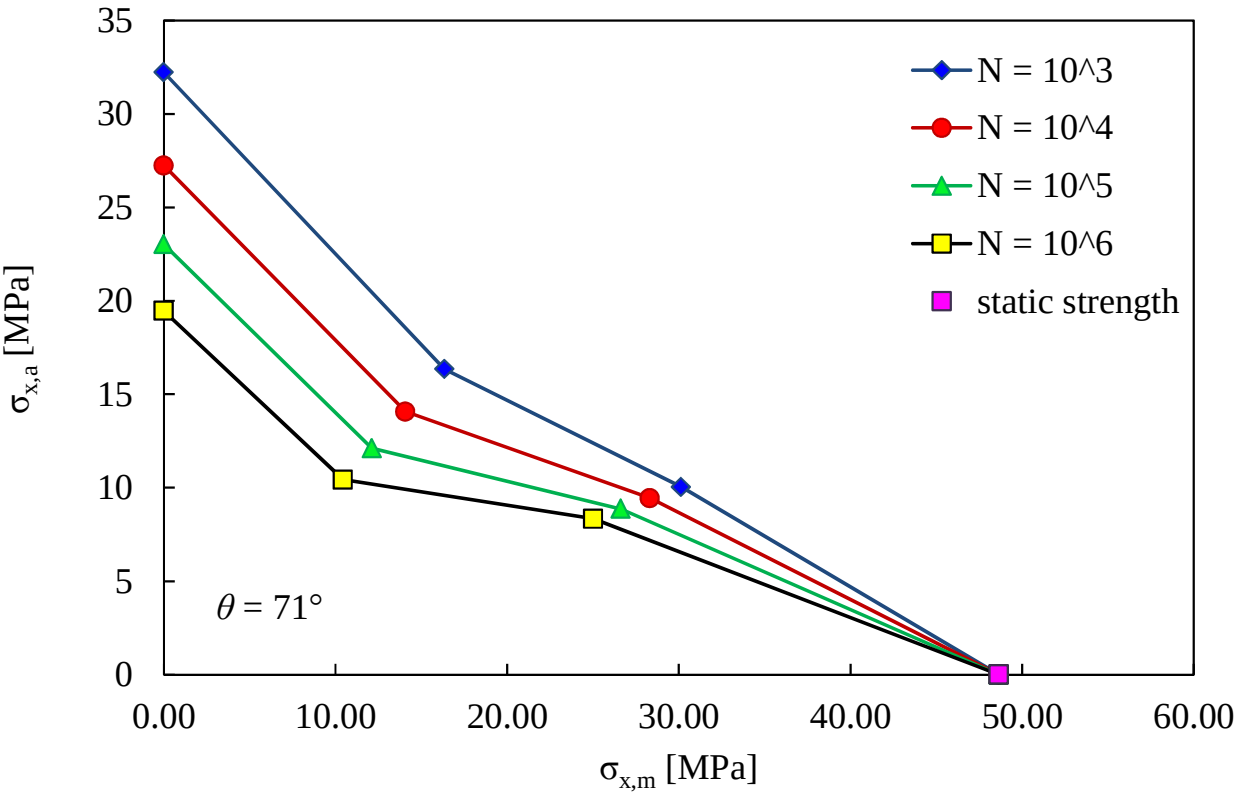

Figure 2.10 – $\sigma_{2,a}$- $\sigma_{2,m}$ diagram for experimental data by El Kadi and Ellyin, $\theta = 71°$.

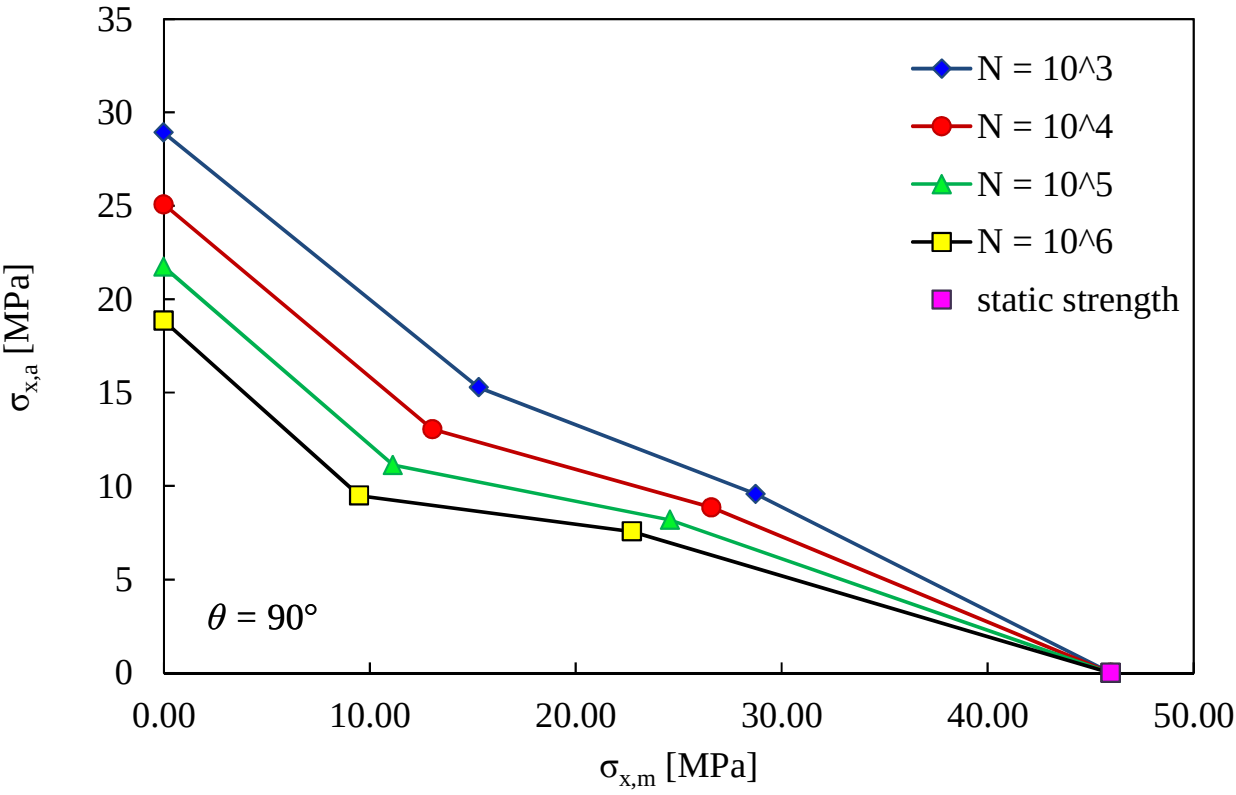

Figure 2.11 – $\sigma_{2,a}$- $\sigma_{2,m}$ diagram for experimental data by El Kadi and Ellyin, $\theta = 90°$.

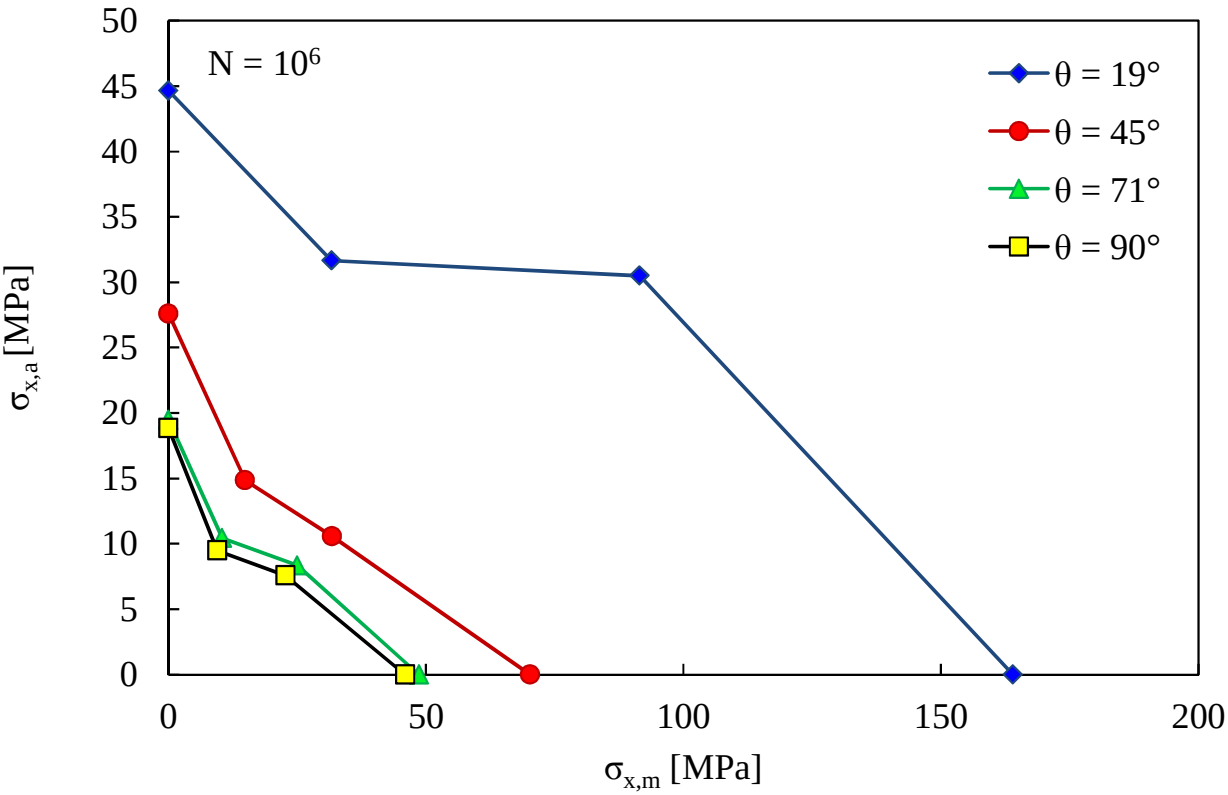

Figure 2.12 – $\sigma_{2,a}$- $\sigma_{2,m}$ diagram for experimental data by El Kadi and Ellyin, N = 10^6.

2.1.1.1 – Failure modes

For what concerns the failure of the specimens, El Kadi and Ellyin stated just that for all off-axis angles, all the specimens had an identical brittle fracture, that was matrix dominated and parallel to the fibers orientation. For the 0° specimens, instead, the failure mode depended on the magnitude of the stress, being characterized by sudden fibers breakage at higher stress levels and by progressive damage with delamination at lower stress. Hence, at a macroscopic level, no difference in failure modes was detected at different stress ratios.

2.1.2 – Experimental data by Kawai and Suda (2004)

Kawai and Suda [11] carried out a series of fatigue tests on unidirectional flat carbon/epoxy laminates, fabricated from prepregs tapes of P2053-17 (T800H/2500, TORAY), with fibers angles $\theta = 0,\ 10,\ 15,\ 30,\ 45,\ 90°$. Tests were conducted at a frequency of 10 Hz, under stress ratios R = 0.5, 0.1, -1 (-0.3 for $\theta = 0°$). Tension-compression tests were conducted using anti-buckling guides. Their results are shown in Figures 2.13 to 2.20. As for El Kadi and Ellyin data, it was chosen not to

report the fatigue curves for $\theta = 0°$ since in this work the interest is focused on the matrix-dominated behavior.

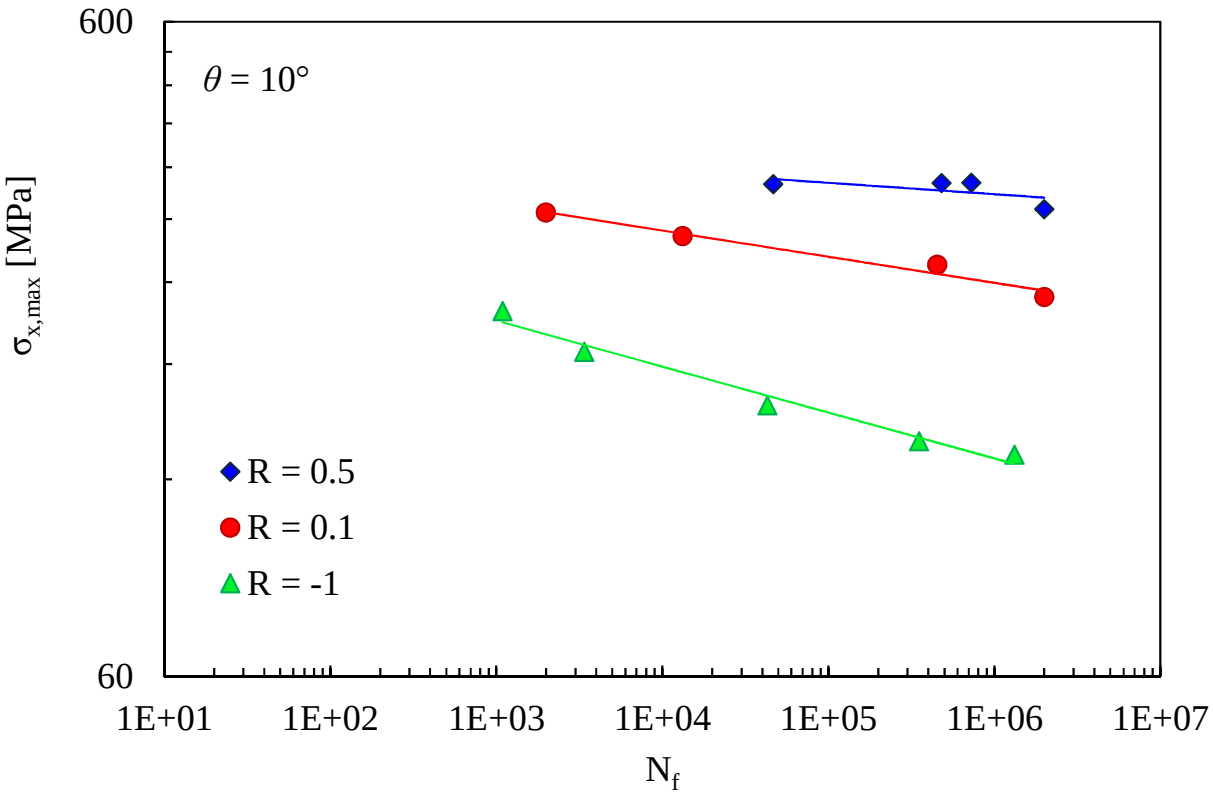

Figure 2.13 – Experimental data by Kawai and Suda for $\theta = 10°$ at R = 0.5, 0.1, -1.

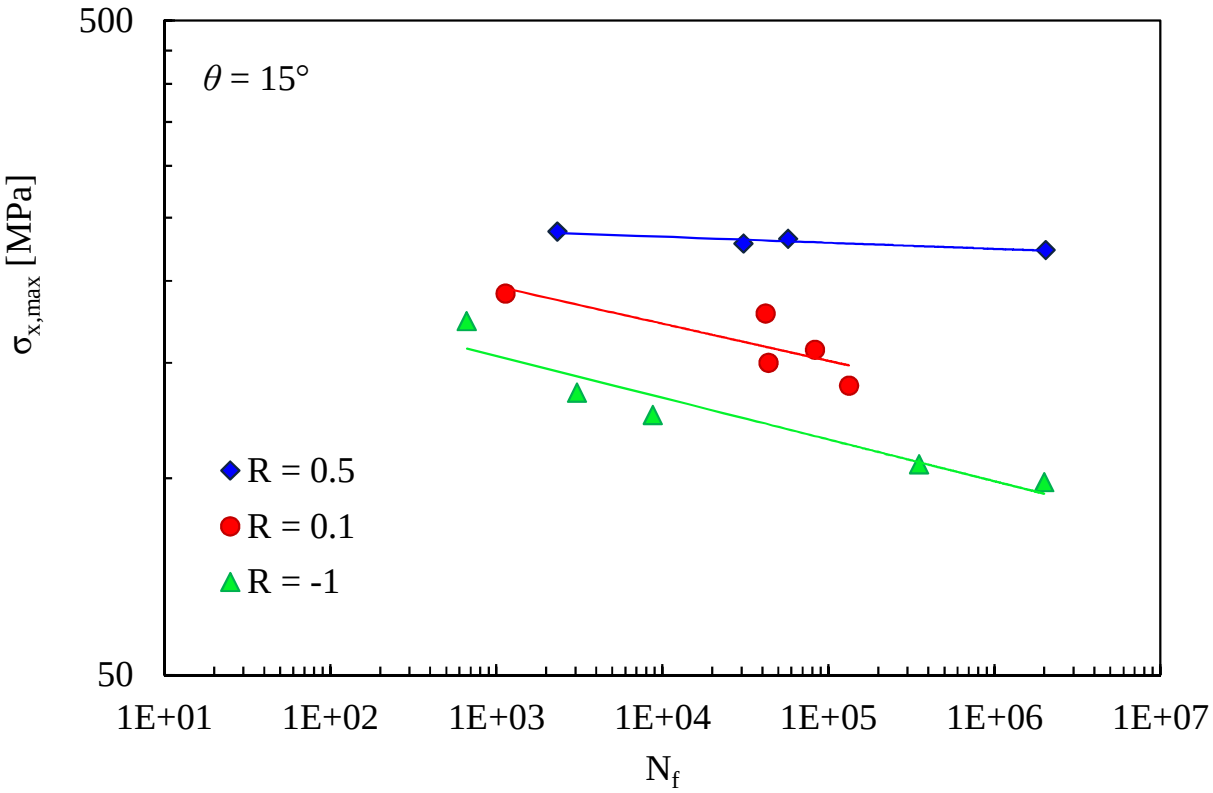

Figure 2.14 – Experimental data by Kawai and Suda for $\theta = 15°$ at R = 0.5, 0.1, -1.

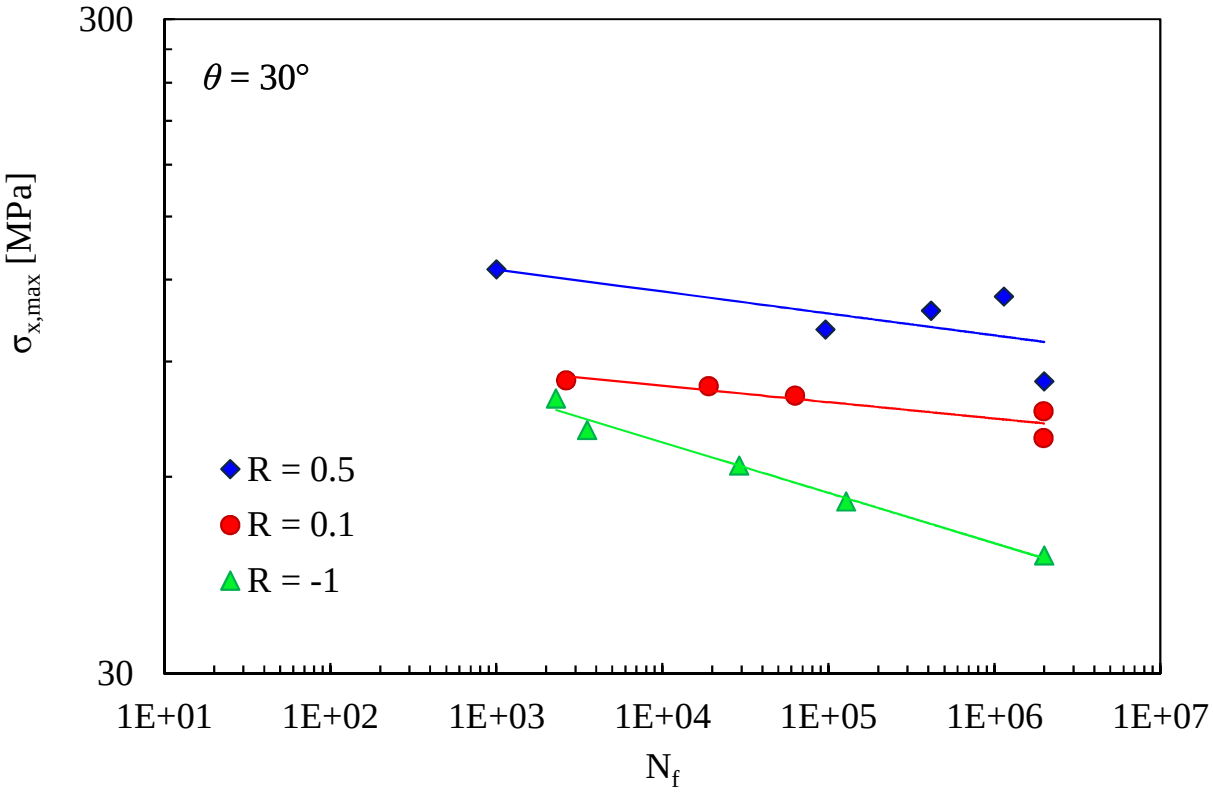

Figure 2.15 – Experimental data by Kawai and Suda for $\theta = 30°$ at R = 0.5, 0.1, -1.

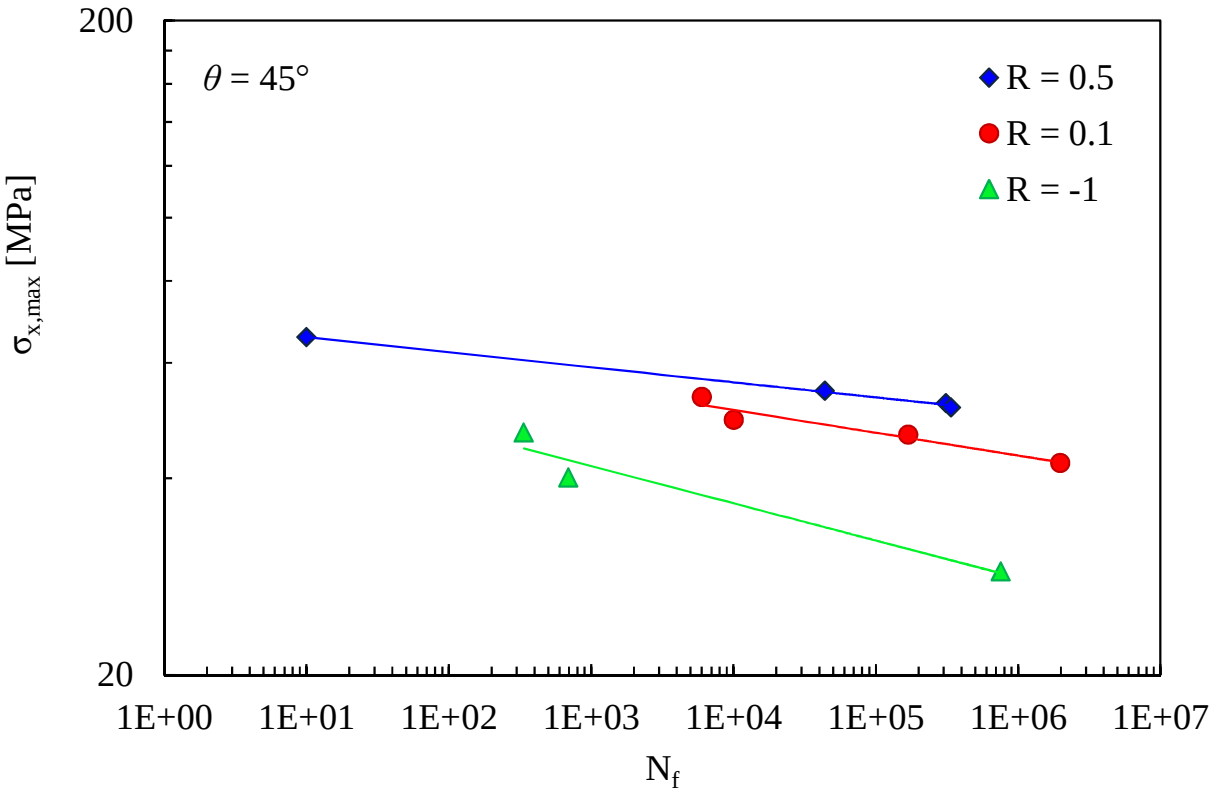

Figure 2.16 – Experimental data by Kawai and Suda for $\theta = 45°$ at R = 0.5, 0.1, -1.

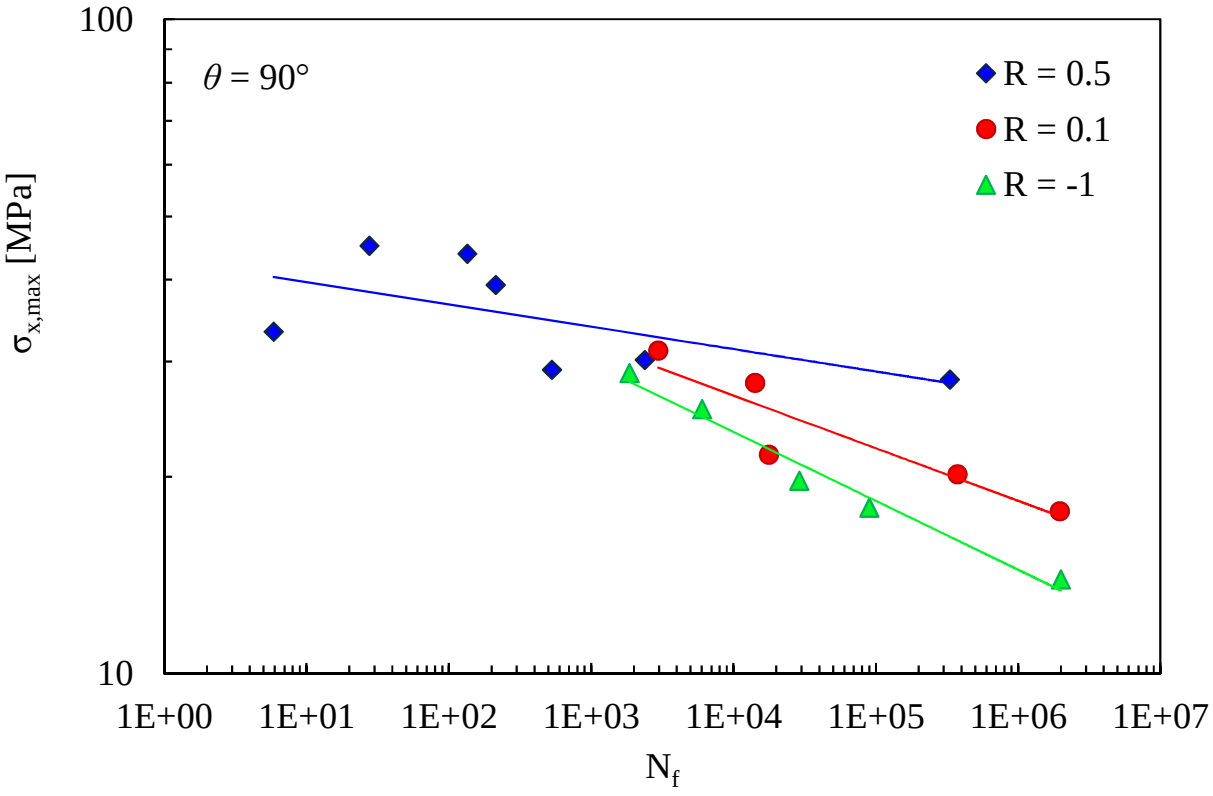

Figure 2.17 – Experimental data by Kawai and Suda for $\theta = 90°$ at R = 0.5, 0.1, -1.

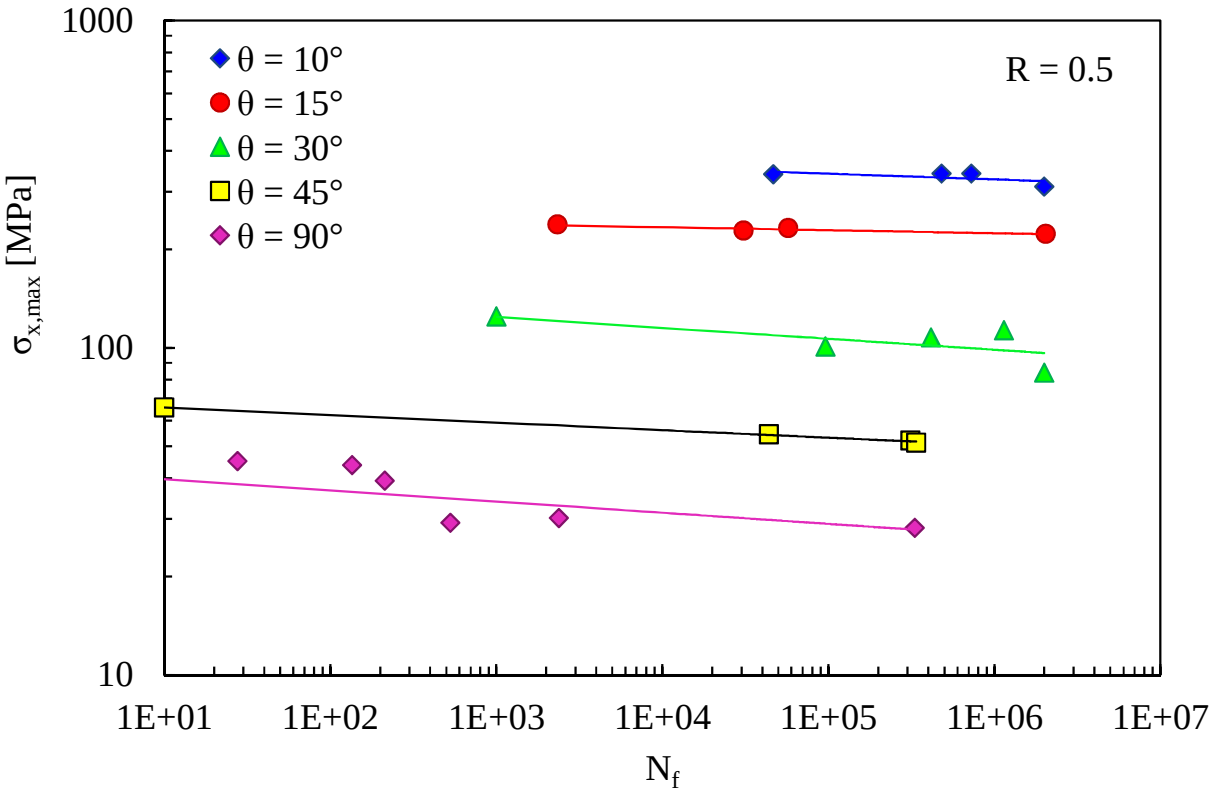

Figure 2.18 – Experimental data by Kawai and Suda at R = 0.5 for $\theta = 10,\ 15,\ 30,\ 45,\ 90°$.

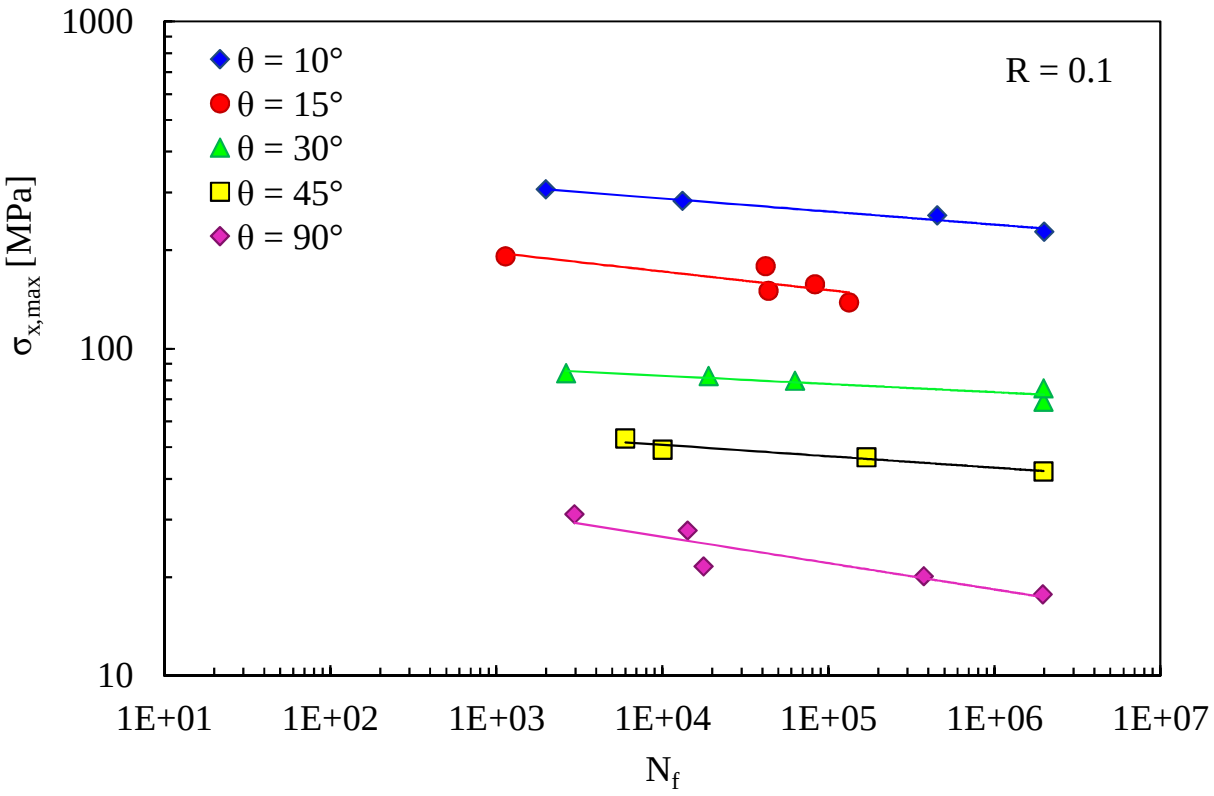

Figure 2.19 – Experimental data by Kawai and Suda at R = 0.1 for $\theta = 10,\ 15,\ 30,\ 45,\ 90°$.

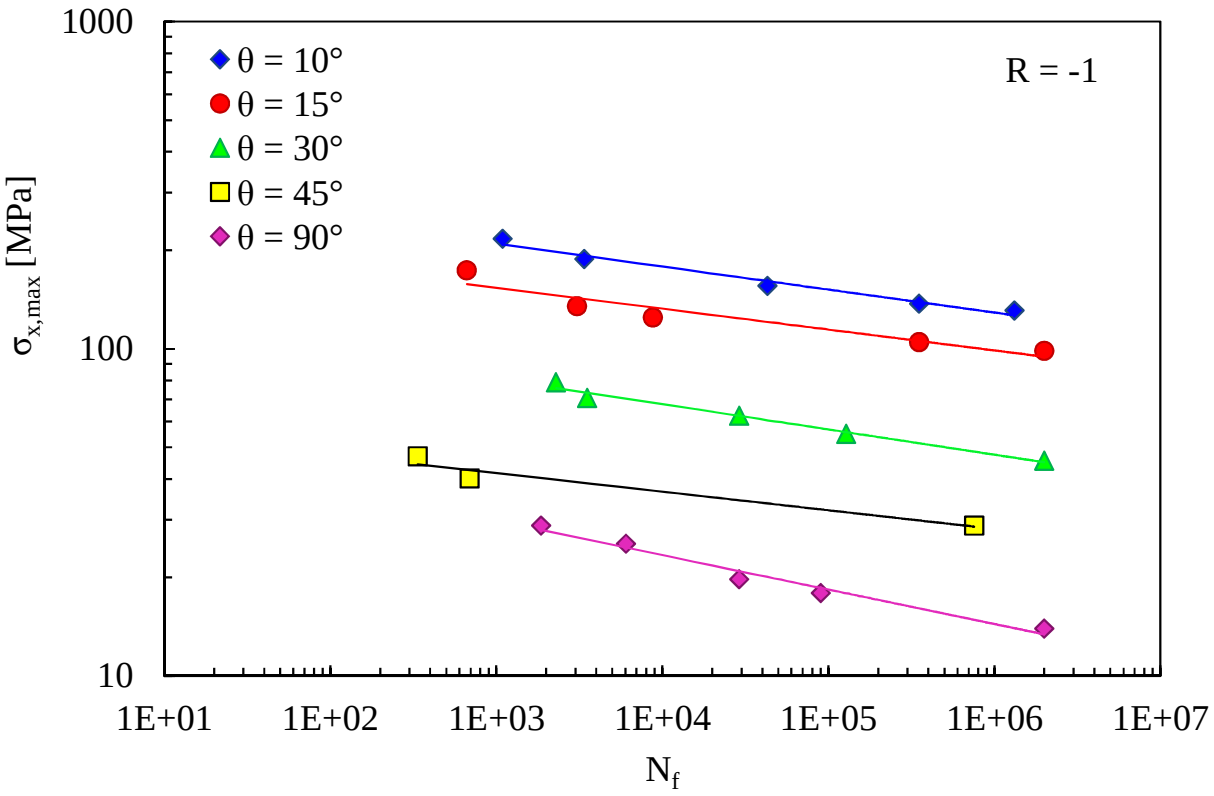

Figure 2.20 – Experimental data by Kawai and Suda at R = -1 for $\theta = 10,\ 15,\ 30,\ 45,\ 90°$.

These data confirm the trends shown by El Kadi and Ellyin: a lower fatigue life for lower stress ratios, for all fibers orientations; and steeper curves for lower stress ratios, with the only exception of $\theta = 30°$ (Figures 2.13 to 2.17). In this set of data there is no overlapping of fatigue curves. However, this is not necessarily in contrast with the results by El Kadi and Ellyin, since they tested R = 0 while Kawai and Suda R = 0.1. The effect of the stress ratio appears to be the same for all the fibers angles (Figures 2.18 to 2.20), as found by El Kadi and Ellyin.

It has to be pointed out that the anti-buckling guide may have influnced the results, in particular because it narrows down the zone in which the damage can take place (this problem may be overcome by tubular specimens, that were used in the present experimental campaign).

In analogy with what was done for the data by El Kadi and Ellyin, $\sigma_{2,a}$- $\sigma_{2,m}$ (Haigh-type, or "constant fatigue life") diagrams are drawn from the data set by Kawai and Suda, and reported in Figures 2.21 to 2.26 (again, the data regarding $\theta = 0°$ are chosen not to be reported in this work). The results are the same as El Kadi and Ellyin's ones: lower stress ratios allow the material to withstand larger stress amplitudes for a fixed number of cycles to failure, and the curves are steeper for lower N; the data seem to reasonably converge towards the data points representing the static

strength in the x direction. The effect of stress ratio appears to be qualitatively the same for all the off-axis angles (Figure 2.26).

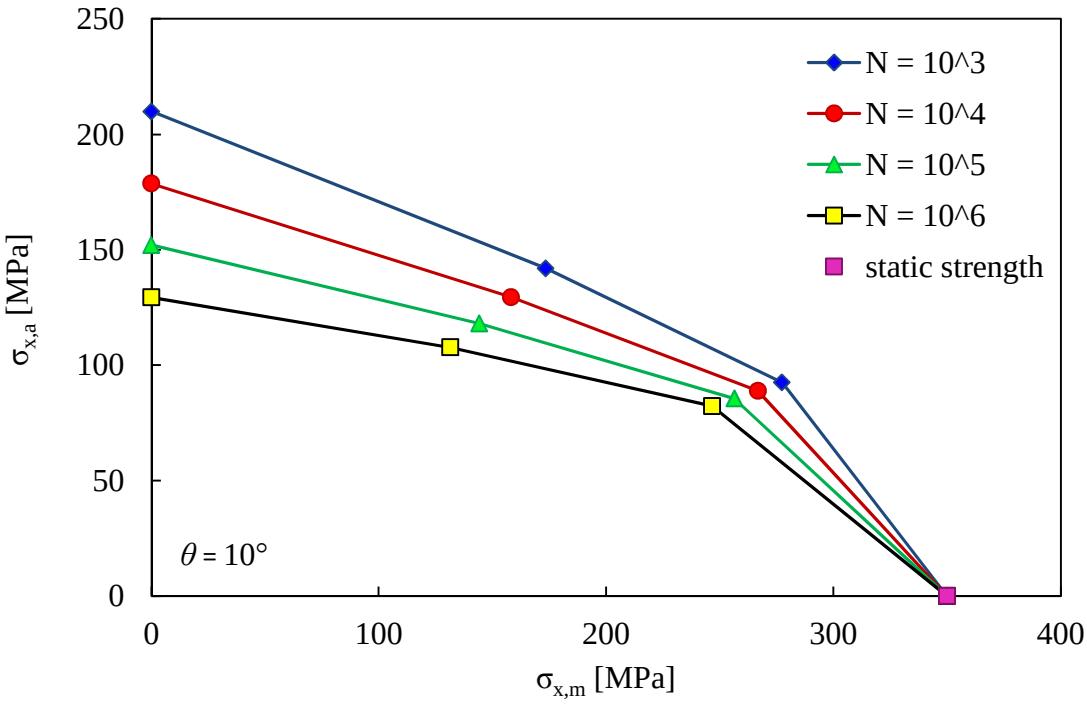

Figure 2.21 – $\sigma_{2,a}$- $\sigma_{2,m}$ diagram for experimental data by Kawai and Suda, $\theta = 10°$.

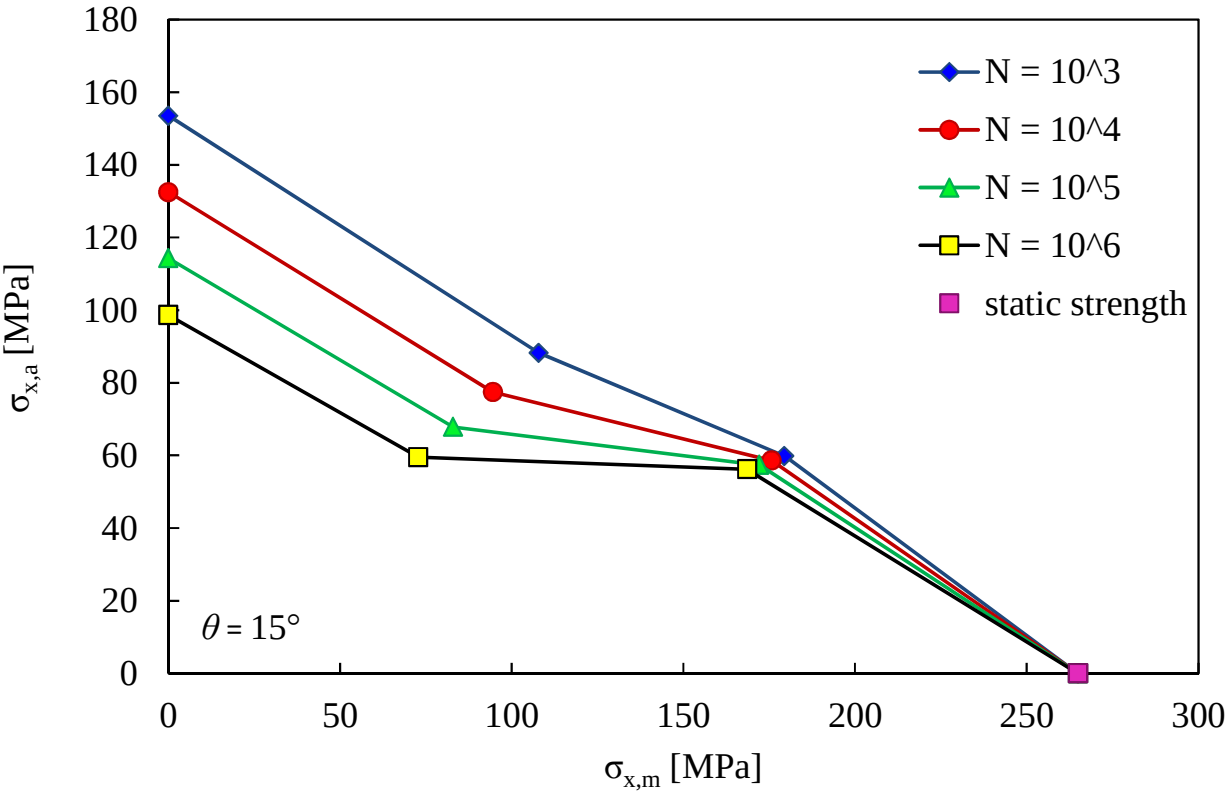

Figure 2.22 – $\sigma_{2,a}$- $\sigma_{2,m}$ diagram for experimental data by Kawai and Suda, $\theta = 15°$.

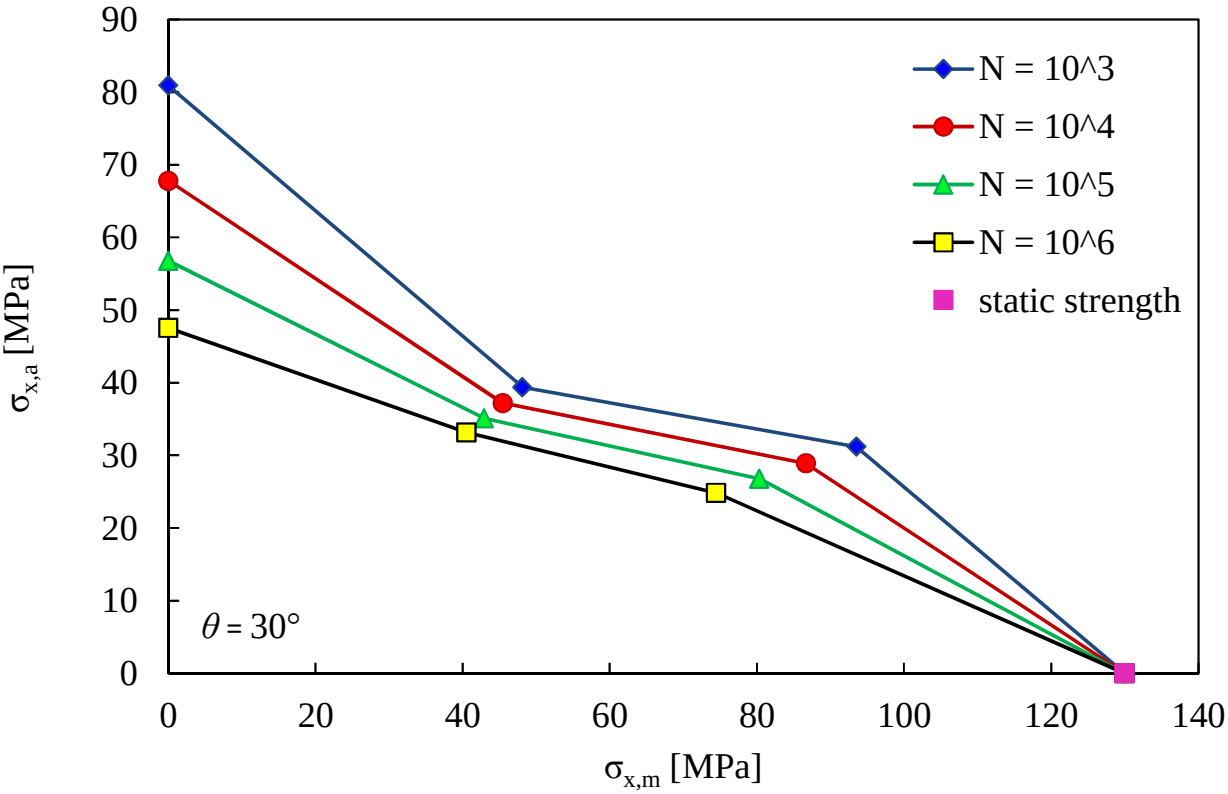

Figure 2.23 – $\sigma_{2,a}$- $\sigma_{2,m}$ diagram for experimental data by Kawai and Suda, $\theta = 30°$.

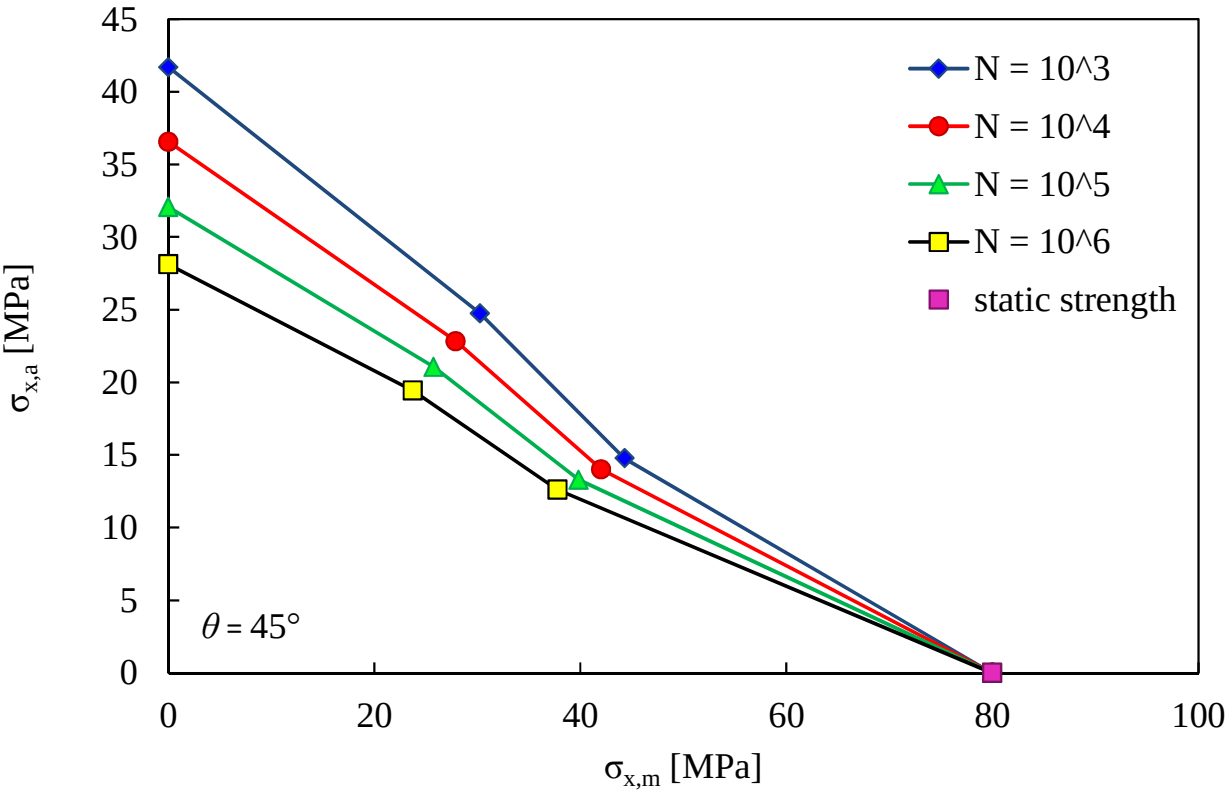

Figure 2.24 – $\sigma_{2,a}$- $\sigma_{2,m}$ diagram for experimental data by Kawai and Suda, $\theta = 45°$.

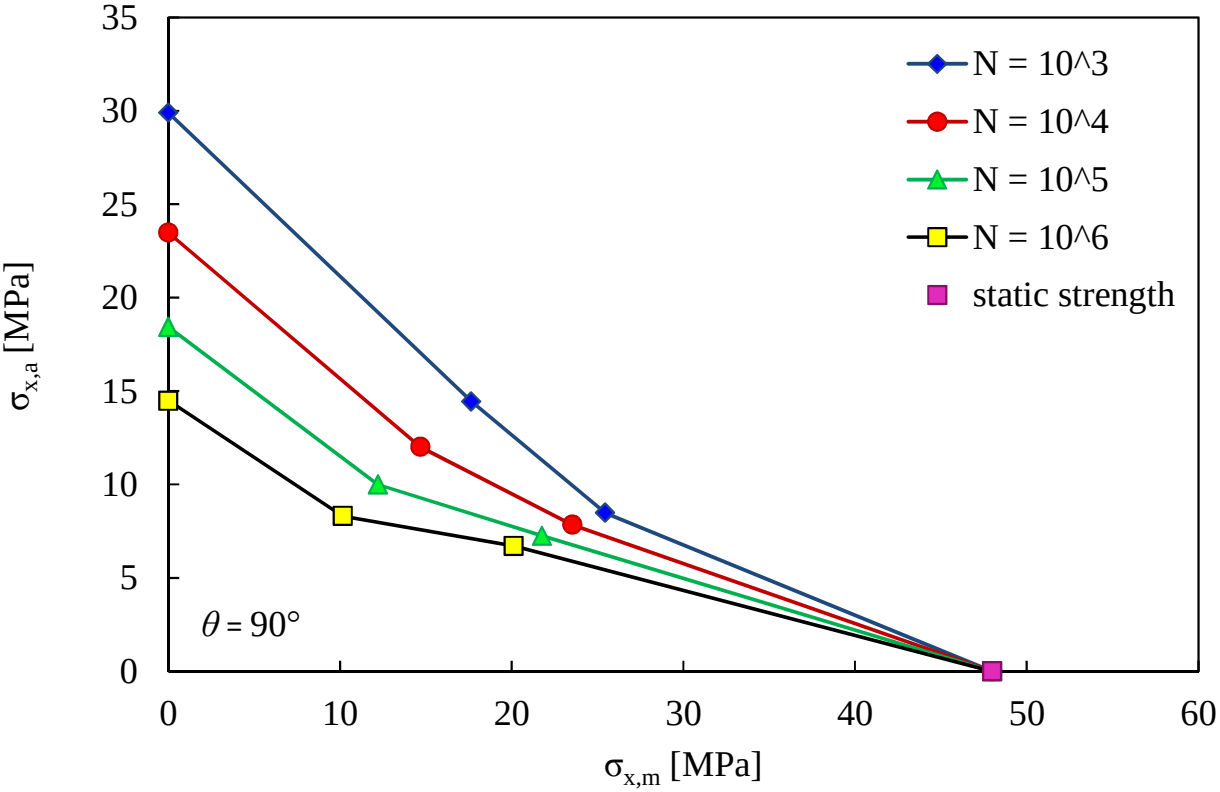

Figure 2.25 – $\sigma_{2,a}$- $\sigma_{2,m}$ diagram for experimental data by Kawai and Suda, $\theta = 90°$.

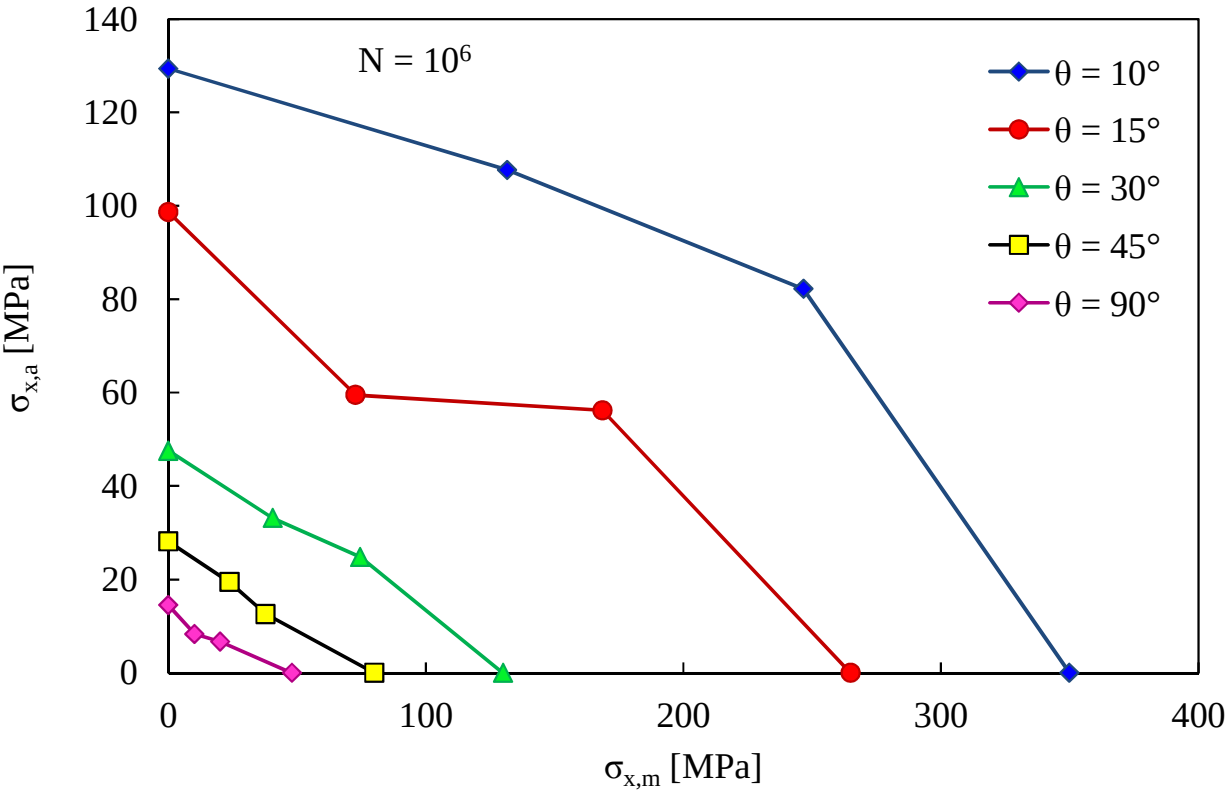

Figure 2.26 – $\sigma_{2,a}$- $\sigma_{2,m}$ diagram for experimental data by Kawai and Suda, $N = 10^6$.

2.1.2.1 – Failure modes

Kawai and Suda analyzed more deeply than El Kadi and Ellyin the fatigue failure modes under the different stress ratios: at R = 0.5 the specimen failed with parallel splitting in the fiber direction for $\theta = 0°$, while they failed in through-thickness cross sections along fibers for $0° < \theta \leq 90°$ (Figure 2.27); failures at R = 0.1 were very similar to the previous ones. In the case of $R = -1$ (-0.3), instead, the fatigue failure occurred in cross-section parallel to fiber and thickness directions for $30° \leq \theta \leq 90°$, while for $\theta = 10°, 15°$ it took place either in a similar way or in a local buckling mode with kinking (the variability being given by the local buckling instability just before the ultimate fatigue failure occurs);

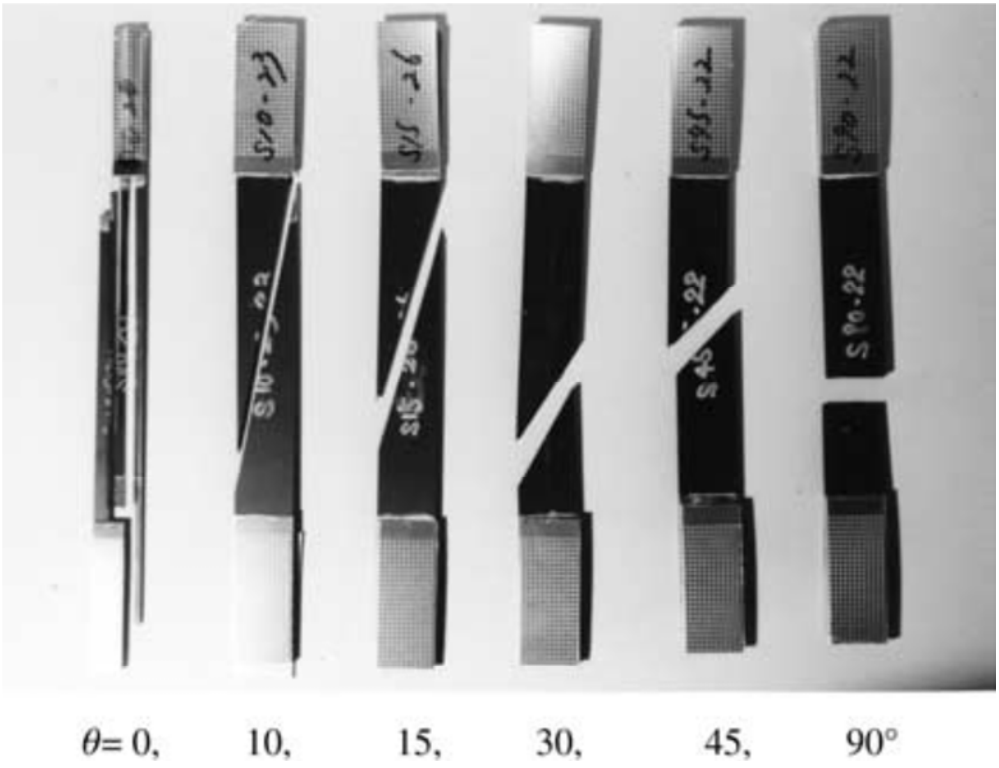

Figure 2.27 – Failure of Kawai and Suda specimens at R = 0.5 (taken from [11]).

Figure 2.28 – Failure of Kawai and Suda specimens at R = -0.1 (-0.3) (taken from [11]).

2.2 – Experimental data on tubular specimens

The only work in literature on the effect of the stress ratio on the fatigue life of composite tubes is the one by Qi and Cheng [17], in 2007. These authors studied the effect of the biaxiality ratio $\lambda = \tau_{xy}/\sigma_{yy}$ and R on filament wound E-glass/epoxy tubes with the configuration $[\pm\theta]_3$, in which $\theta = 35°, 55°, 70°$, at a frequency of 2 Hz. In particular, $\lambda = 0.5, 1, 2$ and $R = 0, -1$ were used for $\theta = 55°$ whereas just $\lambda = 0.5, 1$ and $R = 0, -1$ for $\theta = 35°$ and 70°. Their results concerning the effect of stress ratio are reported in Figure 2.29 (the final separation was considered as failure by the authors), and show that the curves at R = 0 are higher than the ones found at R = -1, and slightly steeper.

Although Qi and Cheng used tubular specimens, that are the same used in this experimental campaign (see Chapter 3), their data are not useful for the present investigation, that is focused on the matrix dominated behavior of a single lamina. Also, what is of interest here is when the first crack nucleates and not when the complete separation of the specimen occurs.

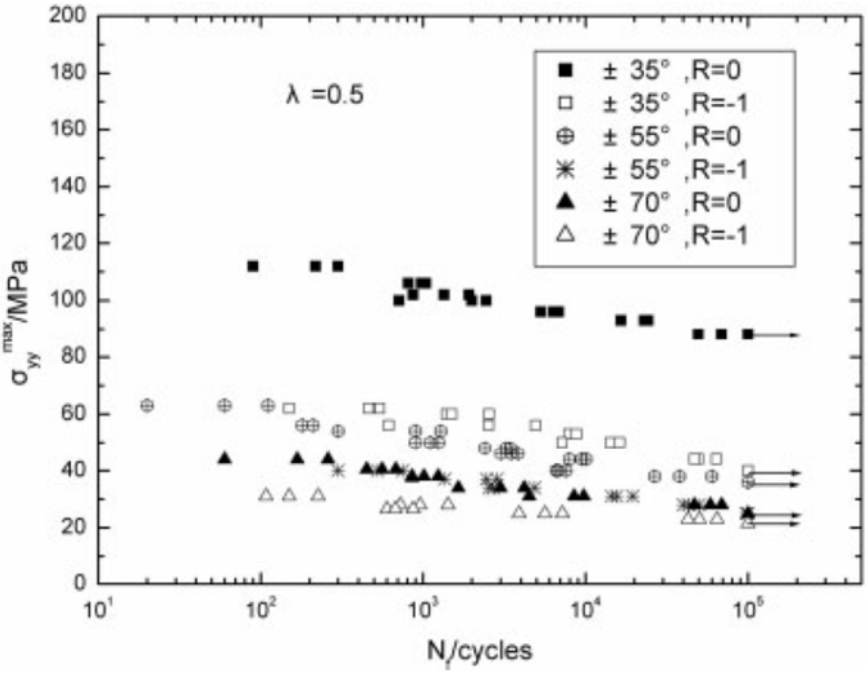

Figure 2.29 – Experimental data by Qi and Cheng for θ = ±35°,±55°,±70° at $R = -1,\ 0$ and λ = 0.5, taken from [17].

2.3 – Literature models that include the effect of stress ratio on the fatigue life

Although, as stated in the previous section, not many experimental data concerning the effect of stress ratio on fatigue life of composite materials are present in literature, several are the authors that looked for a way to consider the effect of this parameter in their fatigue life-predicting models. In this section, the works of these authors are presented in chronological order, focusing more on how the stress ratio is taken into account than on a thorough derivation of the models themselves.

2.3.1 – El Kadi and Ellyin's model (1994)

El Kadi and Ellyin [6] conducted an extensive testing on glass/epoxy specimens at $R = -1,\ 0,\ 0.5$, for fibers angles $\theta = 0,\ 19,\ 45,\ 71,\ 90°$, as described in section 2.1. They propose a life-prediction model based on the strain energy, starting from the considerations that failure results as a consequence of damage accumulation and that the damage is caused by an irrecoverable part of the stored energy:

$$\mathrm{d}W_{\text{damage}} = \mathrm{d}W_{\text{supplied}} - (\mathrm{d}Q + \mathrm{d}W_{\text{recoverable}}) \tag{2.1}$$

Since it is difficult to measure the heat loss ($\mathrm{d}Q$), El Kadi and Ellyin assume that the damage is proportional to the supplied energy:

$$\mathrm{d}W_{\text{damage}} \propto \mathrm{d}W_{\text{supplied}} \tag{2.2}$$

For non-negative stress ratios ($R \geq 0$), the strain energy is given by:

$$\Delta W^{+} = \frac{1}{2}(\sigma_{\max}\varepsilon_{\max} - \sigma_{\min}\varepsilon_{\min}) \tag{2.3}$$

For the uniaxial case, equation (2.3) can be re-written

$$\Delta W^{+} = \frac{1}{2} S_{11} (\Delta\sigma)^2 \left[\frac{(1+R)}{(1-R)}\right] \tag{2.4}$$

where S_{11} is the (1,1) element of the compliance matrix in the global (x,y) coordinate system and $\Delta\sigma$ is the stress range. By observing their experimental data, El Kadi and Ellyin hypothesize, for a generic off-axis angle, the following relationship between the strain energy and the number of reversals to failure ($2N_f$):

$$\Delta W^+ = k(\theta)(2N_f)^{\alpha(\theta)} \tag{2.5}$$

in which $k(\theta)$ is the intercept at $2N_f = 1$ and $\alpha(\theta)$ is the slope of the curve in a log-log coordinate system. The forms of the functions $k(\theta)$ and $\alpha(\theta)$ are found by fitting the experimental data. In particular, $\alpha(\theta)$ is found possible to be considered constant (and equal to α), while $k(\theta)$ results to be about the same as the maximum monotonic strain energy under tensile load, W_f^+, for the same fibers orientation angle. By normalizing the strain energy respect to $k(\theta)$, defining the *normalized strain energy*

$$\Psi^+ = \frac{\Delta W^+}{k(\theta)} = \frac{\Delta W^+}{W_f^+(\theta)} = (2N_f)^{\alpha} \tag{2.6}$$

El Kadi and Ellyin's model manages to collapse the experimental fatigue curves at $R = 0,\ 0.5$ for several fibers angles to a single – although not very narrow – band.

For negative stress ratios ($R < 0$) the expression of the normalized strain energy becomes:

$$\Psi = \Psi^+ + \Psi^- = \frac{\Delta W^+}{W_f^+} + \frac{\Delta W^-}{W_f^-} = (2N_f)^{\alpha} \tag{2.7}$$

where ΔW^- is the strain energy in the compression phase and W_f^- is the monotonic value of the strain energy under compressive load. It can be noticed that equation (2.7) can be used as a general expression for any stress ratios, not only for negative ones. By means of it all the experimental data by El Kadi and Ellyin at $R = 0,\ 0.5,\ -1$ collapse into a single band, which anyway still remain quite large.

2.3.2 – Fawaz and Ellyin's model (1994)

Fawaz and Ellyin [7] propose a model, based on empirical observations, according to which the S–N curve of a general lamina under general loading conditions can be drawn from a reference S–N curve, obtained from a known lamina under known loading conditions (no specific impositions are requested to for the reference curve). In particular, if the reference curve is described by the equation

$$S_r = m_r \log(N) + b_r \tag{2.8}$$

then, according to Fawaz and Ellyin, the generic curve can be found, defining $\lambda_C = \sigma_y / \sigma_x$ and $\lambda_T = \tau_{xy} / \sigma_x$, through

$$S(\lambda_C, \lambda_T, \theta, R, N) = f(\lambda_C, \lambda_T, \theta)[g(R) m_r \log(N) + b_r] \tag{2.9}$$

in which $f(\lambda_C, \lambda_T, \theta)$ is assumed to be equal to the ratio between the static strength along the x-direction under the actual loading parameters $\lambda_C, \lambda_T, \theta$ and the static strength along the x direction under the reference loading parameters $\lambda_{C,r}, \lambda_{T,r}, \theta_r$, and the dependence on the stress ratio is explicated in this way:

$$g(R) = \frac{\sigma_{\max}(1-R)}{[\sigma_{\max,r} - \sigma_{\min,r}]} = \frac{(1-R)}{(1-R_r)} \tag{2.10}$$

where $[\sigma_{\max,r} - \sigma_{\min,r}]$ and R_r are, respectively, the stress range and the stress ratio applied to obtain the reference curve. It can be seen that, according to this model, the stress ratio is therefore hypothesized to have influence only on the slope of the fatigue curve, in particular the lower is R, the steeper is the curve, respect to the reference one. This model predicts with good accuracy the experimental data by El Kadi and Ellyin [6] for R = 0 and R = 0.5, while no comparing was reported in [7] concerning R = -1.The fact that the intercept of the fatigue curve in hypothesized not to be dependent on the stress ratio seems to be in accordance with El Kadi and Ellyin's data (at constant fibers angle).

2.3.3 – Plumtree and Cheng's model (1999)

Plumtree and Cheng [8] propose a life-predicting model based on the Smith-Wattson-Topper parameter, $P_N = \sigma_{\max}\Delta\varepsilon$ (it has the same units as a strain energy density). From the observation that the tip of a crack which formed in the matrix is subjected to two displacements – one due to an opening mode normal to the fibers (σ_{22}) and the other to an in-plane sliding or shear, parallel to the fibers (τ_{12}) – Plumtree and Cheng define the parameter

$$\Delta W_{tot}^{*} = \Delta W_1^{*} + \Delta W_2^{*} = \sigma_{22,\max}\Delta\varepsilon_{22} + \tau_{12,\max}\Delta\gamma_{12}/2 \qquad (2.11)$$

where $\sigma_{22,\max}$ and $\tau_{12,\max}$ are the maximum stresses in the fracture plane, that is assumed to be always parallel to the fibers, and they are numerically evaluated. The effect of the stress ratio on the fatigue life becomes evident if the strains in the previous equation are re-written:

$$\begin{aligned}\Delta\varepsilon_{22} &= \varepsilon_{22,\max}(1-R)\\ \Delta\gamma_{12} &= \gamma_{12,\max}(1-R)\end{aligned} \qquad (2.12)$$

ΔW_{tot}^{*} is assumed to be linear respect to N_f in a log-log scale. Applied to the experimental data obtained by El Kadi and Ellyin [6], this model succeeds in collapsing the fatigue curves obtained for R = 0.5, R = 0 and R = -1 to a single curve, although the scatter band is not very narrow, in particular because of the R = -1 data. Plumtree and Cheng suggested that this may be due to the fact that under tension-compression loading the damage is influenced also by fibers buckling, not considered in the definition of ΔW^{*}.

2.3.4 – Miyano et al.'s model (1999)

With the objective to find a fatigue-life model that could take in consideration the frequency (f), the temperature (T) and the stress ratio (R), Miyano et al. [9] hypothesizes a linear dependence fatigue strength upon stress ratio. Assuming also that the failure process is the same under CSR (continuous strain rate), creep and fatigue loadings, that the same time-temperature superposition principle is valid for all those types of loading, and that the damage cumulate linearly for non-decreasing stress process, they propose the following formula:

$$\sigma_f(t_f; f, R, T) = \sigma_{f:1}(t_f; f, T)R + \sigma_{f:0}(t_f; f, T)(1 - R) \quad (2.13)$$

in which the expression $(t_f; f, R, T)$ indicates that the strength is a function of the time to failure ($t_f = N_f / f$) for a given combination of f, R, T; $\sigma_f(t_f; f, R, T)$ is the fatigue strength, $\sigma_{f:0}(t_f; f, T)$ the master curve for fatigue strength at $R = 0$ (obtainable from tests with a single frequency at different temperatures) and $\sigma_{f:1}(t_f; f, T)$ the fatigue strength for $R = 1$ (that is the master curve for creep strength).

To support their model, Miyano et al. conducted some flexural fatigue tests on two carbon/epoxy systems, one with acrylic-derived fibers (T300/2500), the other with pitch-based ones (XN40/25C), and to a carbon/PEEK system (T300/PEEK). Their experimental data for different stress ratios show an analogous effect of this parameter on fatigue life as the one found by El Kadi and Ellyin [6], that is a lower fatigue life for lower R (Figure 2.40, in which the dotted lines represent the least square fit for experimental data of fatigue test at $R = 0.05$ and creep test). In the same figure, it can be seen that this model describes adequately the experimental S–N data for flexural fatigue strength at $R = 0.5$ for the acryl-derived-carbon/epoxy system, but it could not be applied to T300/PEEK and XN40/25C because of the crystallization of PEEK and the time-dependent behavior of the pitch-based carbon fibers, that cause the time-temperature superposition principle for CSR not to hold for creep strength. Moreover, no mention was made in [9] concerning the applicability of the model to negative stress ratios.

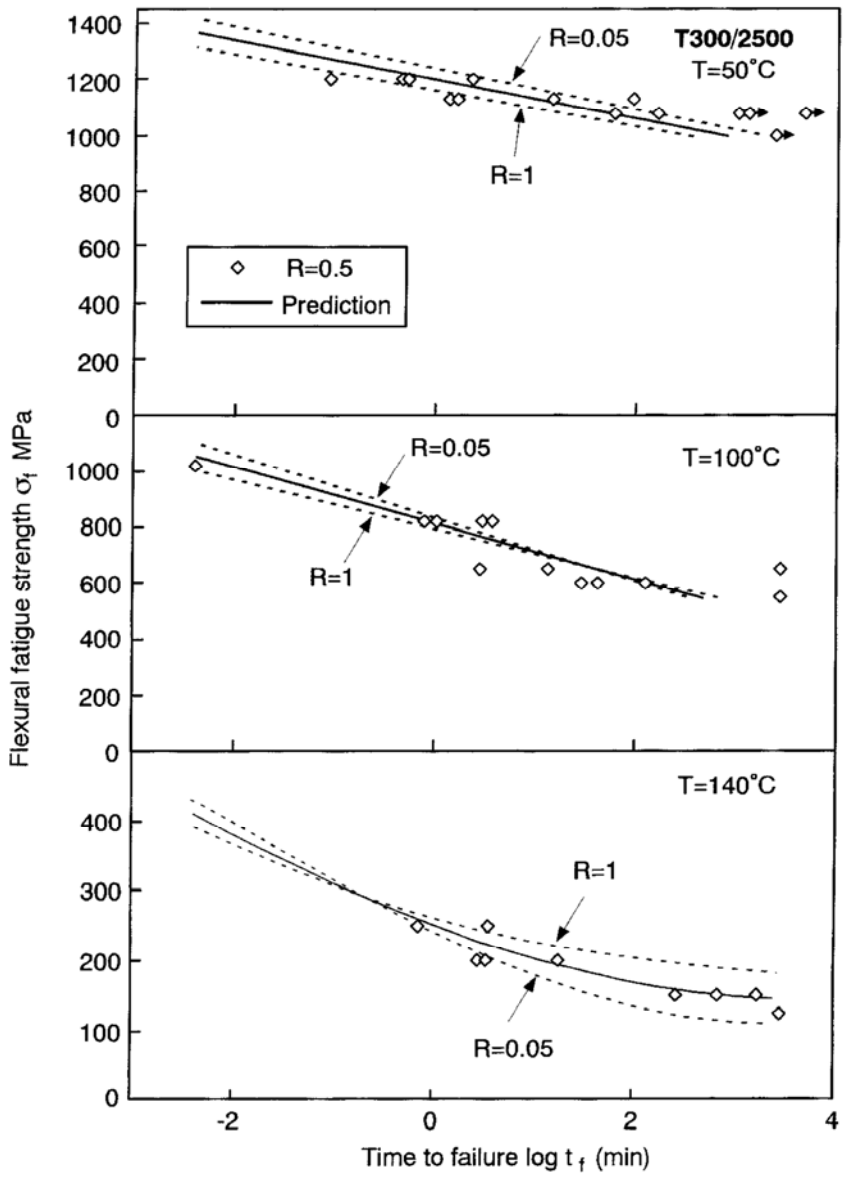

Figure 2.40 – Prevision of the flexural fatigue strength for T300/2500 at $R = 0.5$ at various temperatures by Miyano et al. model.

2.3.5 – Petermann and Plumtree's model (2001)

Petermann and Plumtree [10] developed another energy-based model: from the hypotheses, already mentioned above for Plumtree and Cheng [8], that the fracture plane is always parallel to the fibers (Petermann and Plumtree criticize the energy-based model by El Kadi and Ellyin [6] because it does not consider the fracture plane), and from the observation that the tip of a crack that formed in the matrix is subjected to one displacement due to an opening mode normal to the fibers (σ_{22}) and one displacement due to a shear parallel to the fibers (τ_{12}), they define a *unified fatigue parameter*:

$$W_{tot}^{*} = W_1^{*} + W_2^{*} = \lambda(\sigma_{22,\max}\varepsilon_{22,\max} + \tau_{12,\max}\gamma_{12,\max}) \tag{2.14}$$

where

$$\lambda = \frac{1-R^2}{2} \tag{2.15}$$

and W_1^{*} and W_2^{*} are the strain energy density contributed by, respectively, the stress component normal to the fibers and the pure shear:

$$\begin{aligned} W_1^{*} &= \frac{1}{2}(\sigma_{22,\max}\varepsilon_{22,\max} - \sigma_{22,\min}\varepsilon_{22,\min}) = \frac{1}{2}(1-R^2)\sigma_{22,\max}\varepsilon_{22,\max} \\ W_2^{*} &= \frac{1}{2}(\tau_{12,\max}\gamma_{12,\max} - \tau_{12,\min}\gamma_{12,\min}) = \frac{1}{2}(1-R^2)\tau_{12,\max}\gamma_{12,\max} \end{aligned} \tag{2.16}$$

The parameter, that is very similar to the one defined by Plumtree and Cheng [8], is derived only for tension-tension fatigue, i.e. $R \geq 0$. The stresses and strains in the equations above are calculated numerically, taking the highest combination of both stress components (which results to be in the matrix adjacent to the fiber-matrix interface) and the corresponding strains. Also in this case the relationship between the fatigue parameter and the number of cycles is supposed to be linear in a log-log scale.

Petermann and Plumtree applied their model to the El Kadi and Ellyin's experimental data [6] at $R = 0$ and $R = 0.5$, managing to collapse the fatigue curves of fiber angles $\theta = 19°$, 45° and 71° to a single one, even if the scatter band is still quite large. Their model could also predict, with good agreement, the fatigue curves at $R = 0$, $\theta = 45°$, at $R = 0$, $\theta = 19°$, and at $R = 0$, $\theta = 71°$ from the data obtained at $R = 0.5$, $\theta = 45°$. However, Petermann and Plumtree themselves admit that their model cannot predict fatigue life for negative stress ratios since tension and compression do not contribute in equal parts to the damage development. Also, predictions for $\theta = 90°$ were not shown in their work.

2.3.6 – Kawai and Suda's model (2004)

Kawai and Suda [11] performed fatigue tests on carbon-epoxy unidirectional plain laminates, with different fibers orientation ($\theta = 0°,\ 10°,\ 15°,\ 30°,\ 45°,\ 90°$), at stress ratios $R = 0.5,\ 0.1,\ -1$ for $\theta > 0°$ and $R = 0.5,\ 0.1,\ -0.3$ for $\theta = 0°$, as reported in section 2.1. For what concerns the

modeling, Kawai and Suda choose to ignore the details of the failure processes and assume that the damage development could be described by

$$\frac{d\omega}{dN} = K\Phi^{n(R)}\left(\frac{1}{1-\omega}\right)^{k} \tag{2.17}$$

where ω is a scalar damage variable, K and k are material's constant, the fatigue exponent n is postulated to be dependent on R, and Φ is a fatigue strength parameter, assumed equal to a *non-dimensional effective stress,* $\sigma^{*}_{\max}$, derived from the Tsai Hill static failure criterion:

$$\sigma^{*}_{\max} = \sqrt{\left(\frac{\sigma_{11,\max}}{X}\right)^{2} - \frac{\sigma_{11,\max}\sigma_{22,\max}}{X^{2}} + \left(\frac{\sigma_{22,\max}}{Y}\right)^{2} + \left(\frac{\tau_{12,\max}}{S}\right)^{2}} \tag{2.18}$$

where X, Y and S denote, respectively, the longitudinal strength, the transversal strength and the shear strength of the material. The non-dimensional effective stress can also be written

$$\sigma^{*}_{\max} = \Omega(\theta)\sigma_{x,\max} \tag{2.19}$$

where

$$\Omega(\theta) = \sqrt{\frac{\cos^{4}\theta}{X^{2}} - \frac{\cos^{2}\theta\sin^{2}\theta}{X^{2}} + \frac{\sin^{4}\theta}{Y^{2}} + \frac{\sin^{2}\theta\cos^{2}\theta}{S^{2}}} \tag{2.20}$$

Integrating equation (2.17) by imposing $\omega = 0$ for $N = 0$ and assuming $\omega = 1$ for $N = N_f$, and setting $N_f = 1/2$ for $\sigma^{*}_{\max} = 1$ the following S–N relation is found:

$$2N_f = \frac{1}{(\sigma^{*}_{\max})^{n(R)}} \tag{2.21}$$

that is linear in logarithmic scale. The effect of the stress ratio is in the fatigue exponent, meaning that it is considered to influence only the slope of the fatigue curve. Kawai and Suda find the expression of $n = n(R)$ by simply fitting their experimental data with the function

$$n(R) = A\exp\left(\frac{1}{1-R}\right) \tag{2.22}$$

This model describes the S–N curves of the experimental data of Kawai and Suda themselves with reasonable accuracy, but in some cases with quite large errors (for example for $\theta = 0,\ 45,\ 90°$). Also, the validity of the $n(R)$ function for stress ratios outside the range analyzed by the authors should be proved.

2.3.7 – Kawai's model (2004)

Kawai [12] elaborated a way to account for the effect of R on fatigue life without the need of experimental data. He defines the *modified fatigue strength ratio*

$$\Psi_K = \frac{\sigma_a}{\sigma_B - \sigma_m} = \frac{\frac{1}{2}(1-R)\psi}{1-\frac{1}{2}(1+R)\psi} \tag{2.23}$$

in which σ_a is the alternating stress, σ_m the mean stress, σ_B the experimental static strength and $\psi = \sigma_{x,\max} / \sigma_B$ the *fatigue strength ratio* (the subscript *K* in Ψ_K is for distinguishing the symbol here used from the analogous symbol used by El Kadi and Ellyin). With this parameter, Kawai managed to collapse the all the data by Kawai and Suda [11] to a single band, even if it is quite large. The same result is achieved for the data by El Kadi and Ellyin [6], with a narrower resulting band.

Taking equations (2.19) and (2.20) and noting that $\sigma_{B(pred)} = 1/\Omega(\theta)$, so that

$$\sigma^*_{\max} = \frac{\sigma_{x,\max}}{\sigma_{B,pred}} \tag{2.24}$$

Kawai defines, in analogy with Ψ_K, the non-dimensional scalar quantity (called *modified non-dimensional effective stress*):

$$\Sigma^* = \frac{\sigma_a^*}{1-\sigma_m^*} = \frac{\frac{1}{2}(1-R)\sigma_{\max}^*}{1-\frac{1}{2}(1+R)\sigma_{\max}^*} \tag{2.25}$$

The evolution equation of the scalar fatigue damage (equation (2.17)) is then rewritten:

$$\frac{d\omega}{dN} = K(\Sigma^*)^{n^*}\left(\frac{1}{1-\omega}\right)^k \tag{2.26}$$

where ω is the scalar damage variable, K, n^* and k are materials constant and N is the number of cycles. The integration of equation (2.26) and the imposition of the same conditions as for Kawai and Suda (section 2.3.6), the following relation is drawn:

$$2N_f = \frac{1}{(\Sigma^*)^{n^*}} \tag{2.27}$$

that is a straight line on logarithmic scales. The S–N relationship for each off-axis angle θ can be found from the master S–N relationship, explicating equation (2.25) respect to $\sigma_{\max}$:

$$\sigma_{\max} = \frac{2\Sigma^*}{\Omega(\theta)[(1-R)+(1+R)\Sigma^*]} \tag{2.28}$$

Good prediction of the S–N curves of the data by Kawai and Suda [11] and by El Kadi and Ellyin [6] is reached with this model.

2.3.8 – Shokrieh and Taheri-Behrooz's model (2006)

Another energy-based model is proposed by Shokrieh and Taheri-Behrooz [13]. Taking the static failure criterion based on strain energy developed by Sandhu, according to which failure occurs when

$$\frac{\sigma_1\varepsilon_1}{X\varepsilon_{1ult}} + \frac{\sigma_2\varepsilon_2}{Y\varepsilon_{2ult}} + \frac{\sigma_6\varepsilon_6}{S\varepsilon_{6ult}} = 1 \tag{2.29}$$

(X, Y, S are the maximum static strengths, *ult* denotes ultimate strains), Shokrieh and Taheri-Behrooz define the fatigue parameter

$$\Delta W_{S-TB}^{*} = \Delta W_{I}^{*} + \Delta W_{II}^{*} + \Delta W_{III}^{*} = \frac{\Delta\sigma_1 \Delta\varepsilon_1}{X\varepsilon_{1ult}} + \frac{\Delta\sigma_2 \Delta\varepsilon_2}{Y\varepsilon_{2ult}} + \frac{\Delta\sigma_6 \Delta\varepsilon_6}{X\varepsilon_{6ult}} \tag{2.30}$$

whose addends are re-writable in the following way in order to explicate the effect of the stress ratio:

$$\Delta W_{I}^{*} = \frac{1}{X\varepsilon_{1ult}}(\sigma_{1,\max}\varepsilon_{1,\max} - \sigma_{1,\min}\varepsilon_{1,\min}) = \frac{1}{X^2}(\sigma_{1,\max}^2 - \sigma_{1,\min}^2) = \frac{1}{X^2}\frac{(1+R)}{(1-R)}(\Delta\sigma_1)^2 \tag{2.31}$$

(the expressions for the other two terms are analogous). The expression for ΔW_{S-TB}^{*} is developed only for positive stress ratios, i. e. tension-tension or compression-compression loadings. Anyway, a general expression, to consider also negative stress ratios, can easily be derived:

$$\Delta W_{1}^{*} = \frac{1}{X^2}\frac{1+\mathrm{sgn}(R)R^2}{(1-R)^2}(\Delta\sigma_1)^2 \tag{2.32}$$

where $\mathrm{sgn}(R)$ denotes the sign of the stress ratio (analogous expressions for the other two terms).

The authors re-adapt then the El Kadi-Ellyin model [6] to their fatigue parameter, hypothesizing the relation

$$\Delta W_{S-TB}^{*} = kN_f^{\alpha} \tag{2.33}$$

where k and α are material constant, independent of the stress ratio and fiber orientation.

This model manages to collapse to a single band the experimental data at different stress ratios obtained by Kawai and Suda [11] and by El Kadi and Ellyin [6] and predicts with good accuracy the fatigue curves of the same data sets.

2.3.9 – Varvani-Farahani et al.'s model (2007)

Varvani-Farahani et al. [14] propose an energy-based criterion that takes in consideration the damage mode involved during fatigue cycling: form the observation that the damage evolution

could be divided into three stages (in order of appearance: matrix cracking, matrix-fibers debonding, fibers cracking), Varvani-Farahani et al. define the total fatigue damage as

$$\Delta W = \Delta W_I + \Delta W_{II} + \Delta W_{III} \tag{2.34}$$

where the addends are the energy-based damage parameter for the three stages mentioned above:

$$\Delta W_I = \left[\frac{\Delta \tau_{\max} \Delta \frac{\gamma_{\max}}{2}}{(\tau_{ult} \frac{\tau_{ult}}{G})_m} \right] \tag{2.35}$$

in which $\Delta \tau_{\max} = \left(\frac{\sigma_1 - \sigma_3}{2}\right)_{r1} - \left(\frac{\sigma_1 - \sigma_3}{2}\right)_{r2}$, $\Delta \frac{\gamma_{\max}}{2} = \left(\frac{\varepsilon_1 - \varepsilon_3}{2}\right)_{r1} - \left(\frac{\varepsilon_1 - \varepsilon_3}{2}\right)_{r2}$, the subscripts *ult* denotes ultimate stress, *m* the matrix phase, *r1* and *r2* the first and the second reversal of fatigue cycle.

$$\Delta W_{III} = \left[\frac{\Delta \sigma_n \Delta \varepsilon_n}{(\sigma_{ult} \frac{\sigma_{ult}}{E})_f} \right] \tag{2.36}$$

where $\Delta \sigma_n = \left(\frac{\sigma_1 + \sigma_3}{2}\right)_{r1} - \left(\frac{\sigma_1 + \sigma_3}{2}\right)_{r2}$, $\Delta \varepsilon_n = \left(\frac{\varepsilon_1 + \varepsilon_3}{2}\right)_{r1} - \left(\frac{\varepsilon_1 + \varepsilon_3}{2}\right)_{r2}$, and the subscript *f* denotes the fiber phase;

$$\Delta W_{II} = \left[\frac{\Delta \tau_{12} \Delta \frac{\gamma_{12}}{2}}{(\tau_{ult} \frac{\tau_{ult}}{G})_m} + \frac{\Delta \sigma_{22} \Delta \varepsilon_{22}}{(\sigma_{ult} \frac{\sigma_{ult}}{E})_f} \right] \tag{2.37}$$

in which stresses and strains are calculated by means of classical lamination theory.

The effect of the stress ratio is included in the proposed parameter (maximum and minimum stresses are indeed present in the expression for ΔW), anyway the model does not succeed in collapsing experimental data at different stress ratios to a single band.

2.3.10 – Chen and Whang's model (2009)

Chen and Whang [15] hypothesize that the damage (D) during fatigue cycling could be expressed by the relation:

$$D(n) = \frac{\log(2N)}{\log(2N_f)} = F_r\left(\frac{\sigma_{\max}}{\sigma_u}\right) F_f(f) F_R(R) \frac{1}{1+\frac{1}{ac}e^{-an}} \tag{2.38}$$

in which F_r, F_f and F_R are corrective functions, f is the frequency, *a* and *c* are parameters to be determined experimentally and $n = \log(2N)$. The S–N relationship is found by imposing $D(n) = 1$ for $N = N_f$. To find the F functions, the authors conducted a series of fatigue tests on $[0]_8$ unidirectional laminates at $R = 0,\ 0.1,\ 0.3,\ 0.5$ and a frequency $f = 5$ Hz (whose results are reported in Figure 2.41) and at various frequencies and $R = 0$, finding, in line with the experimental results by El Kadi and Ellyin [6] and by Kawai and Suda [11], a lower fatigue life for lower R.

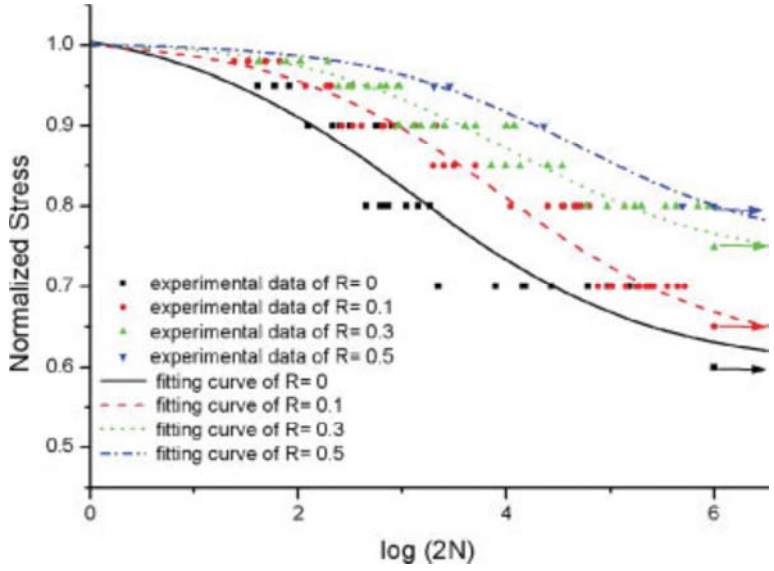

Figure 2.41 – Experimental data by Chen and Whang, for $[0]_8$ at $R = 0,\ 0.1,\ 0.3,\ 0.5$, $f = 5$ Hz.

The damage area ratio, experimentally determined, is taken by the authors as index of damage. The authors, basing on least square regression method, assume that all the F functions are linear in their respective arguments (Figure 2.42 shows the reasonable linearity of F_R against R found by the authors), and the model acceptably predicts the fatigue curve for 0° laminate at $R = 0.1$ and $f = 5$ Hz.

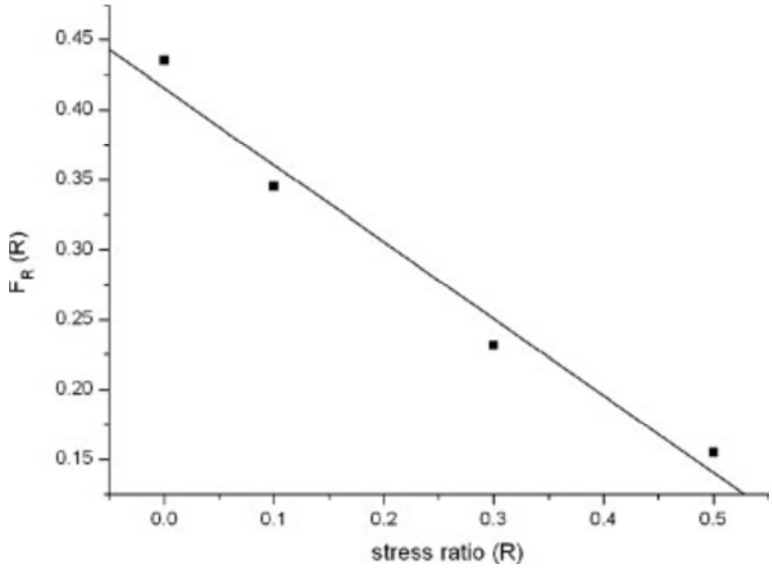

Figure 2.42 – Linearity of the F_R function found by Chen and Whang, at $f = 5$ Hz.

If the hypothesis of linearity is confirmed for values of the loading parameters outside the range analyzed by the authors, this model presents the advantage of needing only a 8 experimental points to find the S–N relationship.

2.3.11 – Kawai and Teranuma's model (2012)

The model recently proposed by Kawai and Teranuma [16] is based on the so called "anisomorphic constant fatigue life (CFL) diagram approach", in which constant fatigue life curves are plotted in the σ_a–σ_m plane. They start from a two-segment CFL (Figure 2.43), based on the hypotheses that the fatigue behavior of a given composite is characterized by the reference fatigue behavior at a critical stress ratio that is equal to the ratio between the static strength in compression and the static strength in tension, $\chi = \sigma_C/\sigma_T$. In this CFL, the curves are described by the equations:

$$-\frac{\sigma_a - \sigma_a^{(\chi)}}{\sigma_a^{(\chi)}} = \begin{cases} \left(\dfrac{\sigma_m - \sigma_m^{(\chi)}}{\sigma_T - \sigma_m^{(\chi)}}\right)^{2-\psi_\chi}, & \sigma_m^{(\chi)} \le \sigma_m \le \sigma_T \\ \left(\dfrac{\sigma_m - \sigma_m^{(\chi)}}{\sigma_C - \sigma_m^{(\chi)}}\right)^{2-\psi_\chi}, & \sigma_C \le \sigma_m \le \sigma_m^{(\chi)} \end{cases} \tag{2.39}$$

in which $\psi_\chi = \sigma_{\max}^{(\chi)} / \sigma_T$ is the fatigue strength ratio associated with the critical stress ratio χ and is treated as a monotonic function of the number of cycles to failure N_f:

$$2N_f = \frac{1}{K_\chi}\frac{1}{(\psi_\chi)^n}\frac{\langle 1-\psi_\chi \rangle^a}{\langle \psi_\chi - \psi_{\chi(L)} \rangle^b} \tag{2.40}$$

where the angular brackets $\langle\ \rangle$ denote the singular function defined as $\langle x \rangle = \max\{0, x\}$ and the terms K_χ, n, a, b, $\psi_{\chi(L)}$ are found by fitting with equation 2.40 the reference fatigue data obtained for the critical stress ratio.

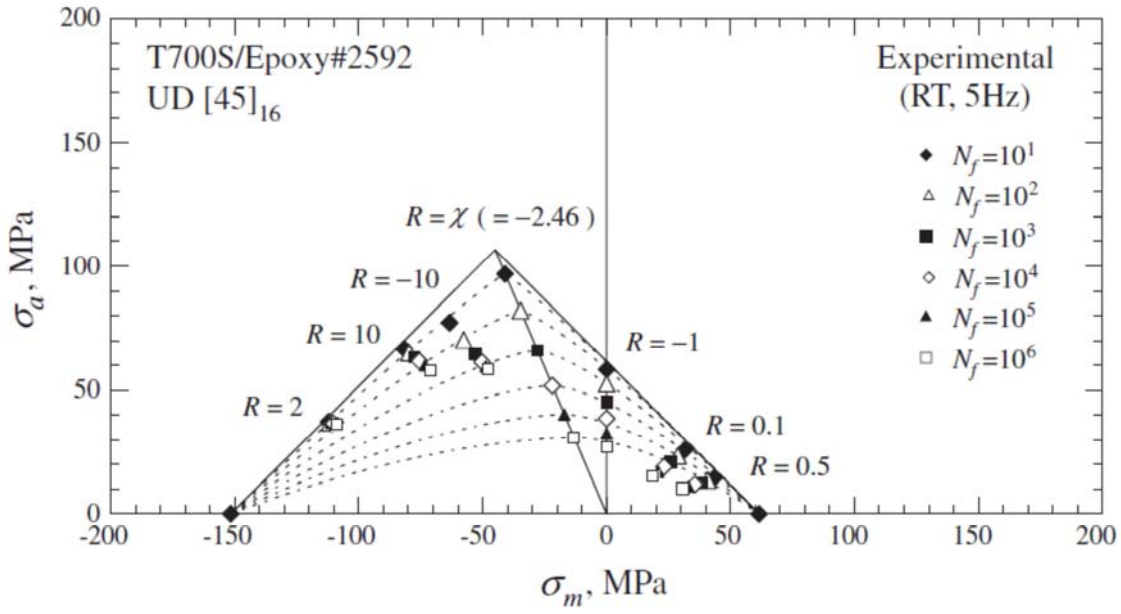

Figure 2.43 – "Two-segment model", taken from [16].

This "two-segment model" showed to be inaccurate in cases in which the composite exhibits a large difference of behavior between the mean stress sensitivity in fatigue under tension-dominated and compression-dominated fatigue loading conditions. The authors developed then a "four-segment model" (Figure 2.44), that include two transitional segments in the right and left neighborhoods of the line relative to the critical stress ratio in the σ_a–σ_m plane, defined using two auxiliary stress ratios (χ_L and χ_R).

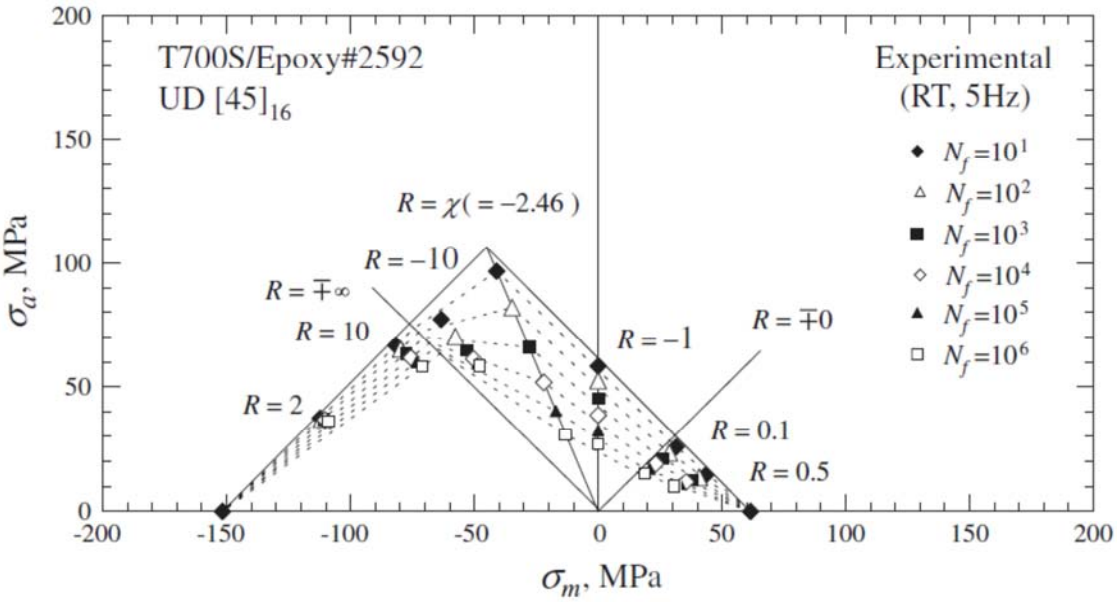

Figure 2.44 – "Four segment model", taken from [16].

The CFL curves are then defined as follows:

(I) Tension dominated zone ($\sigma_m^{(\chi_R)} \le \sigma_m \le \sigma_T$):

$$-\frac{\sigma_a - \sigma_a^{(\chi_R)}}{\sigma_a^{(\chi_R)}} = \left(\frac{\sigma_m - \sigma_m^{(\chi_R)}}{\sigma_T - \sigma_m^{(\chi_R)}} \right)^{2-\psi_{\chi_R}^{k_T}} \tag{2.41}$$

(II) Right transitional zone ($\sigma_m^{(\chi)} \le \sigma_m \le \sigma_m^{(\chi_R)}$):

$$-\frac{\sigma_a - \sigma_a^{(\chi_R)}}{\sigma_a^{(\chi_R)} - \sigma_a^{(\chi)}} = \frac{\sigma_m - \sigma_m^{(\chi_R)}}{\sigma_m^{(\chi)} - \sigma_m^{(\chi_R)}} \tag{2.42}$$

(III) Left transitional zone ($\sigma_m^{(\chi_L)} \le \sigma_m \le \sigma_m^{(\chi)}$):

$$-\frac{\sigma_a - \sigma_a^{(\chi)}}{\sigma_a^{(\chi)} - \sigma_a^{(\chi_L)}} = \frac{\sigma_m - \sigma_m^{(\chi)}}{\sigma_m^{(\chi_L)} - \sigma_m^{(\chi)}} \tag{2.43}$$

(IV) Compression dominated zone ($\sigma_C \le \sigma_m \le \sigma_m^{(\chi_L)}$):

$$-\frac{\sigma_a - \sigma_a^{(\chi_L)}}{\sigma_a^{(\chi_L)}} = \left(\frac{\sigma_m - \sigma_m^{(\chi_L)}}{\sigma_C - \sigma_m^{(\chi_L)}} \right)^{2-\psi_{\chi_L}^{k_C}} \tag{2.44}$$

In the equations above, $\psi_{\chi_R} = \sigma_{\max}^{(\chi_R)} / \sigma_T$ and $\psi_{\chi_L} = \sigma_{\min}^{(\chi_L)} / \sigma_C$ are the fatigue strength ratios associated to, respectively, the right and left auxiliary stress ratios. The exponents k_T and k_C are introduced to add a function that could adjust the rate of change in shape of CFL curve from a straight line to a parabola.

The two auxiliary stress ratios and the relative fatigue strengths for different fatigue life should be determined by experiments, but the authors assume $\chi_L = -\infty$ and $\chi_R = 0$ and approximate the fatigue life at these stress ratio by simply extrapolating it from the linear CFL envelopes on the Tension-Tension segment and on the Compression-Compression segment.

From the construction of the CFL diagrams for longitudinal, transverse, and in-plane shear loading conditions, the authors make use of the modified Tsai-Hill static failure criterion in order to estimate the fatigue life of a composite under general loading conditions, by substituting in it the principal static strengths with the principal fatigue strength (X_f, Y_f, and S_f, respectively for longitudinal, normal and shear stress), drawn from the principal CFL diagrams:

(I) Tension dominated fatigue failure ($\chi(\theta) \le R \le 1$):

$$\left(\frac{\sigma_{11,\max}}{X_f} \right)^2 - \frac{\sigma_{11,\max}\sigma_{22,\max}}{X_f^2} + \left(\frac{\sigma_{22,\max}}{Y_f} \right)^2 + \left(\frac{\tau_{12,\max}}{S_f} \right)^2 = 1 \tag{2.45}$$

(II) Compression dominated fatigue failure ($1 \le R \le +\infty,\ -\infty \le R \le \chi(\theta)$):

$$\left(\frac{\sigma_{11,\max}}{X_f} \right)^2 - \frac{\sigma_{11,\max}\sigma_{22,\max}}{X_f^2} + \left(\frac{\sigma_{22,\max}}{Y_f} \right)^2 + \left(\frac{\tau_{12,\max}}{S_f - \mu_L \sigma_{22,\max}} \right)^2 = 1 \tag{2.46}$$

(μ_L is a term that takes into account the different effect of shear in tension and in compression, evaluated by the authors as equal to 0.35). The critical stress ratio $\chi(\theta) = \sigma_C(\theta) / \sigma_T(\theta)$ can be predicted using the modified Tsai-Hill static failure criterion.

This model presents a very good agreement with experimental data at different off-axis angles and different stress ratio, but it has been tested only on carbon/epoxy systems. The authors themselves admit that care has to be taken in using this model to predict the fatigue life of GFRP, since in some cases they show very distorted shape of CFL envelopes.

Chapter 3

Materials and Methods

The materials, testing machine and experimental procedures used in the experimental campaign are described in this chapter. The aim of the present study is to analyze the matrix dominated behavior of composite materials under multiaxial fatigue loading condition.

3.1 – Possible specimens configurations

As stated in Chapter 1, a multiaxial stress state can be induced both by *internal* and *external* multiaxiality. As a consequence, there are different kinds of tests and specimen geometries that can be adopted for multiaxial testing. The following are the most common (Figure 3.1) [19]:

1) Off-axis loaded flat specimen.
2) Cruciform flat specimen biaxialy loaded.
3) Thin-walled tubes subjected to combined tension-internal pressure or tension-torsion.

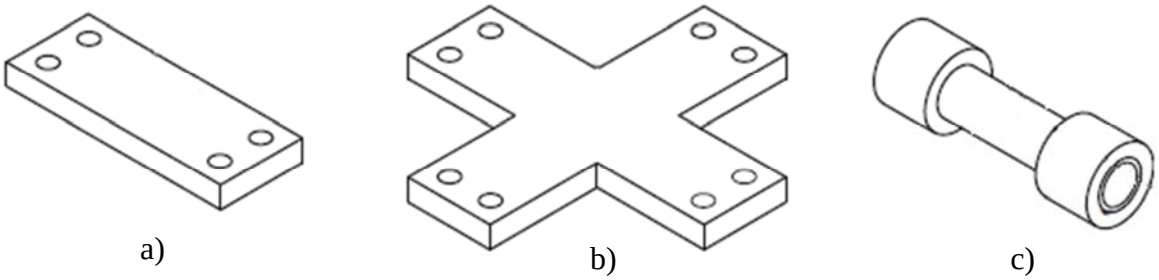

Figure 3.1- Possible specimen geometry: a) flat, b) cruciform, c) tubular.

In the first case, multiaxial stress state is induced by a uniaxial load. This kind of test is simple, the specimen is easily manufactured, and only a uniaxial testing machine is required. On the other hand, it is not possible to obtain stresses along two directions only and care has to be taken in the design of the tabs so as to avoid excessive stress concentrations.

In the second testing mode, multiaxiality is obtained by applying two orthogonal external loads to the arms of the specimen. Depending on the fibers orientation, external or inherent multiaxiality results; in the second case no in-plane shear stresses are induced, it is then impossible to obtain a stress state characterized by the presence of only transverse and shear stresses, which is the one desired in this study in order to study the matrix dominated behavior. Moreover, specimens geometry must be carefully designed in order to obtain a uniform stress distribution and to avoid failure in the arms, and a dedicated testing machine, capable to apply loads in two normal directions, is needed.

Tubular specimens are probably the most used in the investigation of multiaxial behavior of composite materials. As the last case, both external and inherent multiaxiality can be achieved, depending on the fibers winding angle. Multiaxiality can be induced by combined tension-internal pressure or combined tension-torsion. In the first case, a dedicated equipment to pump the oil inside the specimen is required, which makes it less attractive. In addition, it is not possible to obtain a stress state with only transverse and in-plane shear stress. On the contrary, combined tension-torsion configuration requires only a biaxial (tension/torsion) testing machine, and it is the only testing mode that can achieve the stress state mentioned above. Given also the simplicity of specimens preparation and the avoidance of free edge effects (which can influence the results of tests on flat specimens), this kind of test is the most attractive for investigating the matrix-dominated behavior of composite materials under multiaxial fatigue loading, and therefore it was the one chosen for the present experimental campaign.

3.2 – Specimens geometry and stress analysis

In a previous experimental campaign [19], in order to investigate the matrix dominated behavior of composite materials under multiaxial fatigue loading, tubes made of glass/epoxy UD plies were tested, with the fibers oriented at 90° with respect to the tube's axis (Figure 3.2)

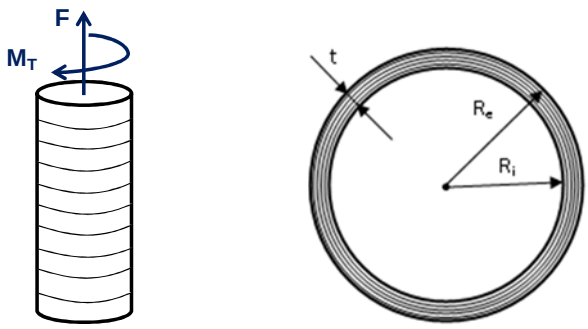

Figure 3.2 – Loading condition and specimen geometrical parameters.

The tensile load F produces a transverse stress σ_2 on the 90° layers, while the external torque M_T generates the in-plane shear stress σ_6. By properly combining the tension and torsion loadings it is possible to obtain different values of the biaxiality ratio λ_{12} (see Chapter 1). The transverse stress can be easily calculated as

$$\sigma_2 = \frac{F}{\pi\left(R_e^2 - R_i^2\right)} \tag{3.1}$$

The shear stress varies linearly from the internal to the external diameter. For the calculation of the biaxiality ratio it was decided to consider its maximum value, that is the value at the external diameter:

$$\sigma_{6,\max} = \frac{M_T}{J_p} R_e \tag{3.2}$$

where J_p is the polar moment of inertia calculated as

$$J_p = \frac{\pi}{2}\left(R_e^4 - R_i^4\right) \tag{3.3}$$

The biaxiality ratio is therefore defined as:

$$\lambda_{12} = \lambda_{12,\max} = \frac{\sigma_{6,\max}}{\sigma_2} \tag{3.4}$$

In order to allow the results obtained on tubular specimens to maintain validity also for flat components, the ratio between the maximum and the minimum shear stresses (respectively at the external and internal diameter) has to be as low as possible. That ratio can be calculated as:

$$\frac{\sigma_{6,\max}}{\sigma_{6,\min}} = \frac{R_e}{R_i} = 1 - \frac{t}{R_i} \tag{3.5}$$

This equation describes also the variation of the biaxiality ratio across the thickness.

Because of the material orthotropy, stresses along the fibers direction (i.e. in the hoop) and in radial direction are induced from the biaxial external loads. Anyway, a previous work [19] showed that they are so small that they could be neglected, and therefore from now on the stress state will be considered purely biaxial.

The geometry of the specimens used in the present experimental campaign are reported in Figure 3.3. At the ends of the specimens, a woven glass/epoxy strip (*tab*) is added, in order for the specimen to be grabbed by the testing machine. The external diameter was chosen in order not to have geometrical constraints issues with the testing equipment.

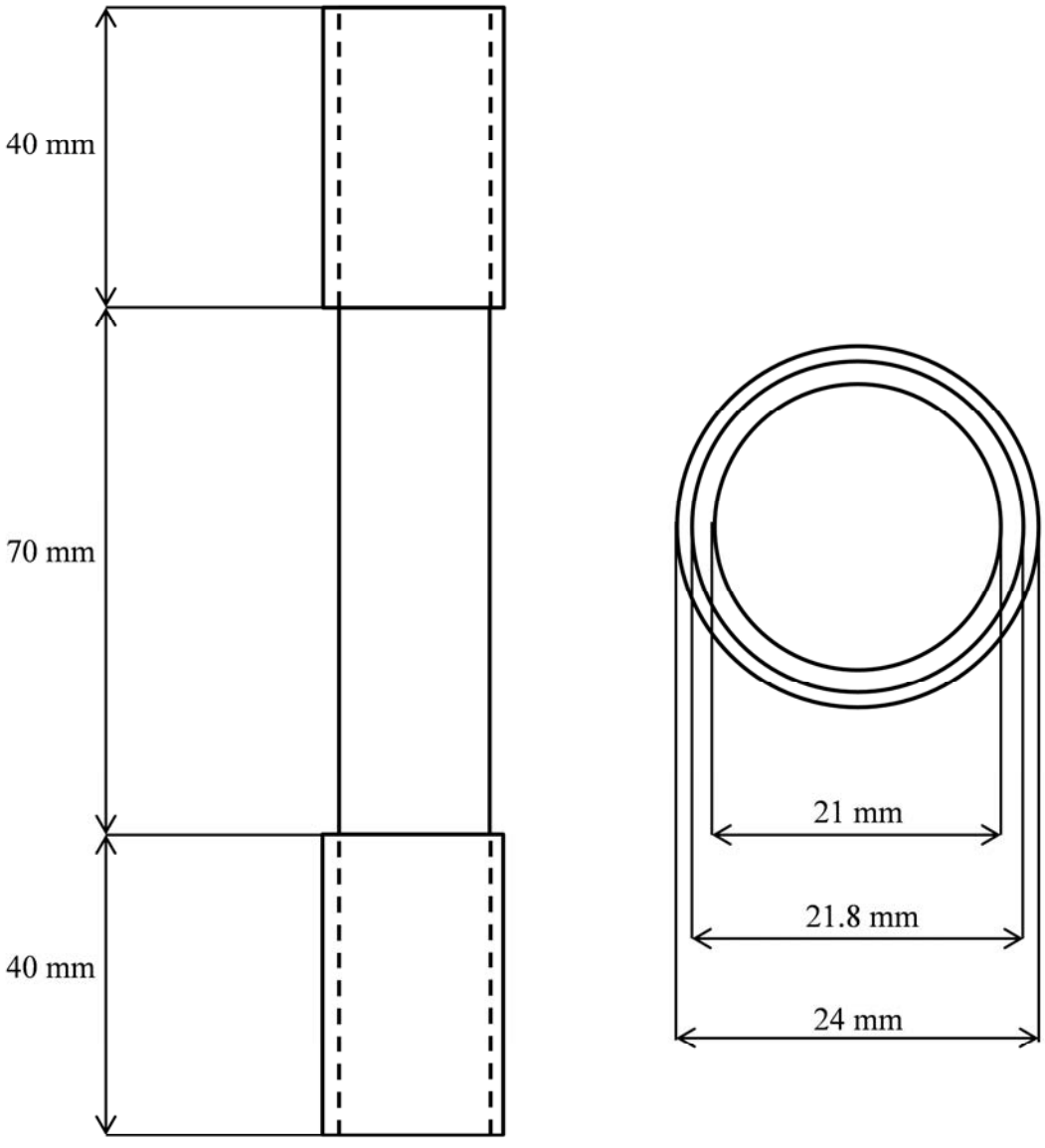

Figure 3.3 – Specimen geometry: a) side, b) top.

3.3 – Specimens materials and production process

The stacking sequence used in the experimental campaign was $[0_T/90_{UD3}/0_T]$ ("TUT sequence"), where the subscript T indicates woven layer whereas UD stands for unidirectional. The woven layers are needed to avoid unstable crack propagation, so as to allow a better study of the damage evolution. Moreover, with the TUT configuration the crack nucleation is not influenced by the presence of surface defects due to the manufacturing process. Even with this configuration, the stresses along the radial direction and along the fibers direction in 90° layers remain negligible [20]. The following materials were used for the specimens (see Table 3.1 for the mechanical properties):

- UE 400 REM, produced by SEAL-Italy: glass/epoxy UD pre-preg, thickness = 0.38 mm, used for the 90° layers;
- EE 106-ET443, produced by SEAL-Italy: glass/epoxy woven pre-preg, thickness = 0.13 mm, used for the internal and external woven layers;
- VV345T, produced by SEAL-Italy: glass/epoxy woven pre-preg, thickness = 0.35 mm, used for the tabs.

	UE 400-REM		**VV345T-DT107A**		**EE106 – ET443**	
	average	**st. dev.**	**average**	**st. dev.**	**average**	**st. dev.**
$\sigma_{1,U}$ (MPa)	973	59	431	15	257	7
$\sigma_{2,U}$ (MPa)	50	6.6	447	21	239	2.5
$\sigma_{6,U}$ (MPa)	98	-	85	-	80	-
E_1 (MPa)	34860	2365	21700	82	17033	491
E_2 (MPa)	9419	692	20880	431	16538	206
G_{12} (MPa)	3193	-	3351	-	3032	-
ν_{12}	0.326	0.015	0.159	0.005	0.159	-

Table 3.1 – Mechanical properties of the materials used in the experiments

The specimens were obtained by cutting 1 m long tubes, produced by *mandrel wrapping* technology, and successively cured in autoclave (one hour at 6 bars and 140°C). The pictures reported in Figures 3.4 taken from [5] (courtesy of SITA COMPOSITI s.r.l.), illustrate the steps of the production process: first, the mandrels are cleaned; the pre-preg skins are then cut, their protective layers are removed, and they are manually attached to the mandrels. A dedicated machine carries out the wrapping. A reinforce strip is made at one of the tubes ends to help the removal of the mandrel after the cure. A heat-shrinkable tape is wrapped around the pre-preg, in order to maximize the volume fraction of fibers, and the curing cycle in autoclave follows. Once the curing process is terminated, the mandrel is removed, as well as the heat-shrinkable tape. The final tube is

then cut in pieces of the desired length, and tabs are attached at their ends and cured in oven (80°C, 8 hours). The final volume fraction of fibers is around 45%.

a) Mandrel cleaning.

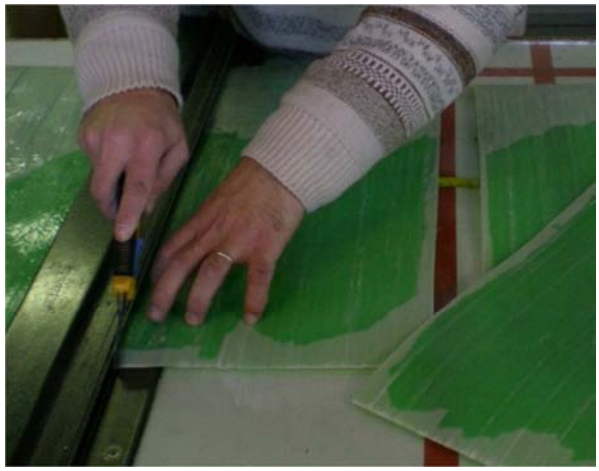

b) Pre-pregs cutting.

c) Protective leaves removal.

d) Attaching pre-pregs to mandrel.

e) Wrapped tube.

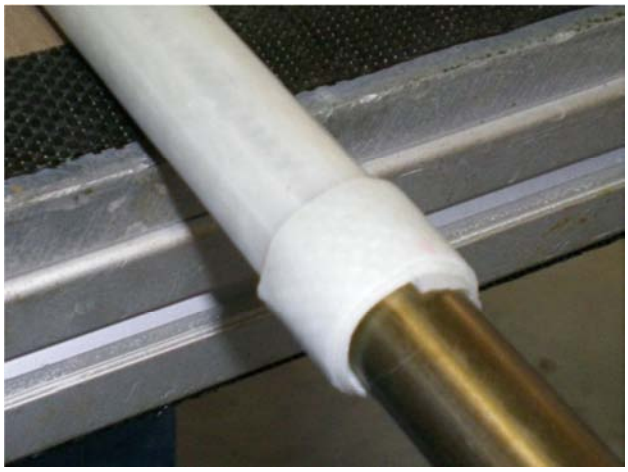

f) Reinforce strip at one end of the tube.

Figure 3.4 – Specimen production process (taken from [5]).

g) Heat-shrinkable tape wrapping machine.

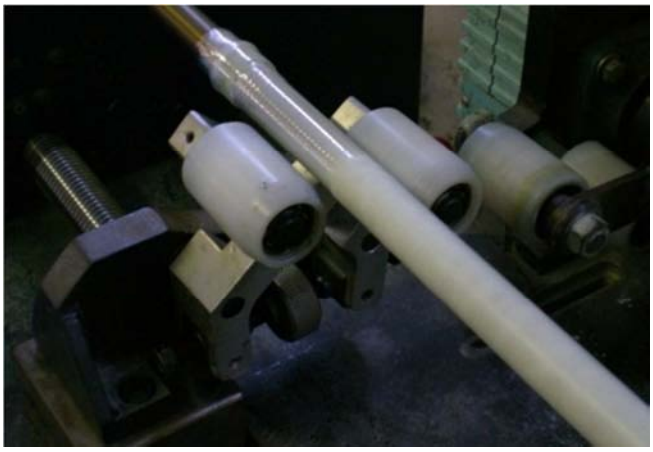

h) Wrapping of heat-shrinkable tape.

i) Autoclave used for curing cycle.

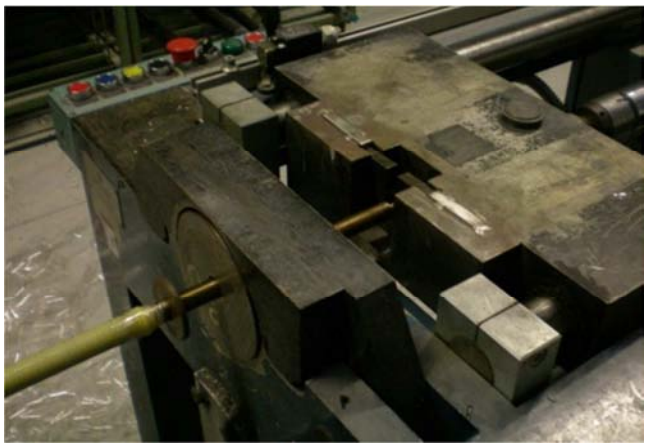

j) Mandrel removal.

k) Final tube.

Figure 3.4 (continued) – Specimen production process (taken from [5]).

l) Specimens cut from the final tube.

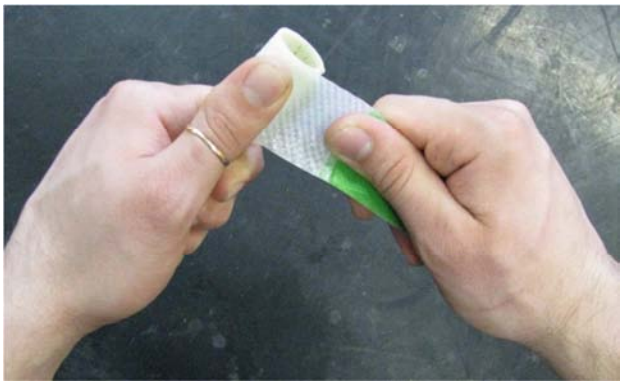

m) Attachment of the tabs.

n) Specimen before tabs curing.

Figure 3.4 (continued) – Specimen production process (taken from [5]).

An attempt to produce the tabs directly integrated with the tube, before its curing, has been made in [5], but deep defects resulted at the end of the tabs (Figure 3.5), that induce damage in an already critical zone.

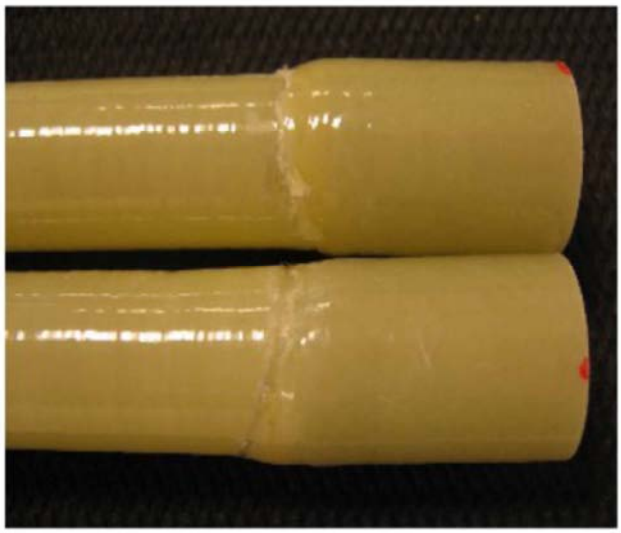

Figure 3.5– Defects in specimens with integrated tabs (taken from [5]).

In the same work, turning the specimen was tried as a solution to the defects at the beginning of the tabs and also to typical surface defects deriving from the production process (such as waving). Anyway, this operation is time and money consuming, and SEM analyses of the new surfaces revealed a lot of broken fibers and matrix cracks, hence the idea was dropped.

In order to avoid specimens cracking due to stress concentrations in correspondence to the end of the tabs, a fillet is made with a two part epoxy structural adhesive and cured in oven at 40°C for 4 hours (Figure 3.6).

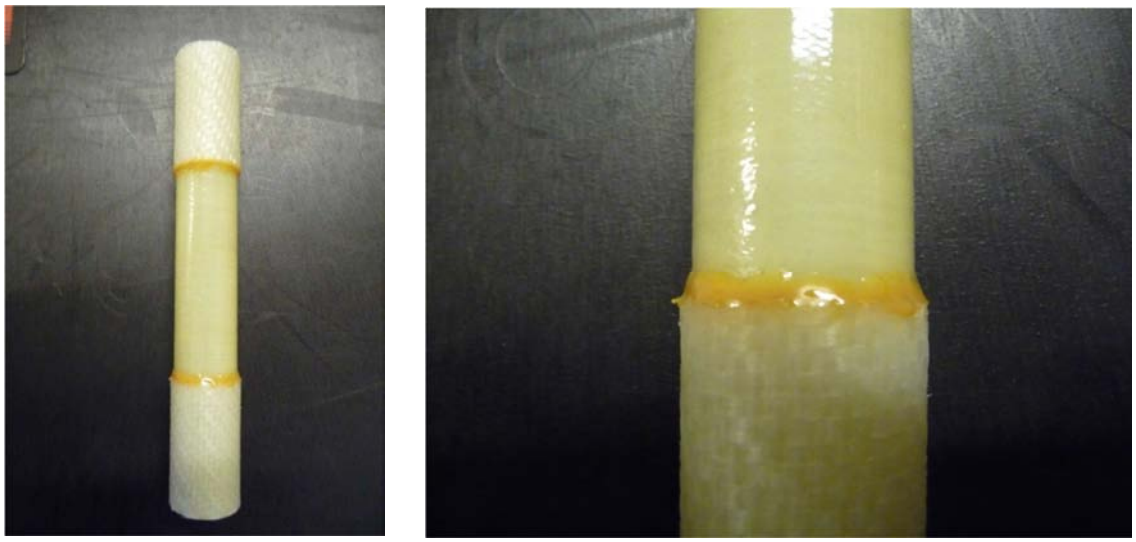

Figure 3.6 – Fillet at the end of the tabs.

3.4 – Testing procedures

Both fatigue and quasi-static tests were conducted in the experimental campaign. The procedures followed for both of them is presented in this section.

3.4.1 – Fatigue tests

The fatigue tests were conducted by means of MTS 809 axial/torsional machine, in load control, at frequency f = 10 Hz, R = -1, 0, 0.5 and λ_{12} = 0, 1, 2 (see paragraph 1.5). The applied loads are in phase and proportionally applied. The damage onset was monitored in two ways: by FLIR SC7600 MW infrared camera (Figure 3.7) and by in situ eye observation with the help of a lighting system inside the specimens, developed in [5] (Figure 3.8). Two aluminum mirrors have been used in order to monitor the back side of the specimens with the infra-red camera.

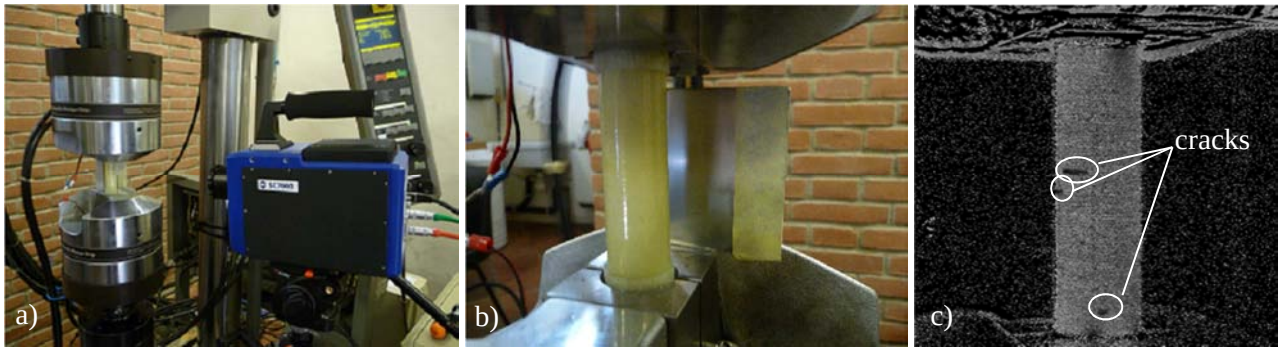

Figure 3.7 – IR monitoring system (a, b) and image obtained with infra-red lock-in analysis (c).

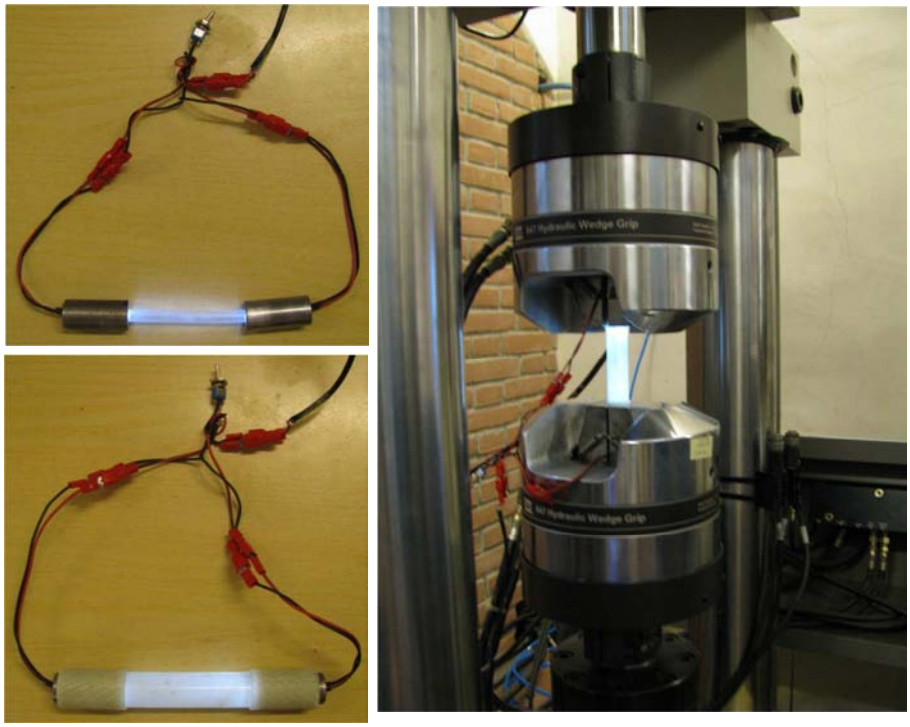

Figure 3.8 – Internal light system (taken from [5]).

Two inner steel cylinders were uses in the clamping regions in order to avoid the specimens failure while closing the grips. Anyway, a very low pressure had to be used in the gripping heads of the machine in order to avoid the fatigue failure inside the tabs.

The crack propagation was monitored only by means of eye observation, stopping the test and marking the position of the crack tips once the crack visibly propagated.

Use of compressed air (Figure 3.9) was made for test at high values of shear stresses in order to keep low the specimens temperature.

Figure 3.9 – Compressed air system.

The axial and torsional stiffness of the specimens have been recorded during every test by means of the displacement/angle sensors and the load cell of the testing machine.

3.4.2 – Quasi-static tests

The same machine used for the fatigue tests was used also for the quasi-static tests (MTS 809 axial/torsional machine), always in load control. Tests were made under pure tension, pure compression, combined tension and shear at λ_{12} = 1, 2, and combined compression and shear at λ_{12} = 1, 2. The applied loads were proportionally applied. The damage onset was monitored by eye-observation and infrared camera (FLIR SC7600 MW).

All the quasi-static tests were conducted at the same loading speed, which was constant and equal to 0.2667 MPa/s. In particular, for the tests with tensile stress a loading of 80 MPa was set to be reached in 300 seconds, whereas for the tests in compression a load of 240 MPa was set to be reached in 900 seconds. This loading speed was slow enough to allow the observation of the damage initiation.

Chapter 4

Quasi-static tests results

In this chapter are shown the results of the quasi-static tests of the present experimental campaign, whereas Chapter 5 is dedicated to the results of the fatigue tests. The materials and the tests procedures used are described in Chapter 3.

4.1 – Tested specimens

In order to obtain the mechanical static properties of the tested materials, 18 specimens were tested, whose geometrical characteristics are reported in Table 4.1, together with the imposed maximum load and the time of the test. In particular, the following formula were used:

$$A = \pi \frac{(D_{ext}^2 - D_{\text{int}}^2)}{4} \tag{4.1}$$

$$J_p = \pi \frac{(D_{ext}^4 - D_{\text{int}}^4)}{32} \tag{4.2}$$

$$F = \sigma_2 A \ \frac{1}{0.86} \tag{4.3}$$

$$Mt = \frac{\tau_{12} J_p}{D_{ext}/2} \frac{1}{0.99} \tag{4.4}$$

$$v_{load} = \frac{\sigma_2}{t(load_{\max})} \tag{4.5}$$

The coefficients 0.86 and 0.99 that appear in equations 4.3 and 4.4 were drawn by previous FEM analyses; the term $load_{\max}$ refers to $F_{\max}$ for all the specimens except for the ones tested in pure shear, for which it is equal to $Mt_{\max}$.

SPECIMEN CODE	D_{int} (mm)	D_{ext} (mm)	A (mm^2)	J_p (mm^4)	F_{max} (N)	Mt_{max} (N*m)	$t(load_{max})$ (s)	v_{load} (MPa/s)
TUT-ST-L0-01	19	21.85	91.4	9583.0	8505.9	0	300	0.2667
TUT-ST-L0-02	19	21.87	92.1	9665.0	8569.7	0	300	0.2667
TUT-ST-L0-03	19	21.93	94.2	9912.5	8761.7	0	300	0.2667
TUT-ST-L0-04	19	21.99	96.3	10162.0	8954.3	0	300	0.2667
TUT-ST-L1-01	19	21.87	92.1	9665.0	8569.7	71.423	300	0.2667
TUT-ST-L1-02	19	21.94	94.5	9953.9	8793.8	73.323	300	0.2667
TUT-ST-L1-03	19	22.01	96.9	10245.6	9018.6	75.232	300	0.2667
TUT-ST-L2-01	19	21.9	93.2	9788.5	8665.7	144.473	300	0.2667
TUT-ST-L2-02	19	21.94	94.5	9953.9	8793.8	146.647	300	0.2667
TUT-ST-L2-03	19	21.88	92.5	9706.1	8601.7	143.388	300	0.2667
TUT-SC-L0-01	19	21.97	95.6	10078.6	-26670.1	0	900	0.2667
TUT-SC-L0-02	19	21.89	92.8	9747.3	-25901.1	0	900	0.2667
TUT-SC-L0-03	19	21.84	91.1	9542.0	-25421.8	0	900	0.2667
TUT-SC-L1-01	19	21.71	86.6	9014.9	-24180.9	-201.330	900	0.2667
TUT-SC-L1-02	19	21.68	85.6	8894.6	-23895.6	-198.918	900	0.2667
TUT-SC-L2-01	19	21.96	95.2	10037.0	-26573.8	-443.208	900	0.2667
TUT-SC-L2-02	19	21.97	95.6	10078.6	26670.1	444.843	900	0.2667
TUT-SC-L2-03	19	22.05	98.3	10413.6	27442.0	457.960	900	0.2667
TUT-ST-Linf-01	19	21.84	91.1	9542.0	0	141.222	300	0.2667
TUT-ST-Linf-02	19	21.92	93.8	9871.1	0	148.419	300	0.2667

Table 4.1 – Geometrical characteristics of tested specimens and applied loads (quasi-static tests).

4.2 – Loading curves

The loading curves obtained in the quasi-static tests are reported in Figures 4.1 to 4.18.

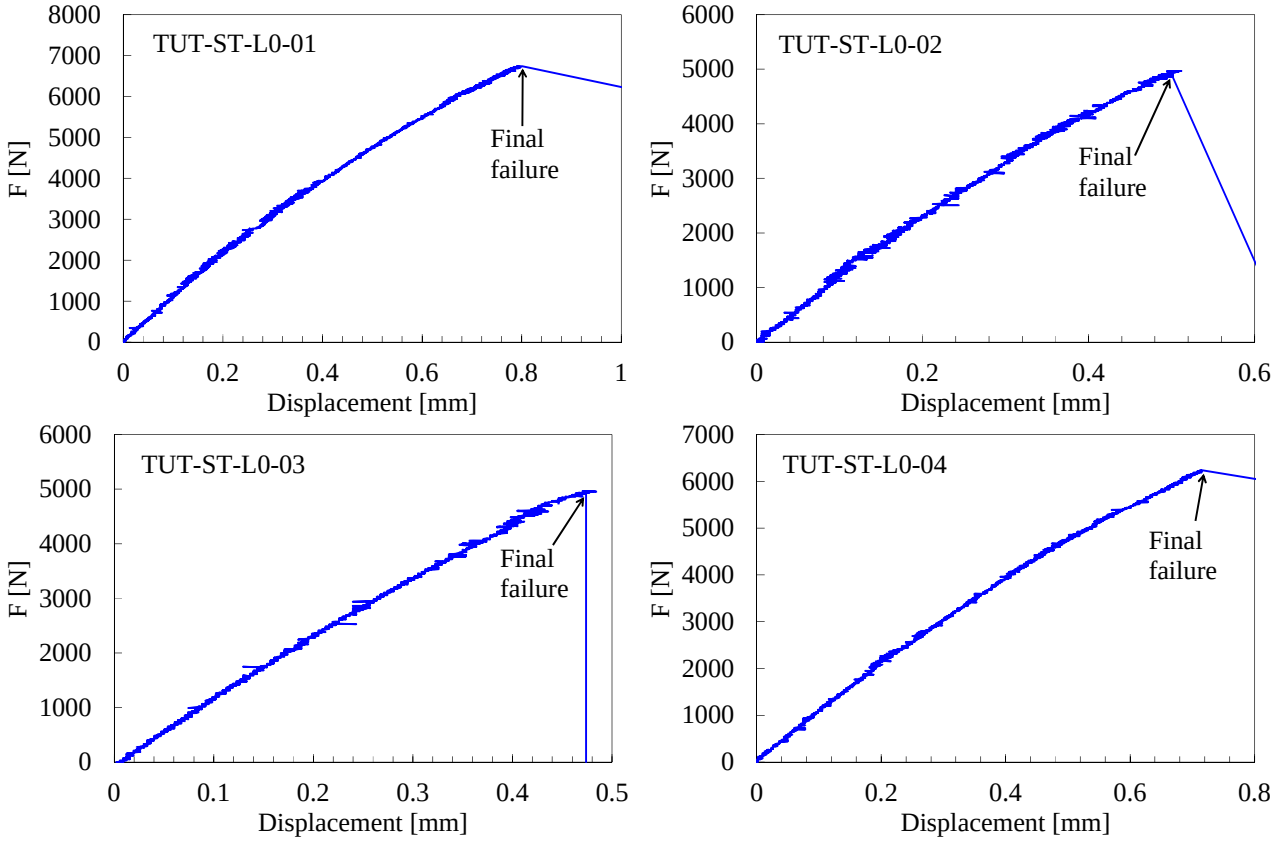

Figure 4.1 – Load-displacement curves for pure tension loading.

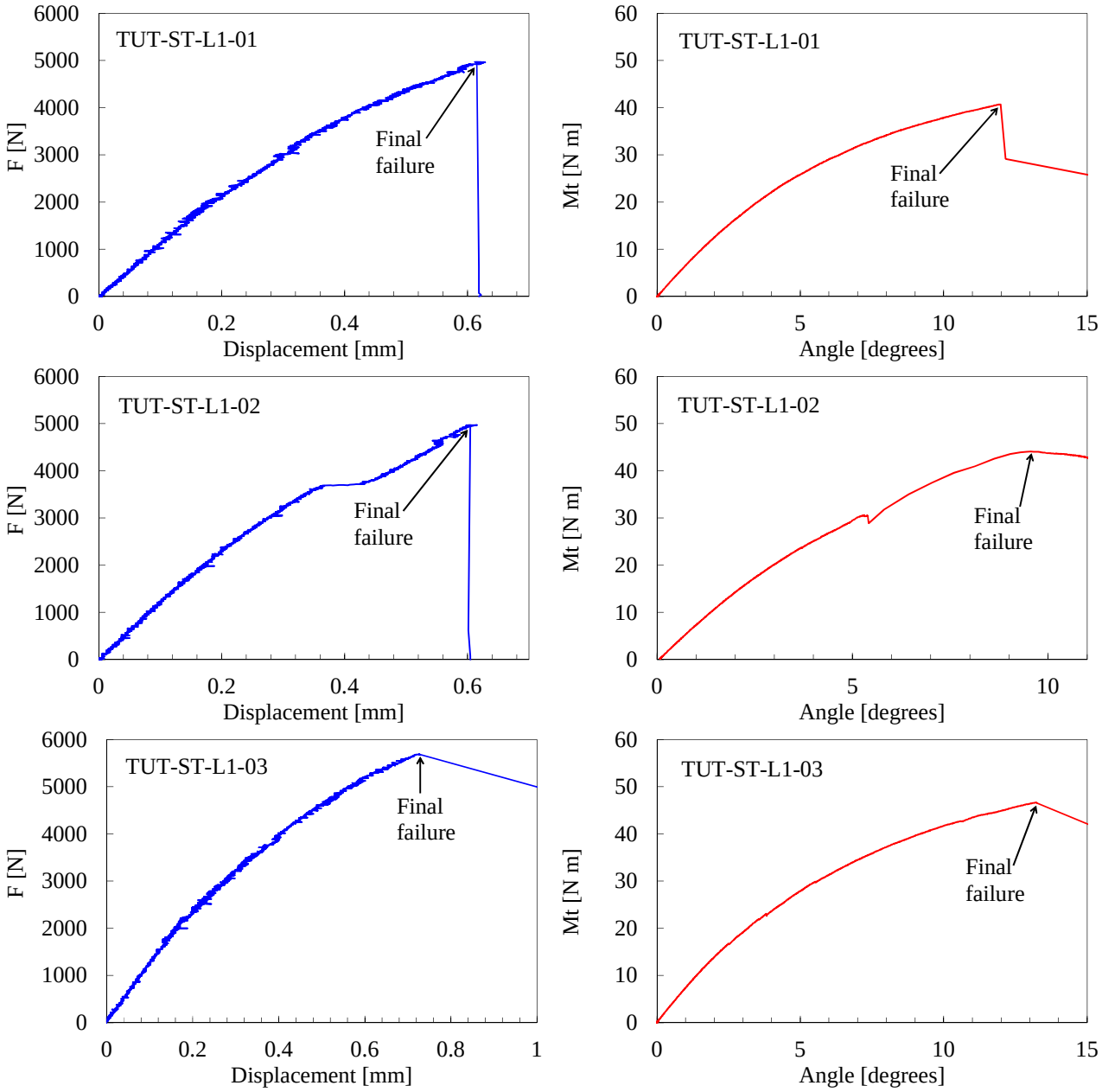

Figure 4.2 – Load-displacement and torque-angle curves for tension-shear loading, $\lambda_{12} = 1$.

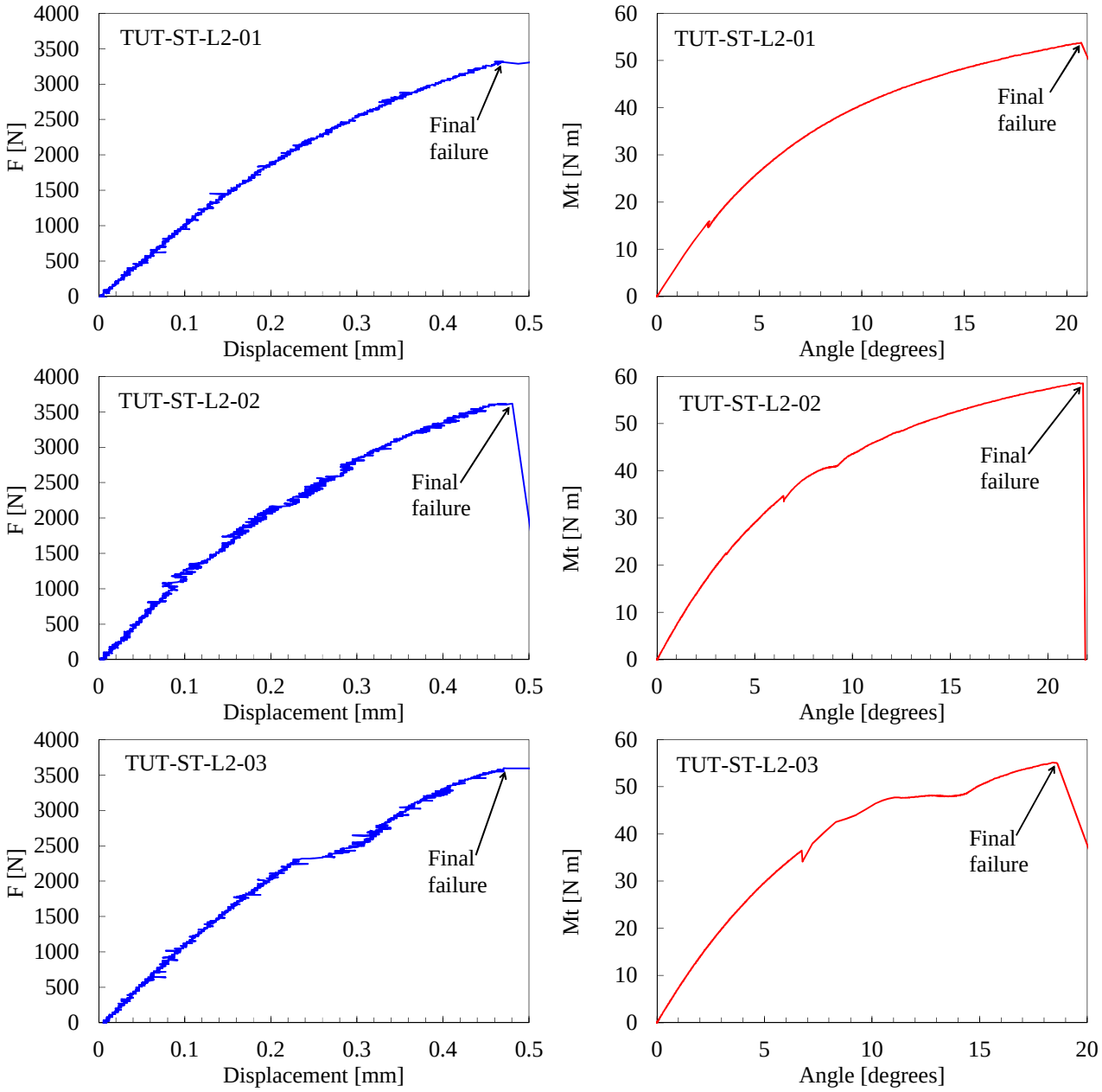

Figure 4.3 – Load-displacement and torque-angle curves for tension-shear loading, $\lambda_{12} = 2$.

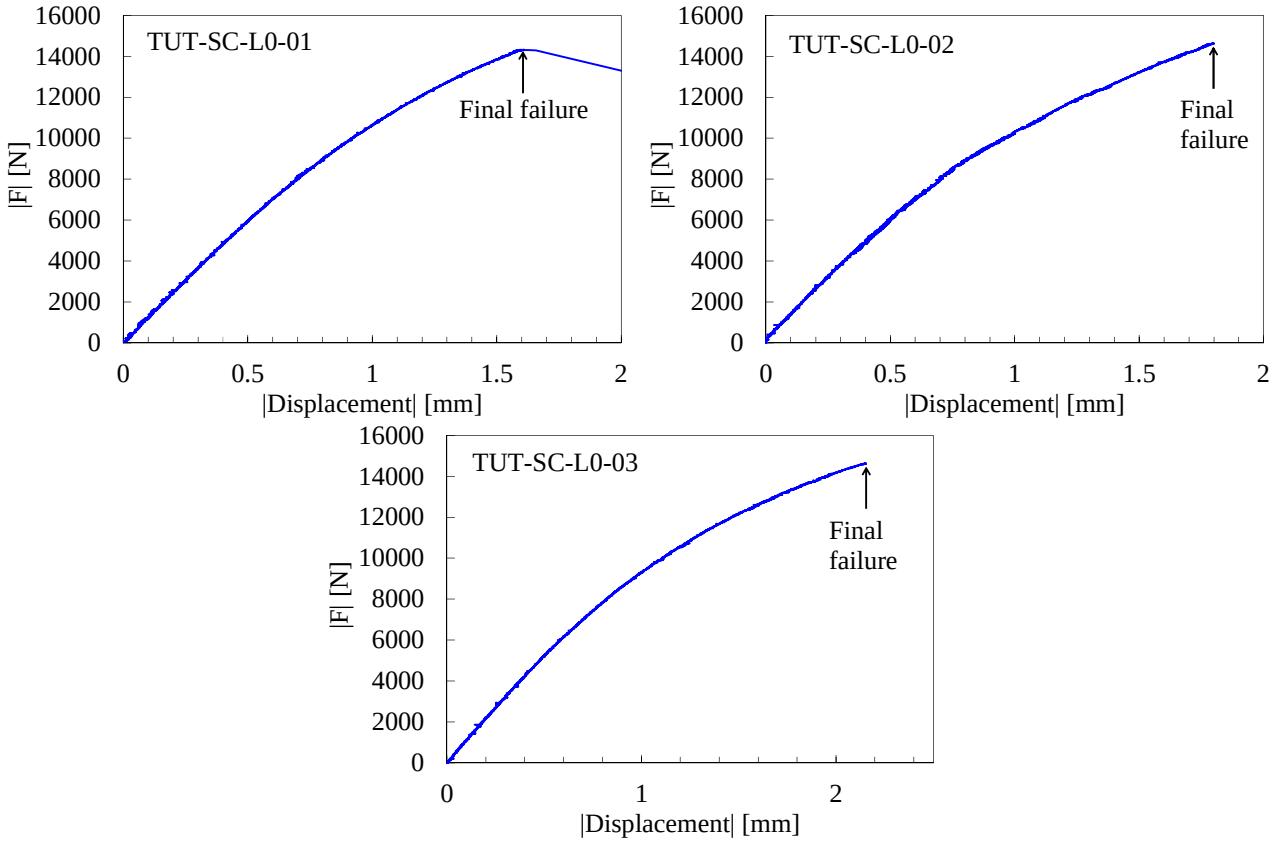

Figure 4.4 – Load-displacement curve for pure compression loading.

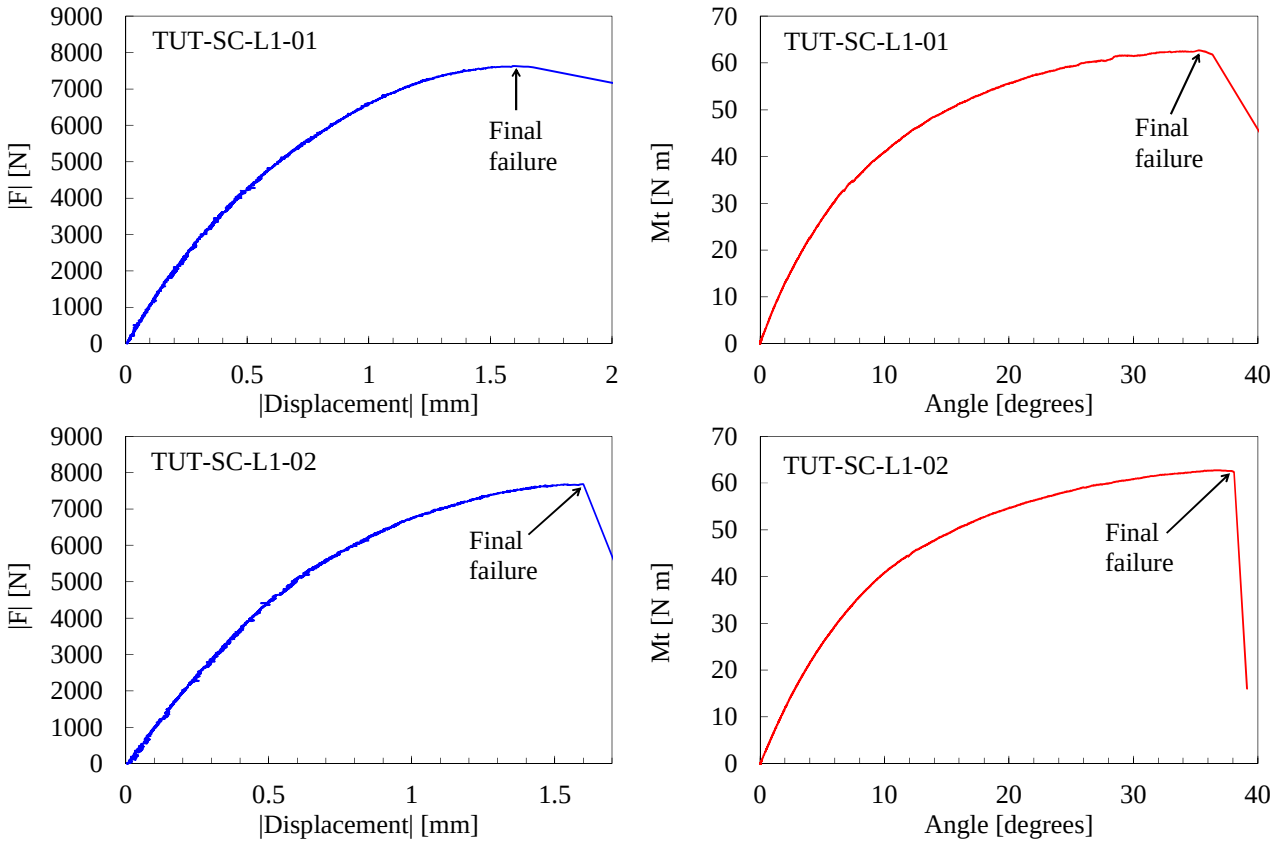

Figure 4.5 – Load-displacement and torque-angle curves for compression-shear loading, $\lambda_{12} = 1$.

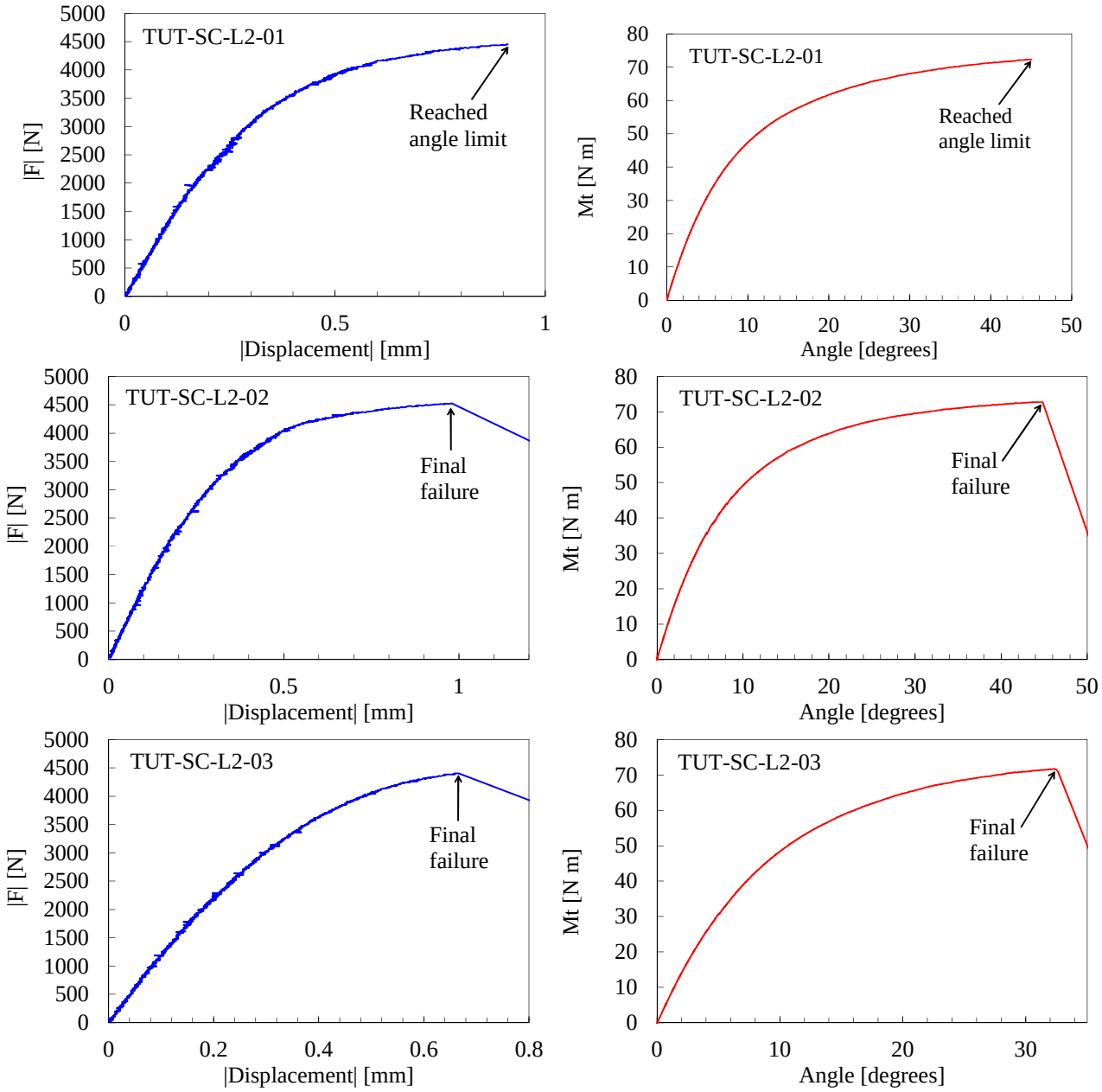

Figure 4.6 – Load-displacement and torque-angle curves for compression-shear loading, $\lambda_{12} = 2$.

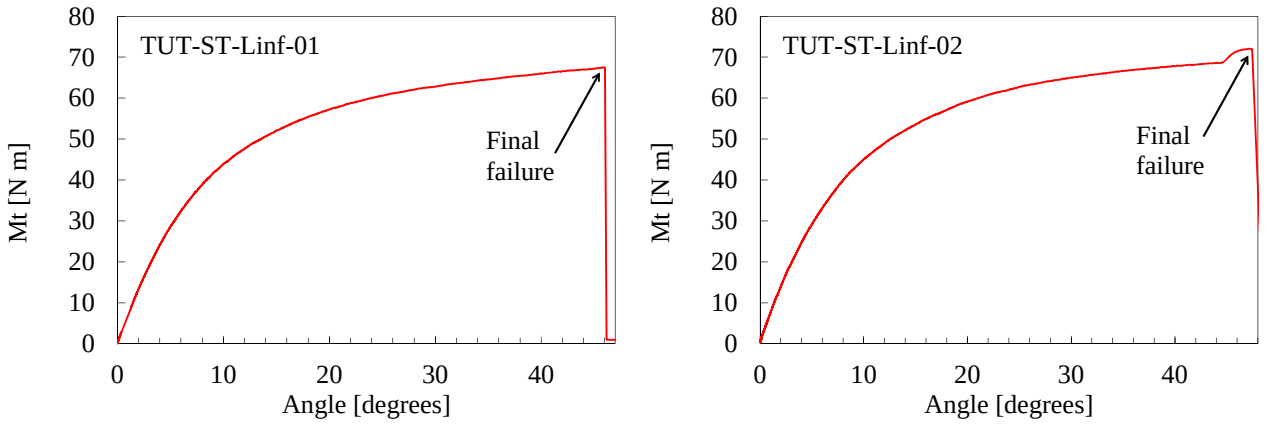

Figure 4.7 – Torque-angle curves for pure shear loading.

In some cases there are discontinuities in the loading curves (particularly evident for the specimens TUT-ST-L1-02 and TUT-ST-L2-03), that are due to slippage phenomena or problems in the controls of the testing machine.

For what concerns the linearity of the curves, it can be observed that under tensile stress the non-linearity is more evident for higher values of λ_{12}, whereas all the curves obtained in the presence of compression show high non-linearity. This is in agreement with the experimental observations on the behavior of the epoxy resin reported in [18], in which it is found that a non-linear behavior was promoted by the presence of the shear stress, and a ductile behavior is typical in the case of compression loading.

In all the tests carried out in the presence of tensile stress the damage initiation, in terms of transverse cracks in the 90° plies, was clearly detectable by means of the infrared camera before the final failure (Figure 4.8). However, the propagation of the nucleated cracks was always unstable, bringing the specimen to the complete failure after a very small load increase after the crack nucleation. A different behavior has been observed for compressive tests: in pure compression the first damage detected by the infrared camera was characterized by sparkles, probably related to the breakage of the fibers of the woven layers; adding a shear stress component lead to a progressive damage diffused over a large area of the specimens (Figure 4.9) and to a final failure that occurred without an evident crack initiation. This facts make difficult the interpretation of the data obtained under compression, since it is hard to tell if the damage initiated in the woven layers or in the 90° layers, that are the only ones whose behavior is of interest in this work.

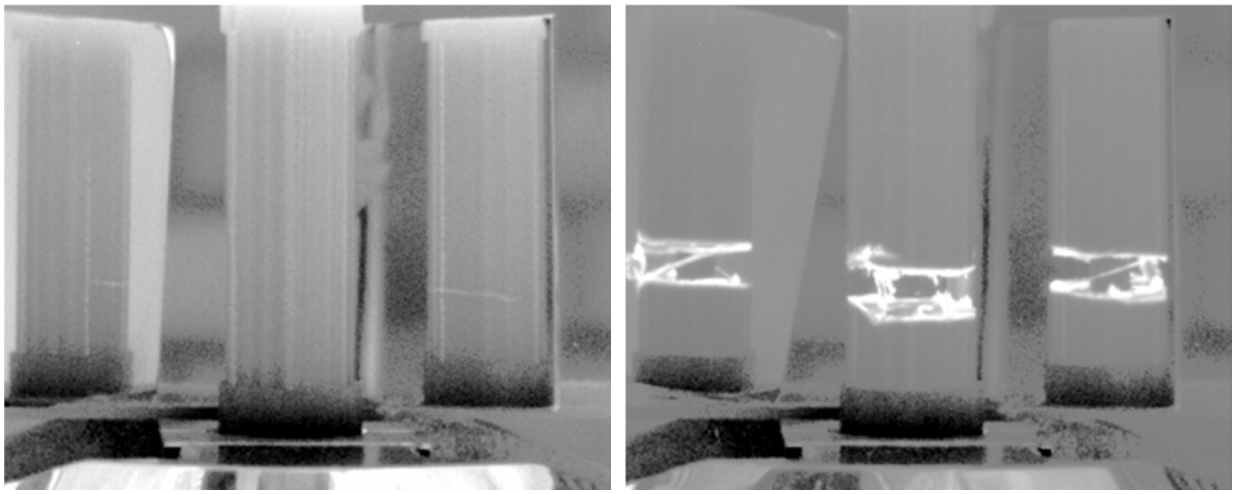

Figure 4.8 – IR pictures of damage initiation and final separation in presence of tensile stress.

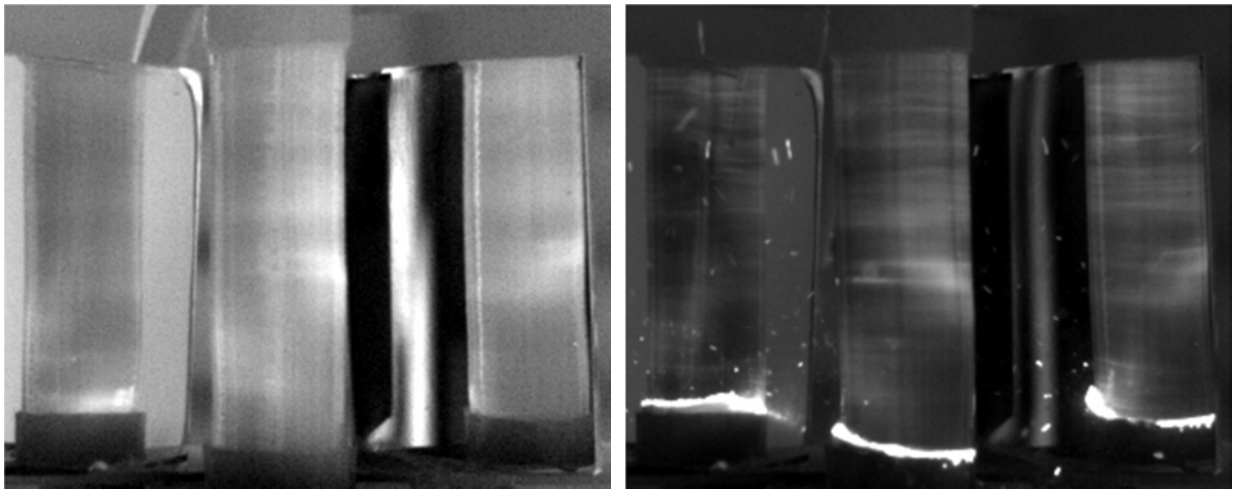

Figure 4.9 – IR pictures of damage initiation and final separation in presence of combined compressive and shear stresses.

4.3 – Strength data

The quasi-static test results are reported in Table 4.2 (in which the subscript “f” stands for “failure”) and in Figure 4.10 on the σ_2-τ_{12} plane. The values of stresses reported are those calculated on the 90° plies. It is once again reminded that the values related to positive values of σ_2 are representative of the transverse strength of the 90° plies, while, in the case of compressive load, it is not clear if they may be related to the failure of the UD plies or external fabric plies.

Specimen code	σ_f	τ_f	σ_f average	σ_f st. dev.	τ_f average	τ_f st. dev.
TUT-ST-L0-01	63.5	0	51.96	9.40	0	0
TUT-ST-L0-02	44.34	0				
TUT-ST-L0-03	44.26	0				
TUT-ST-L0-04	55.74	0				
TUT-ST-L1-01	46.6	46.6	49.28	2.32	49.28	2.32
TUT-ST-L1-02	50.74	50.74				
TUT-ST-L1-03	50.49	50.49				
TUT-ST-L2-01	30.95	61.9	32.04	0.99	64.29	1.98
TUT-ST-L2-02	32.88	65.76				
TUT-ST-L2-03	32.3	64.6				
TUT-SC-L0-01	-125.32	0	-122.01	15.49	0	0
TUT-SC-L0-02	-135.58	0				
TUT-SC-L0-03	-105.13	0				
TUT-SC-L1-01	-75.73	75.73	-76.47	1.04	76.47	1.04
TUT-SC-L1-02	-77.2	77.2				
TUT-SC-L2-01*	---	---	-38.75	0.35	77.5	0.71
TUT-SC-L2-02	-39	78				
TUT-SC-LS-03	-38.5	77				
TUT-ST-Linf-01	0	77	0	78.1	0	1.53
TUT.ST-Linf-02	0	79.2				

* the specimen exceeded the limit angle imposed during the test: the result was not used.

Table 4.2 – Quasi static tests results.

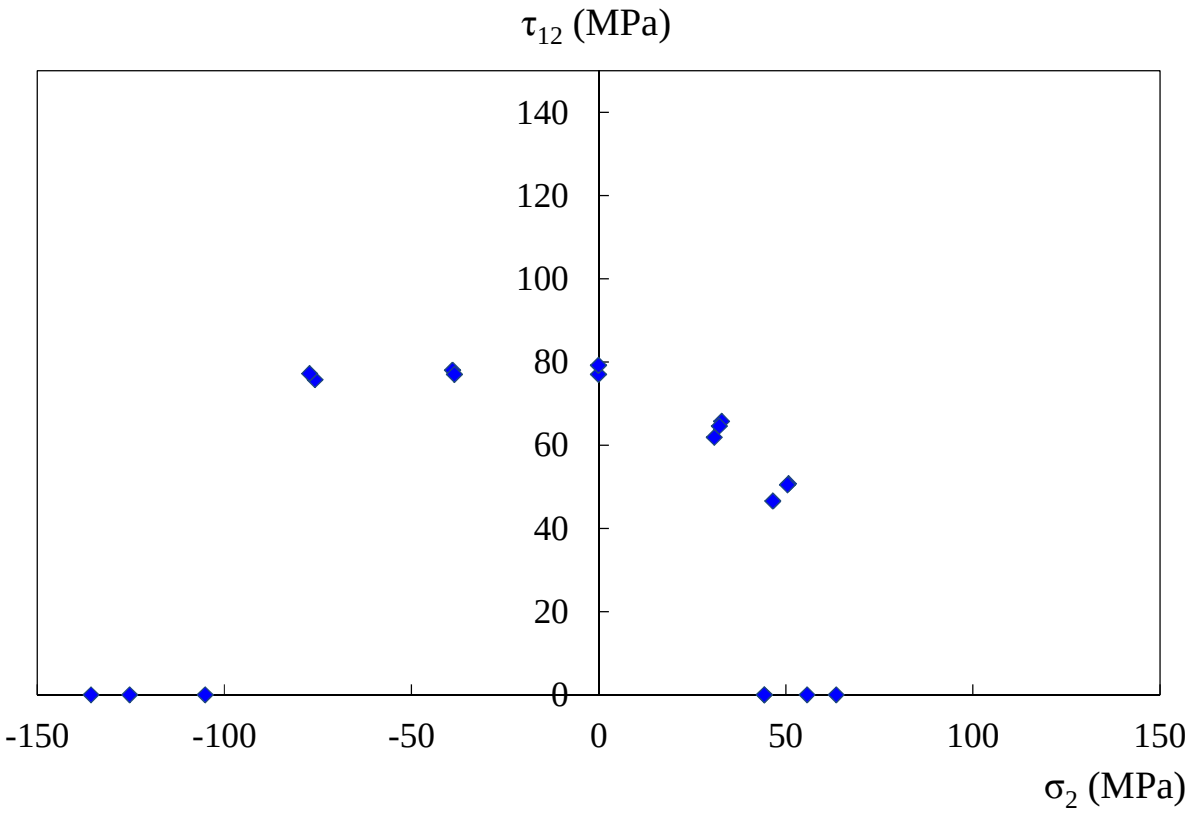

Figure 4.10 – Quasi-static tests results on the σ_2-τ_{12} plane.

Chapter 5

Fatigue tests results

As anticipated in Chapter 4, this chapter is dedicated to the results obtained from the fatigue tests of the present experimental campaign. As for the quasi-static tests, the materials and the tests procedures used are described in Chapter 3.

5.1 – Tested specimens

45 specimens were tested in order to have a full comprehension of the effect of the stress ratio R on the matrix-dominated behavior of composite materials under multiaxial fatigue loading. In Table 5.1 are reported the specimens codes along with their geometrical properties and the applied loads. The formula used in the calculations are the same as the ones used for the quasi-static tests (Equations 4.1 to 4.4).

In some cases, the specimen failed in correspondence of the end of the tabs, where stress concentration occur; in other cases, too many defects were present in the specimen; moreover, sometimes errors occurred in the testing machine control. All the results coming from such cases were not considered in the analysis, and the relative specimens are marked by * in Table 5.1.

Data for the loading condition R = 0, reported later in the plots, were obtained in previous experimental campaigns [20].

SPECIMEN CODE	D_{int} (mm)	D_{ext} (mm)	A (mm^2)	J_p (mm^4)	σ_2 (MPa)	λ_{12} (adim)	τ_{12} (MPa)	F_{max} (N)	F_{min} (N)	Mt_{max} (N*m)	Mt_{min} (N*m)
TUT-L0-30-R-1-01	19	21,25	71,1	7224,5	30	0	0	2481	-2481	0	0
TUT-L0-25-R-1-01	19	21,28	72,1	7337,7	25	0	0	2097	-2097	0	0
TUT-L0-20-R-1-01*	19	21,61	83,2	8615,9	20	0	0	1936	-1936	0	0
TUT-L0-30-R-1-02*	19	21,9	93,2	9788,5	30	0	0	3250	-3250	0	0
TUT-L0-20-R-1-02	19	21,76	88,4	9216,5	20	0	0	2055	-2055	0	0
TUT-L0-25-R-1-02*	19	21,75	88,0	9176,1	25	0	0	2559	-2559	0	0
TUT-L0-33-R05-01*	19	21,9	93,2	9788,5	33	0	0	3575	1787	0	0
TUT-L0-25-R05-01	19	21,74	87,7	9135,7	25	0	0	2549	1274	0	0
TUT-L0-33-R05-02*	19	21,87	92,1	9665,0	33	0	0	3535	1768	0	0
TUT-L0-40-R05-01*	19	21,92	93,8	9871,1	40	0	0	4365	2182	0	0
TUT-L0-40-R05-02	19	21,95	94,9	9995,4	40	0	0	4413	2206	0	0
TUT-L0-35-R05-01*	19	21,79	89,4	9338,2	35	0	0	3638	1819	0	0
TUT-L0-35-R05-02	19	21,9	93,2	9788,5	35	0	0	3791	1896	0	0
TUT-L1-30-R05-01	19	21,9	93,2	9788,5	30	1	30	3250	1625	27,089	13,544
TUT-L0-17-R-1-01	19	21,7	86,3	8974,8	17	0	0	1706	-1706	0	0
TUT-L1-12-R-1-01	19	21,92	93,8	9871,1	12	1	12	1309	-1309	10,917	-10,917
TUT-L1-15-R-1-01	19	21,93	94,2	9912,5	15	1	15	1643	-1643	13,697	-13,697
TUT-L1-17-R-1-01	19	21,85	91,4	9583,0	17	1	17	1807	-1807	15,062	-15,062
TUT-L1-20-R-1-01	19	21,79	89,4	9338,2	20	1	20	2079	-2079	17,315	-17,315
TUT-L2-S7-R-1-01	19	21,68	85,6	8894,6	7	2	14	697	-697	11,604	-11,604
TUT-L2-S12-R-1-01*	19	21,86	91,8	9624,0	12	2	24	1281	-1281	21,346	-21,346
TUT-L1-S35-R05-01	19	21,57	81,9	8457,8	35	1	35	3333	1666	27,725	13,862
TUT-L2-12-R-1-02	19	21,8	89,7	9378,8	12	2	24	1252	-1252	20,859	-20,859
TUT-L1-27-R05-01	19	21,56	81,6	8418,4	27	1	27	2560	1280	21,298	10,649
TUT-L2-11-R-1-01	19	21,66	84,9	8814,7	11	2	22	1087	-1087	18,087	-18,087
TUT-L2-9-R-1-01	19	21,84	91,1	9542,0	9	2	18	953	-953	15,887	-15,887
TUT-L0-37-R05-01	19	21,77	88,7	9257,0	37	0	0	3816	1908	0	0
TUT-L0-S15-R-1-01	19	21,95	94,9	9995,4	15	0	0	1655	-1655	0	0
TUT-L2-S16-R05-01	19	21,85	91,4	9583,0	16	2	32	1701	851	28,353	14,176
TUT-L2-S19-R05-01	19	21,87	92,1	9665,0	19	2	38	2035	1018	33,926	16,963
TUT-L2-S21-R05-01	19	21,88	92,5	9706,1	21	2	42	2258	1129	37,639	18,820
TUT-LS-S22-R05-01	19	21,59	82,6	8536,7	22	2	44	2112	1056	35,147	17,573
TUT-L1-S17-R-1-02	19	21,97	95,6	10078,6	17	1	17	1889	-1889	15,755	-15,755
TUT-L2-S9-R-1-02	19	21,94	94,5	9953,9	9	2	18	989	-989	16,498	-16,498
TUT-L0-S20-R-1-02	19	21,76	88,4	9216,5	20	0	0	2055	-2055	0	0
TUT-L1-S28-R05-02*	19	21,51	79,9	8222,3	28	1	28	2600	1300	21,623	10,811
TUT-L1-S34-R05-01	19	21,62	83,6	8655,5	34	1	34	3305	1652	27,499	13,749
TUT-L1-S15-R-1-02	19	21,95	94,9	9995,4	15	1	15	1655	-1655	13,799	-13,799
TUT-L1-S25-R-1-02*	19	21,97	95,6	10078,6	25	1	25	2778	-2778	23,169	-23,169
TUT-L0-S41-R05-01*	19	21,74	87,7	9135,7	41	0	0	4180	2090	0	0
TUT-L1-S22-R-1-01	19	21.56	81.6	8418.4	22	1	22	2086	-2086	17.354	-17.354
TUT-L2-11-R-1-03	19	21.58	82.2	8497.2	11	2	22	1052	-1052	17.500	-17.500
TUT-L0-S25-R-1-02	19	21.85	91.4	9583.0	25	0	0	2658	-2658	0	0
TUT-L0-S33-R05-01*	19	21.86	91.8	9624.0	33	0	0	3522	1761	0	0
TUT-L0-S33-R05-02	19	21.88	92.5	9706.1	33	0	0	3548	1774	0	0

* result not used in the analysis.

Table 5.1 – Geometrical properties of tested specimens and applied loads (fatigue tests).

5.2 – Effect of the stress ratio on crack initiation

Figures 5.1 to 5.3 show the effect of R on the S–N curves for first crack initiation in the 90° plies. The straight lines are plotted by the least squares method (a power law relationship between the maximum fatigue stress and the number of cycles to failure is supposed), and the arrow that appears in some cases, associated to an experimental point, indicates that the specimen did not show crack initiation at the reported number of cycles (it is referred to those points as "run out" and they were not counted in the data analysis). At a qualitative level, it can be seen that a tension-compression loading leads to lower fatigue life, that is instead higher for larger values of R. Also the slope of the S–N curves appears to be influenced by the stress ratio, being steeper for R = -1 and less steep for R = 0.5. This means that the effect of R is larger at lower stresses (bigger difference in terms of cycles spent for the initiation of the first crack), and the reason is that the larger is the load the closer we are to a static failure, that does not depend on R but only on σ_{max}.

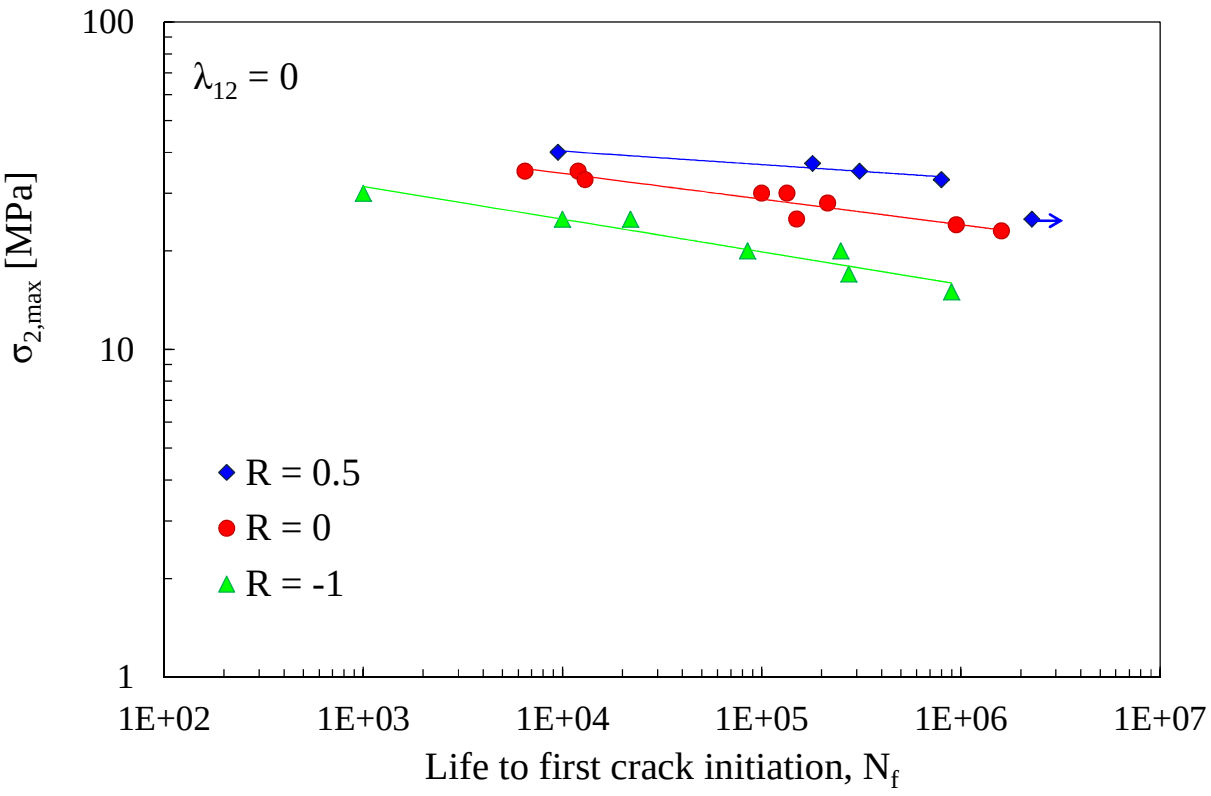

Figure 5.1 – S–N curves for λ_{12} = 0 at R = 0.5, 0, -1.

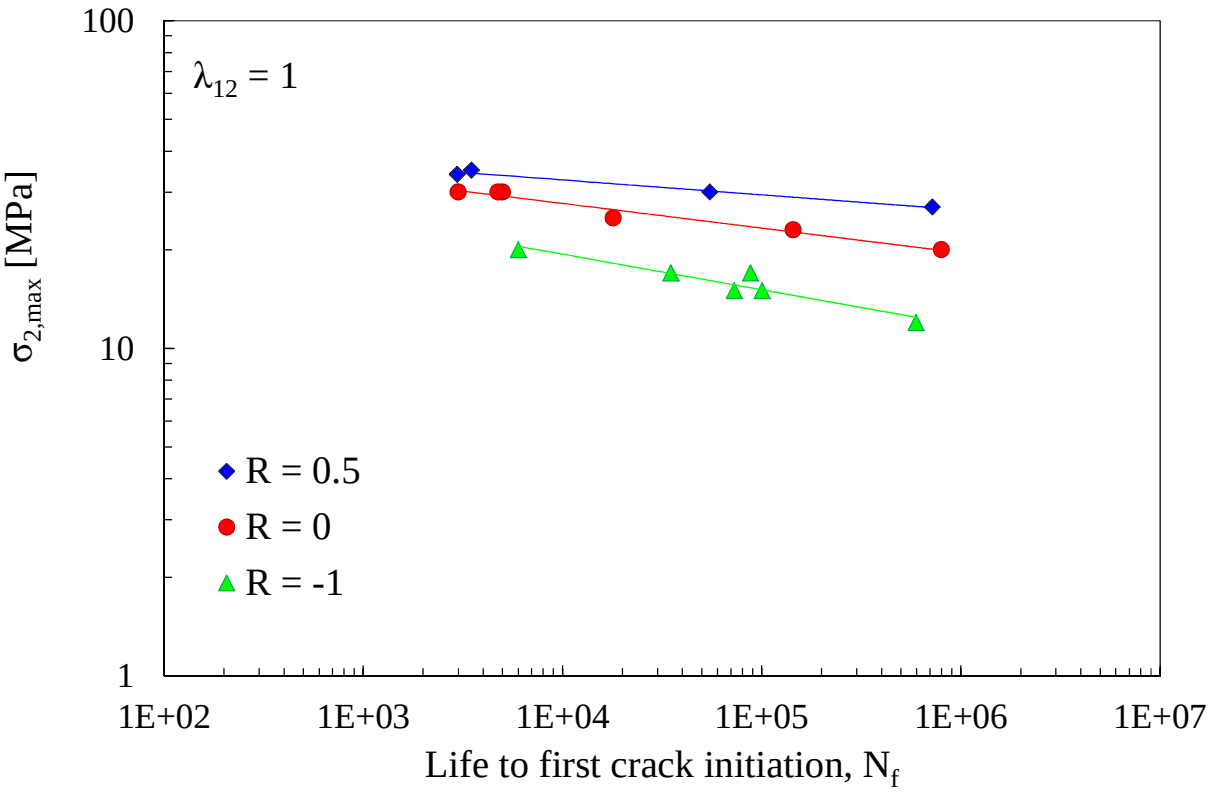

Figure 5.2 – S–N curves for $\lambda_{12} = 1$ at R = 0.5, 0, -1.

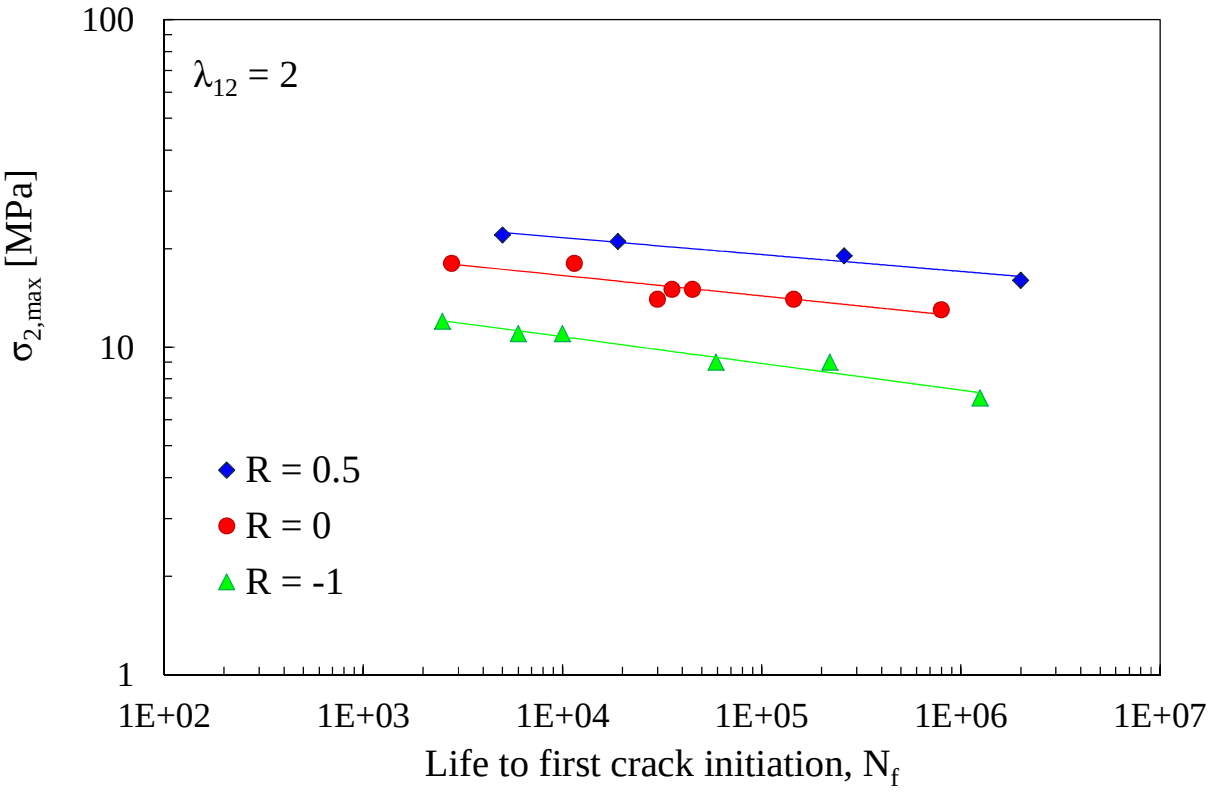

Figure 5.3 – S–N curves for $\lambda_{12} = 2$ at R = 0.5, 0, -1.

In Table 5.2 are reported the equations of the S–N curves, supposed to be linear in the logarithmic scale (the 'fc' subscript stands for 'first crack'). In Figure 5.4 the value of σ_2 corresponding to $N = 10^6$ cycles for different values of R and λ_{12}, drawn from the equation of the curve, is plotted, considering it as a possible quantitative measurement of the influence of the stress ratio on the fatigue life.

λ_{12}	R	Equation
0	-1	$\sigma_{fc} = 62.683\ N^{-0,100}$
0	0	$\sigma_{fc} = 70,876\ N^{-0,078}$
0	0.5	$\sigma_{fc} = 58,922\ N^{-0,041}$
1	-1	$\sigma_{fc} = 52,723\ N^{-0,109}$
1	0	$\sigma_{fc} = 55,445\ N^{-0,075}$
1	0.5	$\sigma_{fc} = 49,732\ N^{-0,046}$
2	-1	$\sigma_{fc} = 22,769\ N^{-0,081}$
2	0	$\sigma_{fc} = 29,444\ N^{-0,062}$
2	0.5	$\sigma_{fc} = 34,708\ N^{-0,052}$

Table 5.2 – Equations of the S–N curves.

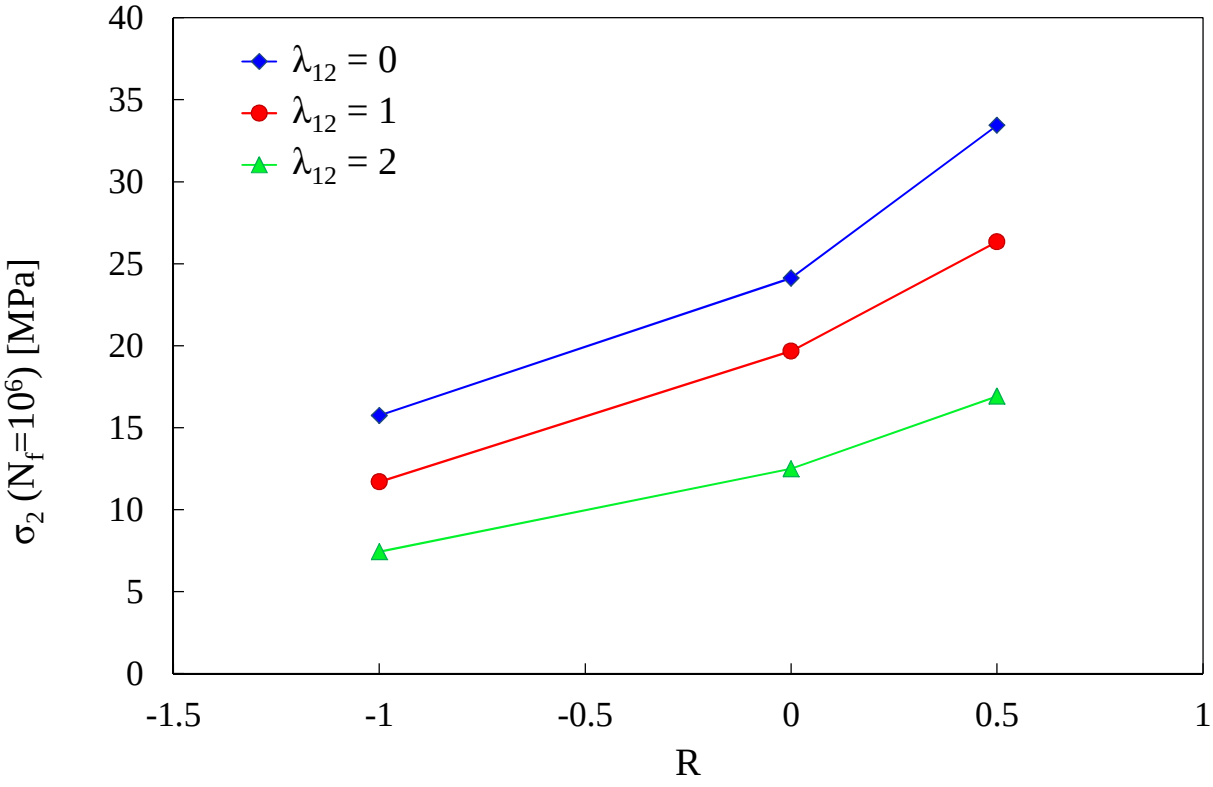

Figure 5.4 – Value of the σ_2 corresponding to $N_f = 10^6$ cycles for different values of R and λ_{12}.

In order to understand if the effect of the stress ratio is dependent on the multiaxiality condition, the data of Figure 5.4 can be normalized respect to the results obtained for R = 0. The influence of the biaxiality ratio does not seem to be very large, and this is true for σ_2 corresponding to N = 10^6 cycles as well as for N = 10^4, 10^5, $2x10^6$ cycles (Figures 5.5 to 5.8). The values of the normalized stresses are reported in Table 5.3.

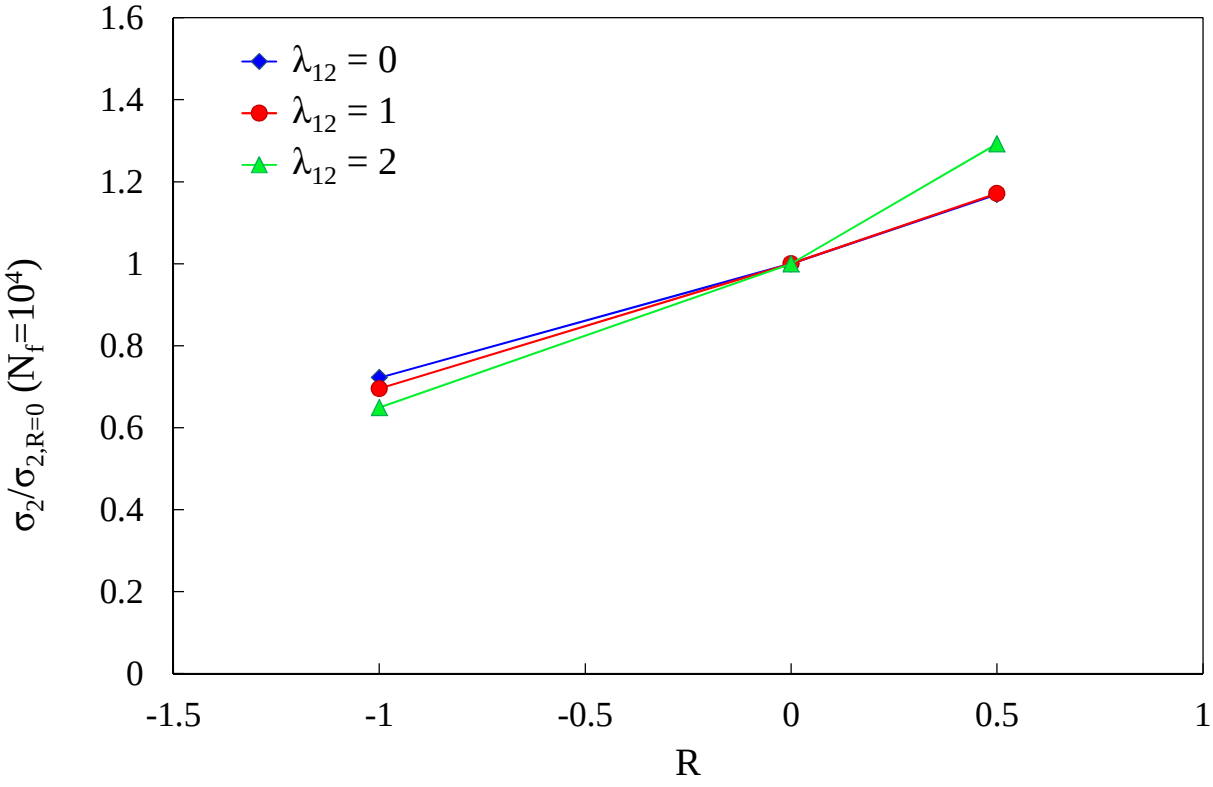

Figure 5.5 – $\sigma_2/\sigma_{2,R=0}$ corresponding to N = 10^4 cycles for the tested values of R and λ_{12}.

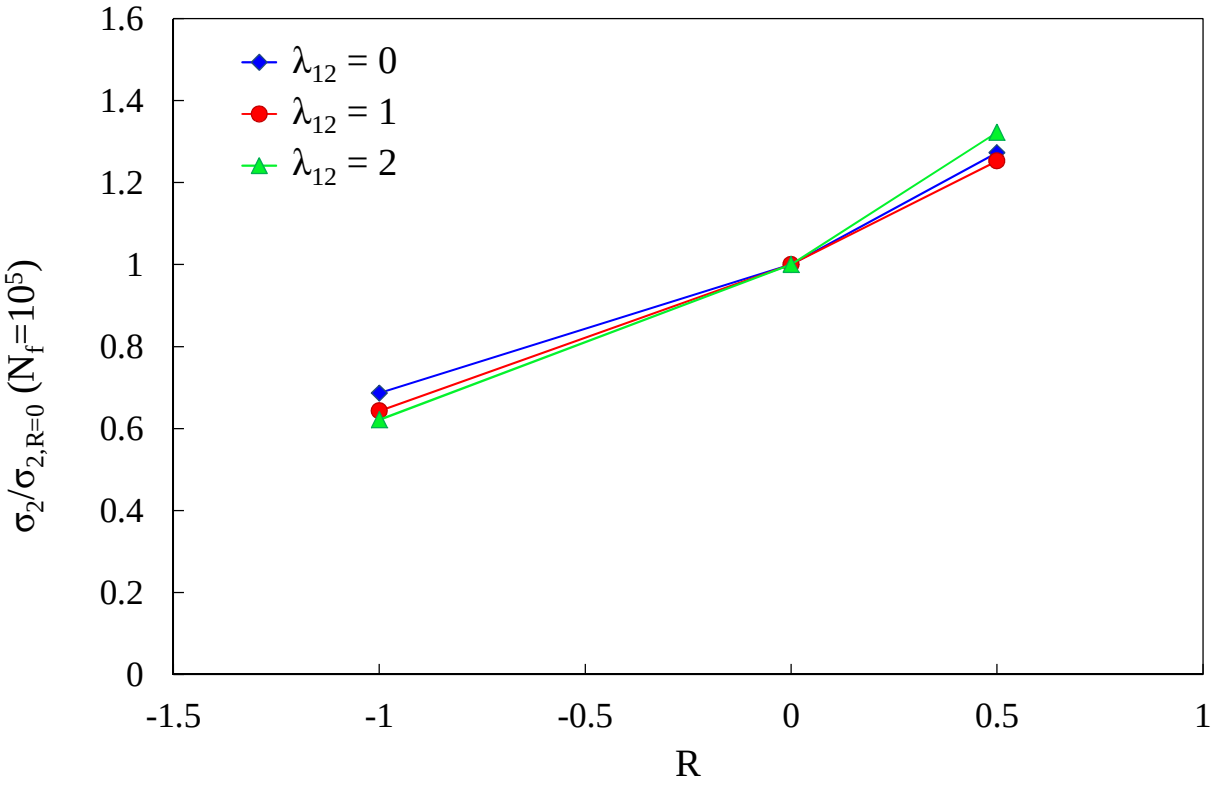

Figure 5.6 – $\sigma_2/\sigma_{2,R=0}$ corresponding to N_f = 10^5 cycles for the tested values of R and λ_{12}.

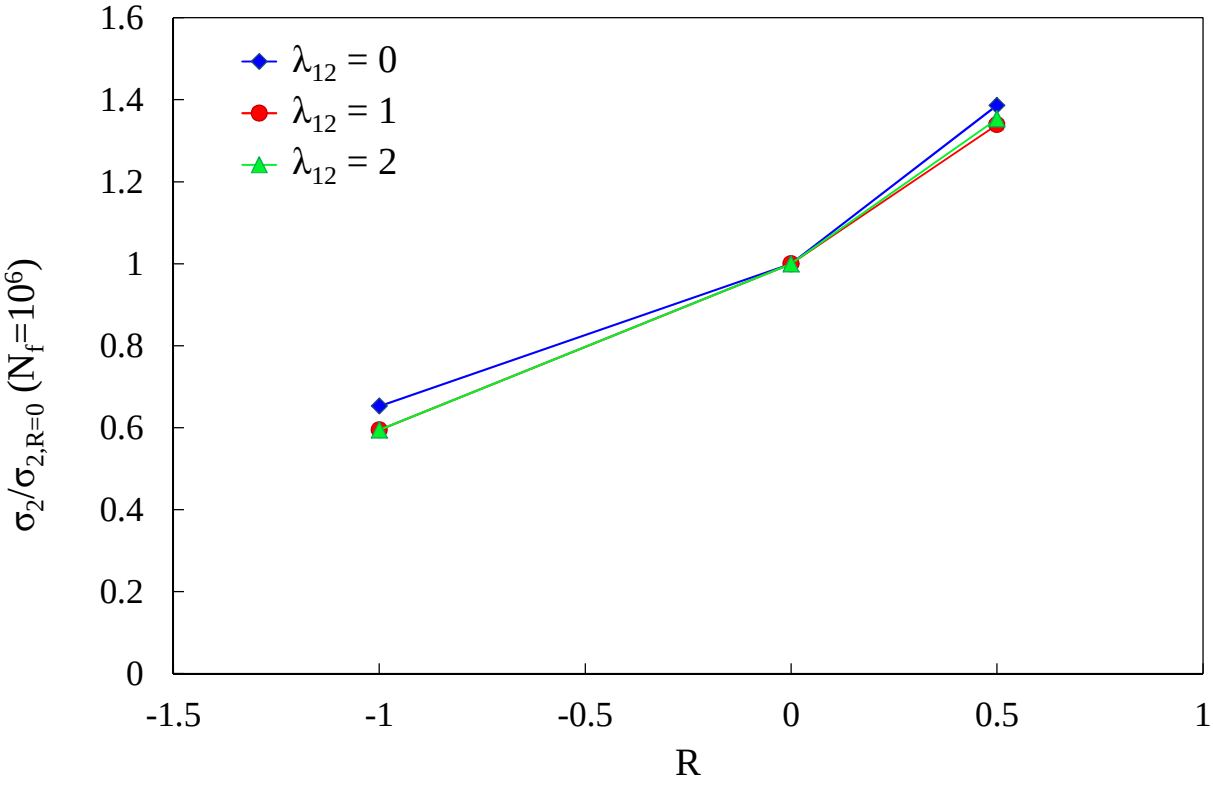

Figure 5.7 – $\sigma_2/\sigma_{2,R=0}$ corresponding to $N_f = 10^6$ cycles for the tested values of R and λ_{12}.

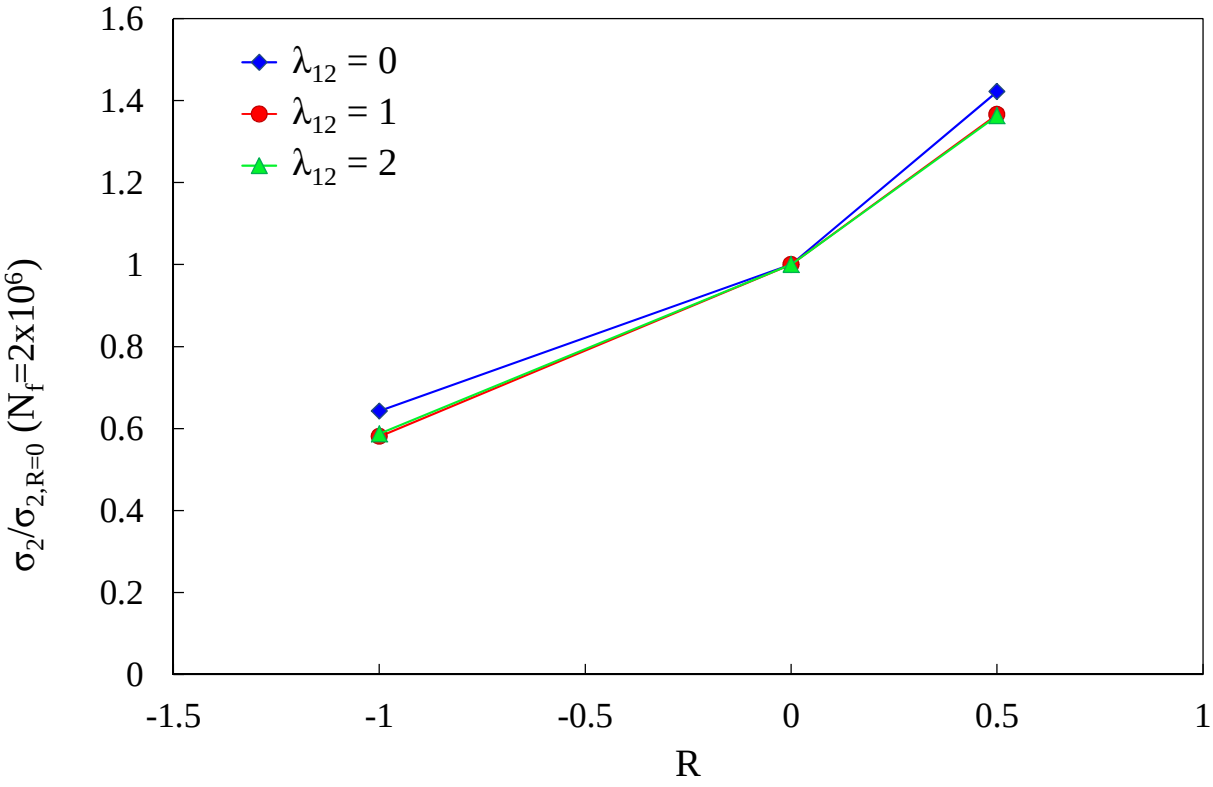

Figure 5.8 – $\sigma_2/\sigma_{2,R=0}$ corresponding to $N_f = 2x10^6$ cycles for the tested values of R and λ_{12}.

λ_{12}	R	σ_2 ($N=10^4$)	σ_2 ($N=10^5$)	σ_2 ($N=10^6$)	σ_2 ($N=2x10^6$)	$\sigma_2/\sigma_{2,R=0}$ ($N=10^4$)	$\sigma_2/\sigma_{2,R=0}$ ($N=10^5$)	$\sigma_2/\sigma_{2,R=0}$ ($N=10^6$)	$\sigma_2/\sigma_{2,R=0}$ ($N=2x10^6$)
0	-1	24.6	19.8	15.7	14.7	0.722	0.687	0.653	0.643
0	0	34.6	28.9	24.1	22.9	1	1	1	1
0	0.5	40.4	36.8	33.4	32.5	1.169	1.273	1.386	1.422
1	-1	19.3	15.0	11.7	10.8	0.695	0.643	0.594	0.581
1	0	27.8	23.4	19.7	18.7	1	1	1	1
1	0.5	32.6	29.3	26.3	25.5	1.172	1.252	1.339	1.366
2	-1	10.8	9.0	7.4	7.0	0.649	0.621	0.595	0.587
2	0	16.6	14.4	12.5	12.0	1	1	1	1
2	0.5	21.5	19.1	16.9	16.3	1.293	1.323	1.353	1.363

Table 5.3 – Values of σ_2 and $\sigma_2/\sigma_{2,R=0}$ for the tested values of R and λ_{12}.

From the equations of the S–N curves (Table 5.2) it is possible to drawn the constant fatigue life diagrams ($\sigma_{2,a} - \sigma_{2,m}$) for the experimental data set, as reported in Figures 5.9 to 5.11. In these plots, all the curves seem to converge towards the point representing the static strength obtained under the same multiaxiality conditions.

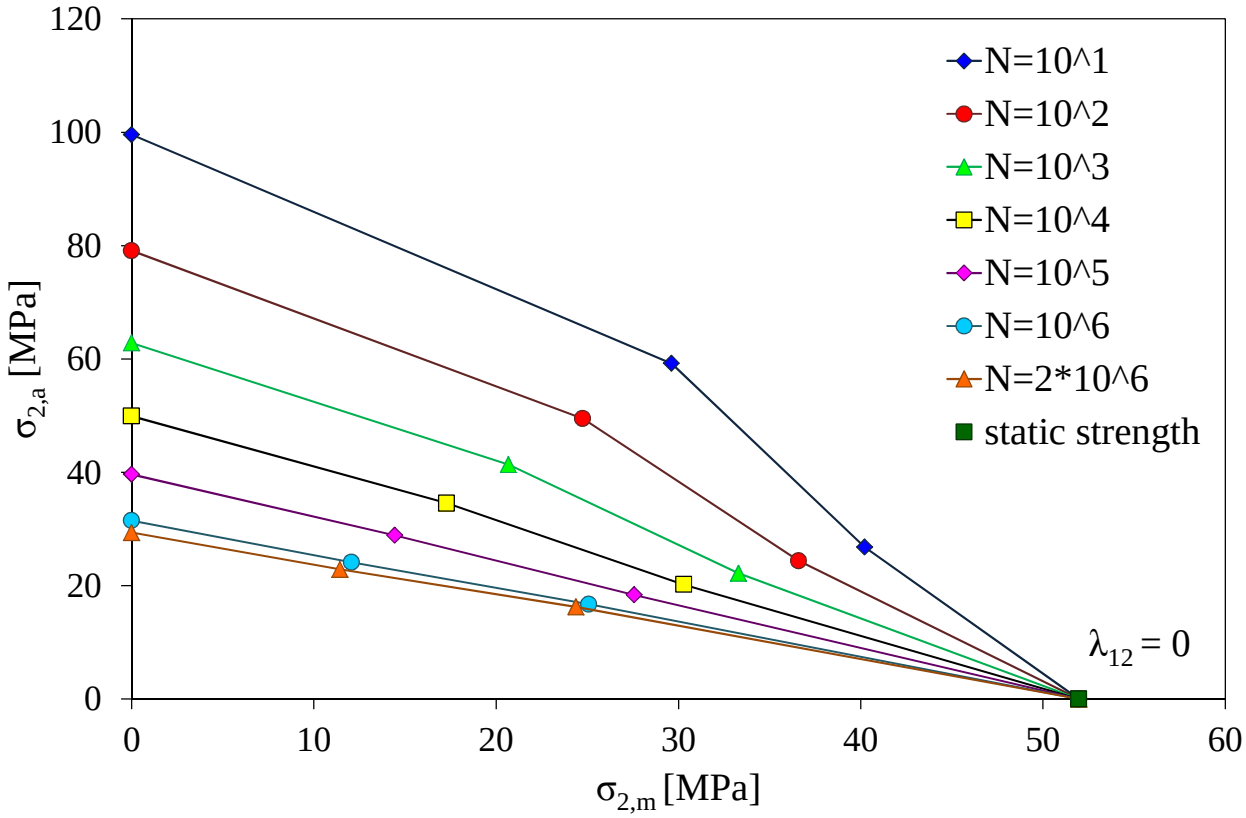

Figure 5.9 – $\sigma_{2,a}$–$\sigma_{2,m}$ diagram (constant fatigue life diagram) for $\lambda_{12} = 0$.

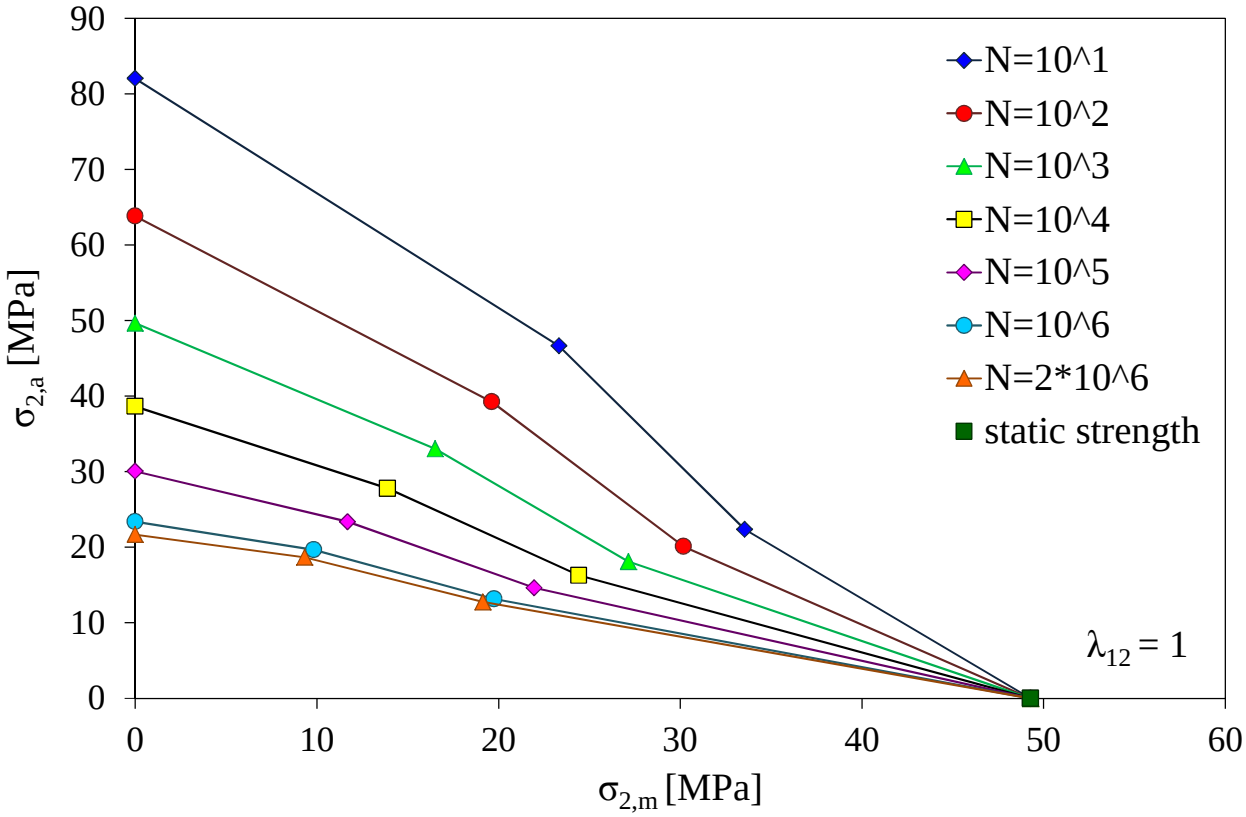

Figure 5.10 – $\sigma_{2,a}$–$\sigma_{2,m}$ diagram (constant fatigue life diagram) for $\lambda_{12} = 1$.

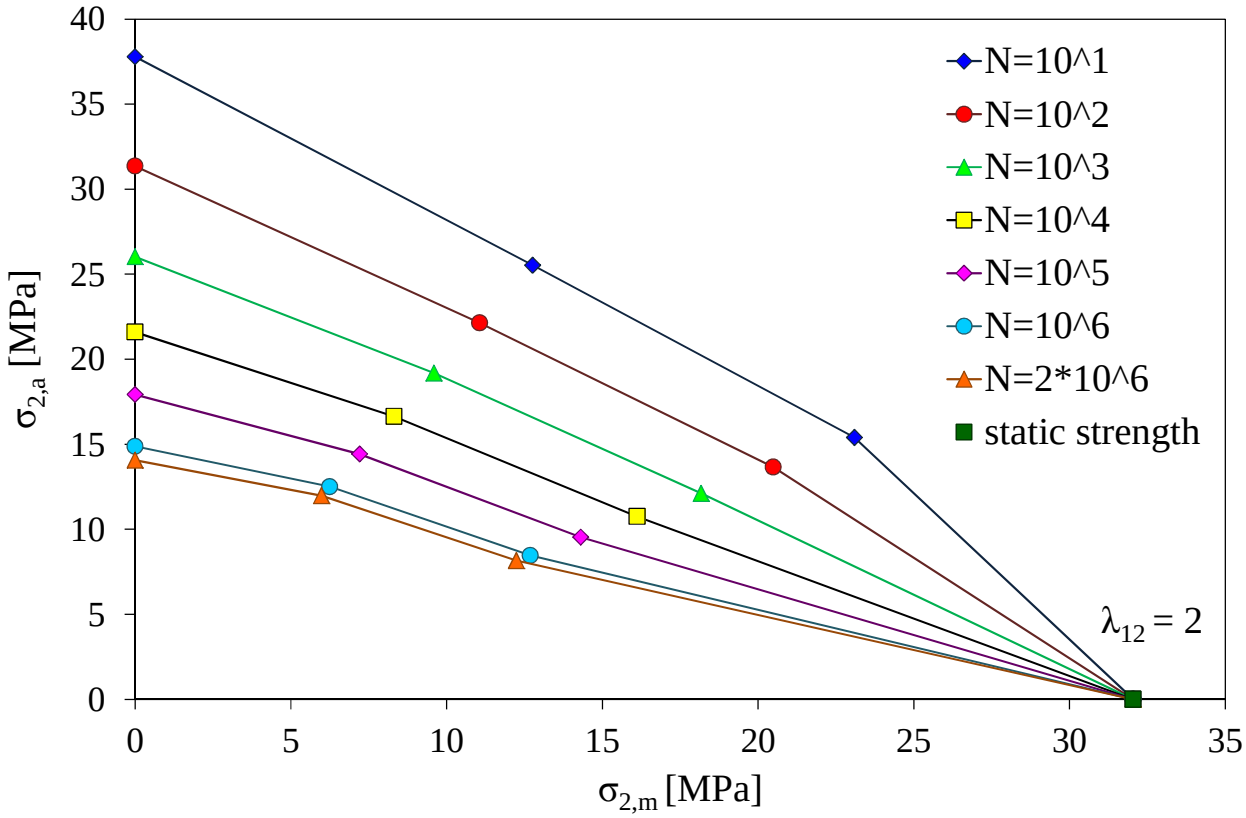

Figure 5.11 – $\sigma_{2,a}$–$\sigma_{2,m}$ diagram (constant fatigue life diagram) for $\lambda_{12} = 2$.

5.3 – Effect of the biaxiality ratio on crack initiation

The effect of the multiaxiality conditions (described by the biaxiality ratio λ_{12}) seems to be qualitatively similar for all the stress ratios (Figures 5.12 to 5.14): the higher λ_{12}, the lower the fatigue life, whereas the slope of the curve seems not to be significantly influenced by this parameter. As above, the lines are drawn by least square method (refer to Table 5.2 for the equations of these curves), and an arrow close to a point means that the test was suspended even if the specimen did not show crack initiation.

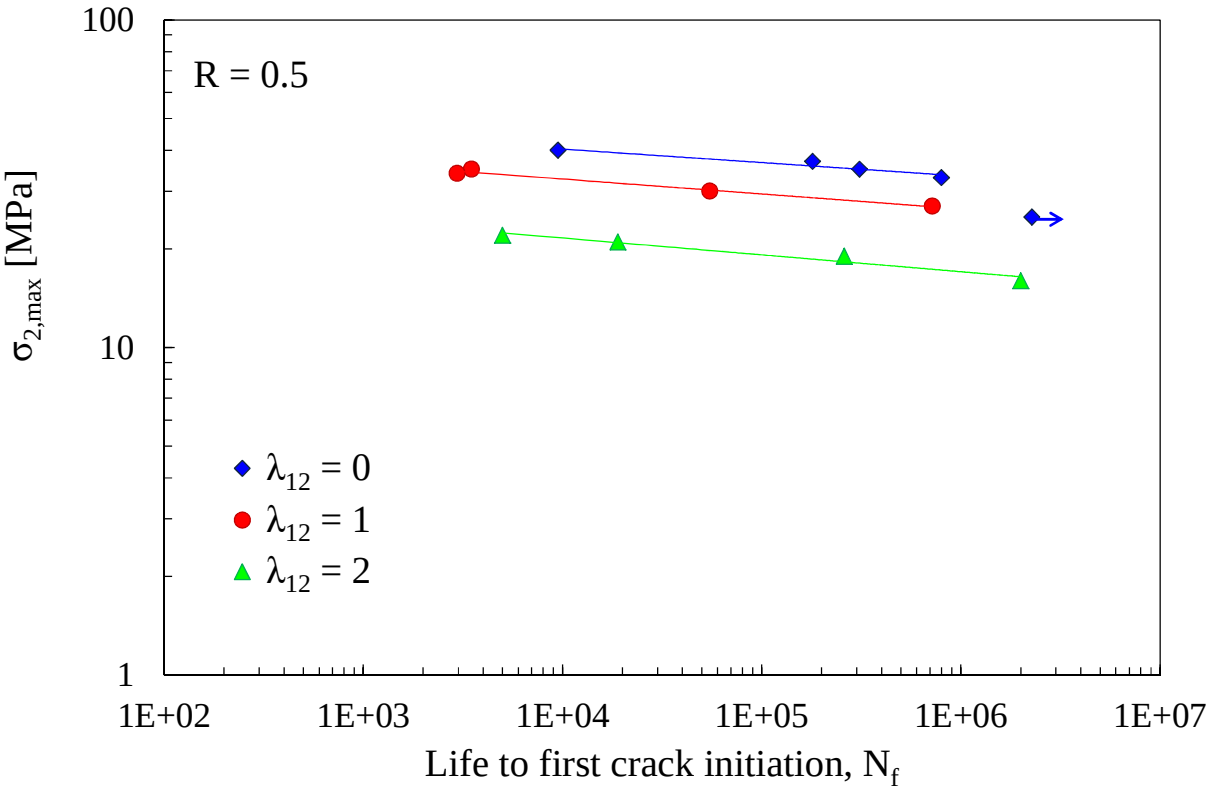

Figure 5.12 – S–N curves for R = 0.5 at λ_{12} = 0, 1, 2.

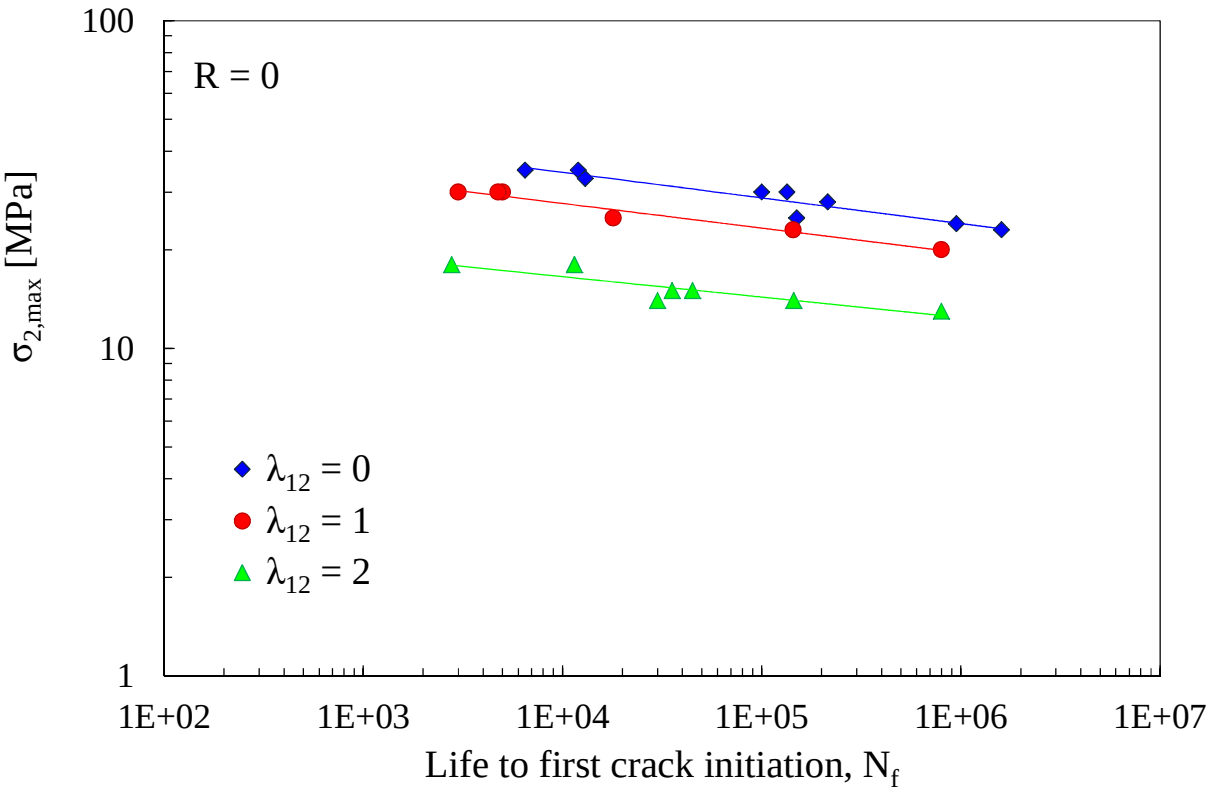

Figure 5.13 – S–N curves for R = 0 at λ_{12} = 0, 1, 2.

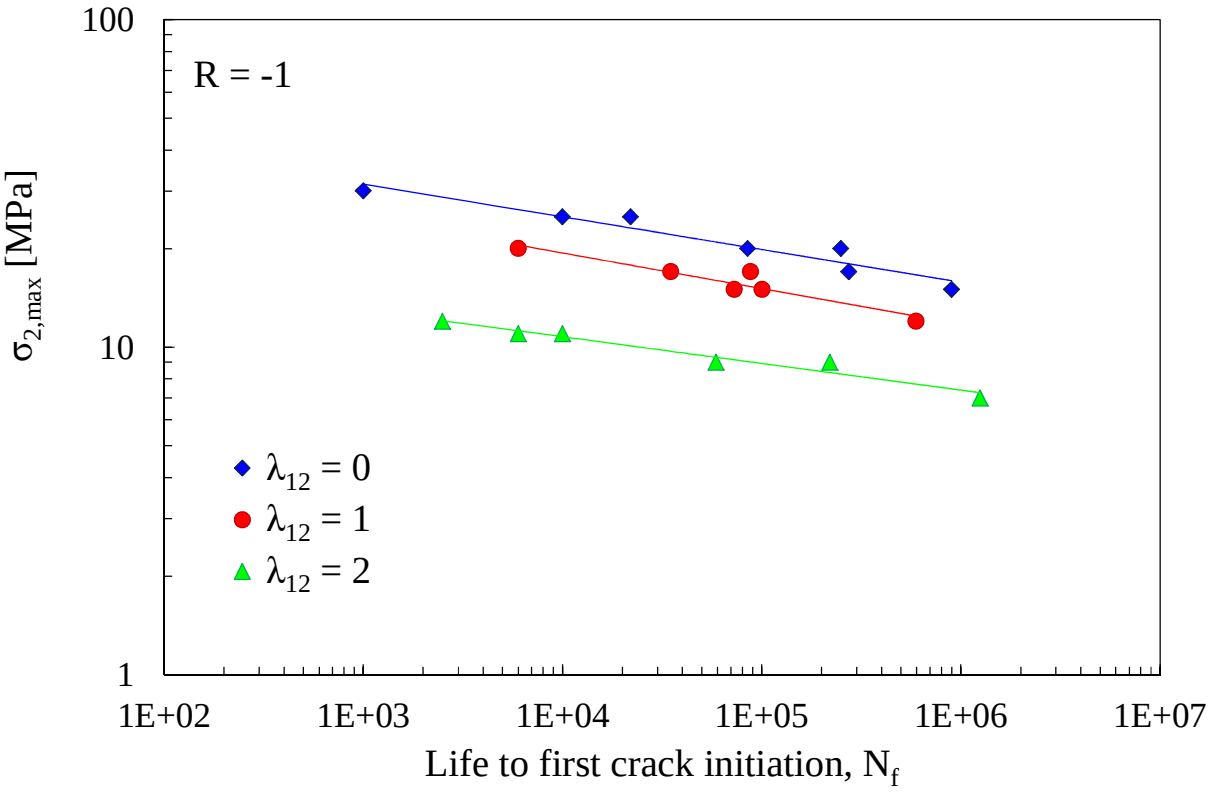

Figure 5.14 – S–N curves for R = -1 at λ_{12} = 0, 1, 2.

5.4 – Effect of stress ratio and biaxiality ratio on crack propagation

The crack propagation was studied by eye-observation of the growth of the cracks nucleated in the same specimens used for the analysis of first crack initiation. In many of the specimens, other cracks nucleated during the propagation test, giving the possibility to obtain more than one experimental point under the same loading conditions. Previous Finite Element Analyses [20] were conducted in order to calculate the value of the Stress Energy Release Rate (G) for mode I and mode II of a crack propagating in the 90° layers into the lay-up of the tested specimens ($[0_T/90_{UD3}/0_T]$, see Chapter 3). In this way it is possible to obtain the crack growth rate (CGR) as a function of $G_{tot} = G_I + G_{II}$, making the results independent from the material lay-up. Moreover, other FEM analyses [20] showed that both the values of G_I and G_{II} reach a constant value after a certain angle of propagation of the crack, meaning that after that angle the crack propagates with constant rate (Figures 5.15 and 5.16).

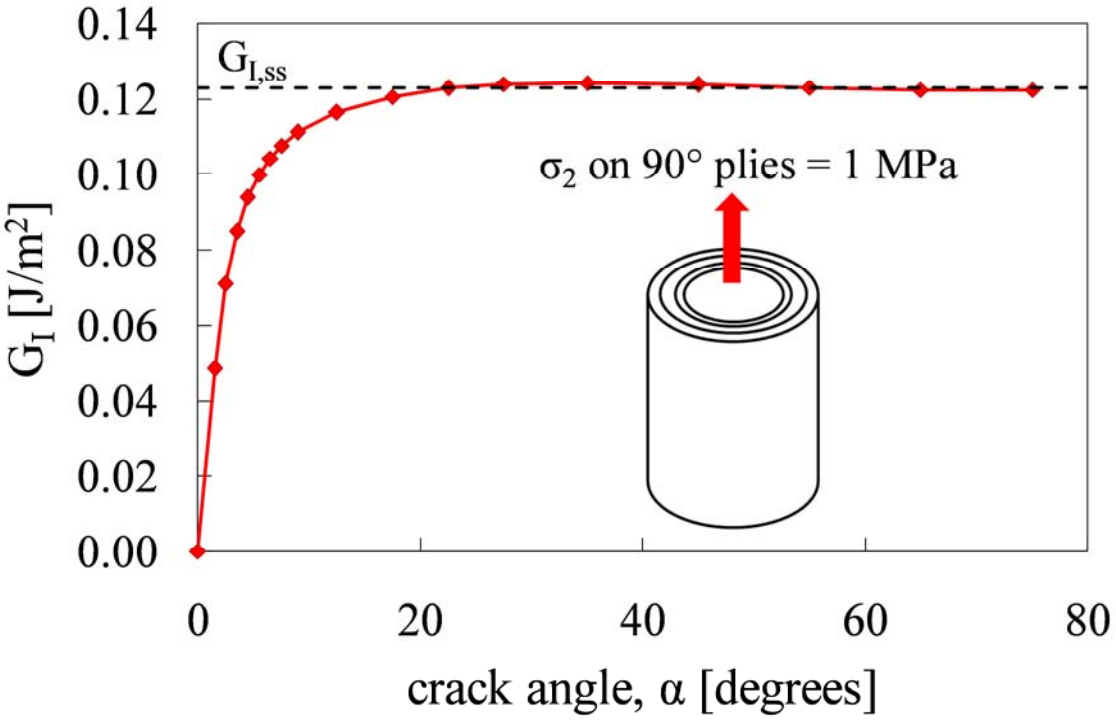

Figure 5.15 – G_I as a function of crack angle for $[0_T/90_{UD3}/0_T]$ configuration, taken from [20].

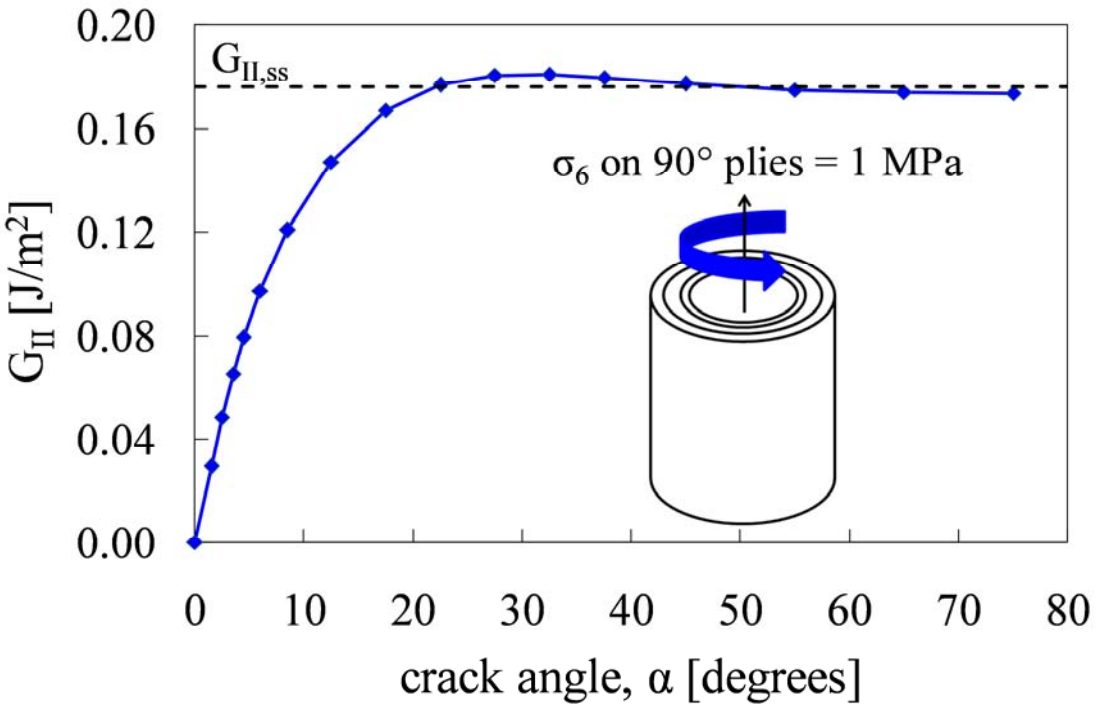

Figure 5.16 – G_{II} as a function of crack angle for $[0_T/90_{UD3}/0_T]$ configuration, taken from [20].

The crack propagation curves obtained for each specimen are reported in Figures 5.17 to 5.22, in which the difference between the crack angle, 2α, and the initial crack angle, $2\alpha_i$, is plotted against the difference between the number of cycles N corresponding to 2α, and the number of cycle N_i at which the crack was detected during the propagation test. The crack angle is drawn from the measurement of the chord relative to the crack according to the following relationship:

$$AB = 2R\sin\frac{2\alpha}{2} \tag{5.5}$$

in which *AB* is the chord denoting the angle, *R* the external radius of the tube and 2α the crack angle. As it is possible to observe in the Figures 5.17 to 5.22, the experimental data scatter is in some cases very large.

As mentioned for the first crack initiation tests, the data relative to the loading condition R = 0, used later on in the analysis of the effect of R on crack propagation, were obtained in a previous work [20].

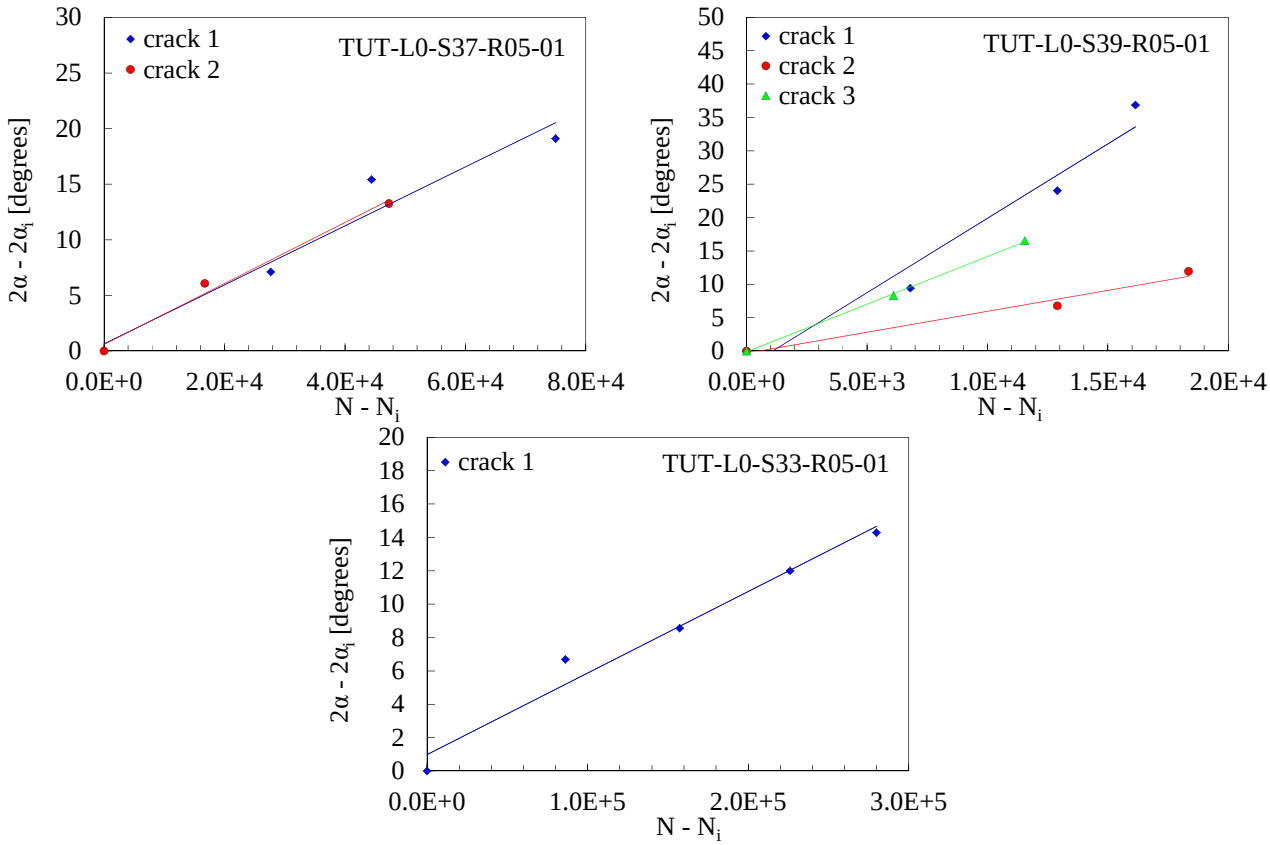

Figure 5.17 – Crack propagation for specimens tested at $\lambda_{12} = 0$, R = 0.5.

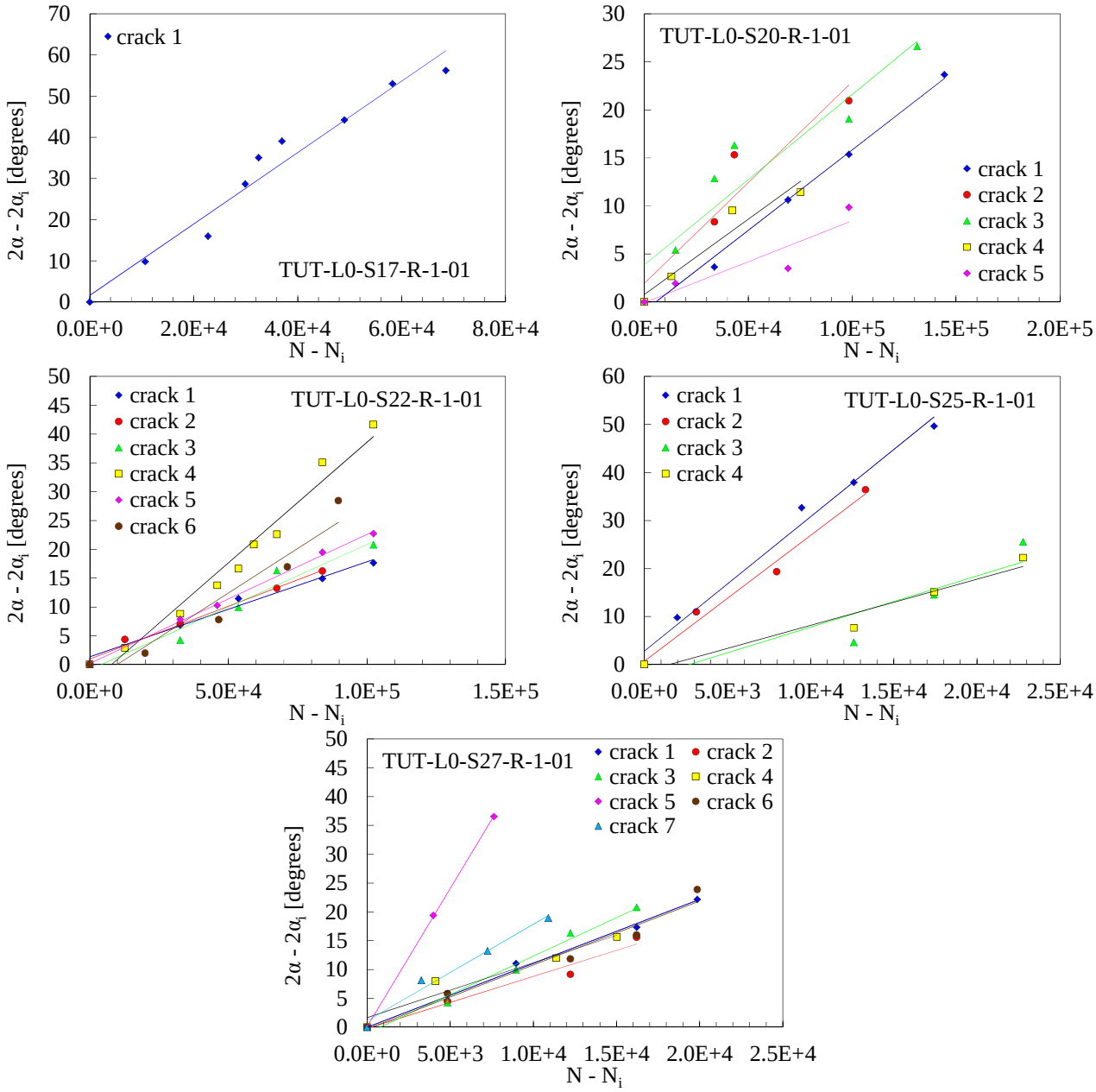

Figure 5.18 – Crack propagation for specimens tested at λ_{12} = 0, R = -1.

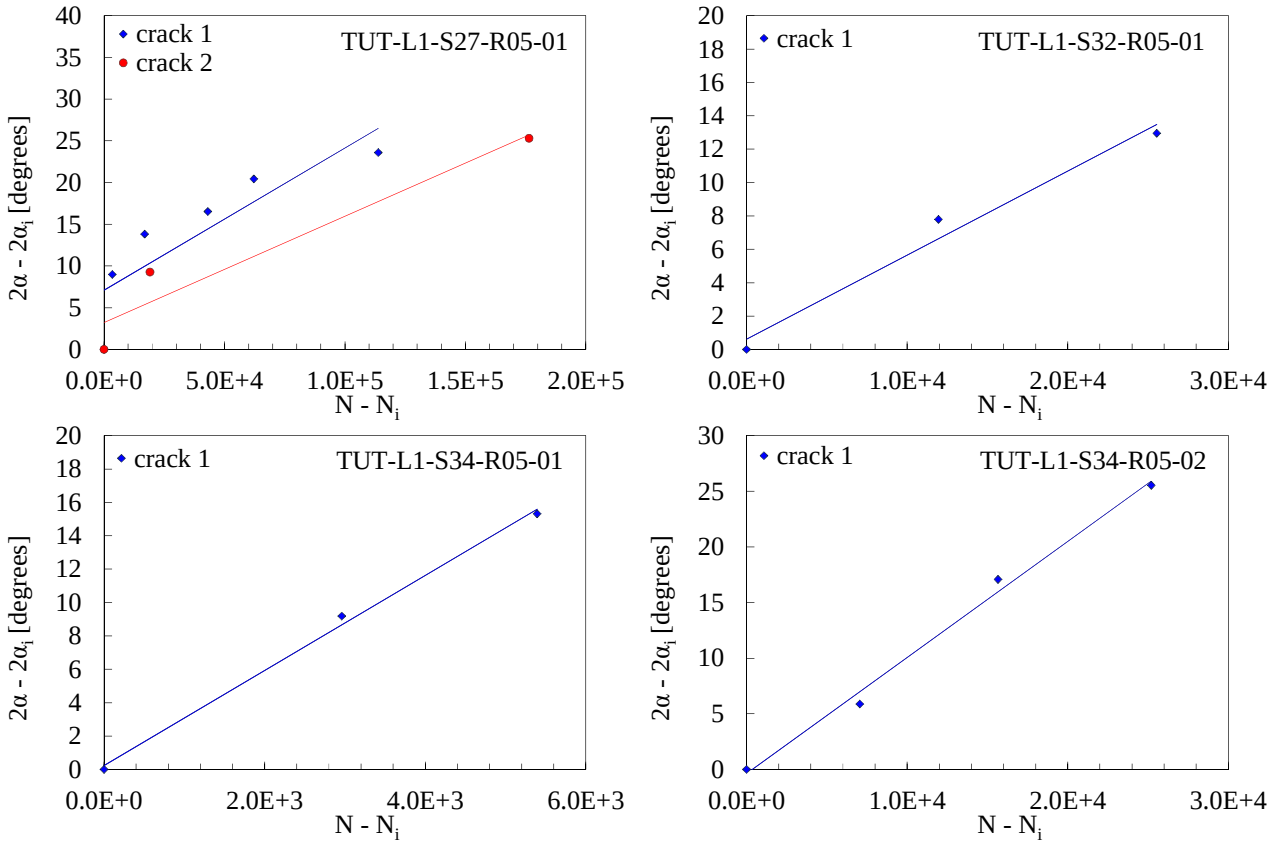

Figure 5.19 – Crack propagation for specimens tested at λ_{12} = 1, R = 0.5.

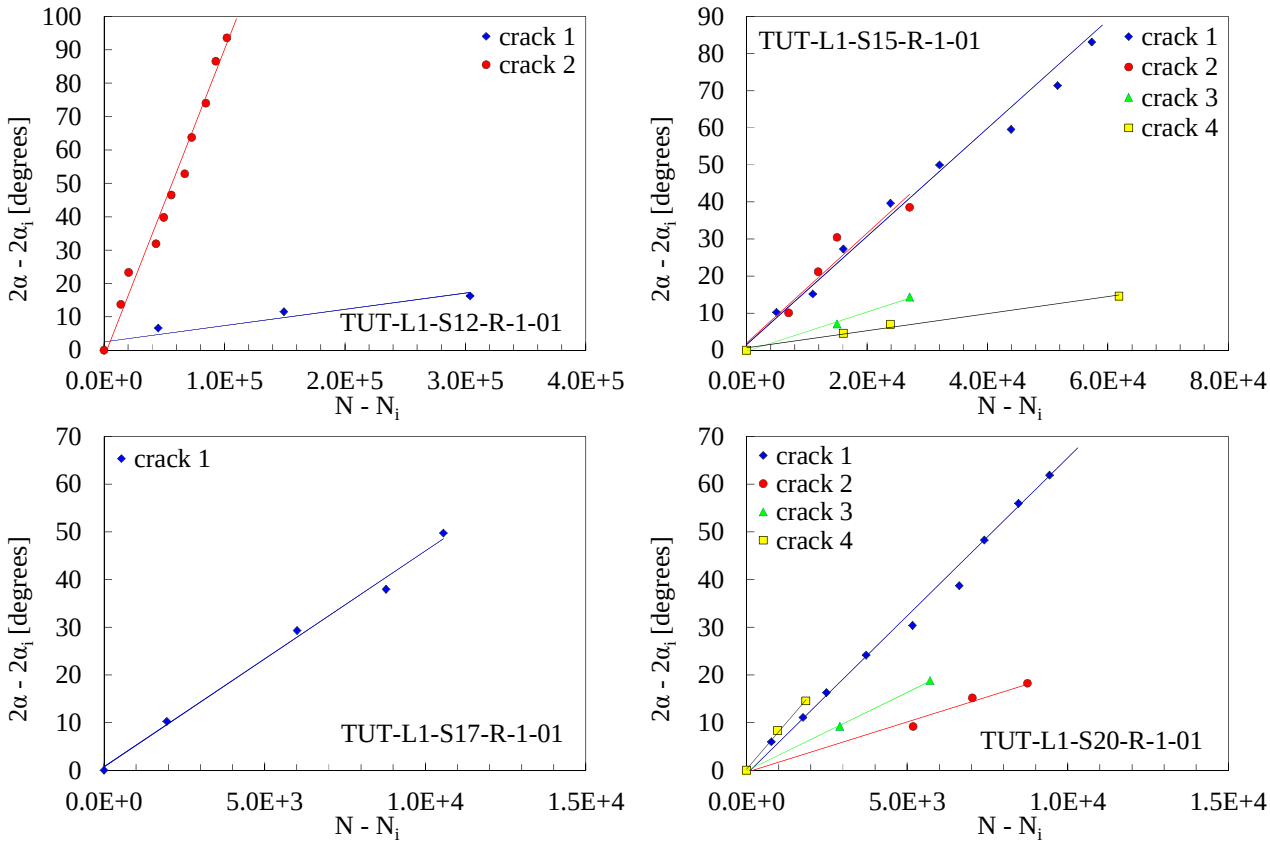

Figure 5.20 – Crack propagation for specimens tested at λ_{12} = 1, R = -1.

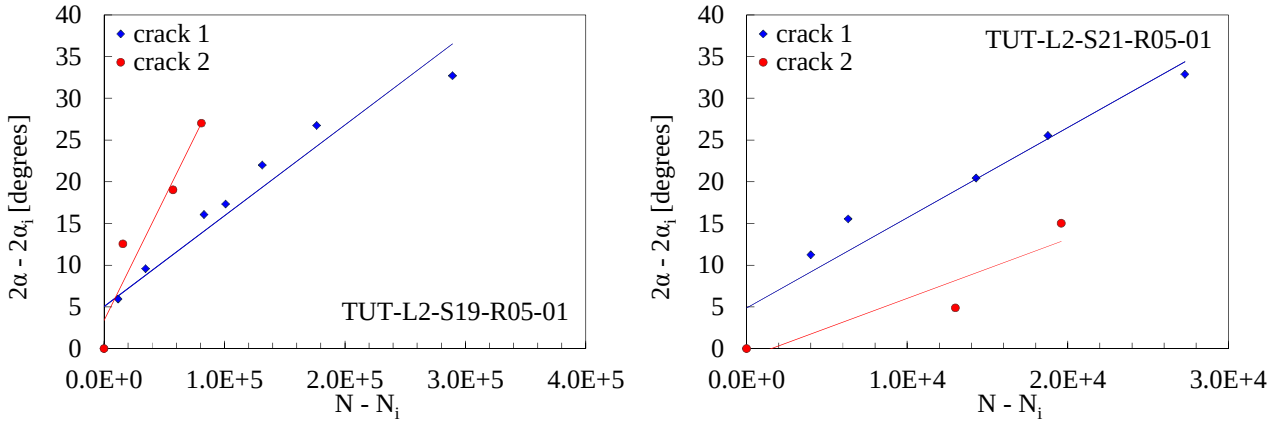

Figure 5.21 – Crack propagation for specimens tested at λ_{12} = 2, R = 0.5.

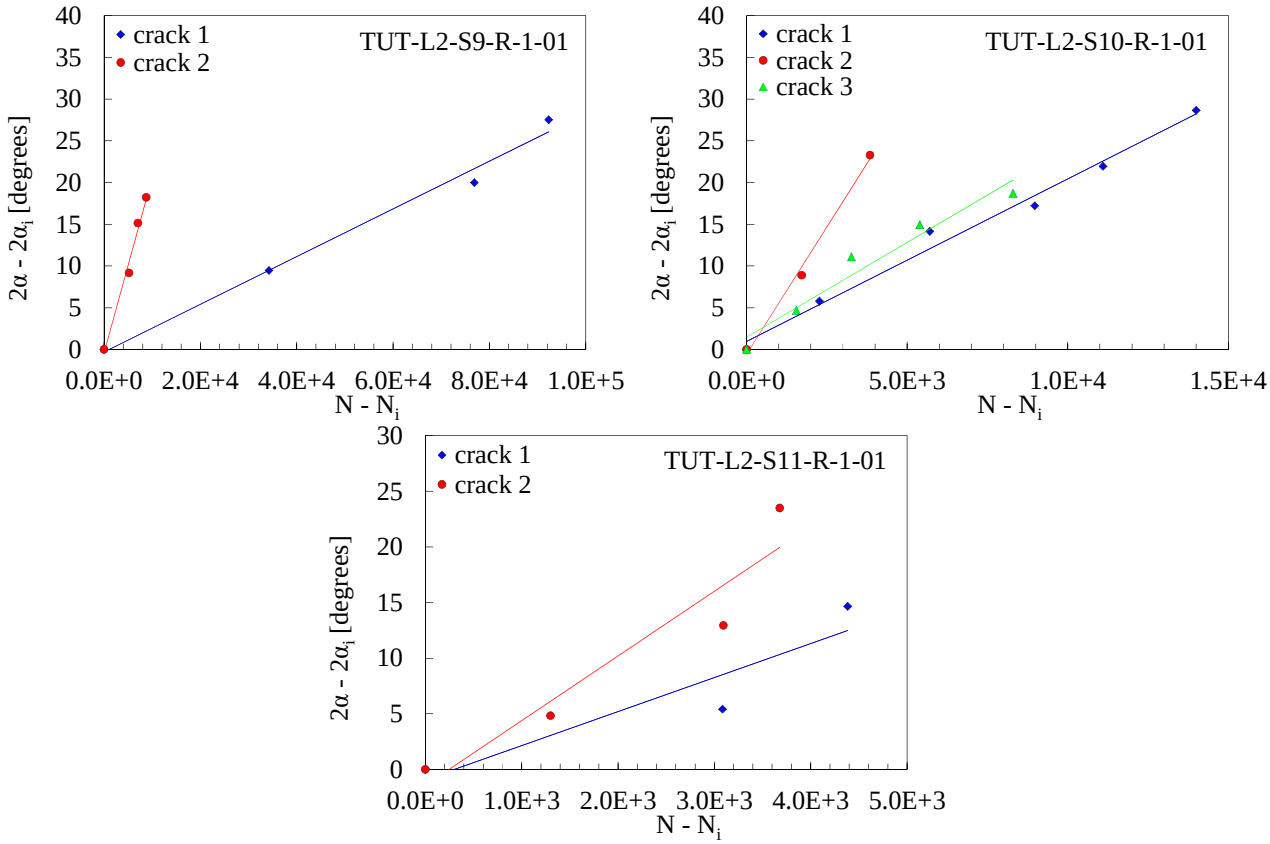

Figure 5.22 – Crack propagation for specimens tested at λ_{12} = 2, R = -1.

The effect of the stress ratio on crack propagation can be seen in the Paris-like curves reported in Figures 5.23 to 5.25. It is remarked here that, since G_I and G_{II} quickly become constant, each point in these figures represents only one propagating crack (hence the term Paris-*like* curves). It is possible to observe that for all the values of the biaxiality ratio, respect to the case R = 0, the presence of compressive loading leads to higher crack growth rate for the same values of G (that is, a lower value of G is needed in order to have the same CGR), whereas R = 0.5 gives lower CGR.

The curves are not only shifted by R, but also their slope appears to be different, being lower for R = -1 and higher for R = 0.5. This means that the effect of R is bigger at lower G_{tot}, which is coherent with the higher influence of R encountered al lower stress level for the first crack initiation. The effect of a compressive stress seems to be also larger at higher λ_{12} (with the increase of λ_{12}, curves for R = -1 get farther respect to the R = 0 curve at the same λ_{12}), implying that adding shear stress to compression influences the CGR more respect to the presence of compression only.

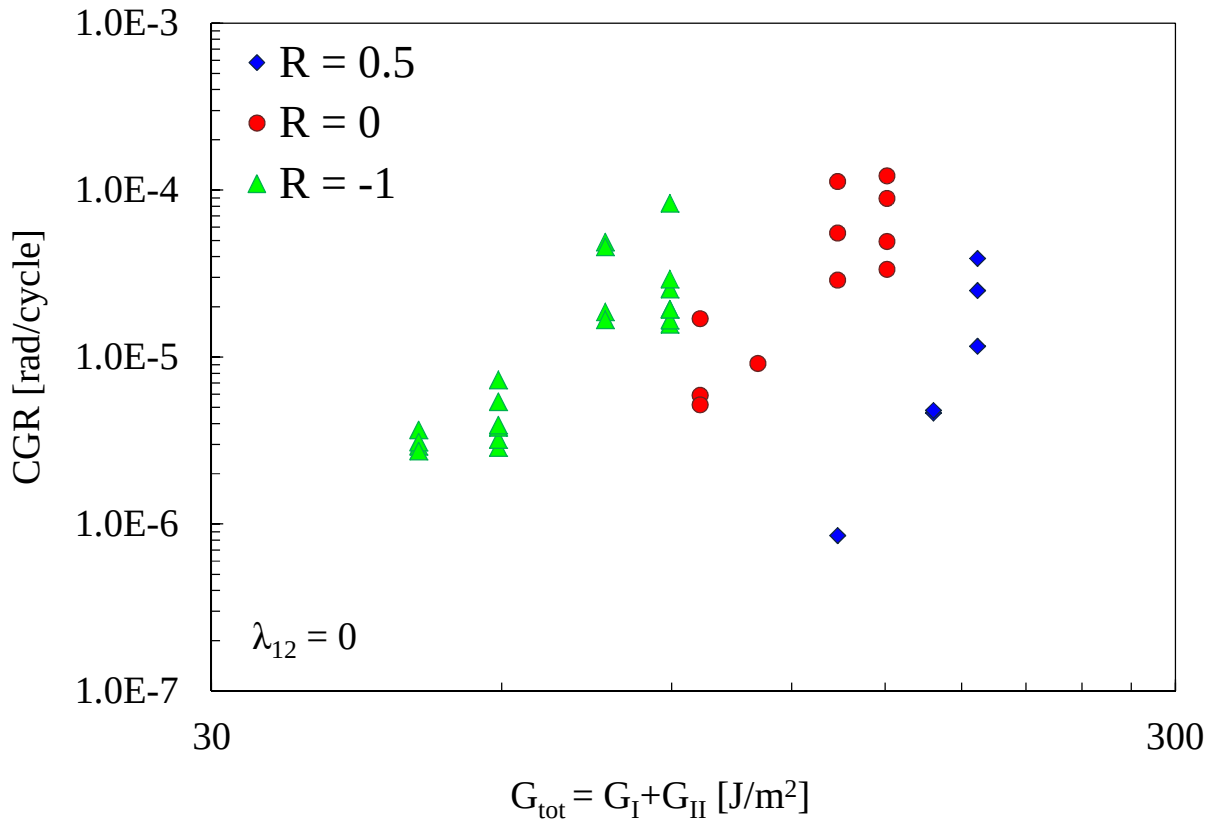

Figure 5.23 – CGR vs G_{tot} for λ_{12} = 0 at R = -1, 0, 0.5.

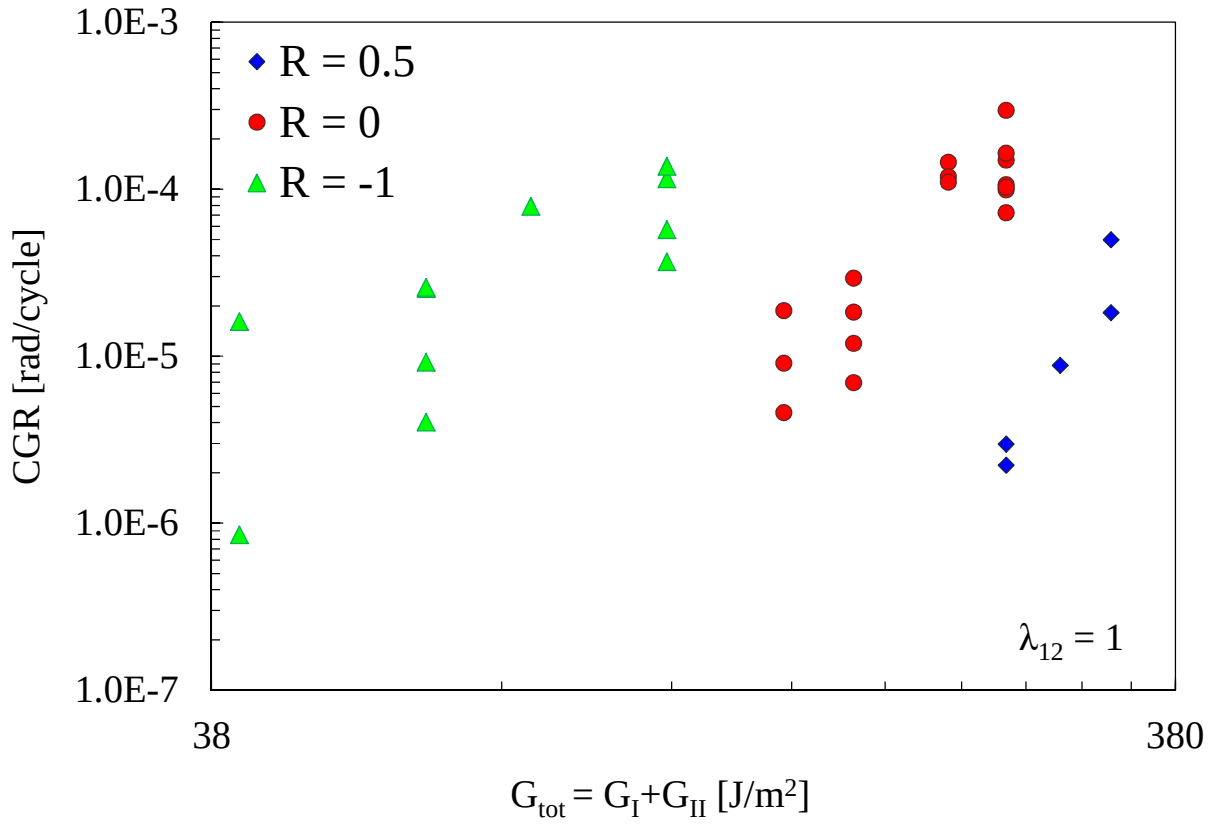

Figure 5.24 – CGR vs G_{tot} for $\lambda_{12} = 1$ at R = -1, 0, 0.5.

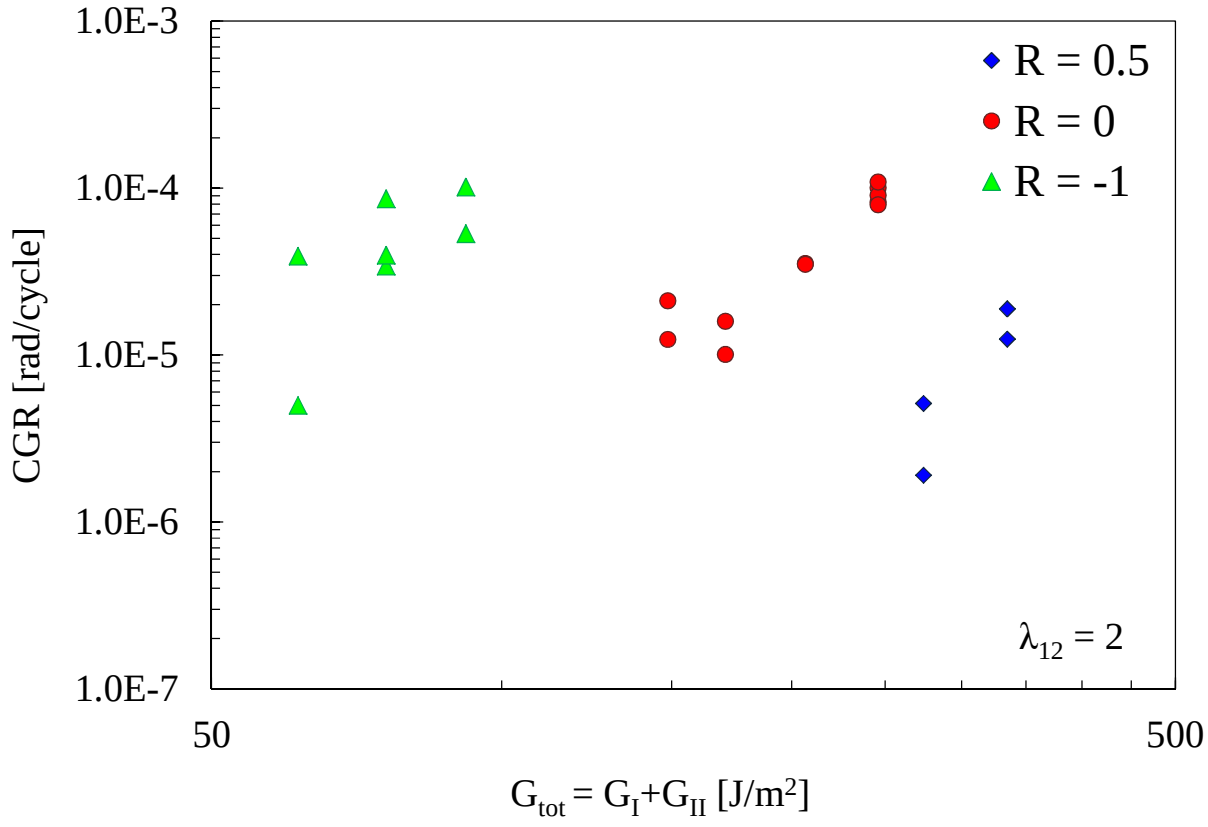

Figure 5.25 – CGR vs G_{tot} for $\lambda_{12} = 2$ at R = -1, 0, 0.5.

The effect of λ_{12} can be seen in Figures 5.26 to 5.28: the gap between the curves at different λ_{12} seems to decrease from R = 0.5 to R = -1 (condition under which they are well overlapped), which is in line with the observations done above for the effect of the stress ratio, according to which the effect of this parameter on crack propagation is larger for lower values of G_{tot}. This trend is particularly evident for the curves at λ_{12} = 0 respect to the curves at λ_{12} = 1 and 2, that remain always close (if not overlapped). It can be noticed that a larger value of λ_{12} brings to lower CGR (for the same value of G_{tot}). The reason is that because of the presence of the fibers, the crack has to propagate parallel to the fibers themselves even if, in presence of shear stress, it would tend to deviate from that direction. As a consequence, the value of G_{tot} needed for the crack to propagate is much larger in presence of shear.

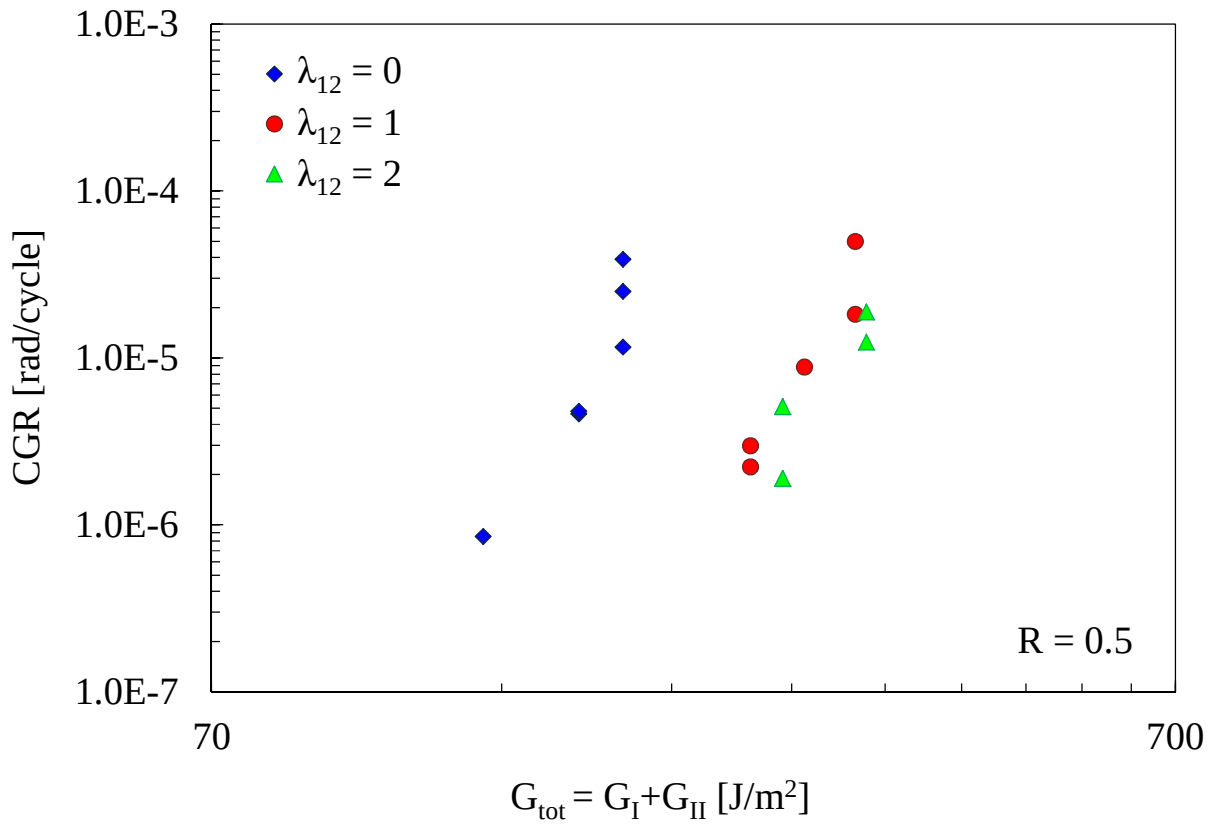

Figure 5.26 – CGR vsG_{tot} for R = 0.5 at λ_{12} = 0, 1, 2.

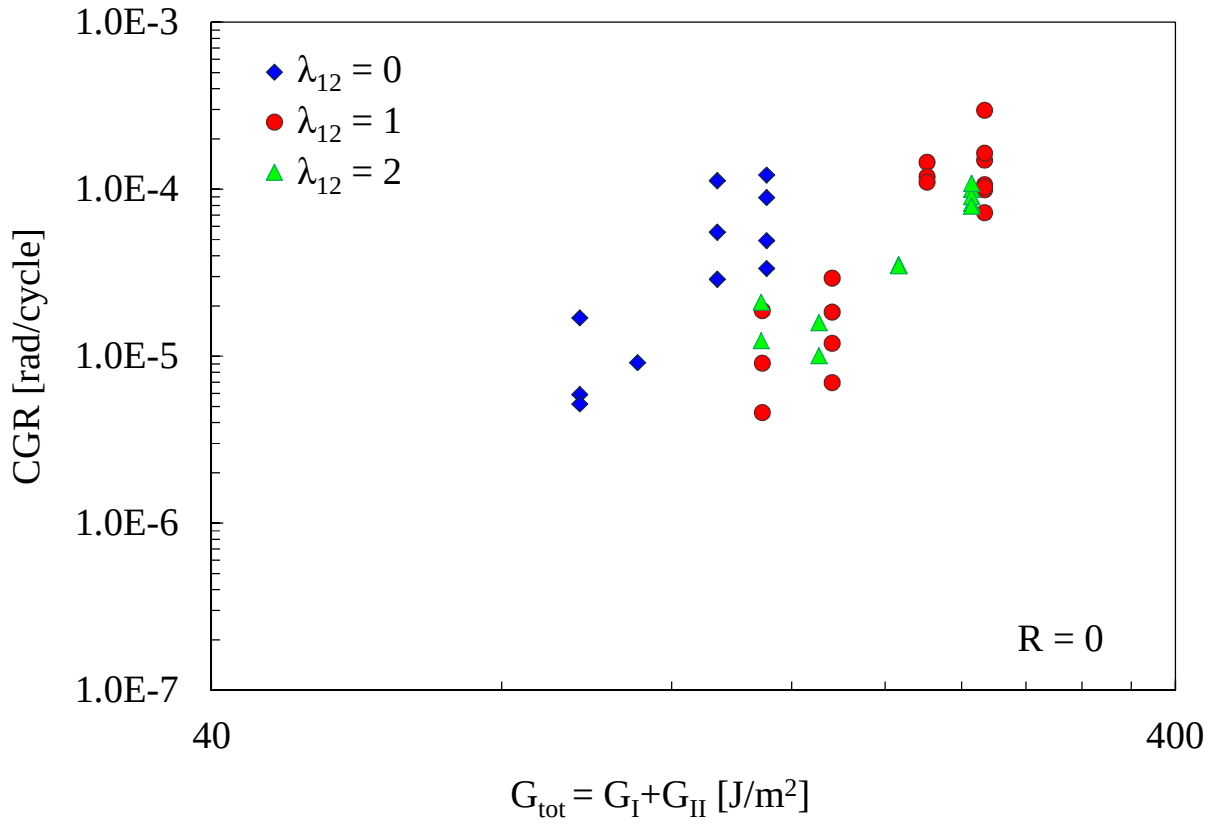

Figure 5.27 – CGR vsG_{tot} for R = 0 at λ_{12} = 0, 1, 2.

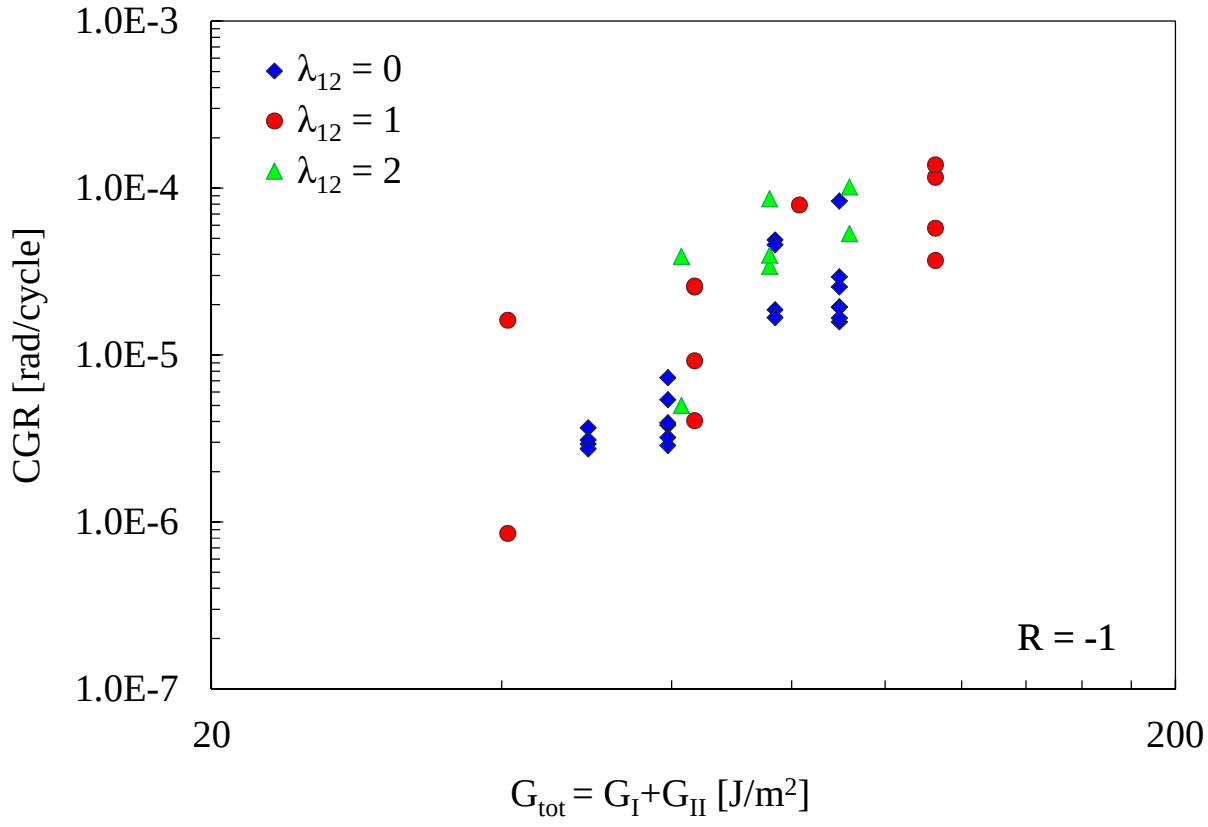

Figure 5.28 – CGR vsG_{tot} for R = -1 at λ_{12} = 0, 1, 2.

5.5 – Fractography

The surface of the broken specimens was observed under a SEM in order to analyze the damage modes at a microscopic scale (Figures 5.29 to 5.35).

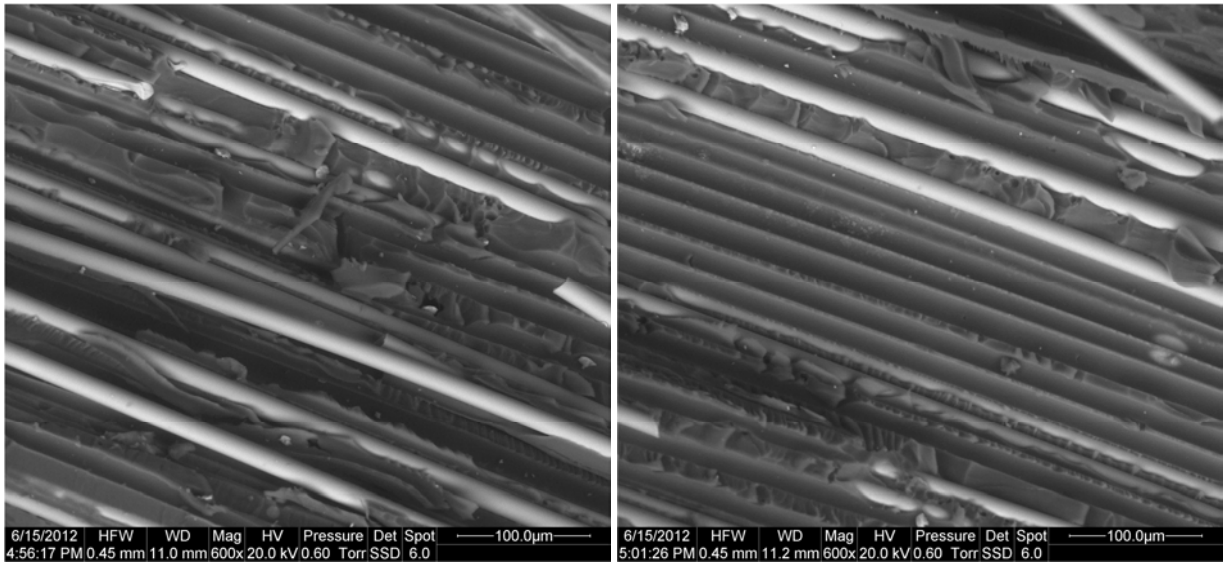

Figure 5.29 – SEM images of the fracture surface for $\lambda_{12} = 0$, R = 0.5.

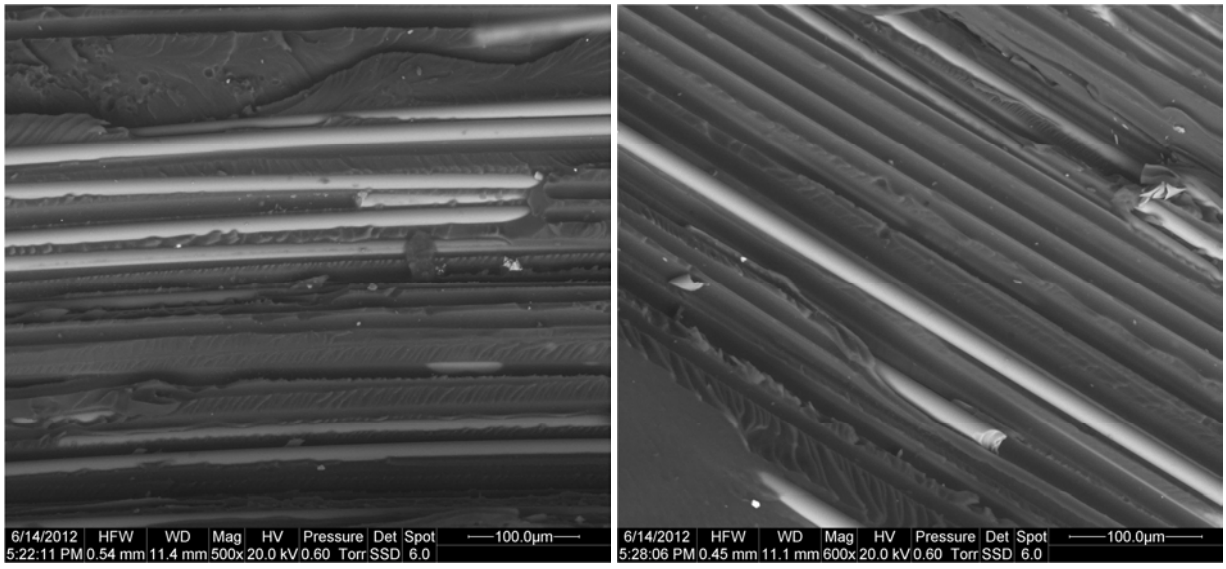

Figure 5.30 – SEM images of the fracture surface for $\lambda_{12} = 0$, R = -1.

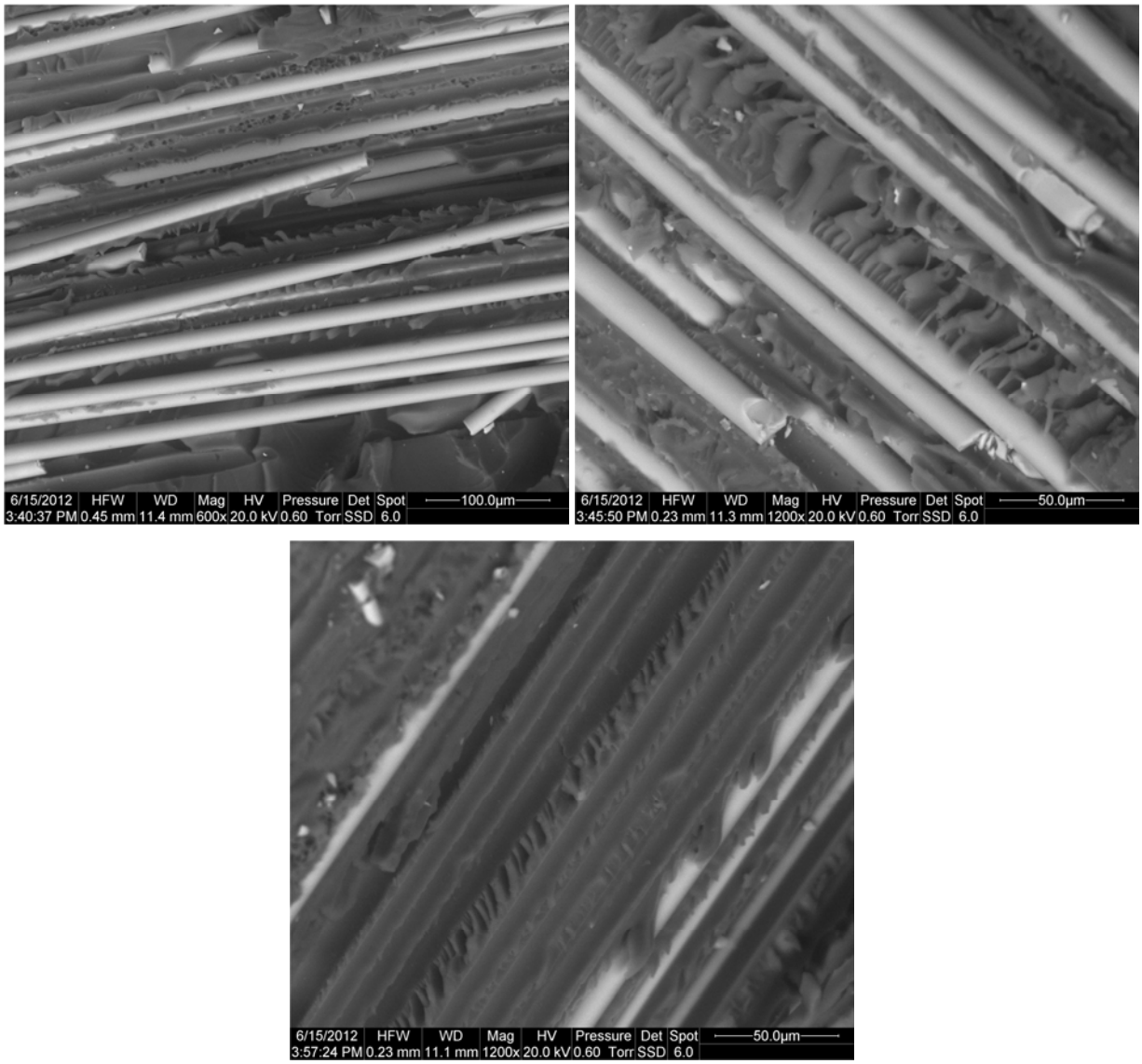

Figure 5.31 – SEM images of the fracture surface for $\lambda_{12} = 1$, R = 0.5.

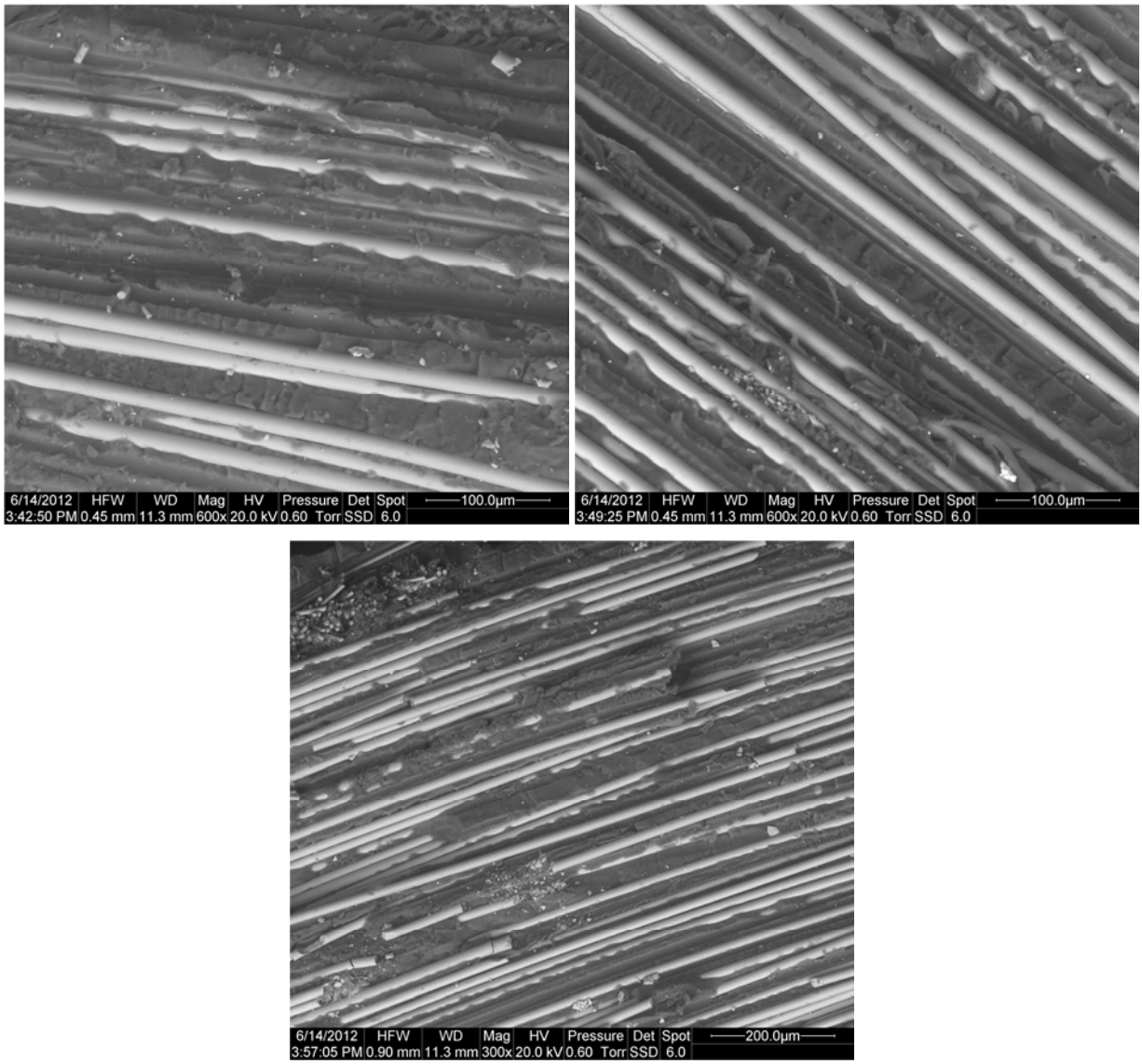

Figure 5.32 – SEM images of the fracture surface for $\lambda_{12} = 1$, R = -1.

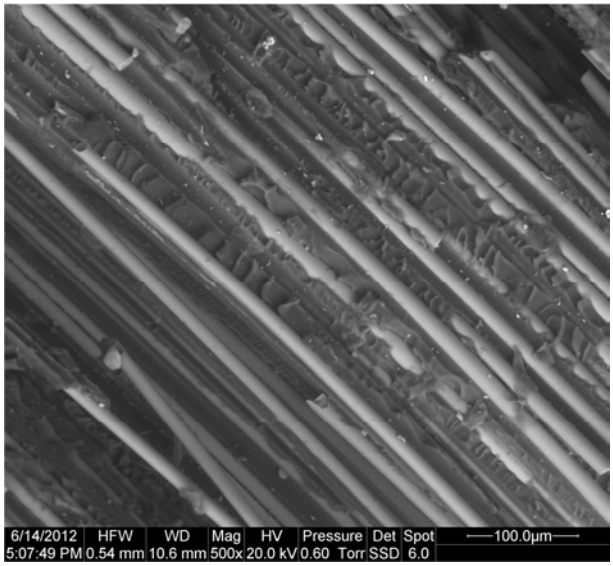

Figure 5.33 – SEM images of the fracture surface for $\lambda_{12} = 2$, R = 0.5.

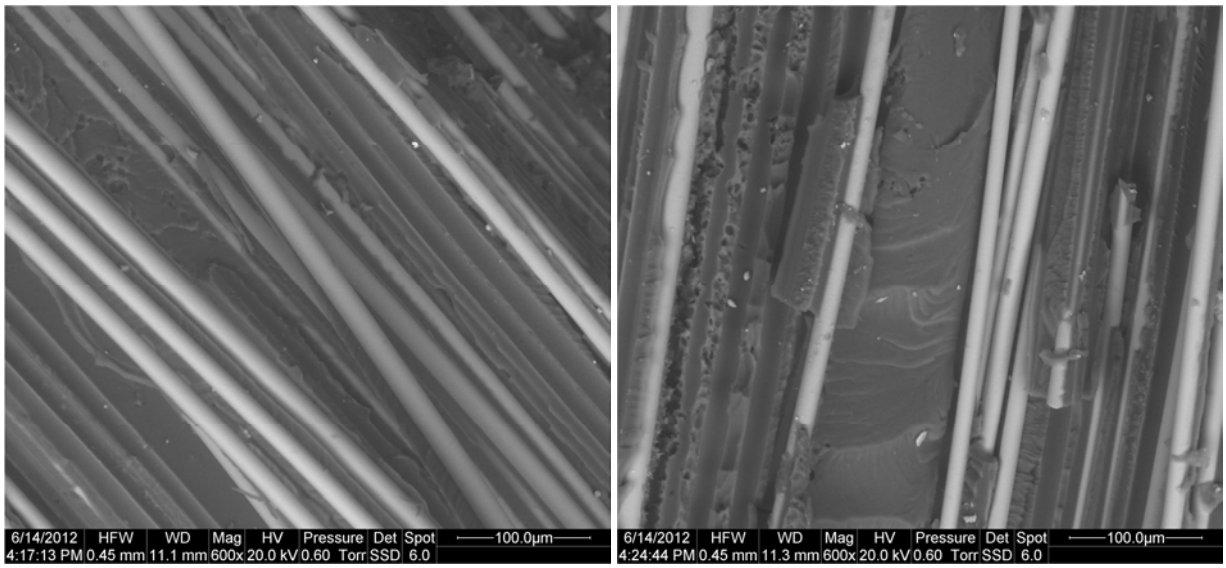

Figure 5.34 – SEM images of the fracture surface for $\lambda_{12} = 2$, R = -1.

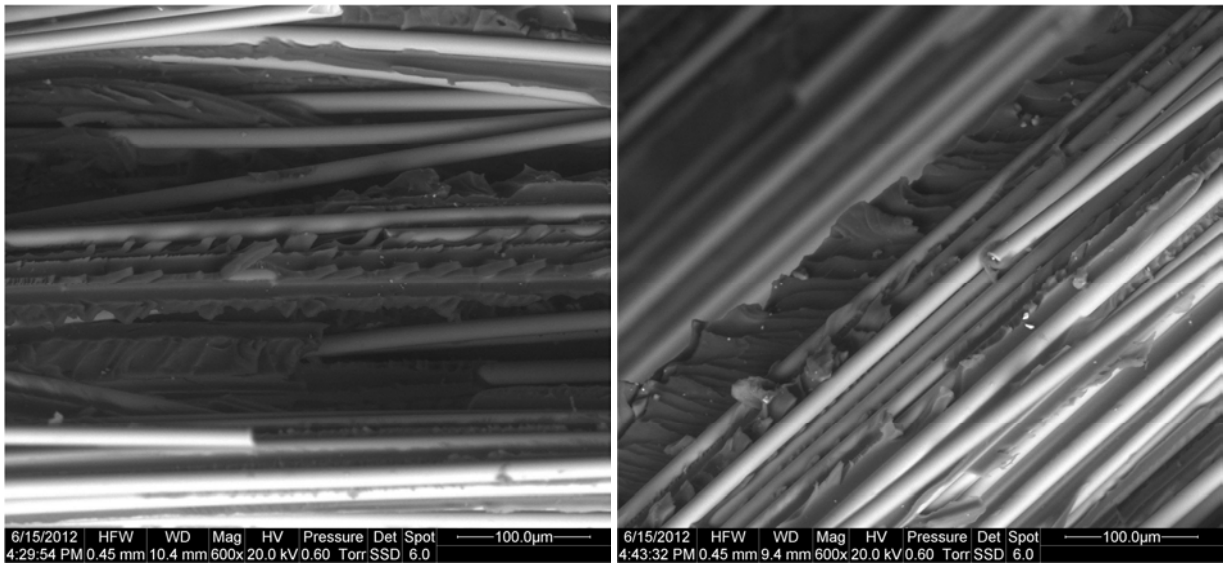

Figure 5.35 – SEM images of the fracture surface for $\lambda_{12} = \infty$, R = 0.

It is possible to observe that for $\lambda_{12} = 0$, R = 0.5 (Figure 5.29) no *shear cusps* (whose morphology can be clearly seen in Figure 5.35) are well detectable: shear cusps in fact raise from the separation plane more than what the present striations do in these pictures. For $\lambda_{12} = 0$, R = -1 (Figure 5.30) a different kind of striations appear, and though they are still not identified as shear cusps, their nature is not clear and it should be investigated more deeply. The absence of shear cusps for these two loading conditions is not surprising, since no shear stress was induced in the specimen. The loading condition $\lambda_{12} = 1$, R = 0.5 (Figure 5.31) leads to clear shear cusps, that instead are not clearly visible under the condition $\lambda_{12} = 1$, R = -1 (Figure 5.32), in which the fracture

surface is very irregular. Also for $\lambda_{12} = 2$, R = 0.5 (Figure 5.33) shear cusps are detectable, whereas for $\lambda_{12} = 2$, R = -1 (Figure 5.34) they are not well defined. It appears then that a negative stress ratio prevents the formation of shear cusps, and the reason could be the presence of a compressive stress and also the fact that the shear stress continuously changes its direction if the stress ratio is negative. It is also possible that the compressive part of the cycles, combined with the torsion loading, creates a large damage on the crack faces, which makes impossible to observe the presence of shear cusps.

From a comparison with the results obtained in [20] relative to a fatigue loading with R = 0, it can be concluded that the damage modes observed for R = 0, R = 0.5 and R = -1 are similar for $\lambda_{12} = 0$; for $\lambda_{12} = 1$ and $\lambda_{12} = 2$ instead the damage mode remains similar for R = 0 and R = 0.5, conversely it is difficult to draw conclusions on the damage modes that occur for R = -1 because of the damage induced by the compressive part of the cycles.

Chapter 6

Validation of the models

In this chapter some of the literature models (see Chapter 2) are validated against the experimental data obtained in this work (Chapters 4 and 5). The models analyzed are the ones considered to be more of interest among the ones applicable to the present experimental data set. In the specific, the following models are here tested: El Kadi and Ellyin's, Fawaz and Ellyin's, Plumtree and Cheng's, Petermann and Plumtree's and Kawai's. The validity of the models is evaluated respect to the multiaxiality condition only, to the stress ratio only and eventually to the combination of both these parameters. All the data are reported on a two-decades scale, in order to allow a first qualitative evaluation of the goodness of the fatigue parameters and a comparison of the models. A new model, based on the fatigue model that is being developed by the Department of Management and Engineering of the University of Padova, is then proposed and applied to the experimental data. The relation between the fatigue parameter and the number of cycles is considered linear in log-log scale in all the literature works that are analyzed here, and the same kind of relation is hypothesized in the new model. The regression curves as well as the curves for 90% and 10% probability of survival are reported for each model when observing the combined effect of the stress ratio and the multiaxiality condition. The relative accuracy of the models (with the exception of Fawaz and Ellyin's, that does not involve a fatigue parameter) is then quantitatively evaluated by comparing the ratio between the fatigue parameter for the 90% and 10% probabilities of survival at N = 10^6 cycles, found hypothesizing a log-normal distribution of the fatigue life (this ratio is defined as T_σ for the stress-based models and as T_W for the energy-based models).

6.1 – Application of El Kadi and Ellyin's model

El Kadi and Ellyin's model is described in Section 2.3.1. For the calculation of W_f^+ e W_f^- the behavior of the material was approximated to linear elastic.

6.1.1 – Effect of the stress ratio

The results concerning the effect of the stress ratio, in terms of the fatigue parameter Ψ, are reported for λ_{12}=0, 1, 2, respectively, in Figures 6.1 to 6.3. Although the curves appear to be closer, the fatigue parameter Ψ does not manage to collapse them well, in particular the curves for R = -1 remain always relevantly under the others. It has to be pointed out that the approximation to a linear elastic behavior of the material underestimate the energy accumulated more in compression than in tension, so if more appropriate calculations of W_f^+ e W_f^- were made, the curves for R = -1 would probably be even more separated from the ones for R = 0.5, 0.

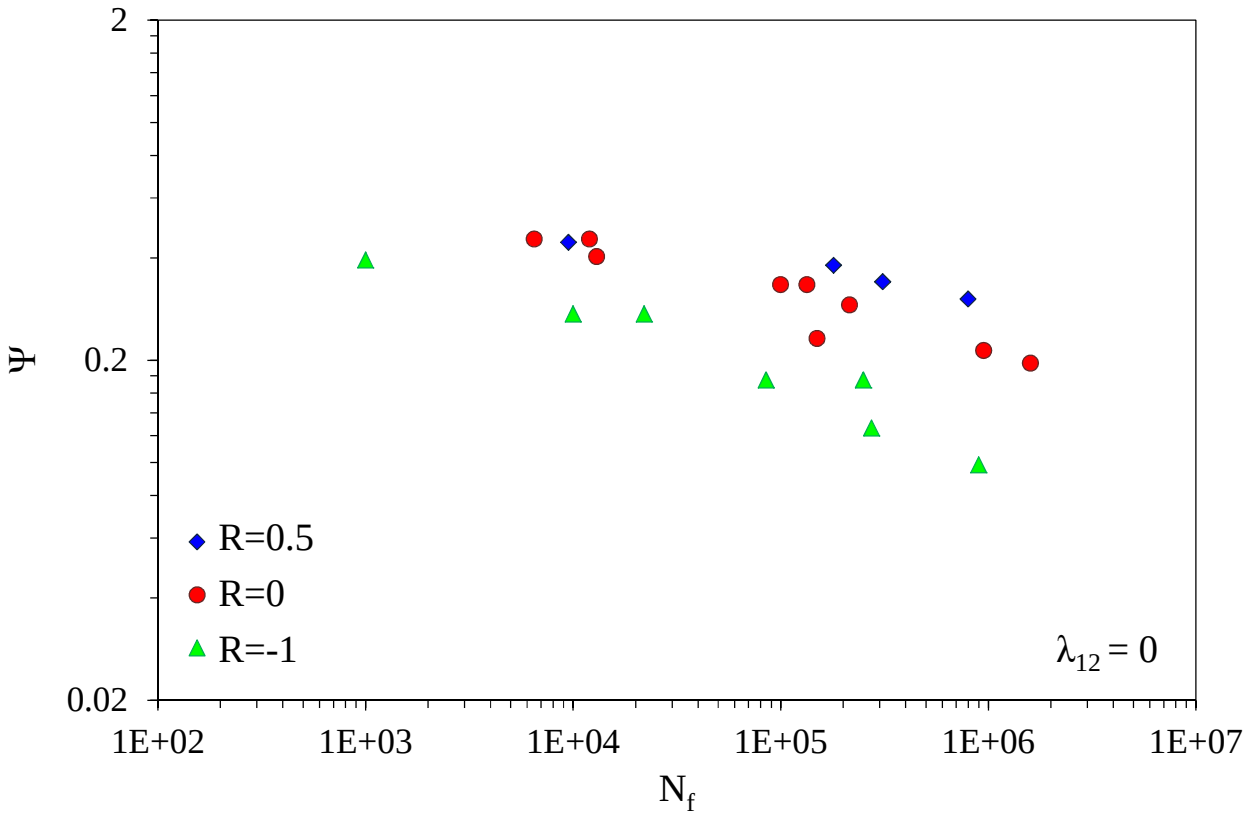

Figure 6.1 – El Kadi and Ellyin's fatigue parameter Ψ evaluated at R = 0.5, 0, -1 for λ_{12} = 0.

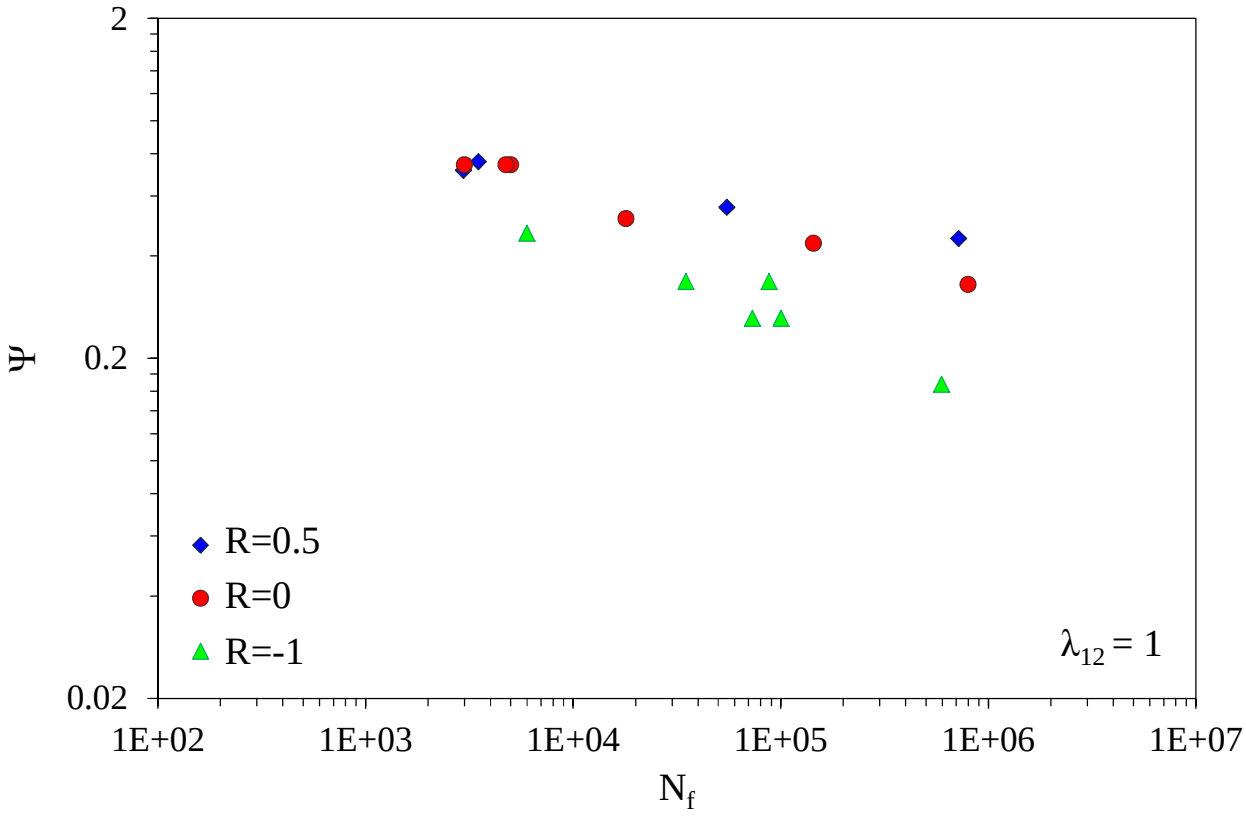

Figure 6.2 – El Kadi and Ellyin's fatigue parameter Ψ evaluated at R = 0.5, 0, -1 for $\lambda_{12} = 1$.

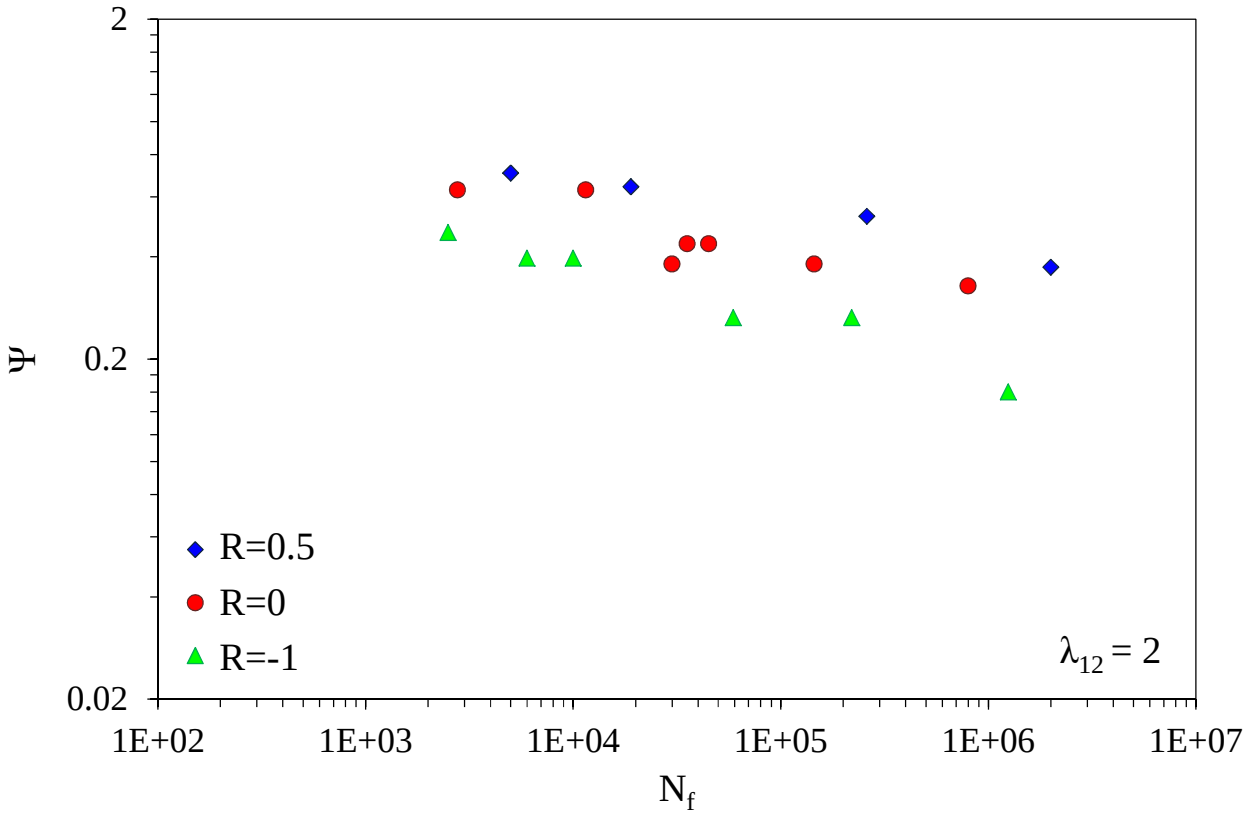

Figure 6.3 – El Kadi and Ellyin's fatigue parameter Ψ evaluated at R = 0.5, 0, -1 for $\lambda_{12} = 2$.

6.1.2 – Effect of the multiaxiality conditions

Figures 6.4 to 6.6 show that El Kadi and Ellyin's model has a certain validity for taking into account the effect of the multiaxiality conditions: the curves at different λ_{12} = 1, 2 seems to be in the same scatter band, but the curves at λ_{12} = 0 remain separated. The reason of this may be a change in the mechanism that leads to crack initiation under different multiaxiality conditions (in particular in presence or absence of shear stresses) [20, 21].

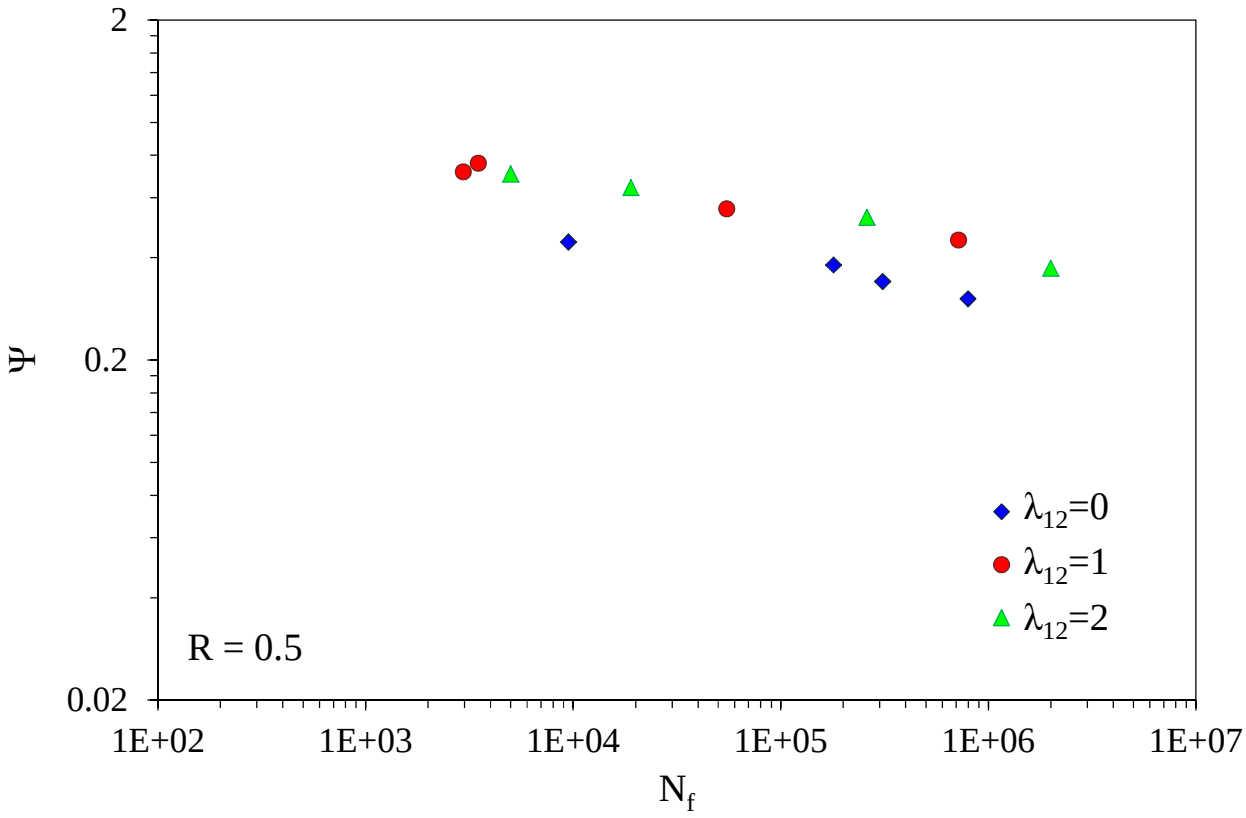

Figure 6.4 – El Kadi and Ellyin's fatigue parameter Ψ evaluated at λ_{12} = 0, 1, 2 for R = 0.5.

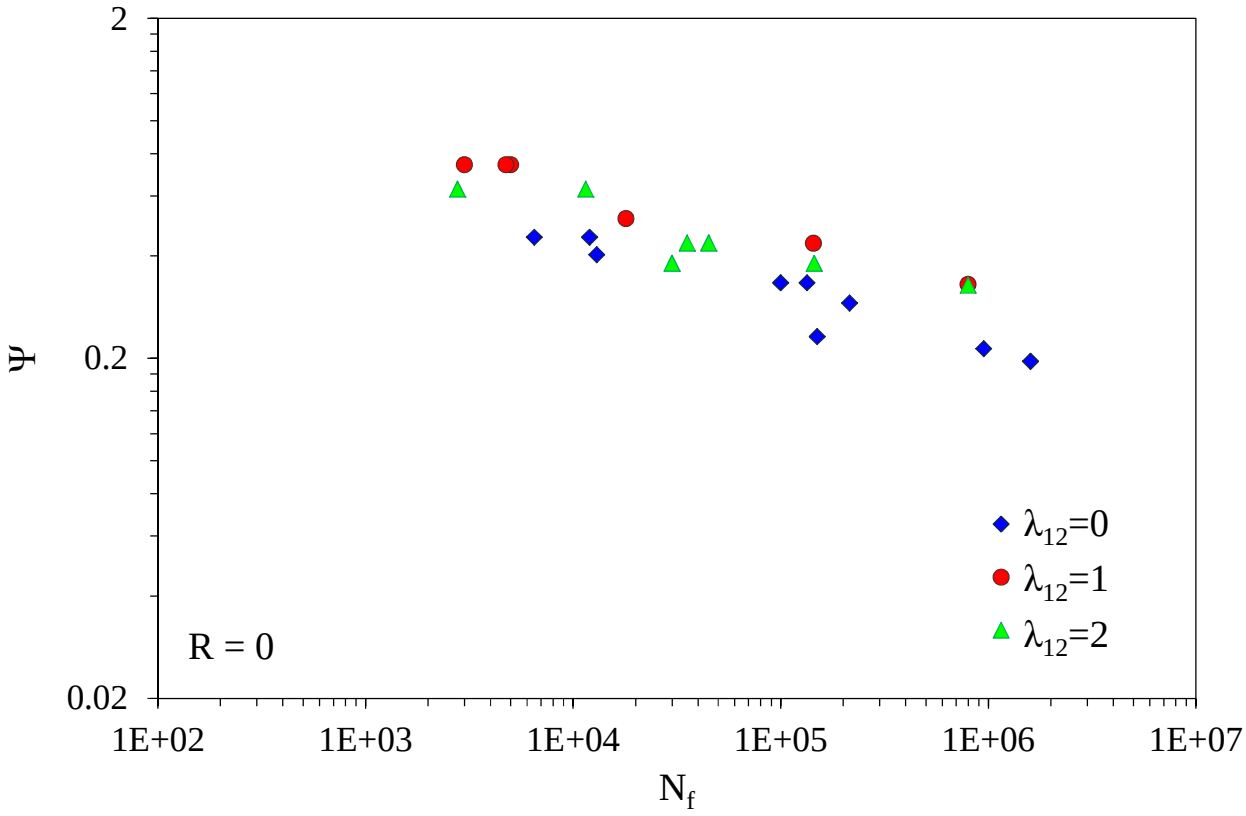

Figure 6.5 – El Kadi and Ellyin's fatigue parameter Ψ evaluated at λ_{12} = 0, 1, 2 for R = 0.

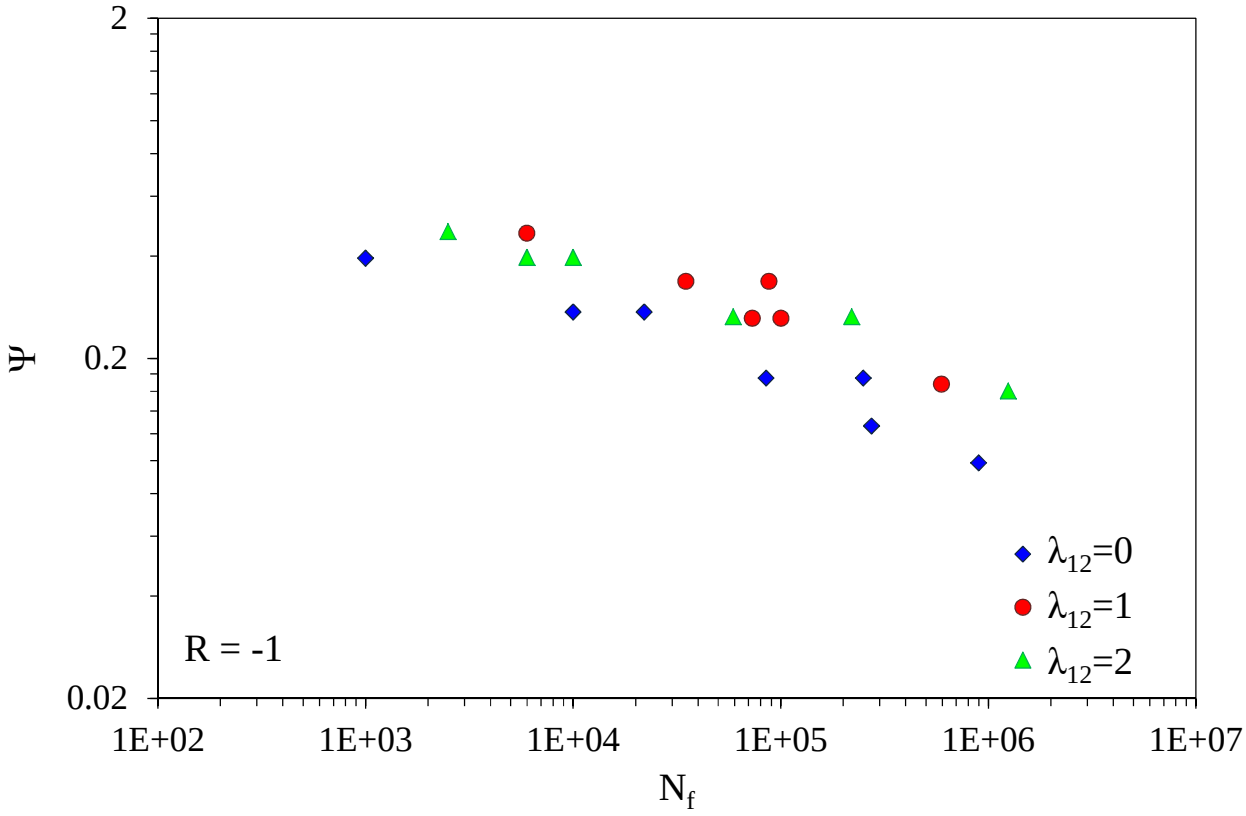

Figure 6.6 – El Kadi and Ellyin's fatigue parameter Ψ evaluated at λ_{12} = 0, 1, 2 for R = -1.

6.1.3 – All the experimental data

In Figure 6.7 all the data are plotted together, in order to observe the global validity of the model for the combined effect of the stress ratio and the multiaxiality conditions. It is clear that the scatter band is very large, in particular because of the data at R = -1 (triangles in Figure 6.7), that are sensibly under the ones at R = 0.5, 0, which seems instead to be reasonably in the same scatter band.

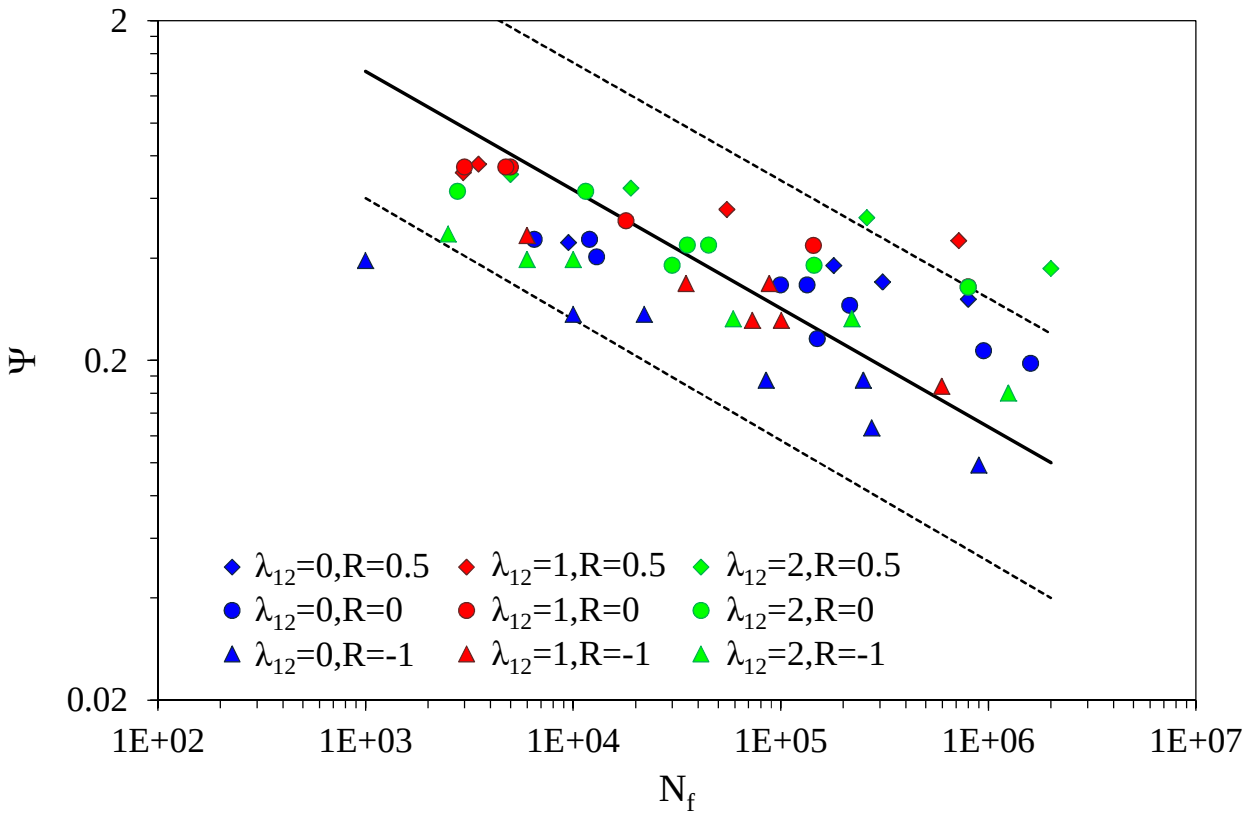

Figure 6.7 – El Kadi and Ellyin's fatigue parameter Ψ evaluated for all the experimental data.

6.1.4 – Possible modification of El Kadi and Ellyin's model

Given the fact that the largeness of the scatter is caused mainly by the data at R = -1, and that El Kadi and Ellyin's model separately normalizes the energy accumulated by the material during the tensile and compressive parts of the cycles, a modified fatigue parameter is proposed, hypothesizing that the static behavior under compression does not influence the fatigue behavior under tension-compression loading. The new fatigue parameter, Ψ', is defined as follows:

$$\Psi' = \frac{\Delta W^+ + \Delta W^-}{W_f^+} = (2N_f)^\alpha \qquad (6.1)$$

This new parameter gives better results than the original one, as can be seen in Figure 6.8, which is in support of the hypothesis mentioned above; despite this the scatter band still remains quite large.

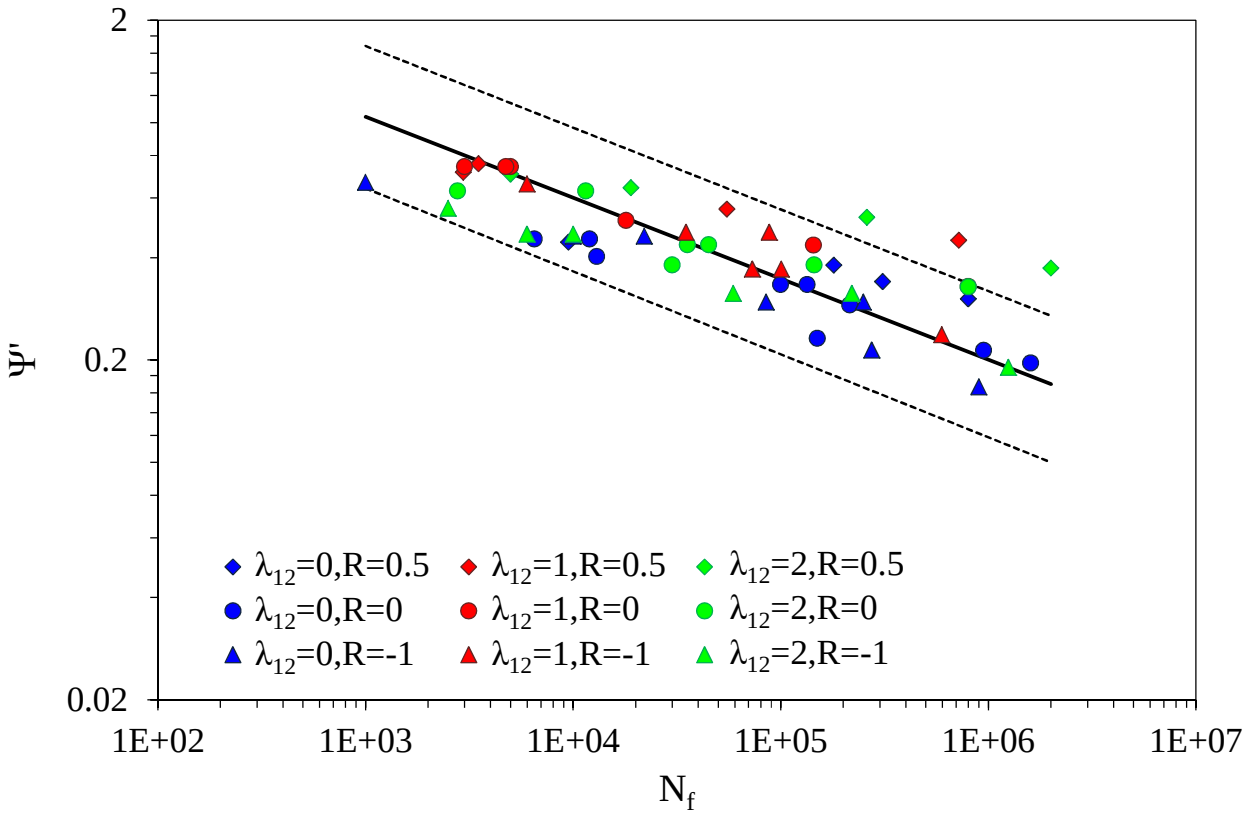

Figure 6.8 – Modified El Kadi and Ellyin's fatigue parameter, Ψ', evaluated for all the experimental data.

6.2 – Application of Fawaz and Ellyin's model

Fawaz and Ellyin's model is described in Section 2.3.2. In this case the authors do not define a fatigue parameter, but they draw the equation of a S–N curve from the equation of a reference S–N curve. In this case, the S–N curve for R = 0, $\lambda_{12} = 0$ is chosen as reference. In Table 6.1 are reported the equations of the S-N curves drawn by least square method from the experimental data (hypothesizing a power-law) and the equations obtained through this model from the reference curve. The tensile static strengths were considered in all the cases.

λ_{12}	R	Experimental slope	Experimental intercept	Static strength	Predicted slope	Error %	Predicted intercept	Error %
0	0	-0.078	70.876	51.96	-0.078	0.00	70.876	0.00
0	0.5	-0.041	58.922	51.96	-0.039	4.88	58.922	0.00
0	-1	-0.1	62.683	51.96	-0.156	56.00	62.683	0.00
1	0	-0.075	55.445	49.28	-0.074	1.36	52.585	5.16
1	0.5	-0.046	49.732	49.28	-0.037	19.59	47.167	5.16
1	-1	-0.109	52.723	49.28	-0.148	35.74	50.004	5.16
2	0	-0.062	29.444	32.04	-0.048	22.42	18.156	38.34
2	0.5	-0.052	34.708	32.04	-0.024	53.75	21.402	38.34
2	-1	-0.081	22.769	32.04	-0.096	18.76	14.040	38.34

Table 6.1 – Fawaz and Ellyin's model applied to all the experimental data.

The errors on the prediction of both the slope and the intercept are in some cases very large, in particular for R = -1 and λ_{12} = 2 loading conditions. Since the authors do not provide any specific features of the reference curve, no other attempts are made in choosing it.

6.3 – Application of Plumtree and Cheng's model

Plumtree and Cheng's model is described in Section 2.3.3. The behavior of the epoxy matrix was approximated to linear elastic for the calculation of the strain ranges (stresses and strains involved in this model are the ones in the matrix phase). The matrix was considered also isothropic, with the following typical elastic properties: E = 3200 MPa, ν = 0.37.

6.3.1 – Effect of the stress ratio

The fatigue parameter defined by Plumtree and Cheng seems to describe well the effect of the stress ratio on the fatigue life: as reported in Figures 6.9 to 6.11, the curves for different values of R, at constant λ_{12}, are all well collapsed in a single scatter band.

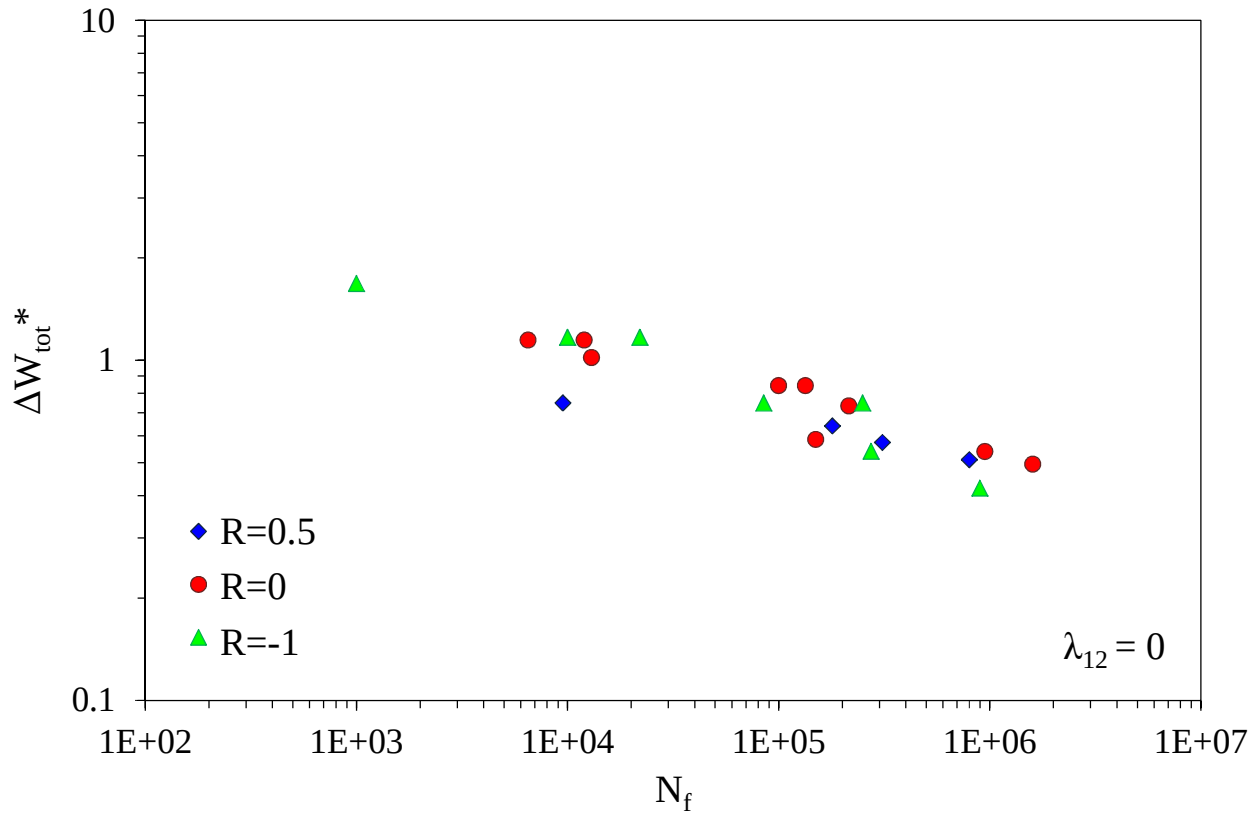

Figure 6.9 – Plumtree and Cheng's fatigue parameter ΔW_{tot}^* evaluated at R = 0.5, 0, -1 for $\lambda_{12} = 0$.

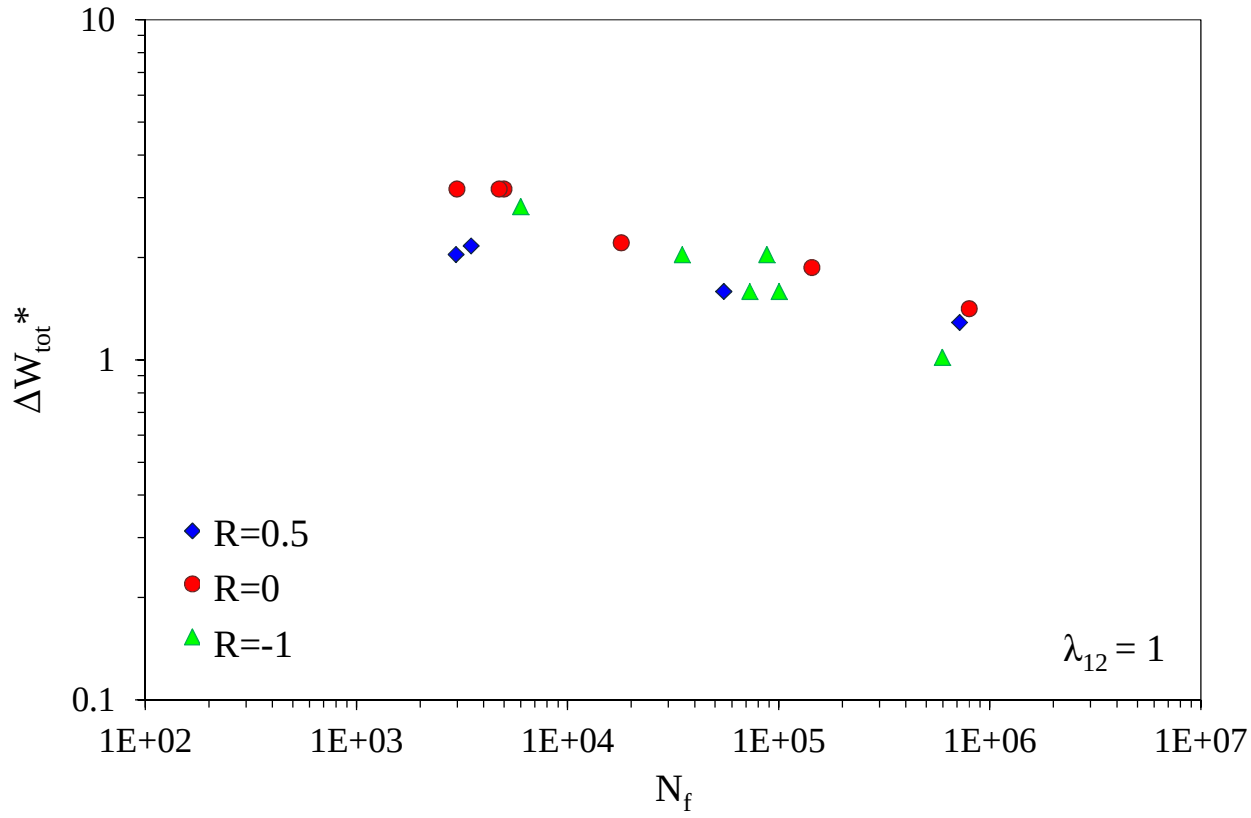

Figure 6.10 – Plumtree and Cheng's fatigue parameter ΔW_{tot}^{*} evaluated at R = 0.5, 0, -1 for $\lambda_{12} = 1$.

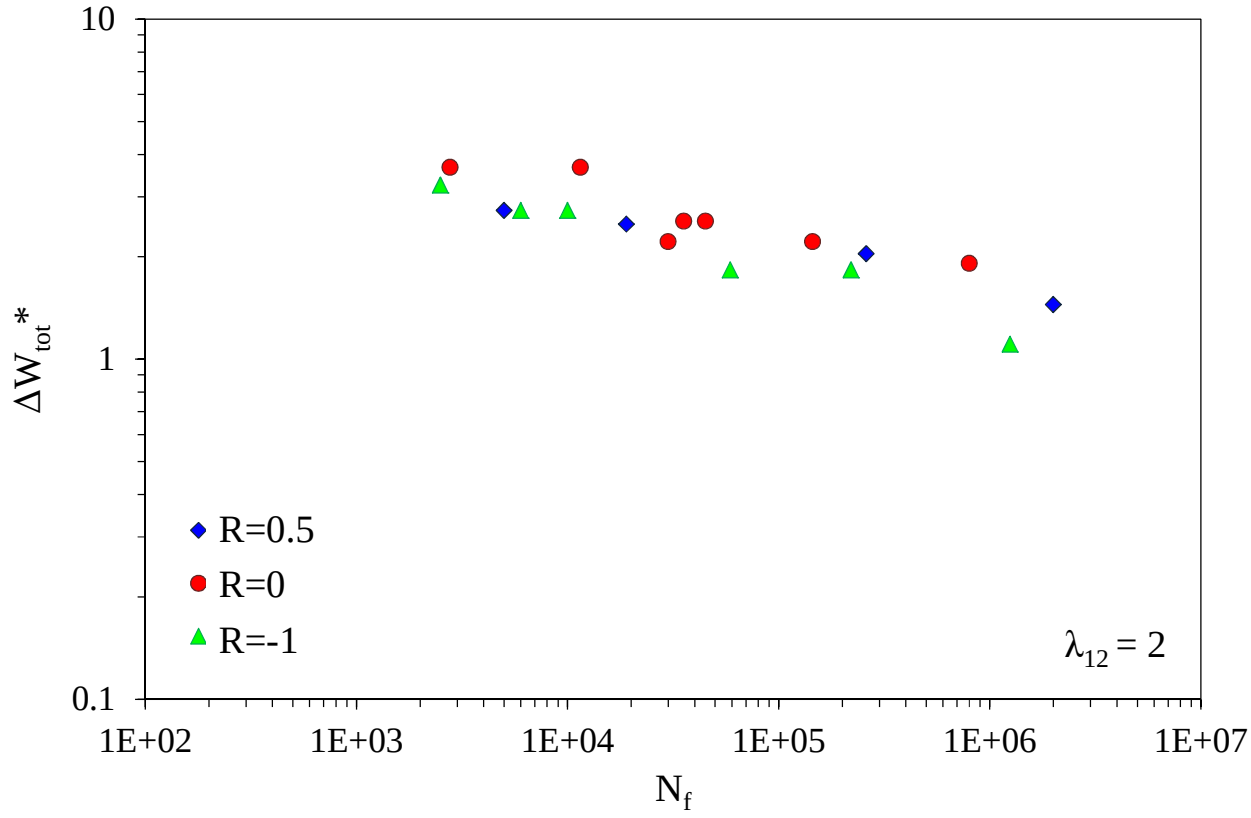

Figure 6.11 – Plumtree and Cheng's fatigue parameter ΔW_{tot}^{*} evaluated at R = 0.5, 0, -1 for $\lambda_{12} = 2$.

6.3.2 – Effect of the multiaxiality conditions

Conversely to its efficiency in describing the effect of R, Plumtree and Cheng's model does not manage to take into good account the effect of the multiaxiality conditions (Figures 6.12 to 6.14): although the curves for $\lambda_{12} = 1, 2$ appears to be overlapped (or at least close to each other in the case of R = 0.5), the curve for $\lambda_{12} = 0$ remains in all cases markedly separated from them. As mentioned above for El Kadi and Ellyin's model, this may be due to a change in the damage mode under different loading conditions.

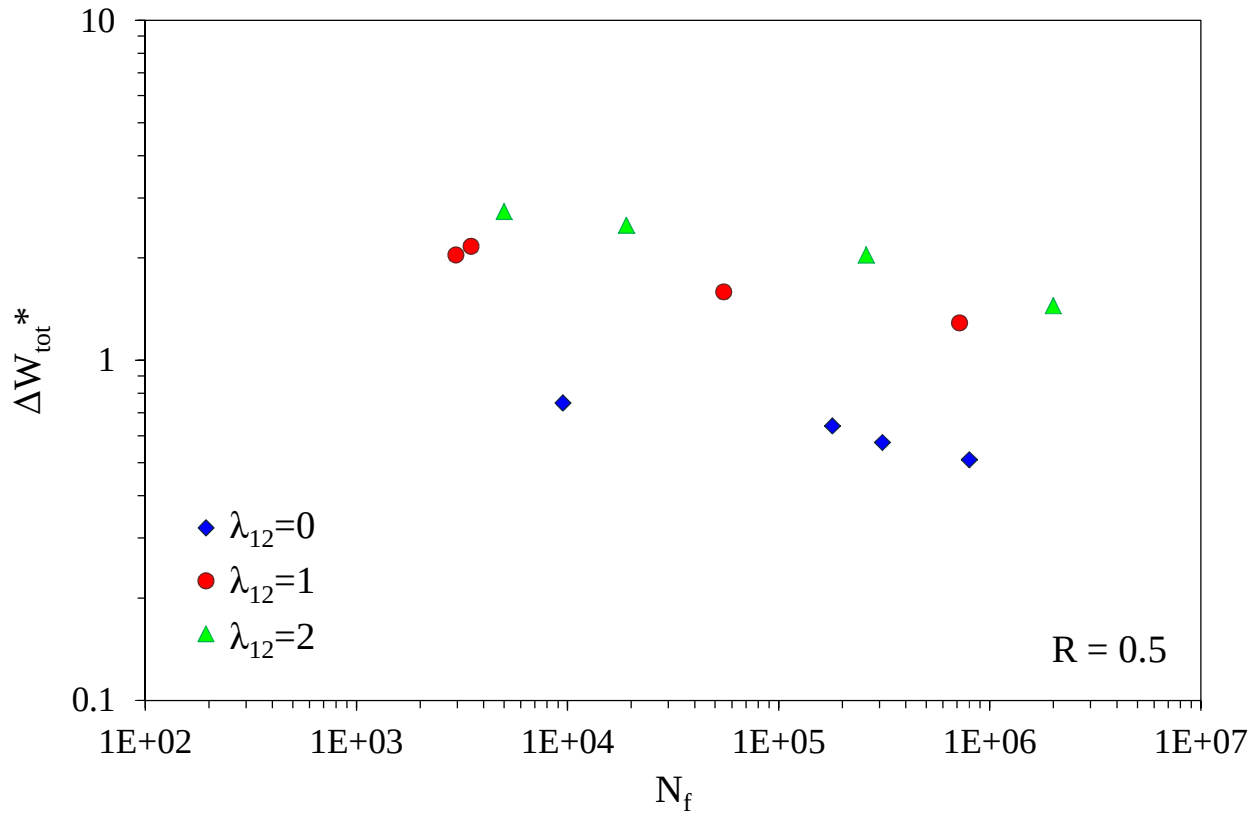

Figure 6.12 – Plumtree and Cheng's fatigue parameter ΔW^{*}_{tot} evaluated at λ_{12} = 0, 1, 2 for R = 0.5.

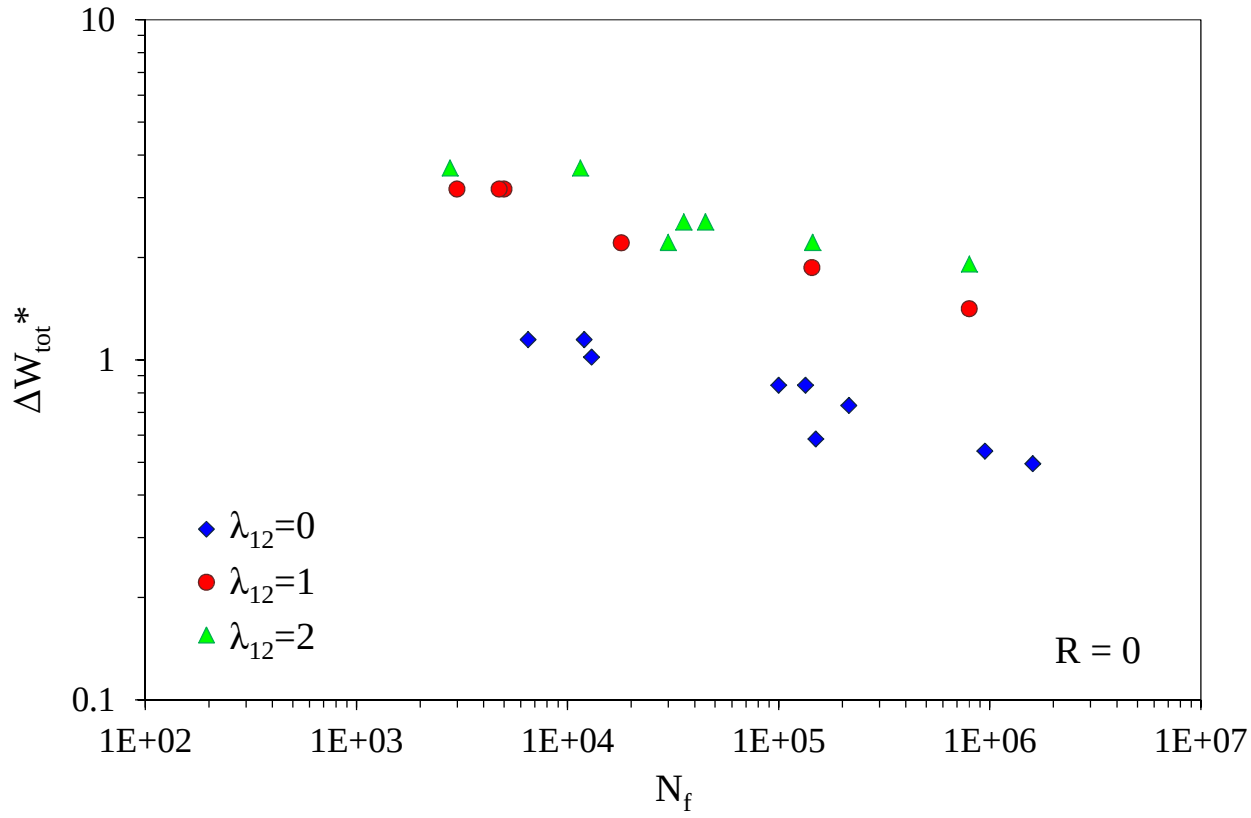

Figure 6.13 – Plumtree and Cheng's fatigue parameter ΔW^*_{tot} evaluated at λ_{12} = 0, 1, 2 for R = 0.

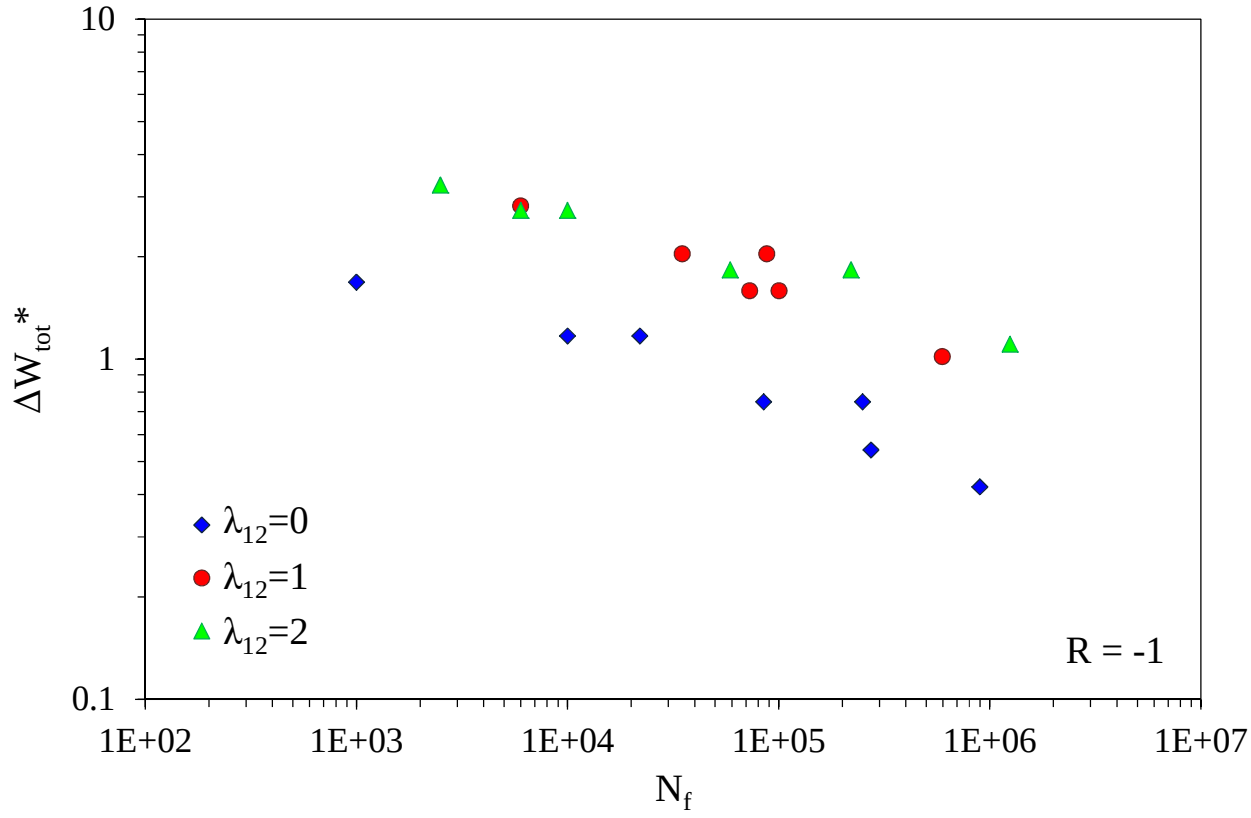

Figure 6.14 – Plumtree and Cheng's fatigue parameter ΔW^*_{tot} evaluated at λ_{12} = 0, 1, 2 for R = -1.

6.3.3 – All the experimental data

The accuracy of Plumtree and Cheng's model in describing the combined effect of the stress ratio and the multiaxiality condition can be seen in Figure 6.15. The gap between the data for λ_{12} = 0 and the data for λ_{12} = 1, 2 (that are in the same scatter band) is clearly evident.

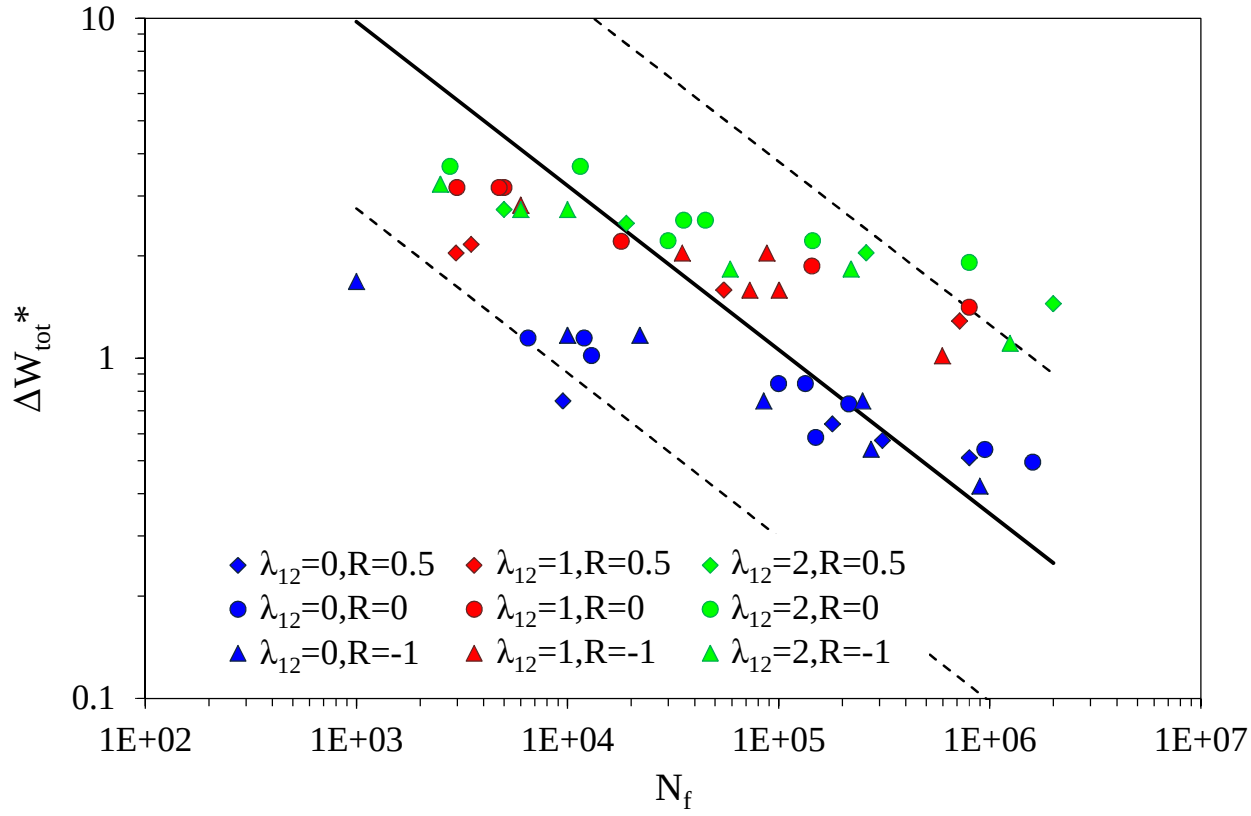

Figure 6.15 – Plumtree and Cheng's fatigue parameter ΔW_{tot}^{*} for all the experimental data.

6.3.4 – Possible modification of Plumtree and Cheng's model

Since the problem of the model appears concern the effect of the multiaxiality conditions, a possible way to increase its accuracy may lie in the normalization of the data respect to the static parameter ΔW_{tot}^{*} calculated under the same multiaxiality conditions, defined as

$$\Delta W_{static}{}^{*} = \Delta W_{1,f}{}^{*} + \Delta W_{2,f}{}^{*} = \sigma_{22,\max,f}\Delta\varepsilon_{22,f} + \tau_{12,\max,f}\Delta\gamma_{12,f}/2 \qquad (6.2)$$

in which the subscript *f* denotes the static failure. Given the definition of Plumtree and Cheng's fatigue parameter, it is chosen to consider in equation 6.2 always the static strength obtained in tensile tests (and not in compression); also in this case the material was considered to have a linear elastic behavior for the calculation of the strain ranges. The modified fatigue parameter is then

$$\Delta W_{tot,n}{}^{*} = \frac{\Delta W_{1}{}^{*} + \Delta W_{2}{}^{*}}{\Delta W_{static}{}^{*}} = \frac{\sigma_{22,\max}\Delta\varepsilon_{22} + \tau_{12,\max}\Delta\gamma_{12}/2}{\Delta W_{static}{}^{*}} \qquad (6.3)$$

where the subscript *n* stands for *normalized*. This new parameter seems to describe better the effect of the stress ratio and the multiaxiality conditions than the original one: as can be seen in Figure 6.16, all the data are now in the same scatter band, even if it is still not satisfactorily narrow.

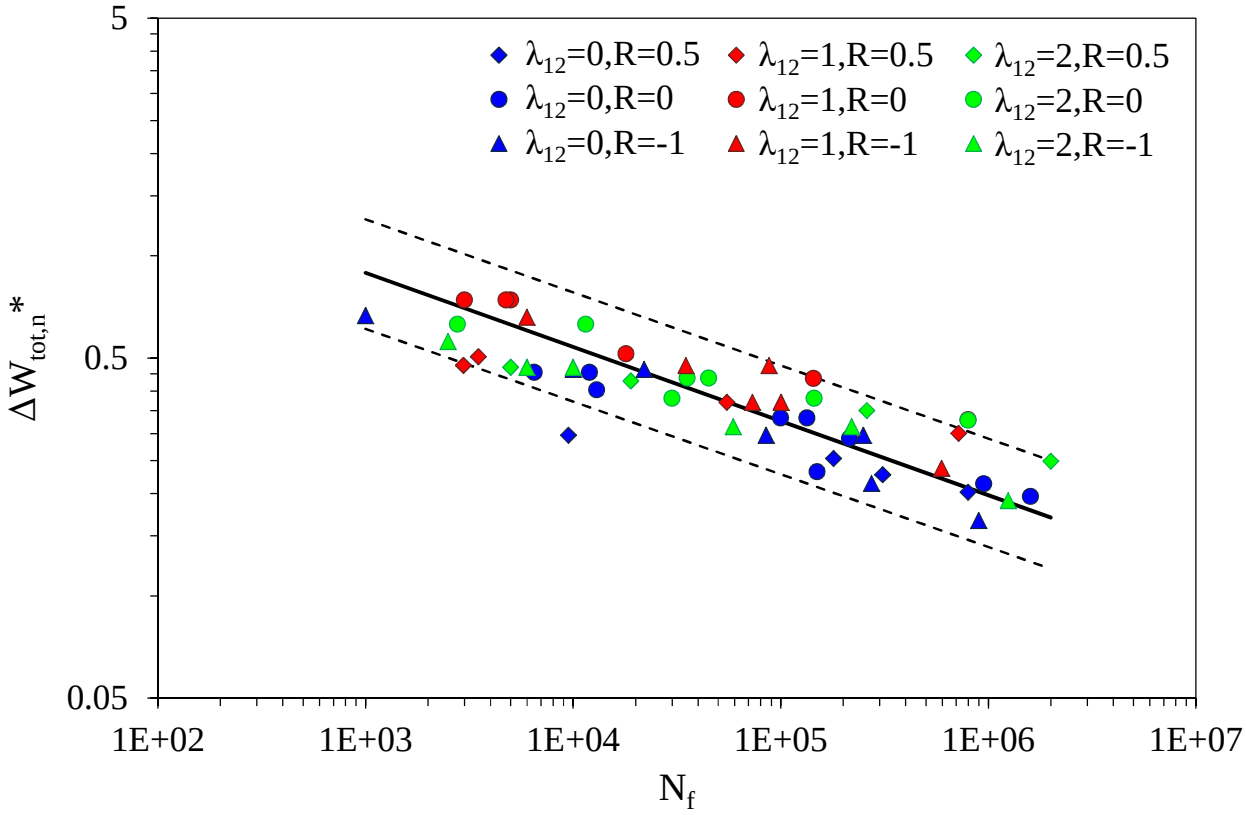

Figure 6.16 – Modified Plumtree and Cheng's fatigue parameter, $\Delta W_{tot,n}$ *, evaluated for all the experimental data.

6.4 – Application of Petermann and Plumtree's model

Petermann and Plumtree's model is described in Section 2.3.5. For the calculation of the strains a linear elastic behavior of the epoxy matrix is hypothesized (as for Plumtree and Cheng's model). The elastic properties of the matrix are the same reported in Section 6.3.

6.4.1 – Effect of the stress ratio

Petermann and Plumtree's model appears to describe the effect of the stress ratio at constant λ_{12} well enough (Figures 6.17 to 6.19), but it can be noticed that the curves for R = 0.5, 0, -1 get more separated as λ_{12} increases.

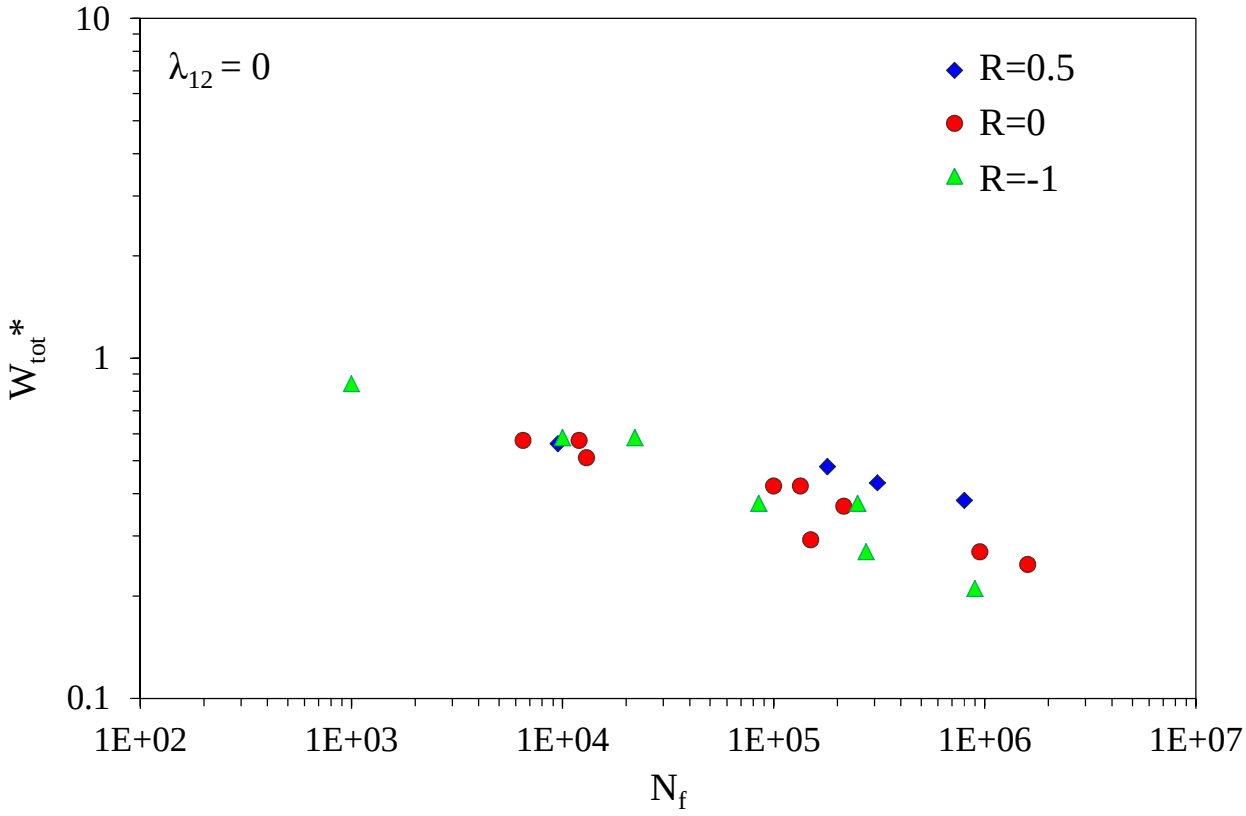

Figure 6.17 – Petermann and Plumtree's fatigue parameter W_{tot}^* at R = 0.5, 0, -1 for $\lambda_{12} = 0$.

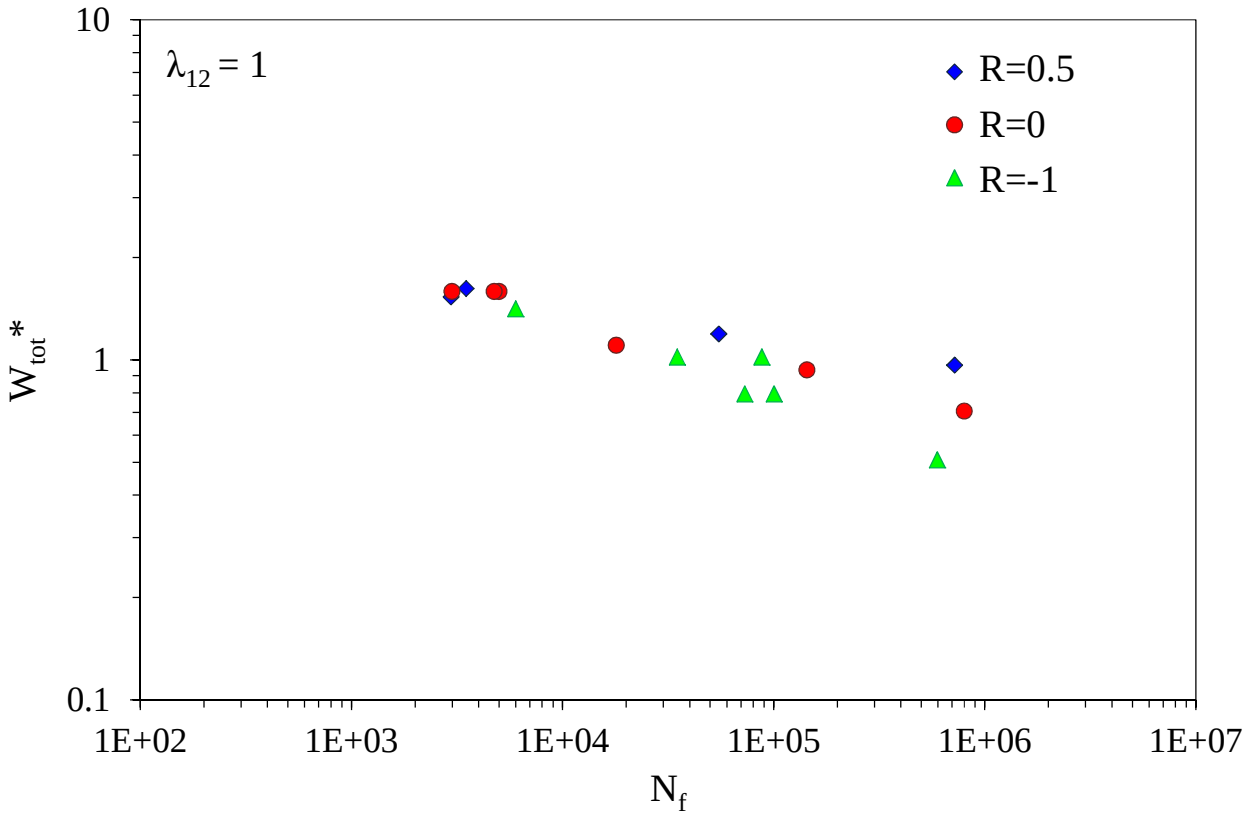

Figure 6.18 – Petermann and Plumtree's fatigue parameter W^*_{tot} at R = 0.5, 0, -1 for λ_{12} = 1.

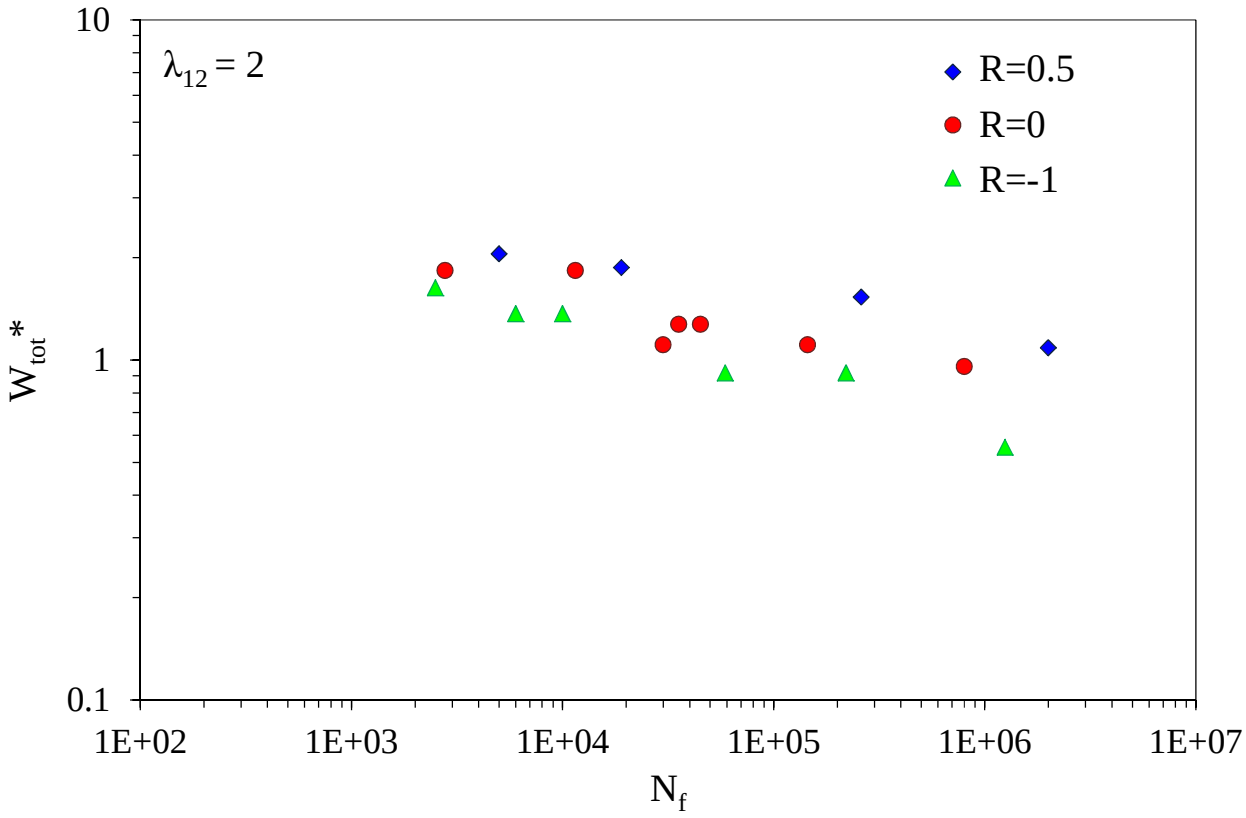

Figure 6.19 – Petermann and Plumtree's fatigue parameter W^*_{tot} at R = 0.5, 0, -1 for λ_{12} = 2.

6.4.2 – Effect of the multiaxiality conditions

The effect of the multiaxiality conditions are not properly considered in this model (Figures 6.20 to 6.22), in particular the problem appears to be the same as Plumtree and Cheng's model: the data for λ_{12} = 0 lie always under the ones for λ_{12} = 1, 2, that are instead well overlapped (just close in the case of R = 0.5).

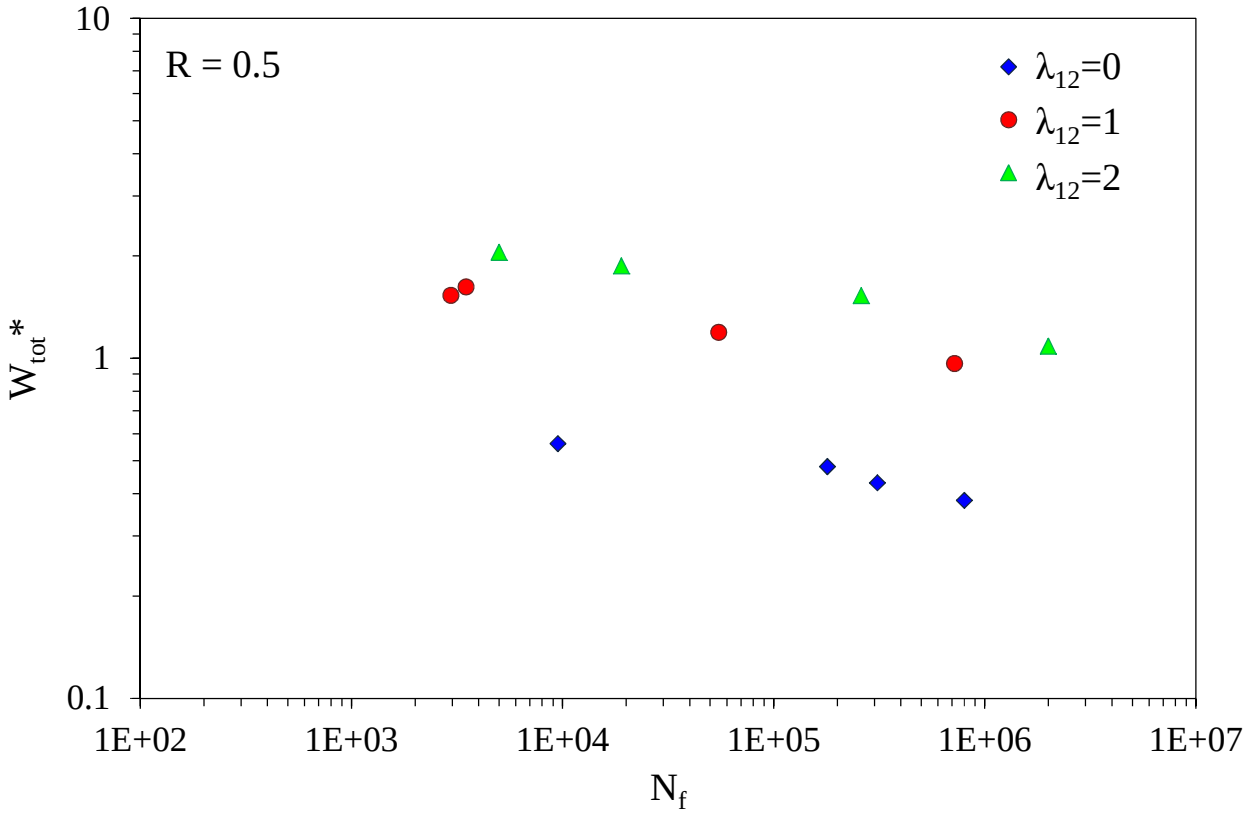

Figure 6.20 – Petermann and Plumtree's fatigue parameter W^{*}_{tot} at λ_{12} = 0, 1, 2 for R = 0.5.

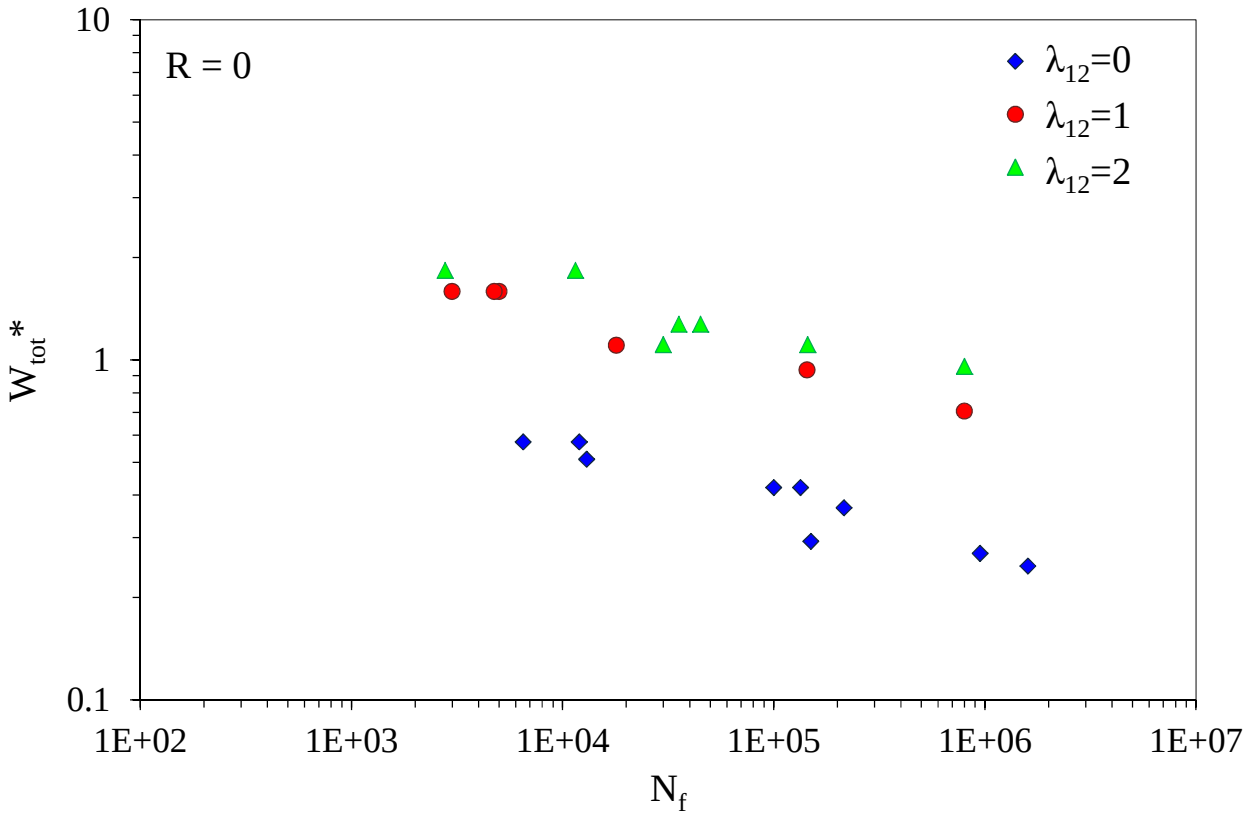

Figure 6.21 – Petermann and Plumtree's fatigue parameter W^*_{tot} at λ_{12} = 0, 1, 2 for R = 0.

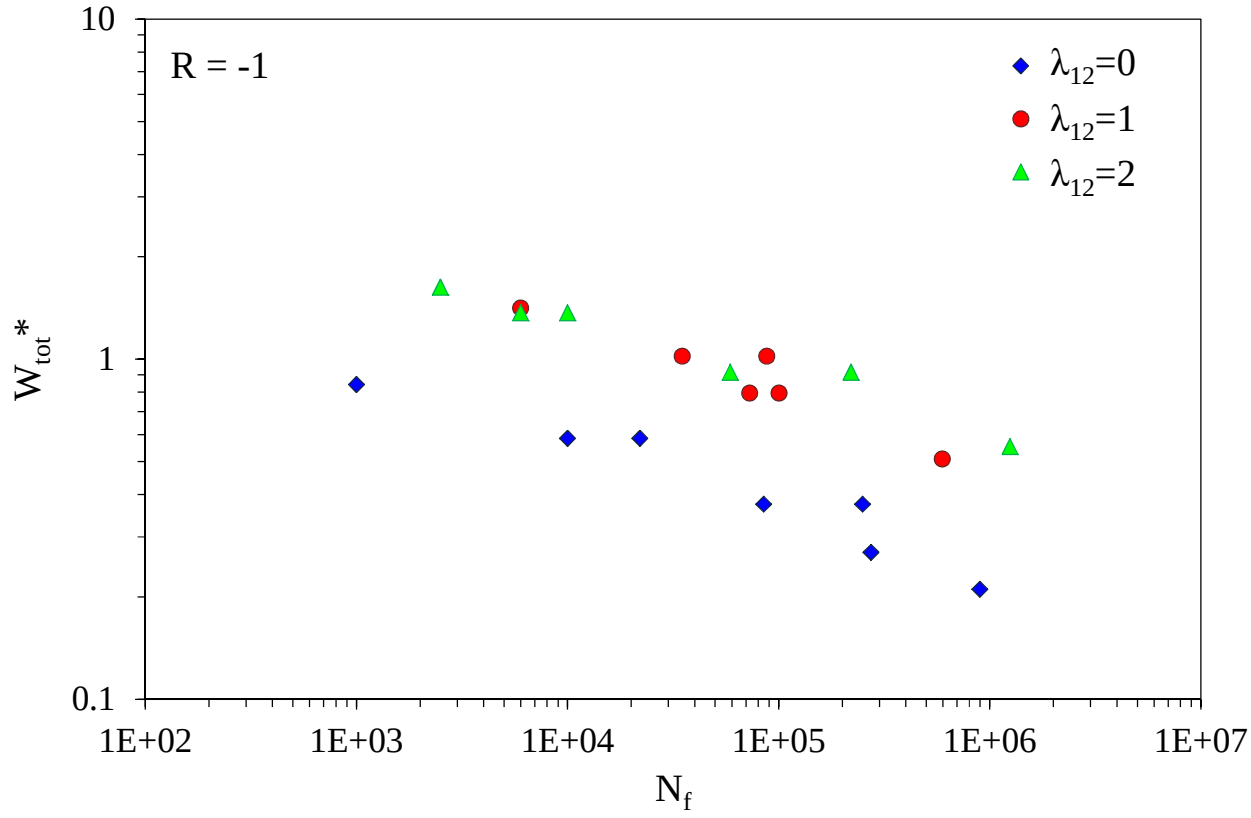

Figure 6.22 – Petermann and Plumtree's fatigue parameter W^*_{tot} at λ_{12} = 0, 1, 2 for R = -1.

6.4.3 – All the experimental data

The global accuracy of Petermann and Plumtree's fatigue parameter over the effect of the stress ratio and the multiaxiality conditions appears to be insufficient (Figure 6.23): if the data for λ_{12} = 1 and 2 are reasonably in the same scatter band, the data for λ_{12} = 0 are distinctly above them, as happened for Plumtree and Cheng's model.

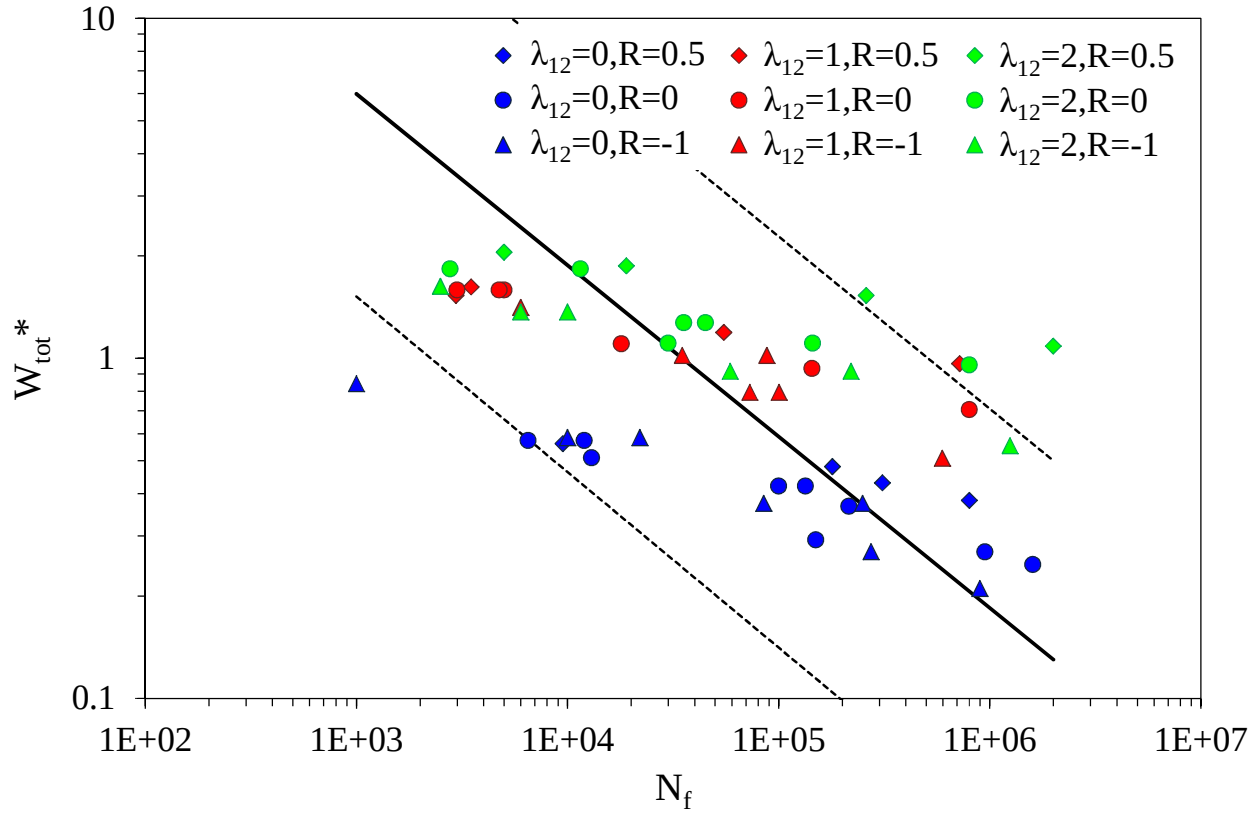

Figure 6.23 – Petermann and Plumtree's fatigue parameter W_{tot}^{*} evaluated for all the experimental data.

6.4.4 – Possible modification of Petermann and Plumtree's model

From the observation that the problem of this model in analogue to Plumtree and Cheng's one, a new fatigue parameter may be defined as above, normalizing W_{tot}^{*} respect to the static parameter calculated under the same multiaxiality conditions:

$$W_{static}* = W_{1,f}* + W_{2,f}* = 0.5*(\sigma_{22,f}\varepsilon_{22,f} + \tau_{12,f}\gamma_{12,f}/2) \qquad (6.4)$$

in which the subscript *f* denotes the static failure. The static strength in the equation can be the ones measured in tension or compression. The first condition will be distinguished by the superscript +, the second by the superscript –. Denoting with $W^{+}*$ the contribute to $W_{tot}*$ of the tensile part of a cycle and with $W^{-}*$ the contribute of the compressive part of a cycle, a new fatigue parameter can be defined in two ways: by normalizing $W^{+}*$ respect to $W_{static}^{+}*$ and $W^{-}*$ respect to $W_{static}^{-}*$, or, from what has been seen from the modification of El Kadi and Ellyin's model, by normalizing both $W^{+}*$ and $W^{-}*$ respect to $W_{static}^{+}*$:

$$W_{tot,ntc}^{*} = \frac{W_1^{+}{}^{*} + W_2^{+}{}^{*}}{W_{static}^{+}{}^{*}} + \frac{W_1^{-}{}^{*} + W_2^{-}{}^{*}}{W_{static}^{-}{}^{*}} \tag{6.5}$$

$$W_{tot,nt}^{*} = \frac{W_1^{+}{}^{*} + W_2^{+}{}^{*} + W_1^{-}{}^{*} + W_2^{-}{}^{*}}{W_{static}^{+}{}^{*}} = \frac{W_1^{*} + W_2^{*}}{W_{static}^{+}{}^{*}} \tag{6.6}$$

where the subscript *ntc* stands for *normalized to tension and compression* whereas *nt* for *normalized to tension*. The application of both these parameters to the experimental data set is reported in Figures 6.24 and 6.25. As for El Kadi and Ellyin's model, the normalization only to the static tensile parameter leads to better results, supporting the hypothesis that the static behavior in compression does not influence the fatigue behavior in presence of a negative stress ratios.

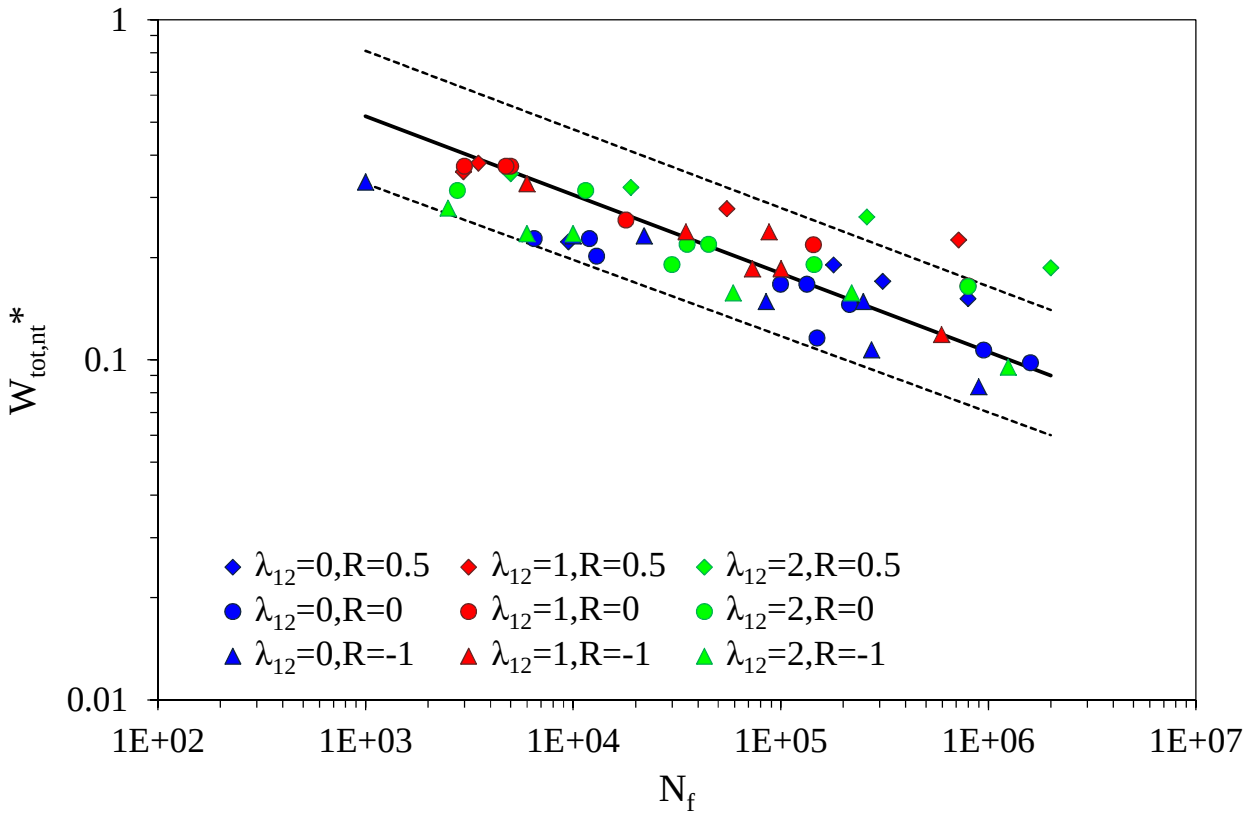

Figure 6.24 – Modified Petermann and Plumtree's fatigue parameter, $W_{tot,nt}^{*}$, evaluated for all the experimental data.

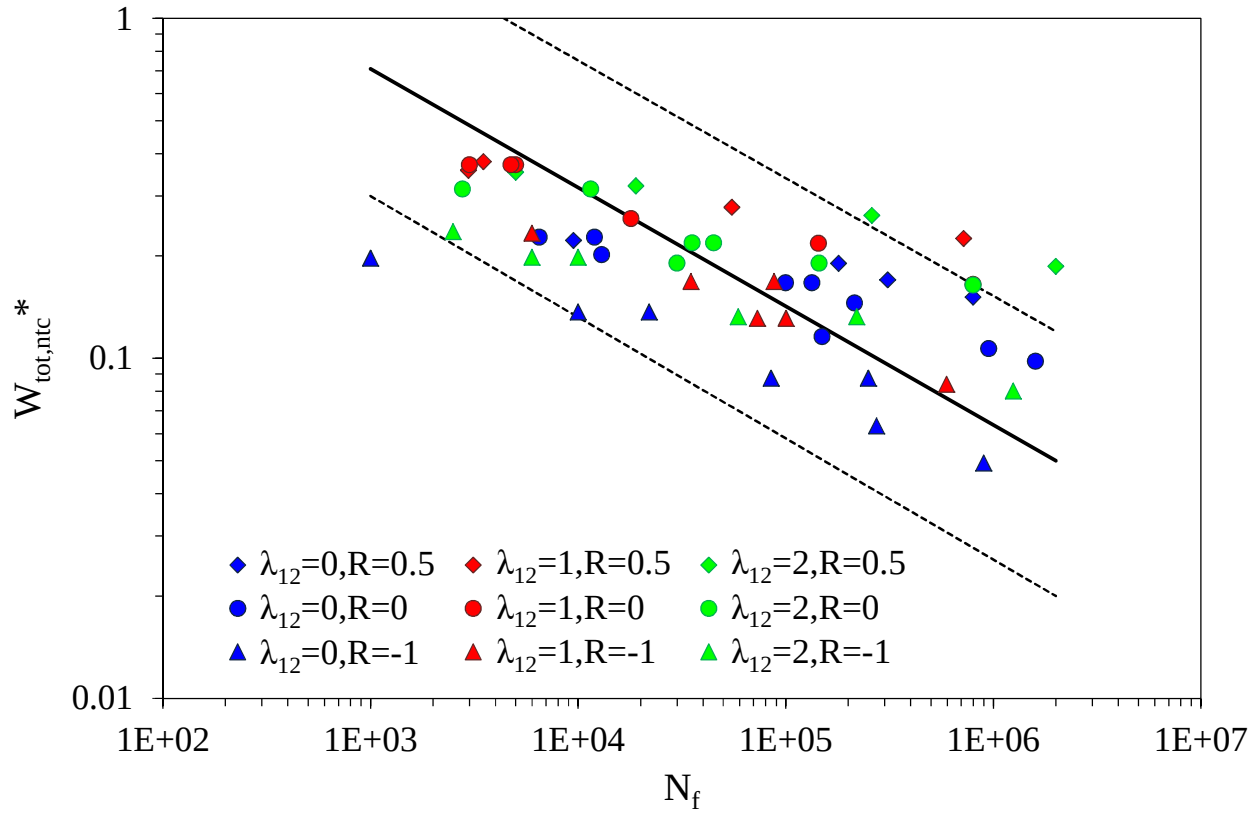

Figure 6.25 – Modified Petermann and Plumtree's fatigue parameter, $W_{tot,ntc}$*, evaluated for all the experimental data.

One more thing to be noticed is that the modified proposed parameters leads exactly to the same results of the original and the modified El Kadi and Ellyin's model, only shifted. The reason of this is that the only difference between Petermann and Plumtree's and El Kadi and Ellyin's models lies in the fact that El Kadi and Ellyin consider the average stresses, whereas Petermann and Plumtree the maximum stresses. Between the average and the maximum stresses there is only a multiplication factor that does not change with the loading conditions, and that become an addition in log–log scale. Therefore, all the data in Figures 6.24 and 6.25 are only shifted of the same quantity respect to the ones in Figures 6.7 and 6.8.

6.5 – Application of Kawai's model

Kawai's model is described in Section 2.3.7. In this Section, both the fatigue parameters defined by Kawai, Ψ_K and Σ^*, are tested.

6.5.1 – Effect of the stress ratio

Both the fatigue parameters defined by Kawai take in good account the effect of the stress ratio at constant λ_{12}, as can be seen in Figures 6.26 to 6.28 for Ψ_K and 6.29 to 6.31 for Σ^*.

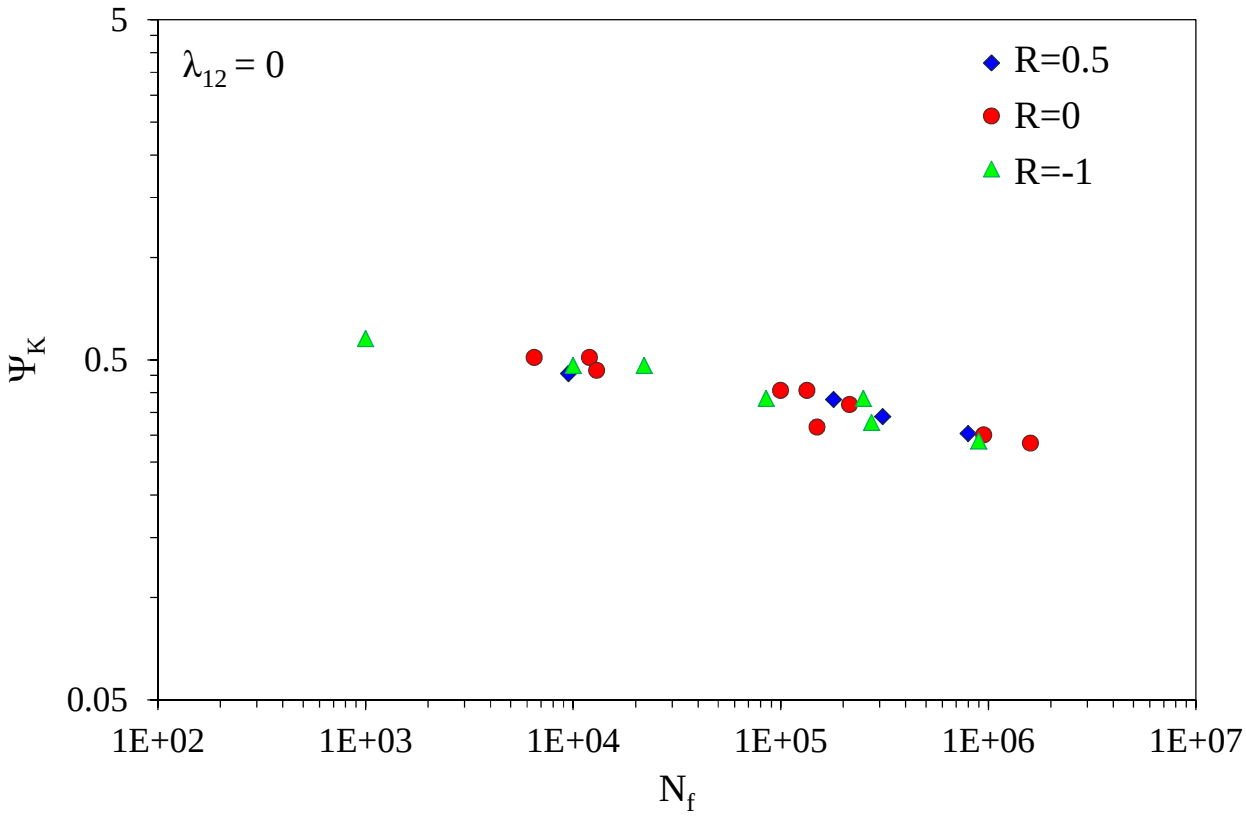

Figure 6.26 – Kawai's fatigue parameter Ψ_K evaluated at R = 0.5, 0, -1 for $\lambda_{12} = 0$.

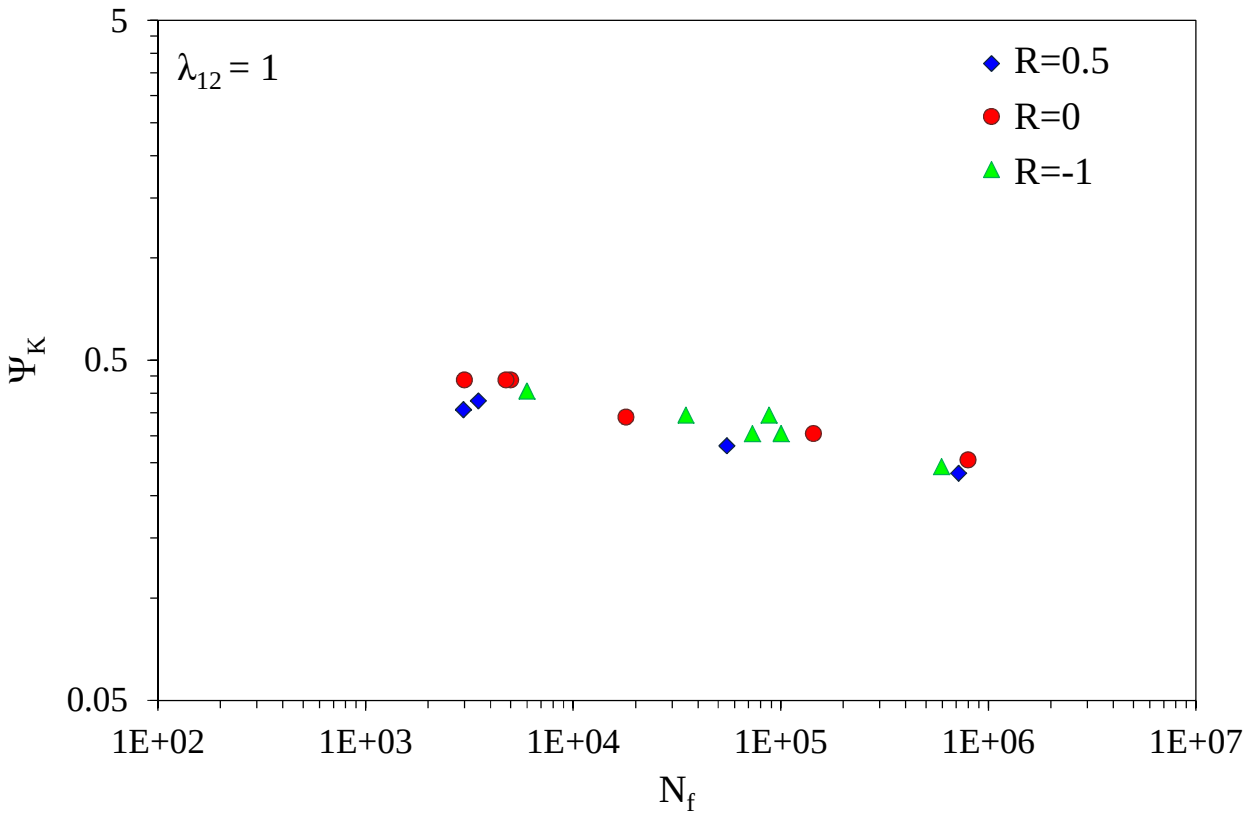

Figure 6.27 – Kawai's fatigue parameter Ψ_K evaluated at R = 0.5, 0, -1 for $\lambda_{12} = 0$.

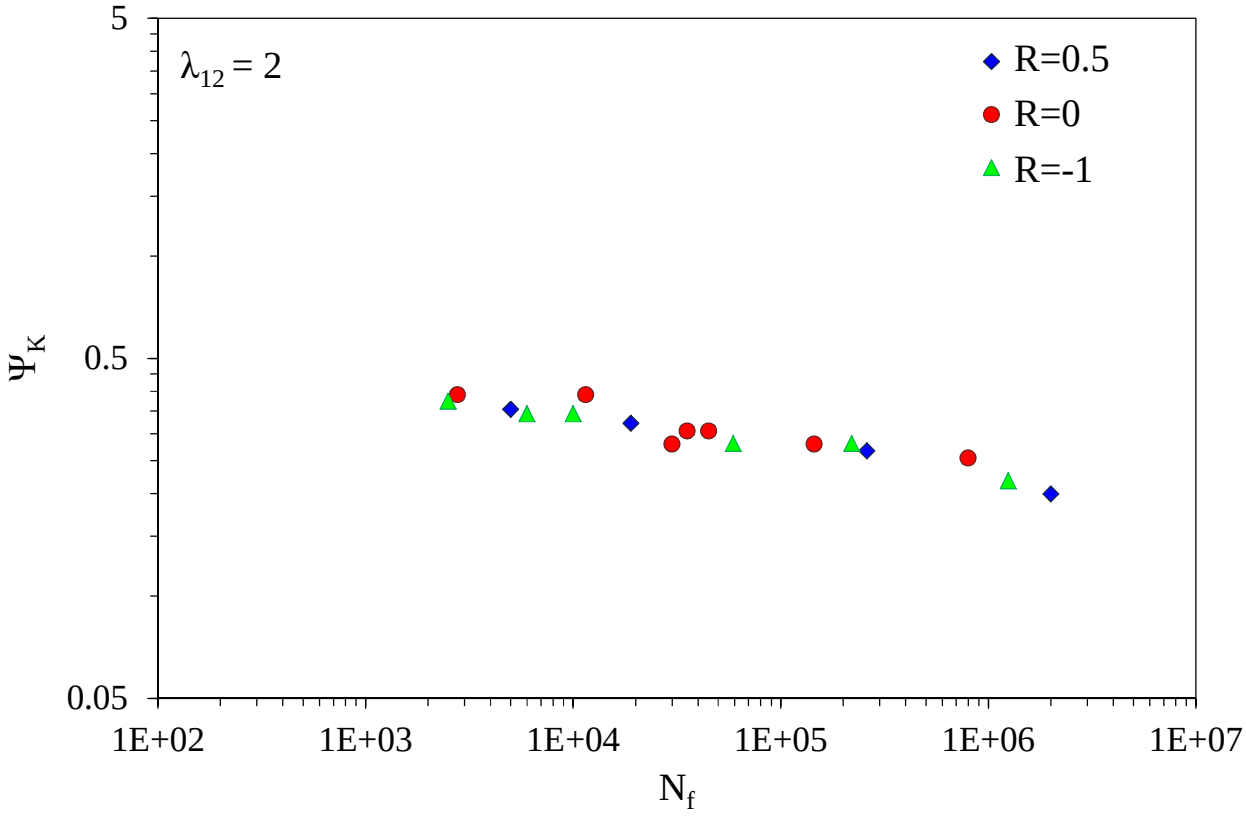

Figure 6.28 – Kawai's fatigue parameter Ψ_K evaluated at R = 0.5, 0, -1 for $\lambda_{12} = 0$.

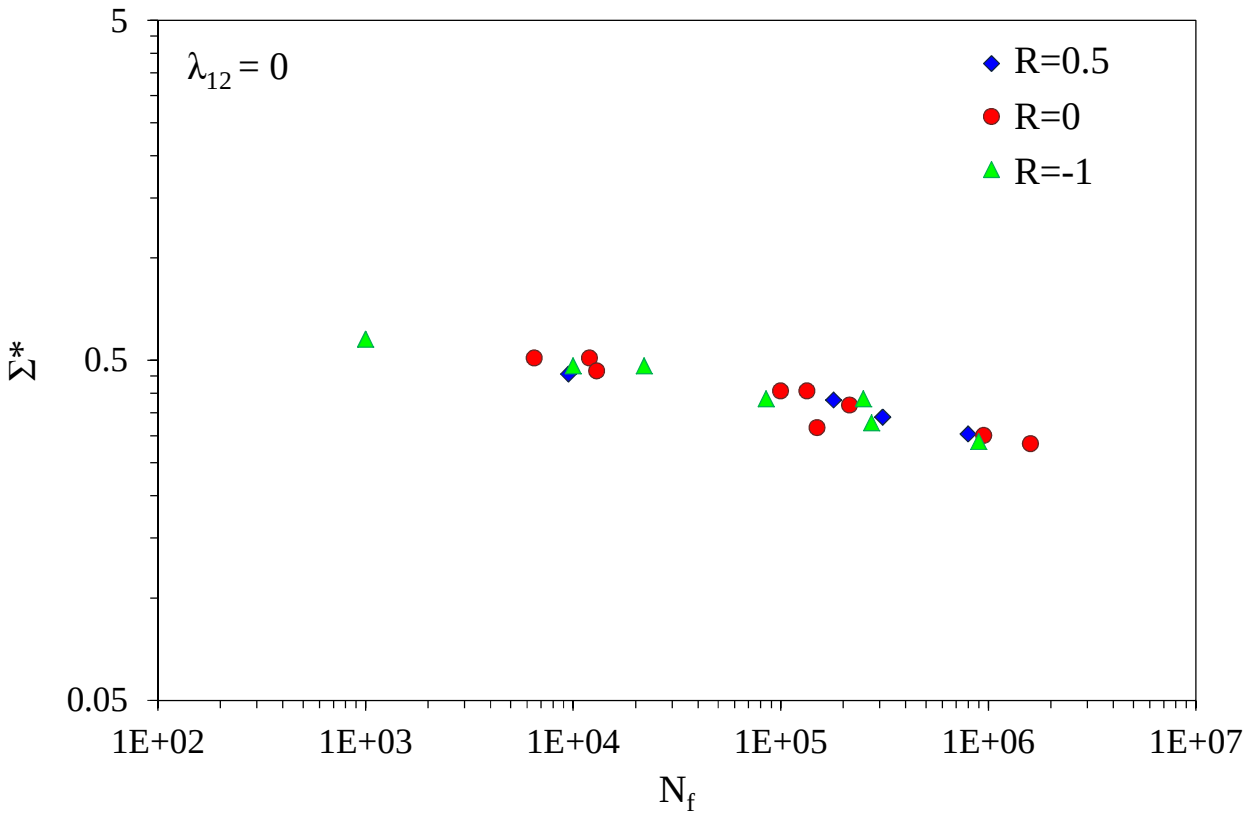

Figure 6.29 – Kawai's fatigue parameter Σ^* evaluated at R = 0.5, 0, -1 for $\lambda_{12} = 0$.

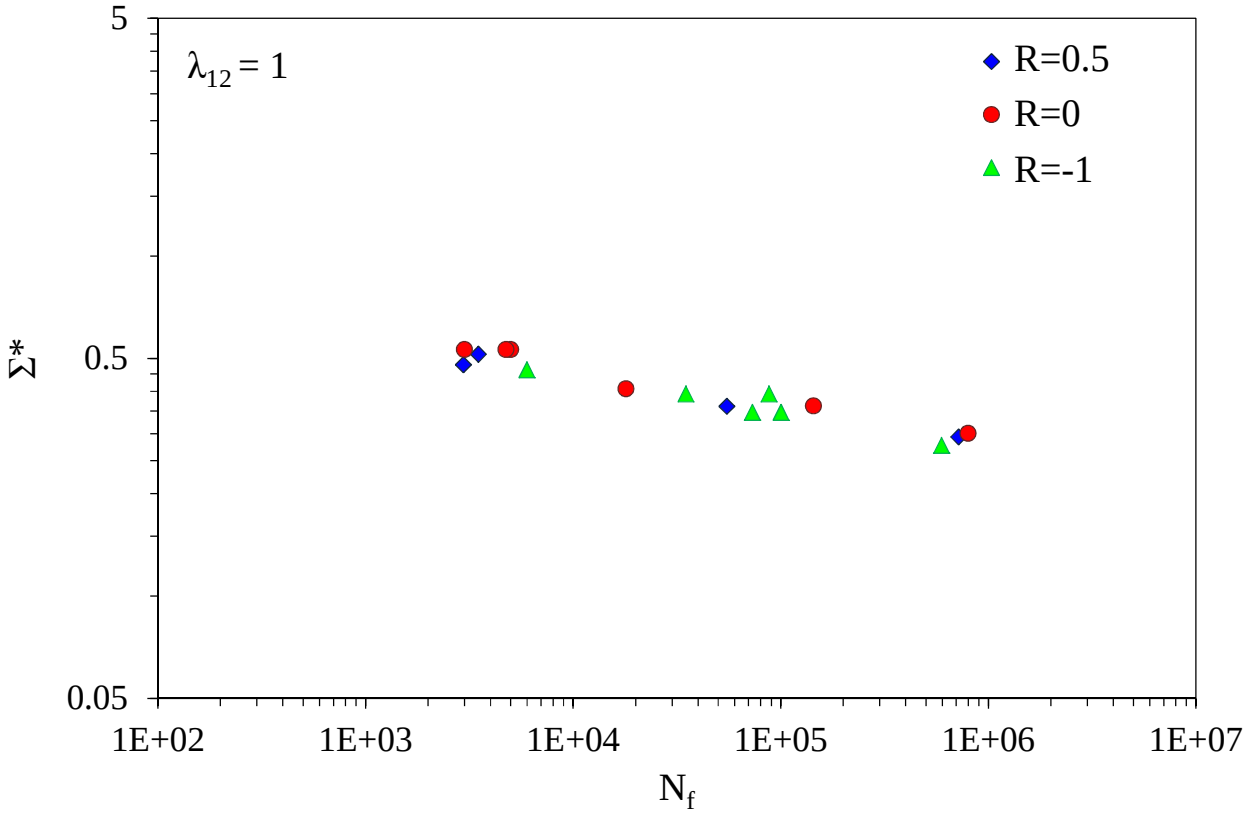

Figure 6.30 – Kawai's fatigue parameter Σ^* evaluated at R = 0.5, 0, -1 for $\lambda_{12} = 0$.

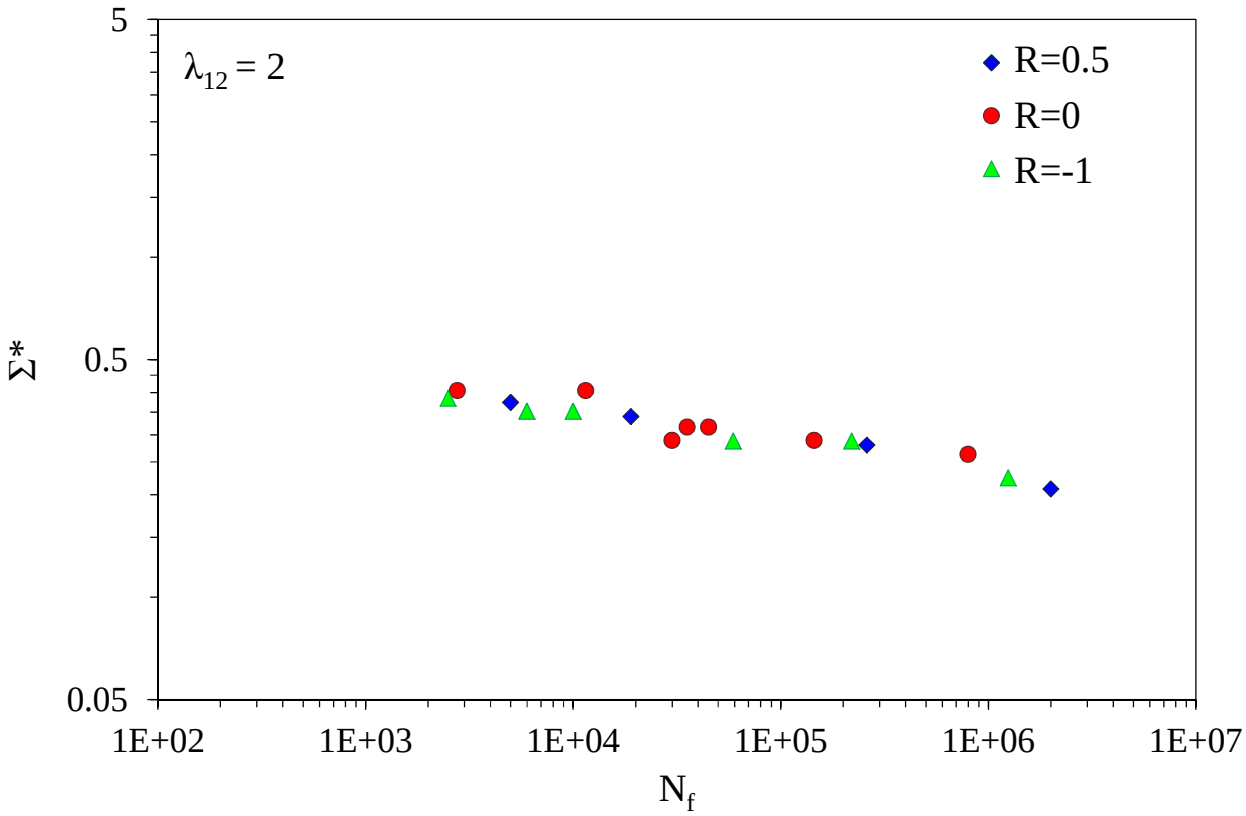

Figure 6.31 – Kawai's fatigue parameter Σ^* evaluated at R = 0.5, 0, -1 for $\lambda_{12} = 0$.

6.5.2 – Effect of the multiaxiality conditions

From the Figures 6.32 to 6.37, in which data at constant stress ratios are reported, can be seen that Kawai's model does not account very well for the effect of the multiaxiality conditions: in fact, in the case of Ψ_K (Figures 6.32 to 6.34) the curves at $\lambda_{12} = 0$ stay always above the ones for $\lambda_{12} = 1$ and 2, that are instead well collapsed; in the case of Σ^* (Figures 6.35 to 6.37) they are instead the curves for $\lambda_{12} = 2$ that are below the other two, that remain instead in the same scatter band. It is then confirmed once again the possibility of a change in the damage mechanism under different loading conditions.

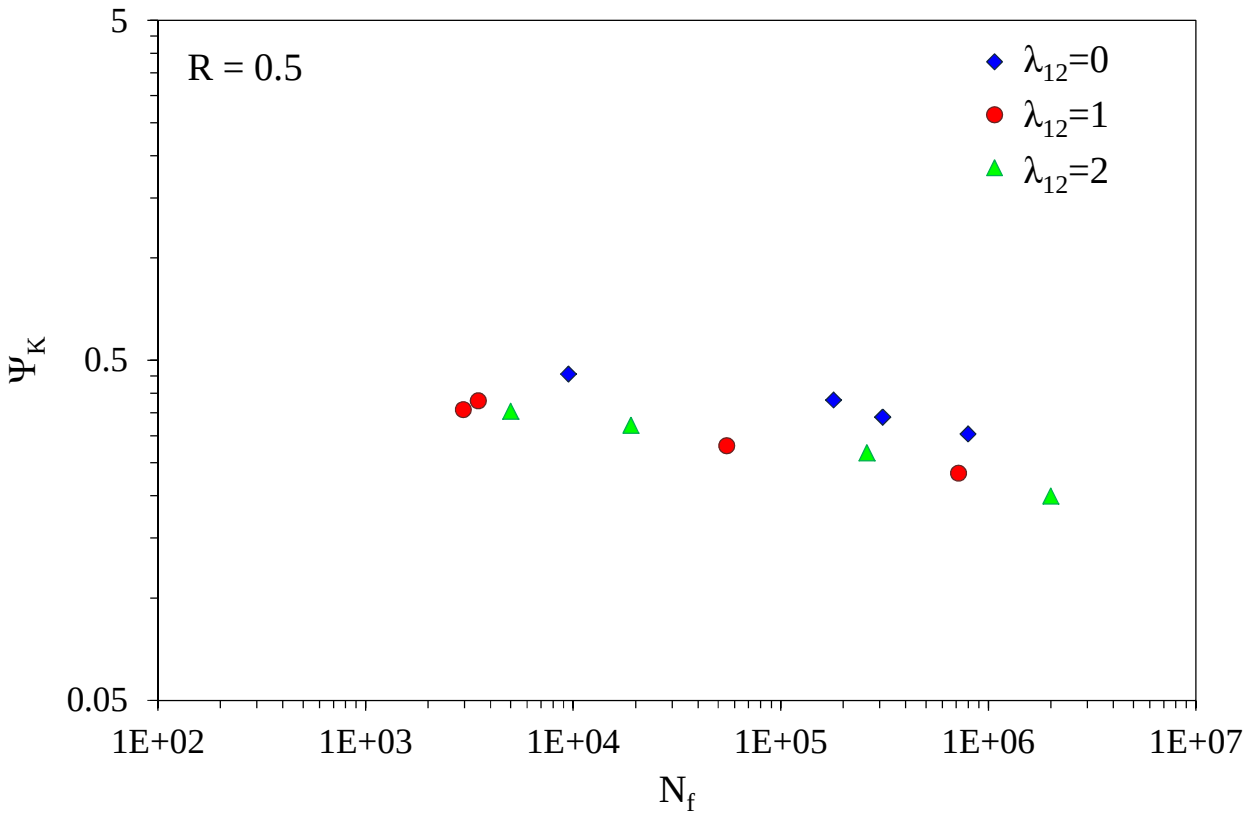

Figure 6.32 – Kawai's fatigue parameter Ψ_K evaluated at λ_{12} = 0, 1, 2 for R = 0.5.

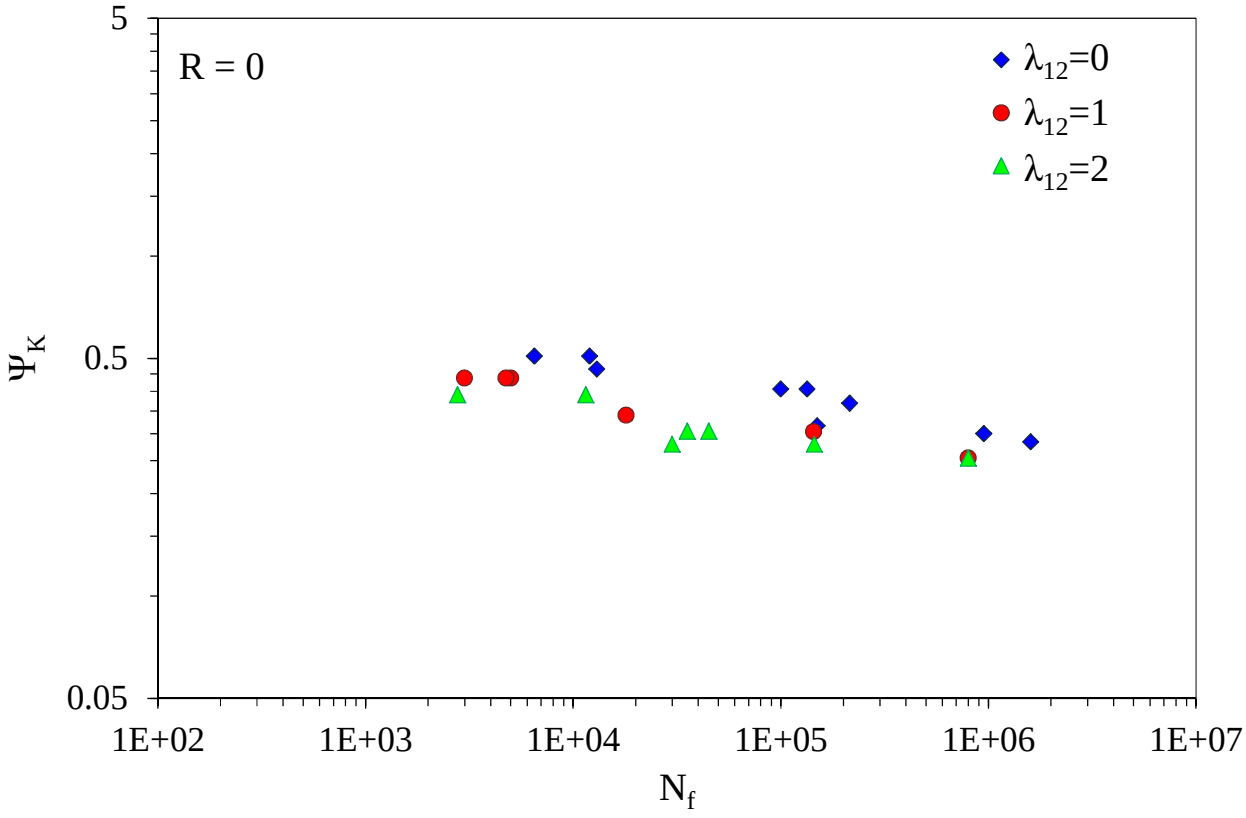

Figure 6.33 – Kawai's fatigue parameter Ψ_K evaluated at λ_{12} = 0, 1, 2 for R = 0.

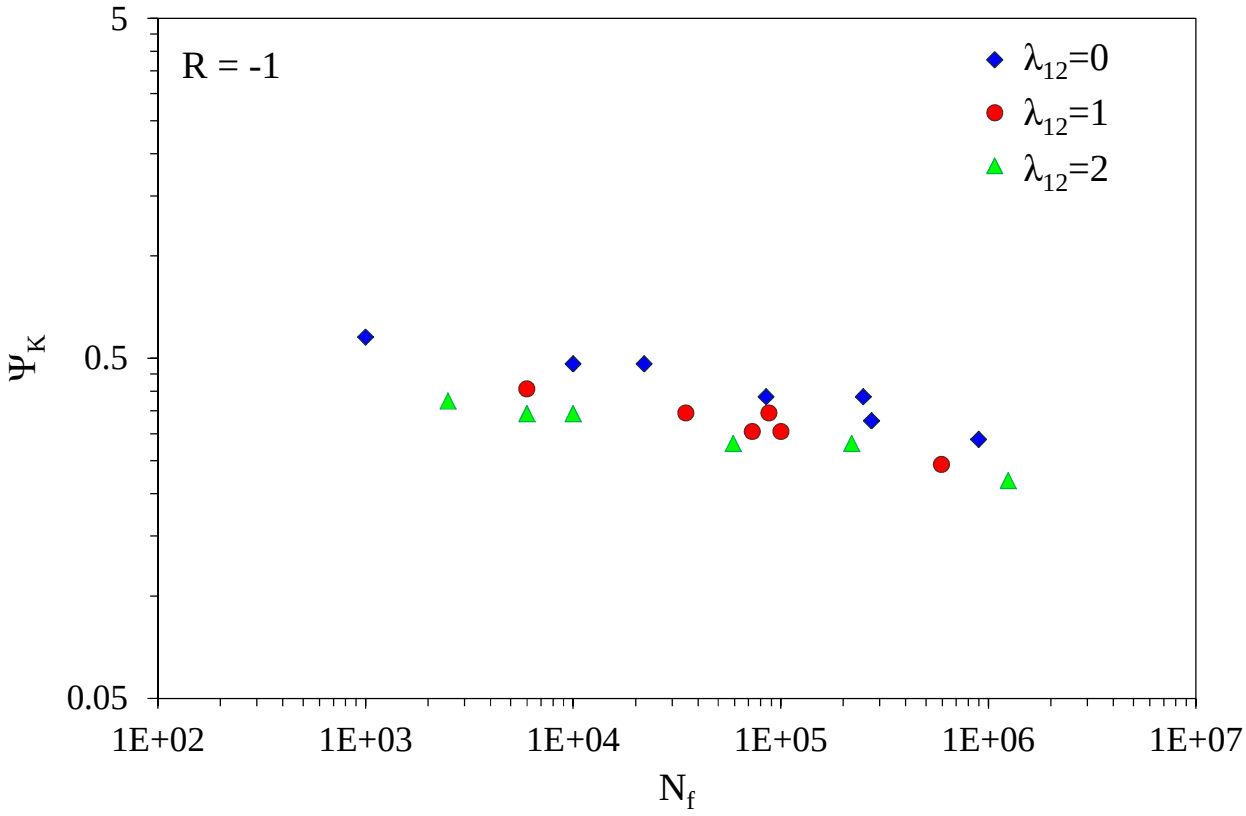

Figure 6.34 – Kawai's fatigue parameter Ψ_K evaluated at λ_{12} = 0, 1, 2 for R = -1.

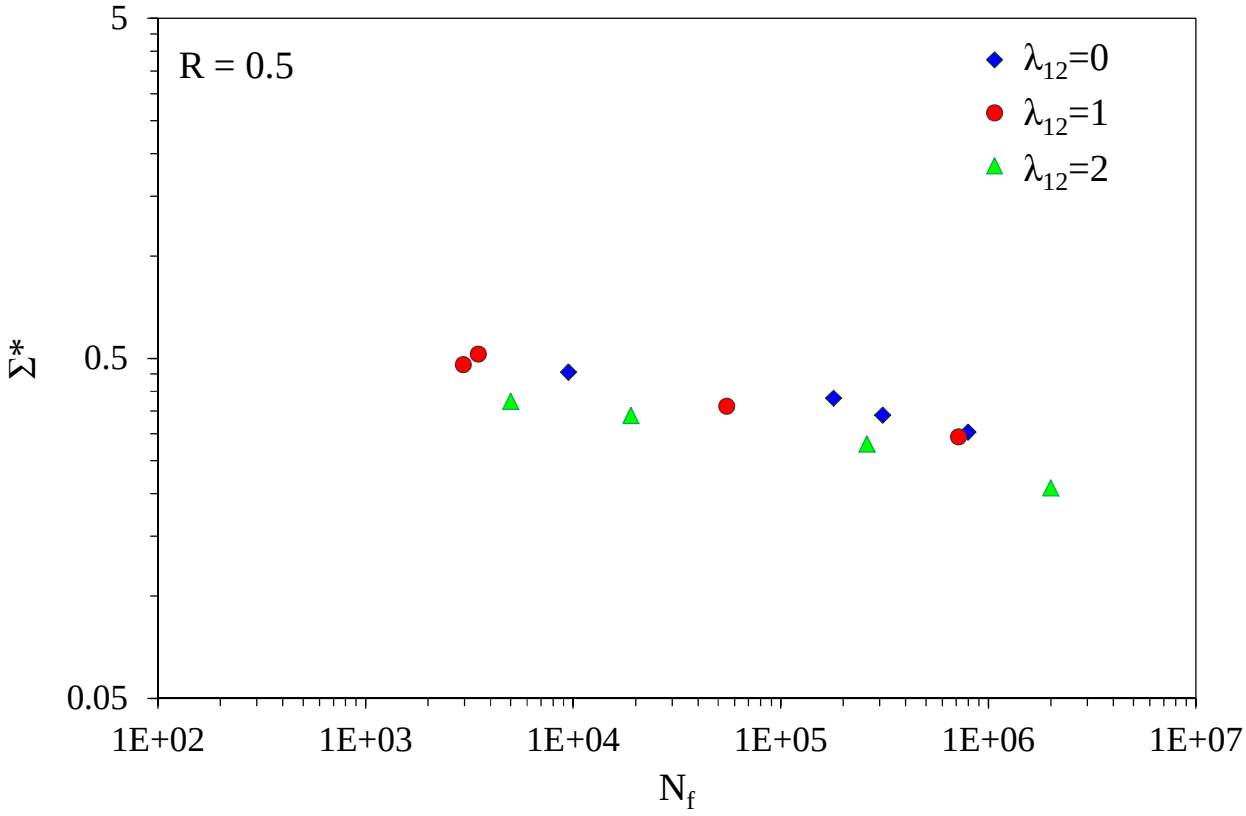

Figure 6.35 – Kawai's fatigue parameter Σ^* evaluated at λ_{12} = 0, 1, 2 for R = 0.5.

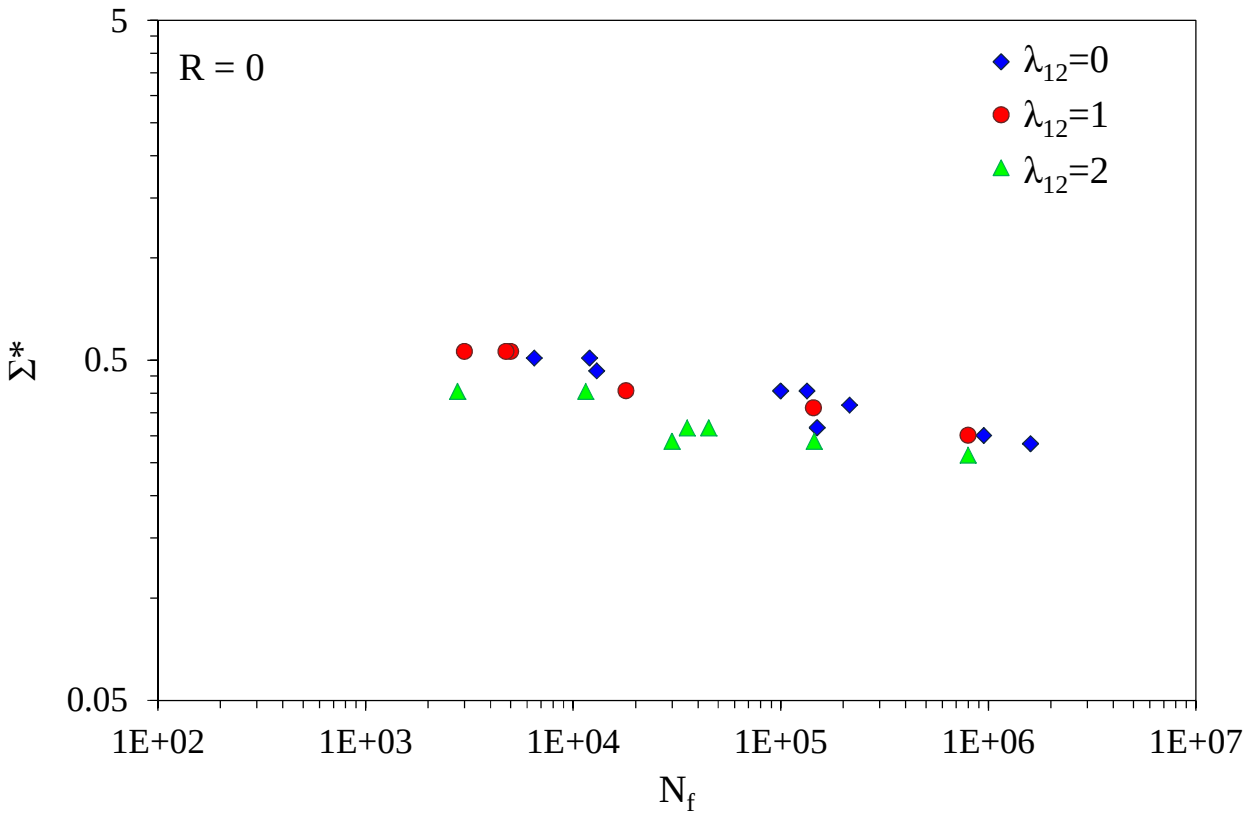

Figure 6.36 – Kawai's fatigue parameter Σ^* evaluated at $\lambda_{12} = 0, 1, 2$ for R = 0.

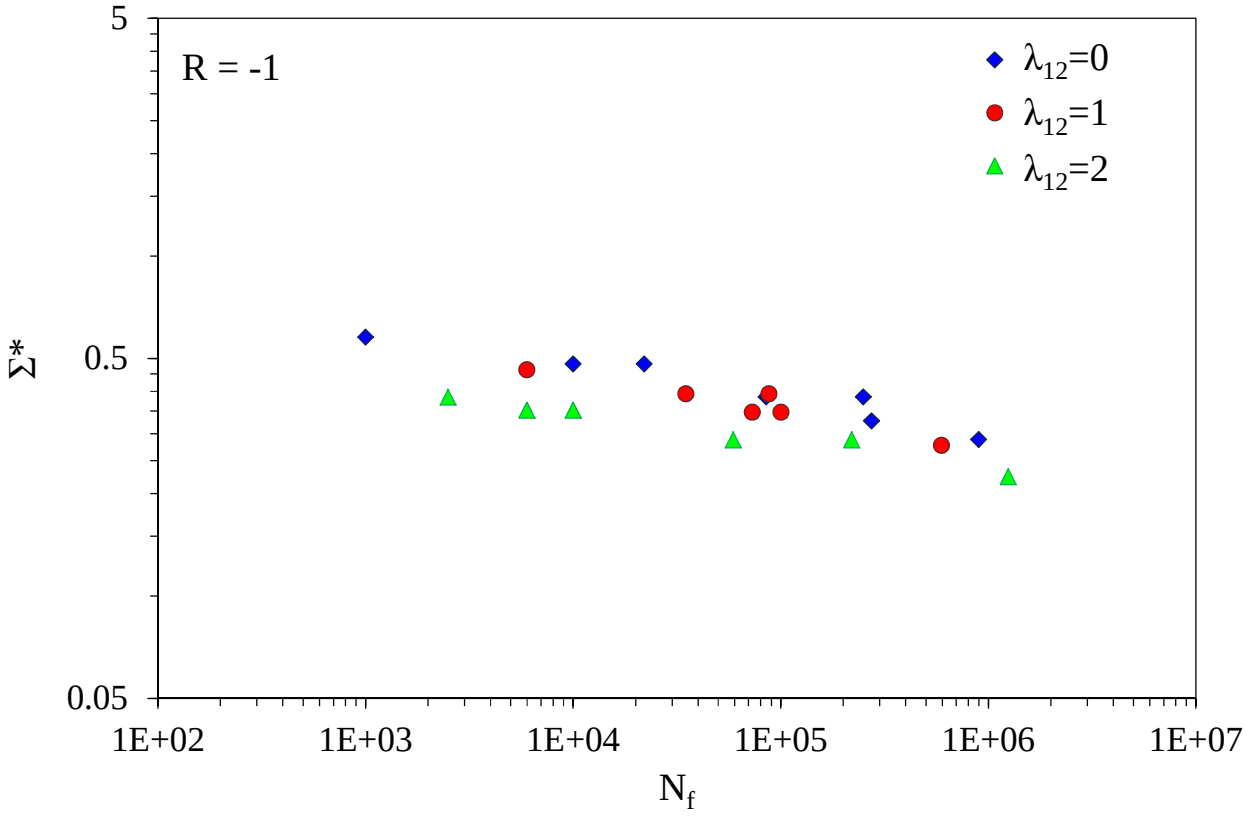

Figure 6.37 – Kawai's fatigue parameter Σ^* evaluated at $\lambda_{12} = 0, 1, 2$ for R = -1.

6.5.3 – All the experimental data

Figures 6.38 and 6.39 show the global validity of Kawai's model for the effect of the stress ratio and the multiaxiality conditions combined together. The model seems to be good. However, in spite of the fact that the scatter band is quite narrow, it is possible to notice that the data for $\lambda_{12} = 0$ in the case of Ψ_K and for $\lambda_{12} = 2$ in the case of Σ^* remain detectably separated from the others.

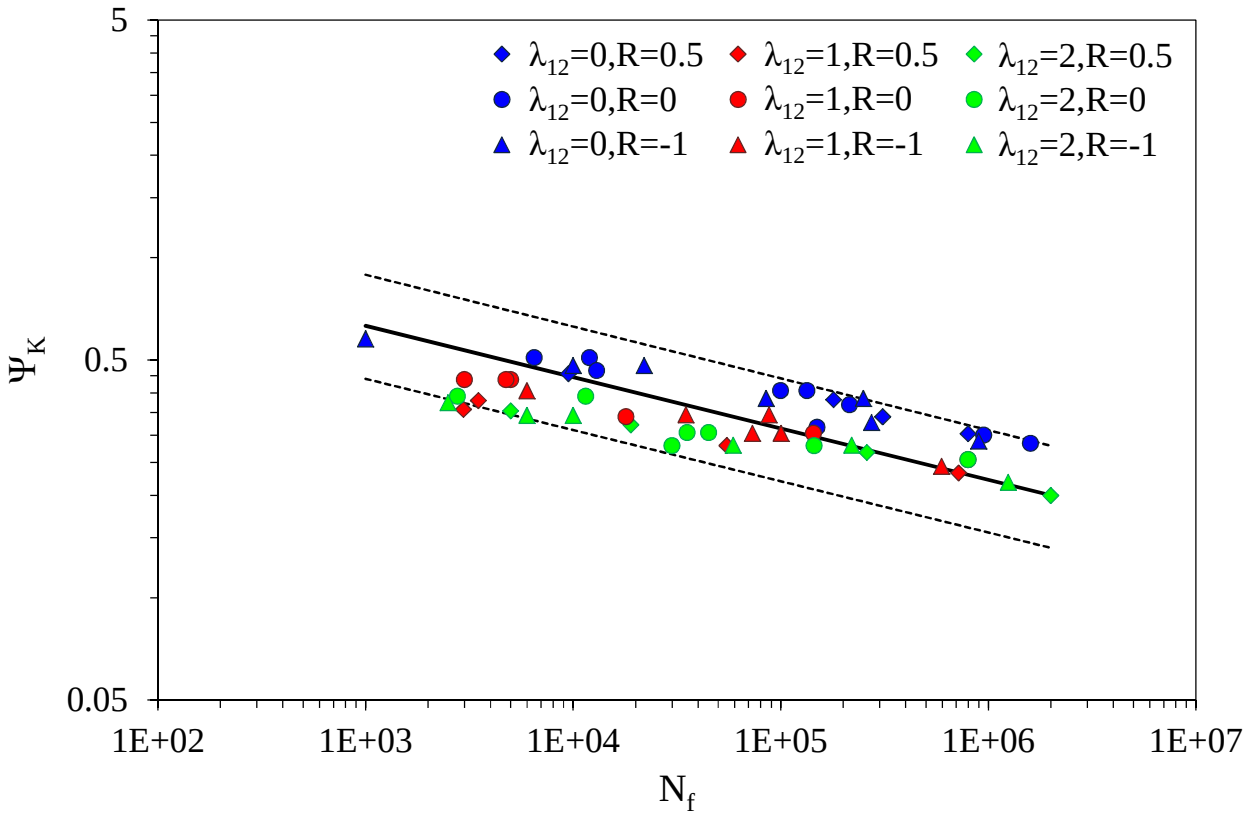

Figure 6.38 – Kawai's fatigue parameter Ψ_K evaluated for all the experimental data.

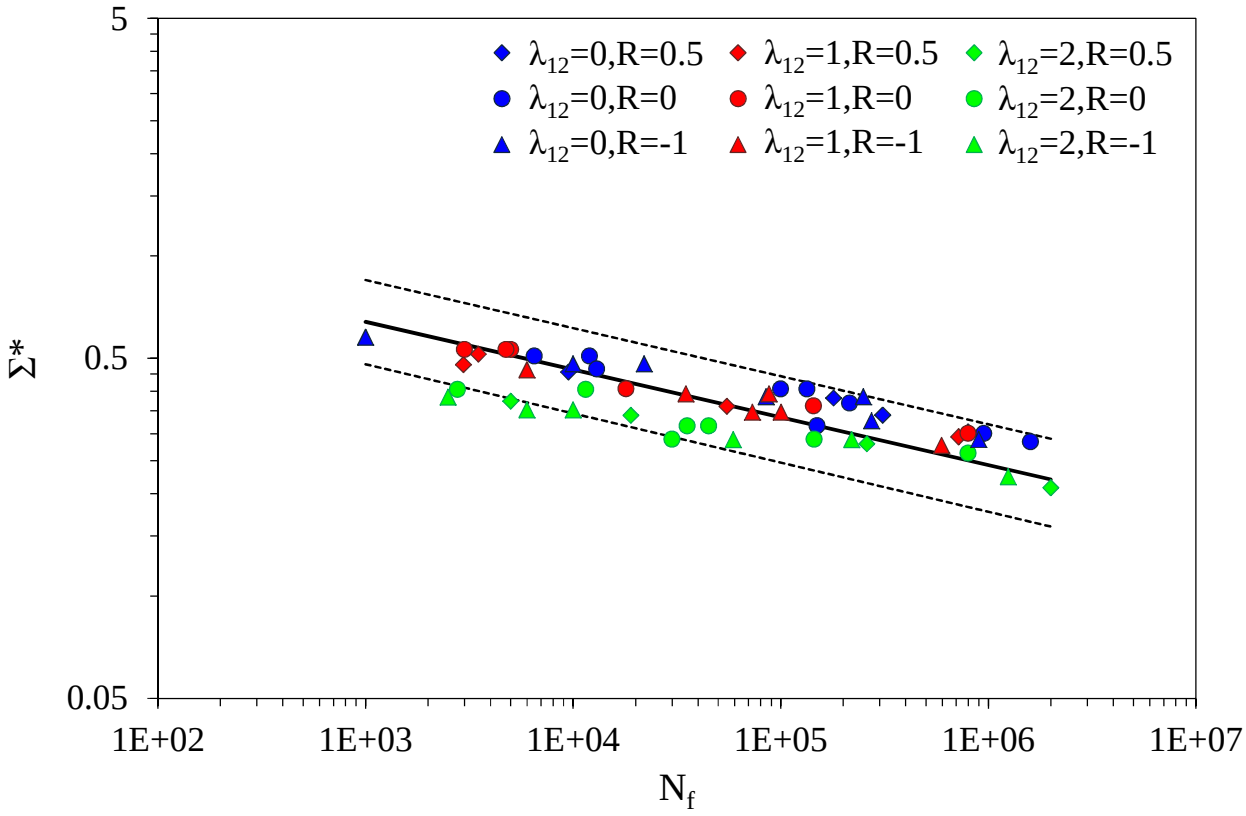

Figure 6.39 – Kawai's fatigue parameter Σ^* evaluated for all the experimental data.

6.6 – A new model

As mentioned in the Introduction, a research team of the Department of Management and Engineering of the University of Padova is currently working on the development of a multiaxiality criterion based on damage mechanisms A complete description of this model can be found in [21], and what follows is only a brief summary.

From the observation that during fatigue cycle the damage initiates in the matrix in the form of the nucleation of cracks that are not parallel to the fibers, but inclined respect to them, it is hypothesized that the fracture plane is perpendicular to the direction of the local maximum principal stress, so that it is the maximum principal stress, generated by the local stress field, that has to be considered for estimating the damage initiation. In cases in which the loading condition is of pure transverse tension, instead, the matrix static failure is mainly caused by cavitation and a good criterion for estimating the failure in such case is the reaching a critical value of the *dilatational energy density*, defined as

$$U_v = \frac{1-2\nu}{6E} I_1^2 \qquad (6.7)$$

in which I_1 is the first stress tensor invariant, calculated considering the local stress fields .

A change in the main damage mode can be expected moving from a condition close to pure transverse stress to one in which the presence of shear stress is large enough. Thus two different parameters are proposed to be used in the life prediction of composite materials: the peak of the local hydrostatic stress (*LHS* = $I_1/3$) in the case of nearly pure transverse stress and the peak of the local maximum principal stress (*LMPS*) for sufficiently large shear stresses; both these quantities can be calculated by means of finite elements analysis. The transition point from one condition to the other can be found as follows: from the experimental S–N data for a loading condition that is close to pure transverse stress and one with shear stress high enough the LMPS and LHS corresponding to $N_f = 10^6$ cycles can be estimated, and from it the related value of the transverse stress. The driving mechanism will be the one with the lower transverse stress. For 90° unidirectional tubes subjected to tension/torsion the trends are reported in Figure 6.40. It appears that the cases λ_{12} = 1 and 2 are controlled by LMPS whereas λ_{12} = 0 by the LHS. Obviously, in reality the transition from one condition to the other will not be drastic, on the contrary the passage will be gradual.

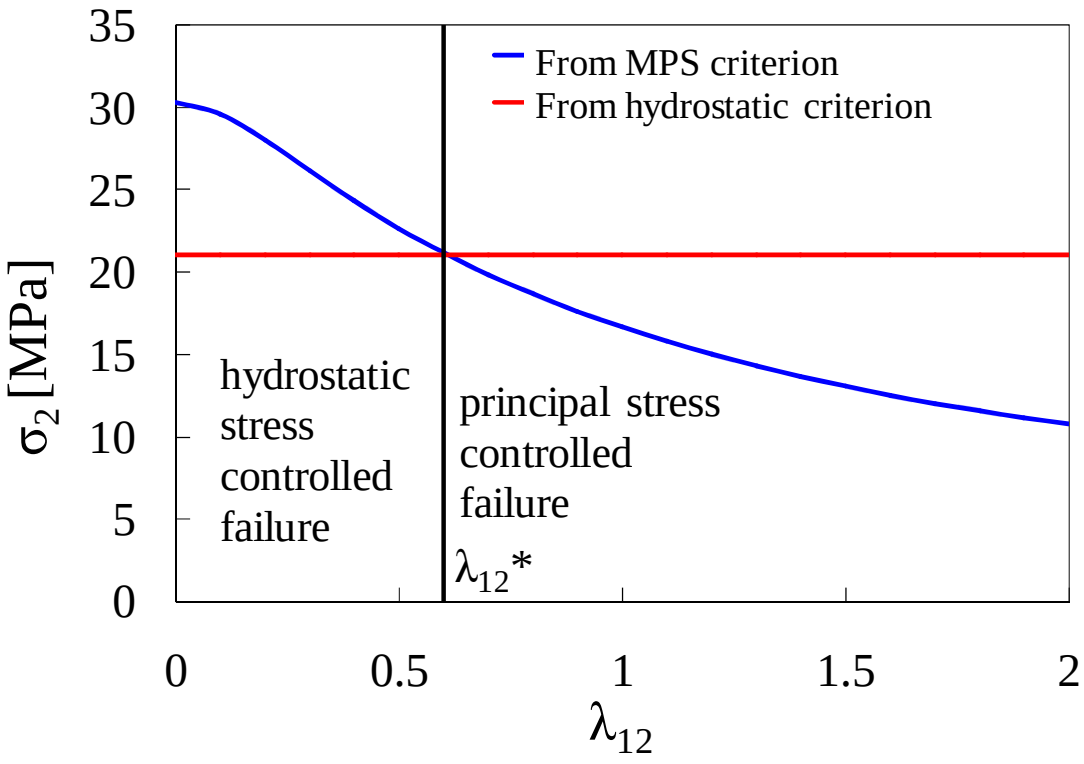

Figure 6.40 – Main damage mechanism as a function of the biaxiality ratio for unidirectional tubes under tension/torsion (taken from [21]).

In order to take into account the effect of the stress ratio, the following fatigue parameters are proposed:

$$\Psi_{LMPS} = \frac{LMPS_a}{LMPS_{static} - LMPS_m} \tag{6.8}$$

$$\Psi_{LHS} = \frac{LHS_a}{LHS_{static} - LHS_m} \tag{6.9}$$

in which the subscripts *a, m* and *static* denote, respectively, amplitude and mean values of the fatigue cycles and value at the static failure.

6.6.1 – Effect of the stress ratio

The model appears to consider with very good accuracy the effect if the stress ratio at constant λ_{12} (Figures 6.41 to 6.43), with the only exception of the curve for λ_{12} = 1, R = 0.5 that anyway only slightly under the other two curves. It is reminded that the case λ_{12} = 0 is driven by the LHS while λ_{12} = 1, 2 by LMPS.

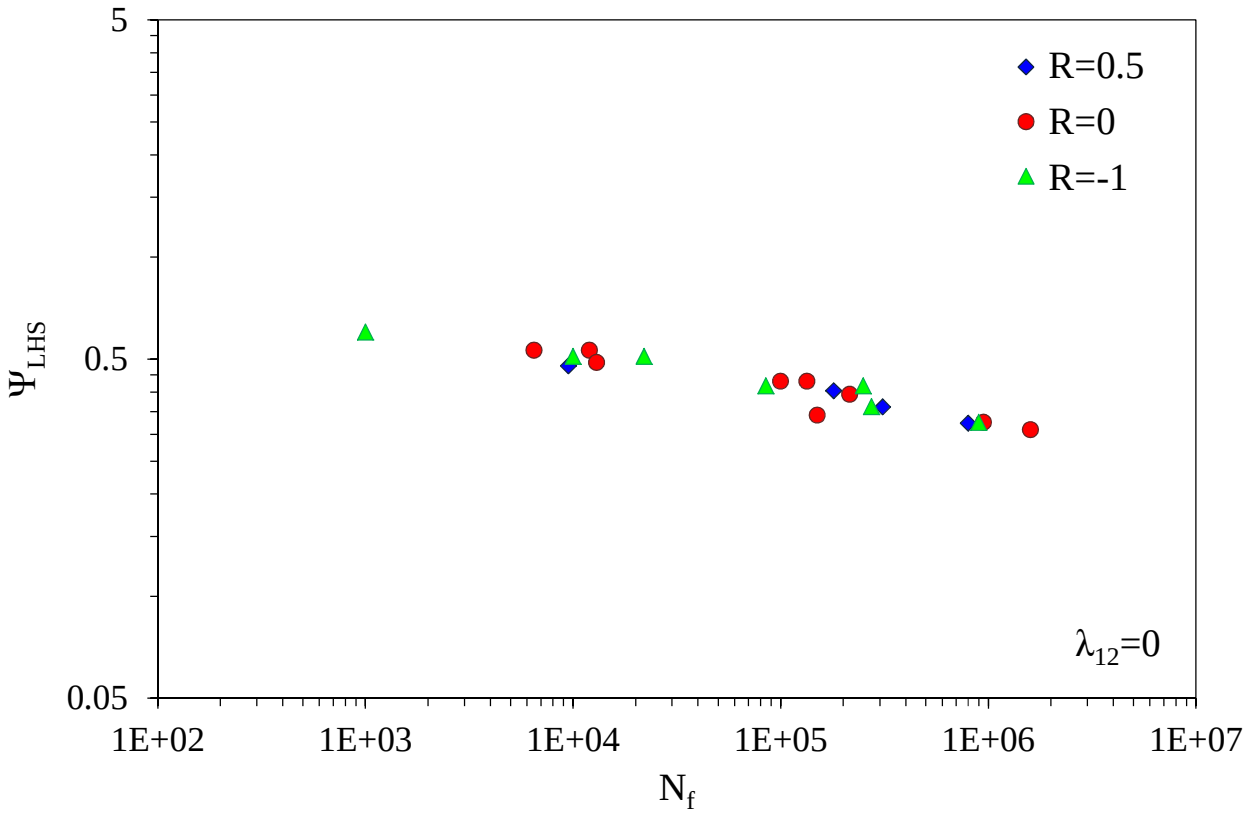

Figure 6.41 – Fatigue parameter Ψ_{LHS} applied to the experimental data at R = 0.5, 0, -1 for λ_{12} = 0.

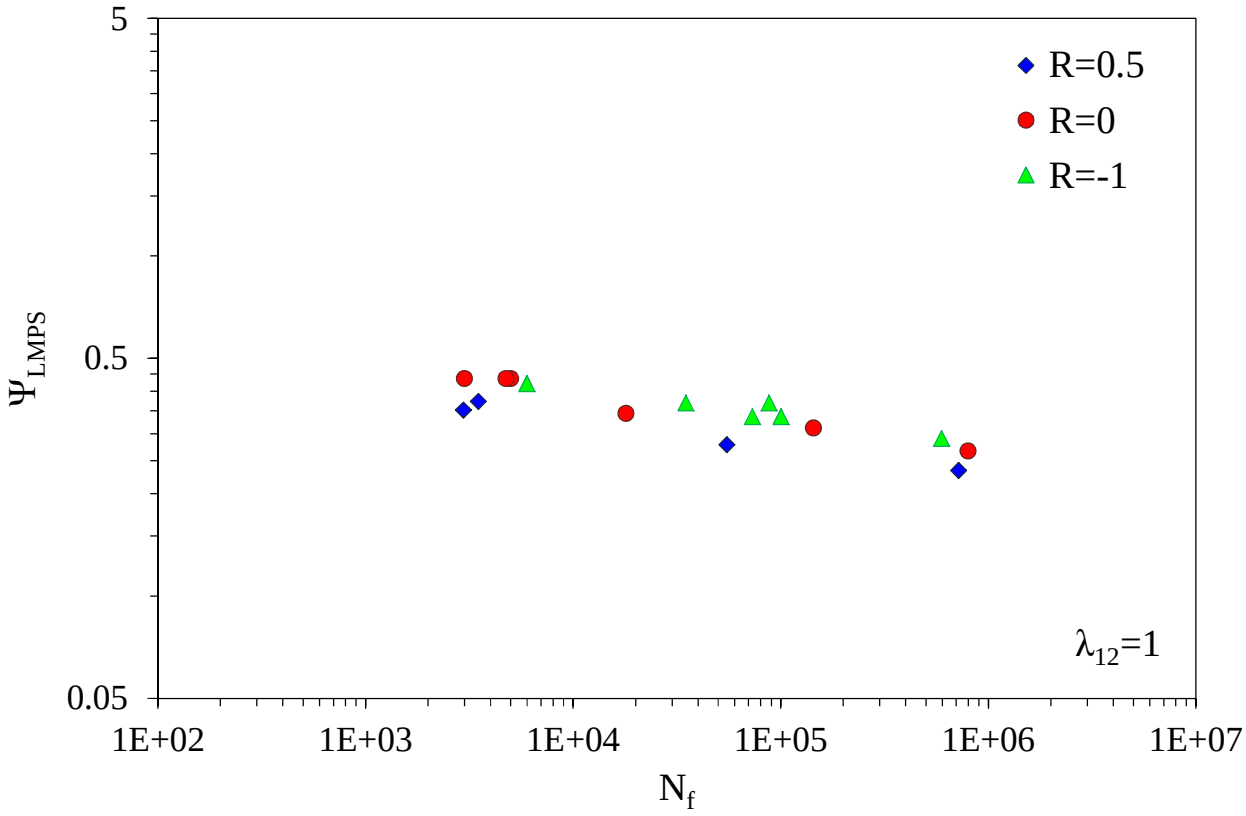

Figure 6.42 – Fatigue parameter Ψ_{LMPS} applied to the experimental data at R = 0.5, 0, -1 for $\lambda_{12} = 1$.

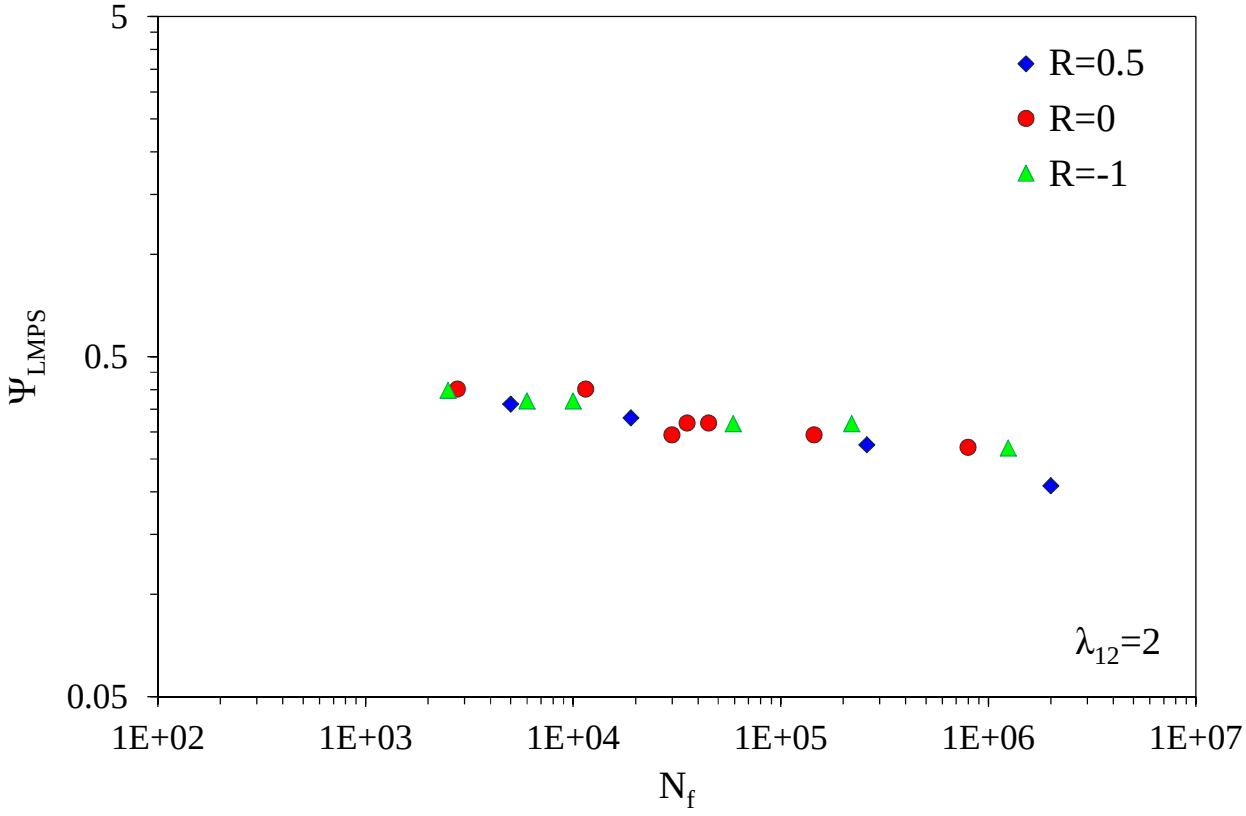

Figure 6.43 – Fatigue parameter Ψ_{LMPS} applied to the experimental data at R = 0.5, 0, -1 for $\lambda_{12} = 2$.

6.6.2 – Effect of the multiaxiality conditions

Also the effect of the multiaxiality conditions is properly taken into account by the this model, as shown in Figures 6.44 to 6.47. Since in the present data set there is only one condition driven by LHS, data for λ_{12} = 0.5 at R = 0, obtained in a previous experimental campaign [20] are here reported in order to check the validity of the LHS fatigue parameter.

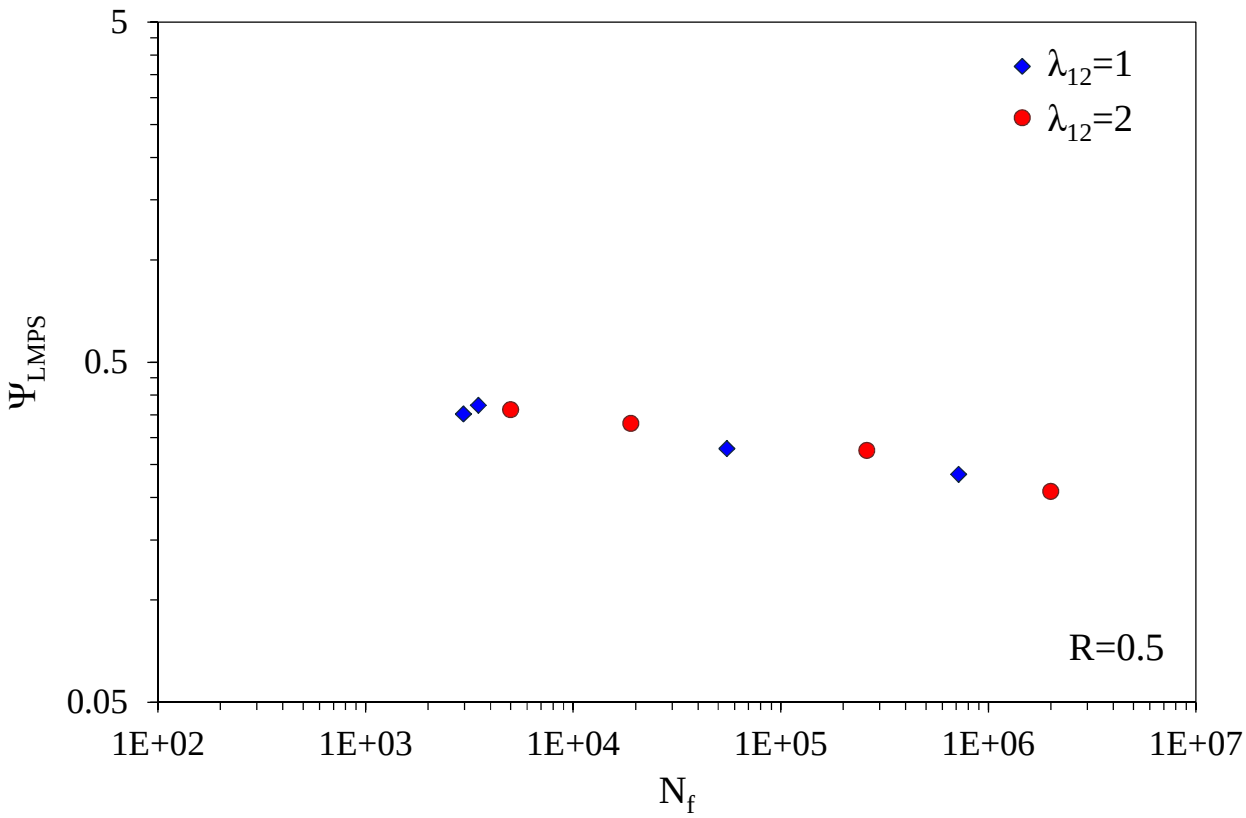

Figure 6.44 – Fatigue parameter Ψ_{LMPS} applied to the experimental data at λ_{12} = 1, 2 for R = 0.5.

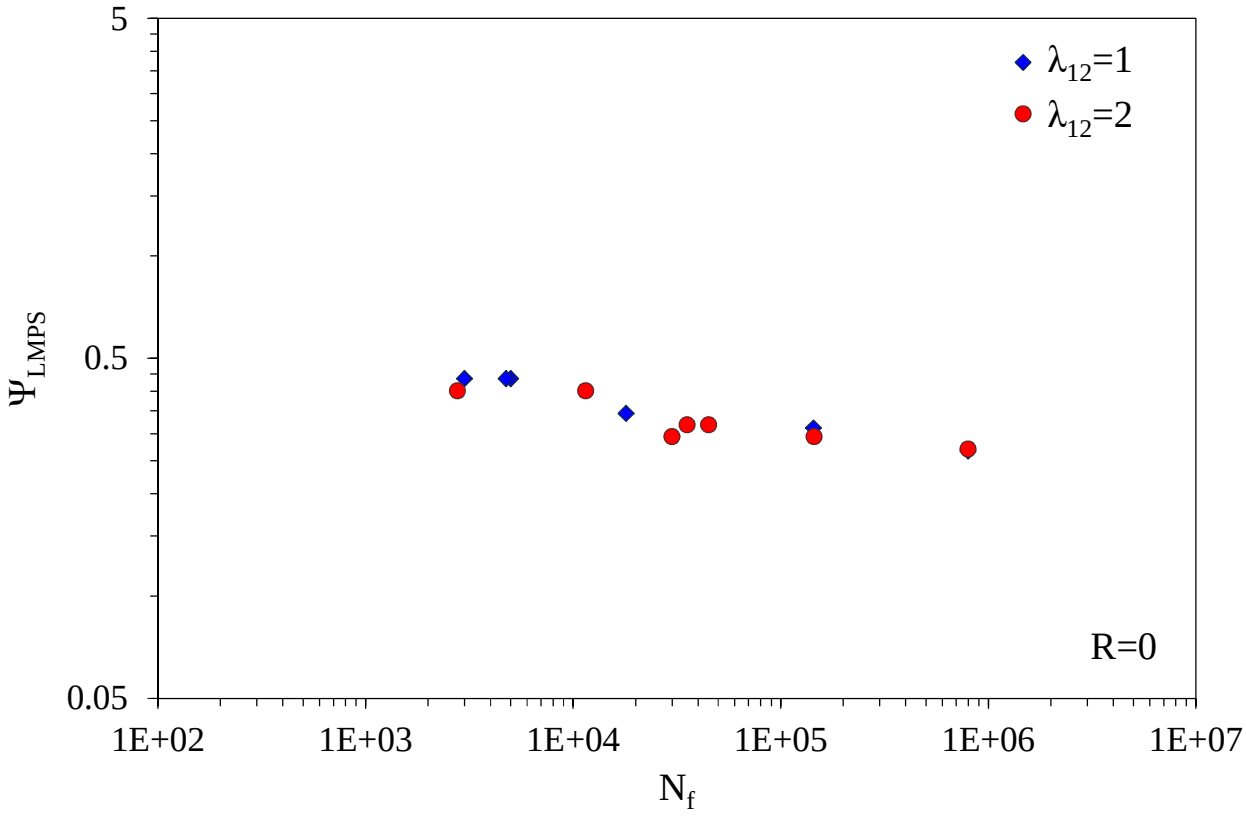

Figure 6.45 – Fatigue parameter Ψ_{LMPS} applied to the experimental data at λ_{12} = 1, 2 for R = 0.

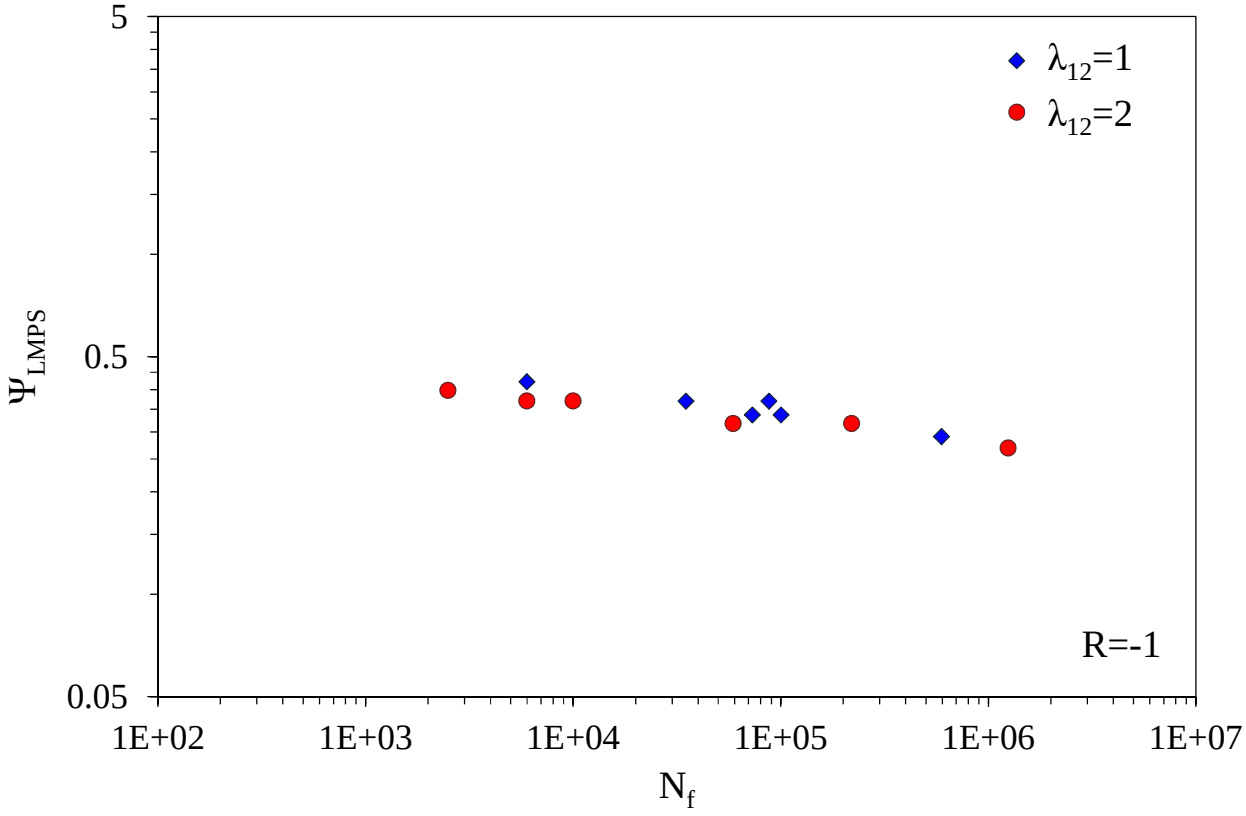

Figure 6.46 – Fatigue parameter Ψ_{LMPS} applied to the experimental data at λ_{12} = 1, 2 for R = -1.

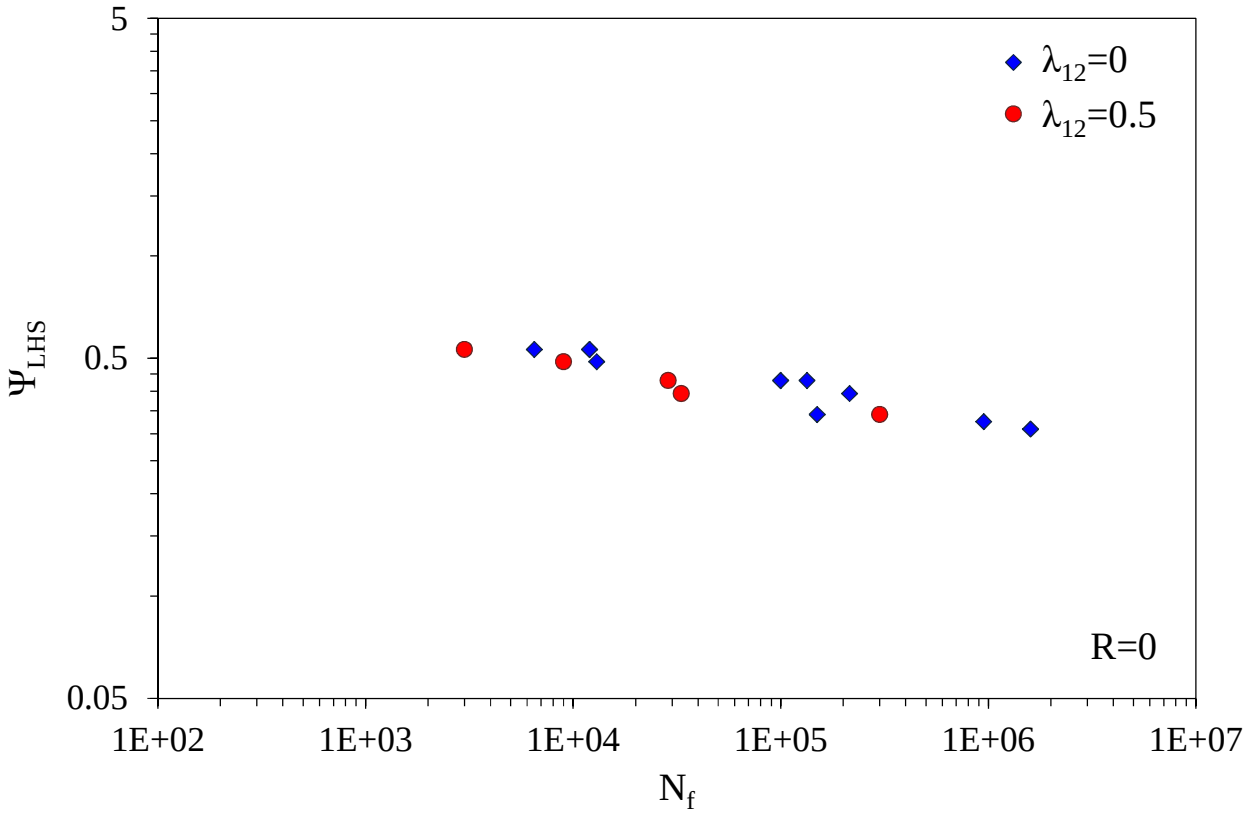

Figure 6.47 – Fatigue parameter Ψ_{LHS} applied to the experimental data at λ_{12} = 0, 0.5 for R = 0.

6.6.3 – All the experimental data

Because of the nature of this model, it is not possible to represent all the data in a single plot, since two different parameters are involved. Anyway, both the fatigue parameters manage to collapse very well the data obtained under the loading conditions in which they dominate, as can be seen in Figures 6.48 and 6.49.

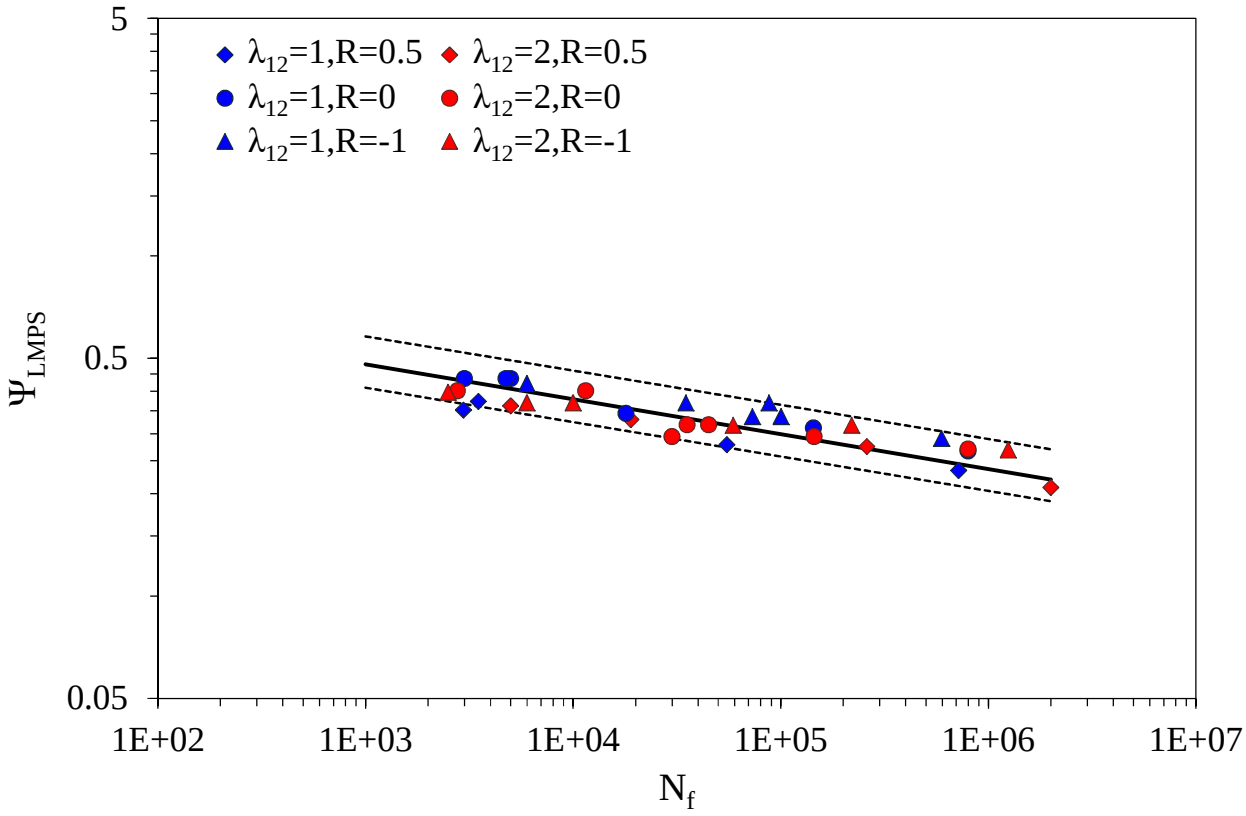

Figure 6.48 – Fatigue parameter Ψ_{LMPS} at λ_{12} = 1, 2 for R = 0.5, 0, -1.

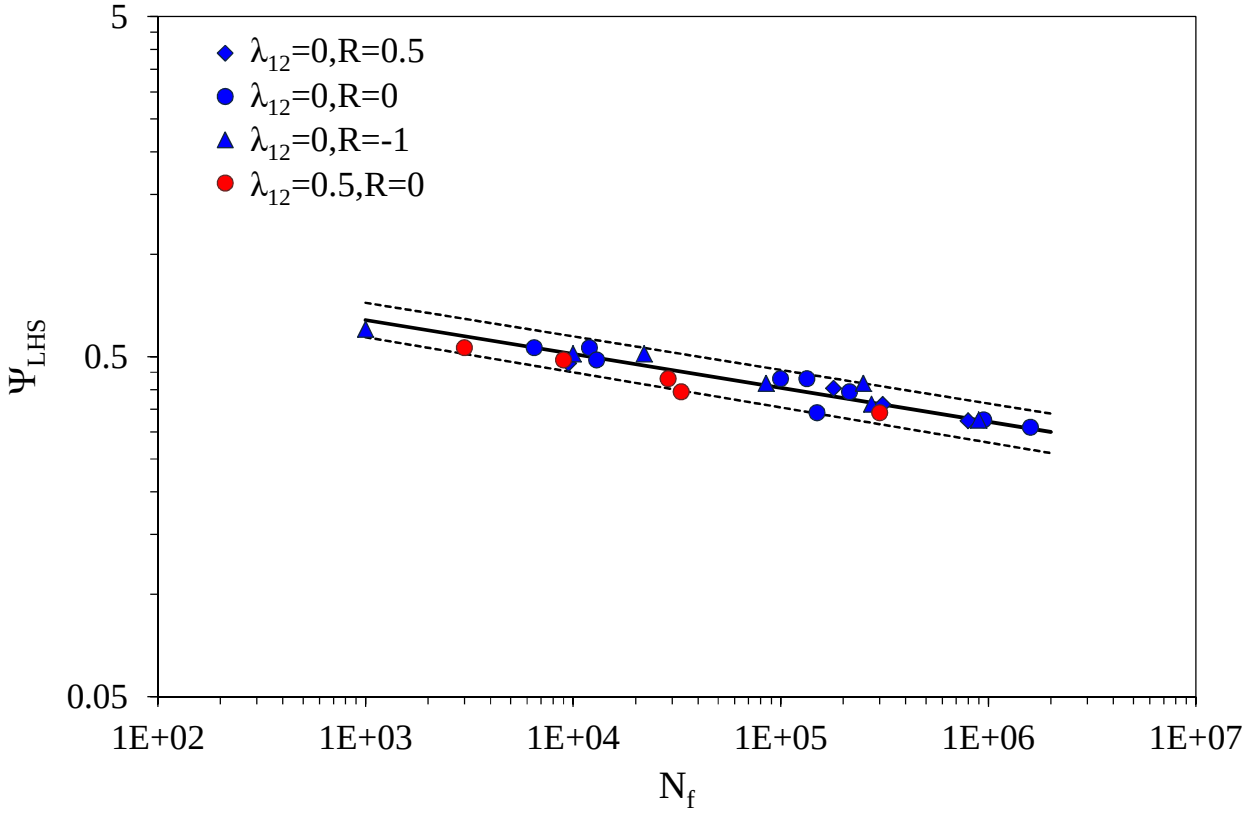

Figure 6.49 – Fatigue parameter Ψ_{LHS} at λ_{12} = 0 for R = 0.5, 0, -1 and at λ_{12} = 0.5 for R = 0.

6.7 – A quantitative comparison between models

A possible quantitative tool for evaluating of the goodness of the models here reported, until now evaluated only at a qualitative level, can be the ratio between the value of the fatigue parameter corresponding to a probability of survival of 90% and the value for a probability of survival of 10%, bot evaluated at N = 10^6 cycles. This ratio is called T_σ for stress-based models and T_W for energy-based models. As previously stated, the relation between the fatigue parameters and the number of cycles is assumed to be linear in a log-log scale for all the analyzed models, and expressed here in the form:

$$fatigue\ \ parameter = bN_f^{\ a} \tag{6.10}$$

And the curves for different probabilities of survival are found by assuming a log-normal distribution of the fatigue life. A square root of the T_W (called always T_σ) must be done in order for the energy-based models to be comparable to the stress-based ones, since energetic parameters are proportional to the square of the stresses. The results of this analysis are reported in Table 6.2.

Model	notes	Fatigue parameter	a	$b_{50\%}$	T_W	T_σ
El Kadi – Ellyin (original)	Energy-based	Ψ	-0.345	15.237	5.567	2.360
El Kadi – Ellyin (modified)	Energy-based	Ψ'	-0.240	5.538	2.613	1.616
Plumtree – Cheng (original)	Energy-based	ΔW_{tot}^*	-0.481	268.339	12.533	3.540
Plumtree – Cheng (modified)	Energy-based	$\Delta W_{tot,n}$ *	-0.217	4.004	2.103	1.450
Petermann – Plumtree (original)	Energy-based	W_{tot}^*	-0.508	199.967	15.545	3.943
Petermann – Plumtree (modified 1)	Energy-based	$W_{tot,ntc}$ *	-0.345	8.205	5.567	2.360
Petermann – Plumtree (modified 2)	Energy-based	$W_{tot,nt}$ *	-0.233	2.485	2.465	1.570
Kawai (original)	Stress-based	Ψ_K	-0.153	1.825	-	2.007
Kawai (original)	Stress-based	Σ*	-0.142	1.713	-	1.760
New model	Stress-based	Ψ_{LMPS}	-0.102	0.983	-	1.420
New model	Stress-based	Ψ_{LHS}	-0.101	1.299	-	1.227

Table 6.2 – Coefficients of the regression curves and values of T_σ.

The quantitative comparison confirms everything that was already said in the previous Sections. In particular, the parameter in literature that best takes into account the effect of combined

multiaxiality and stress ratio appears to be Kawai's one. The modifications that have been proposed to some of those models lead to results that are not just better than the original ones, but also better respect to Kawai's model. The new model that has been proposed, based on the one that is being developed by the Department of Management and Engineering of the University of Padova, reaches the best results overall, along with the advantage that, being based on damage mechanisms, is more general and reliable.

The same conclusions on the performances of the models can be observed in Figures 6.50 to 6.60, in which, for each experimental point, the predicted number of cycles is plotted against the experimental number of cycles. Points close to the bisector in log-log scale are the ones better predicted. Lines relative to errors of 100%, 200% and 400% are also reported in these Figures.

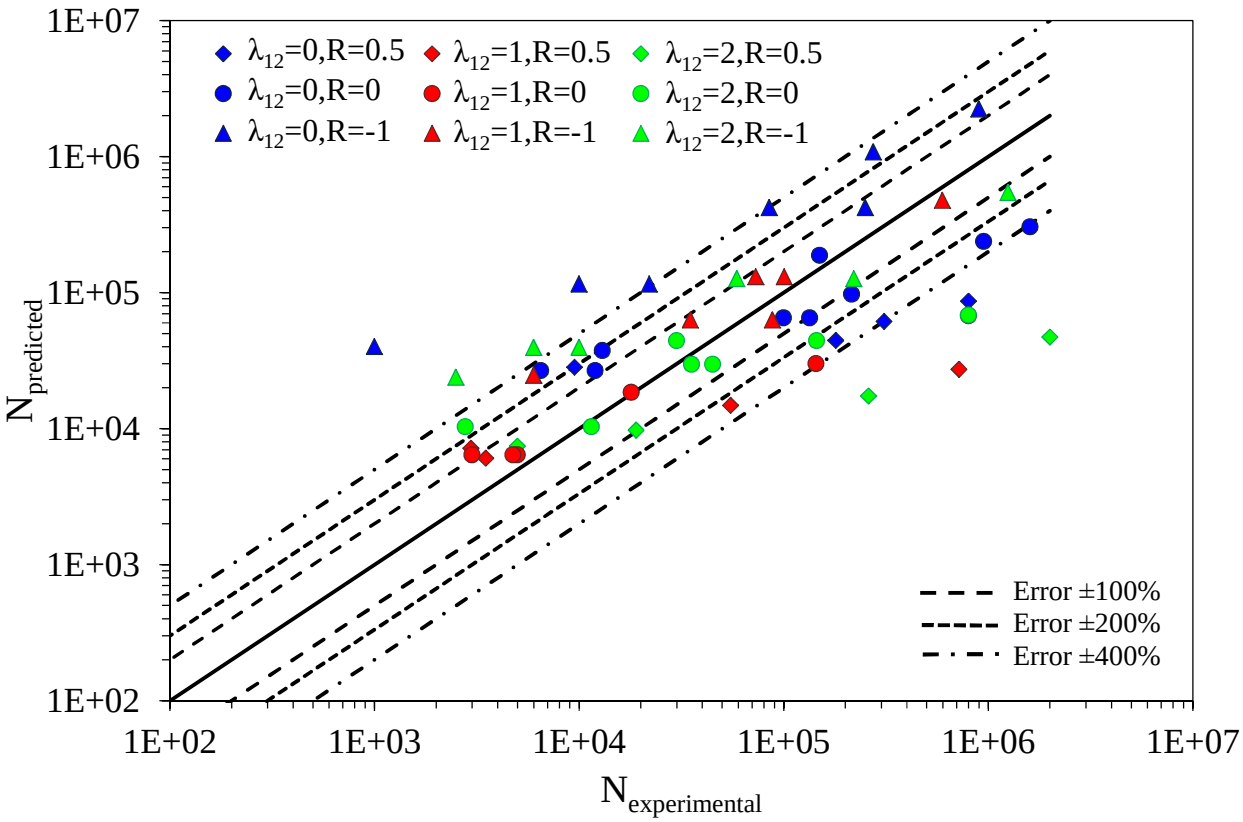

Figure 6.50 – $N_{predicted}$ vs $N_{experimental}$ for El Kadi and Ellyin's model (Ψ).

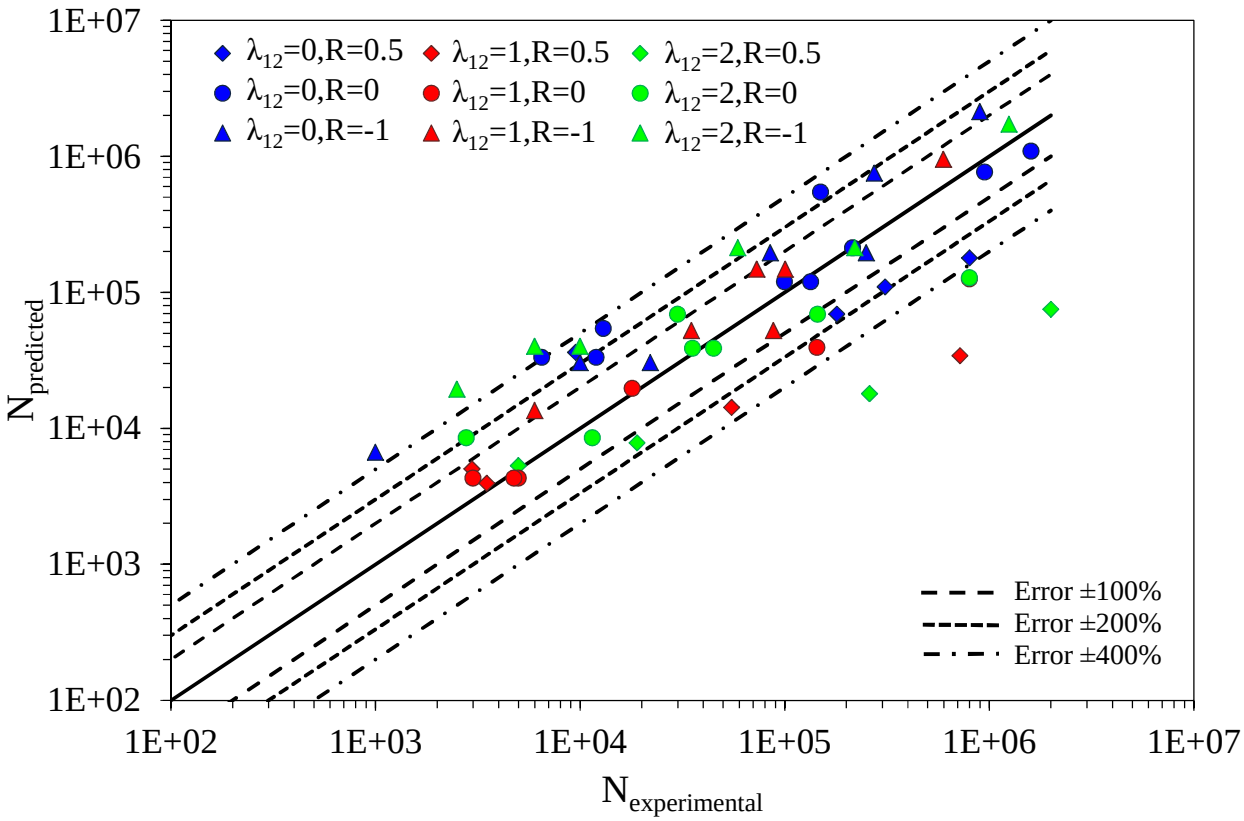

Figure 6.51 – $N_{predicted}$ vs $N_{experimental}$ for modified El Kadi and Ellyin's model (Ψ').

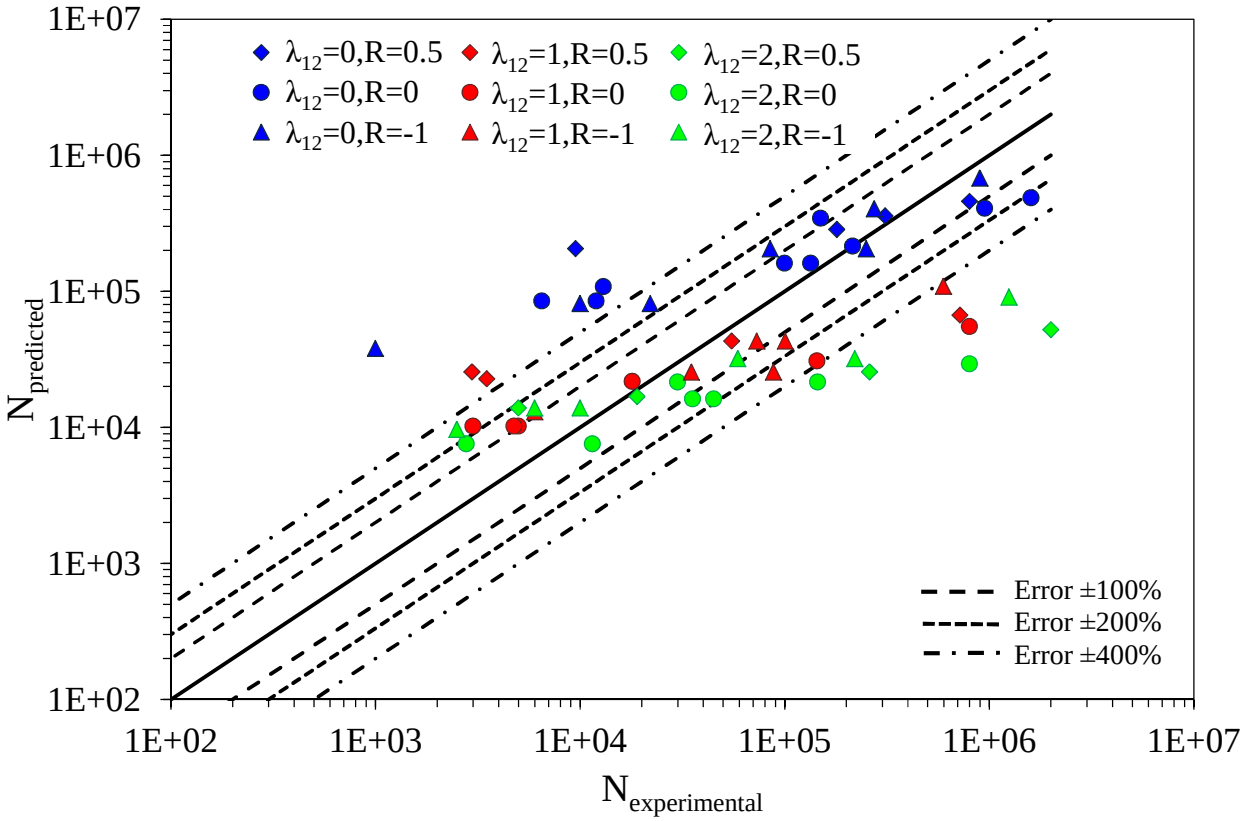

Figure 6.52 – $N_{predicted}$ vs $N_{experimental}$ for Plumtree and Cheng's model (ΔW^{*}_{tot}).

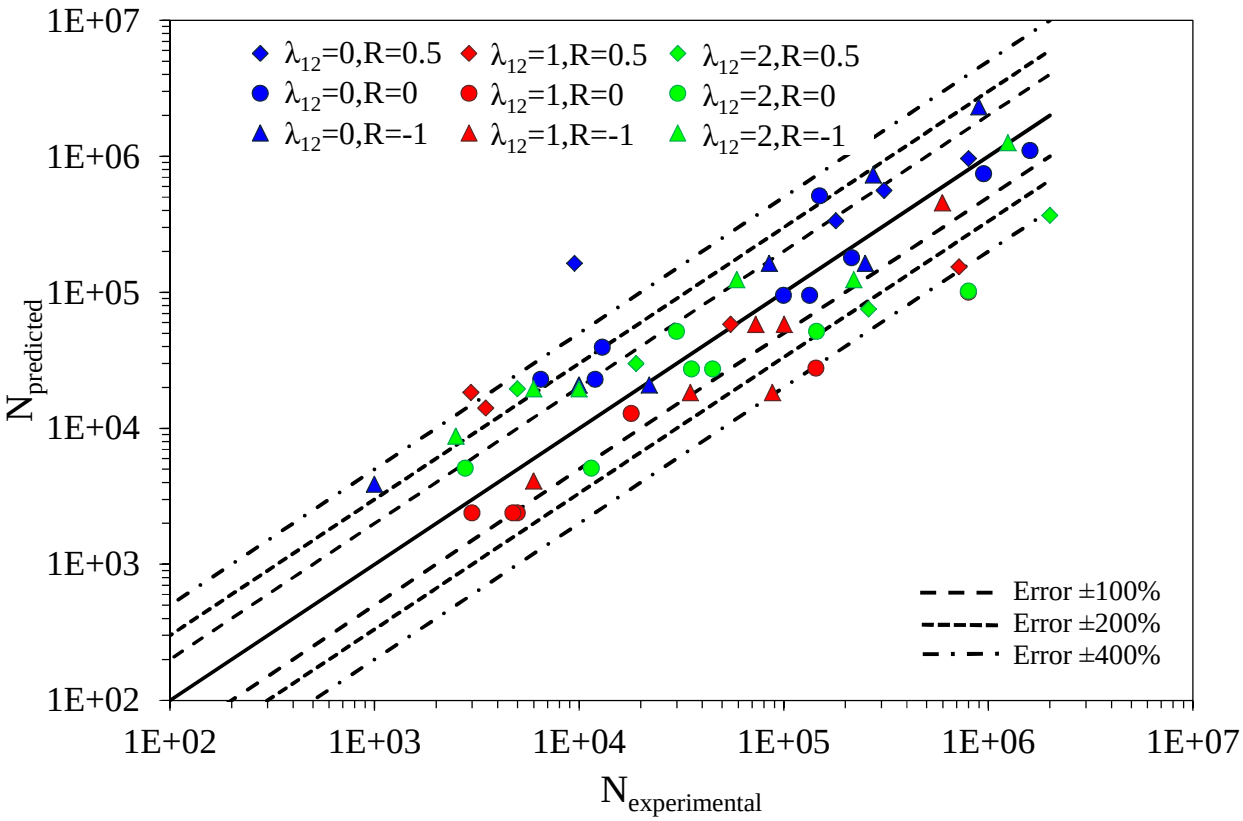

Figure 6.53 – $N_{predicted}$ vs $N_{experimental}$ for modified Plumtree and Cheng's model ($\Delta W_{tot,n}$ *).

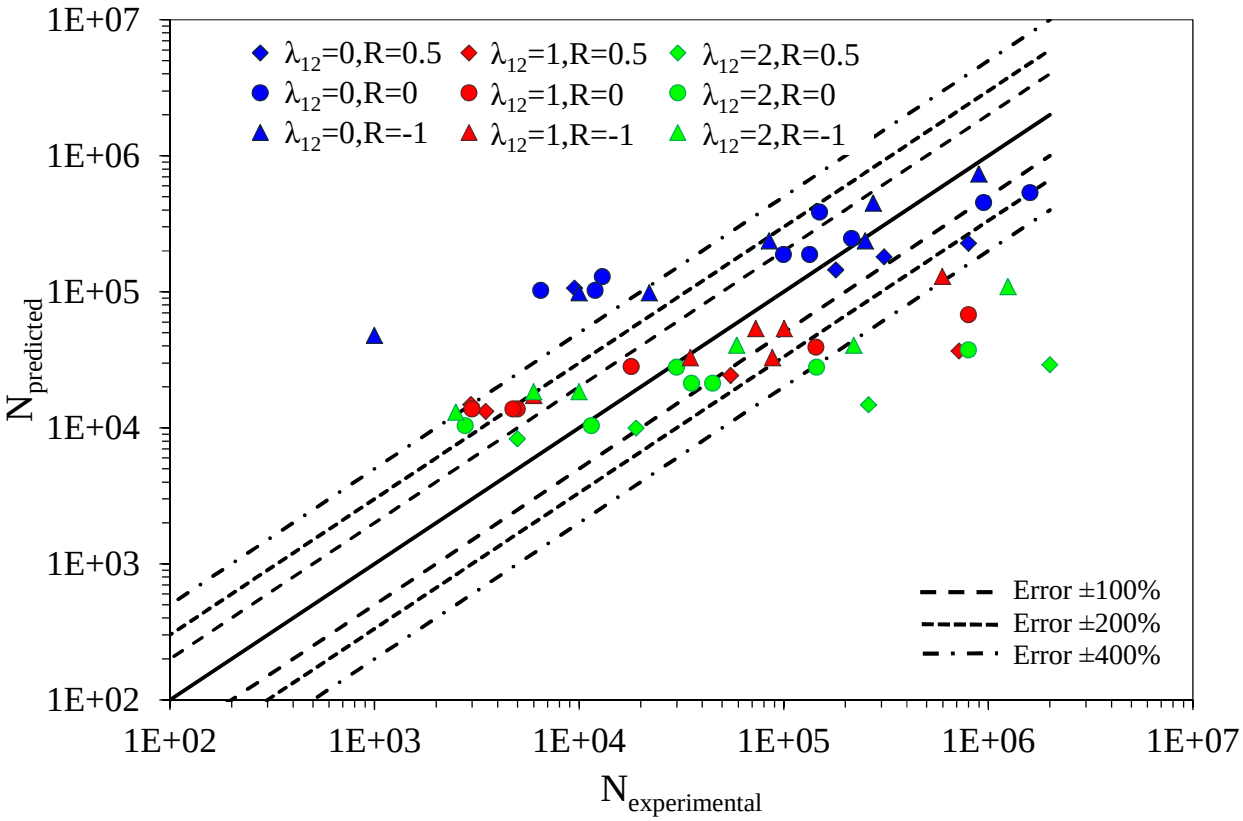

Figure 6.54 – $N_{predicted}$ vs $N_{experimental}$ for Petermann and Plumtree's model (W_{tot}^{*}).

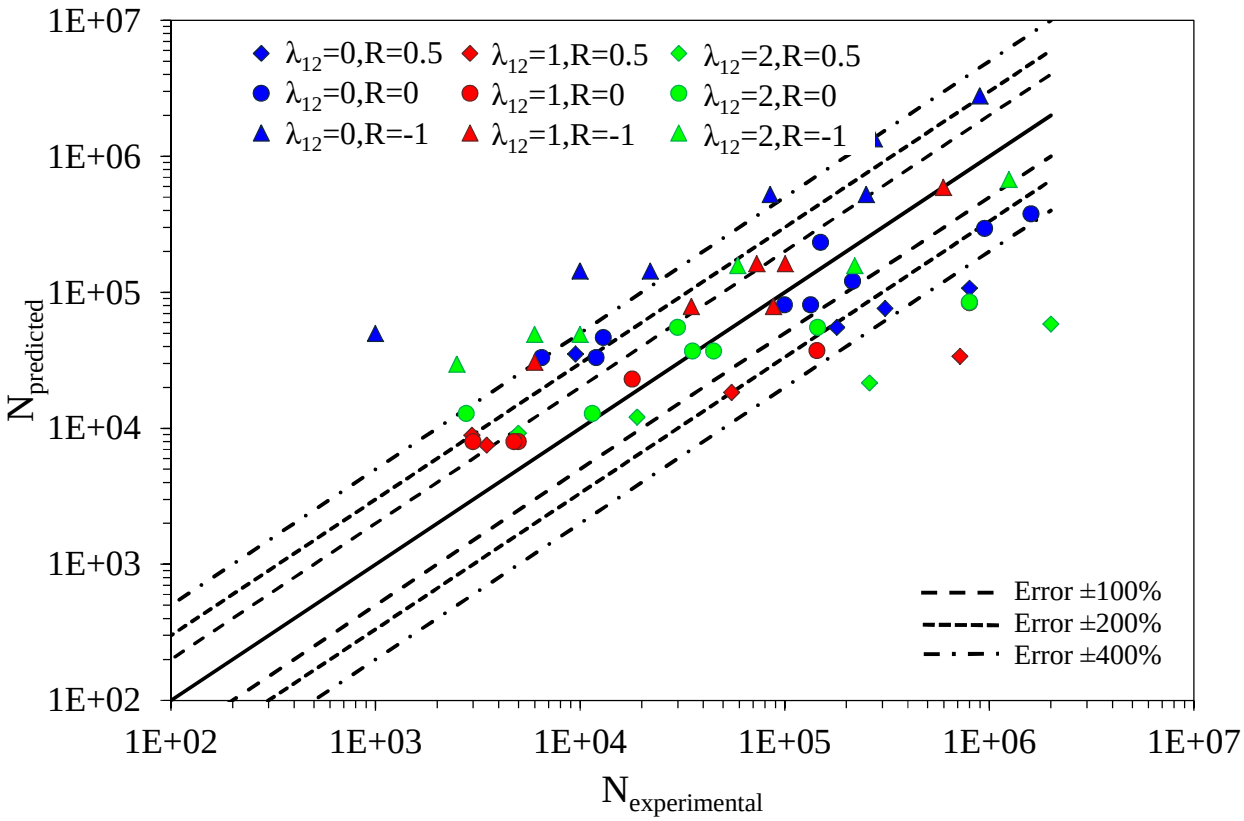

Figure 6.55 – $N_{predicted}$ vs $N_{experimental}$ for modified Petermann and Plumtree's model ($W_{tot,ntc}$ *).

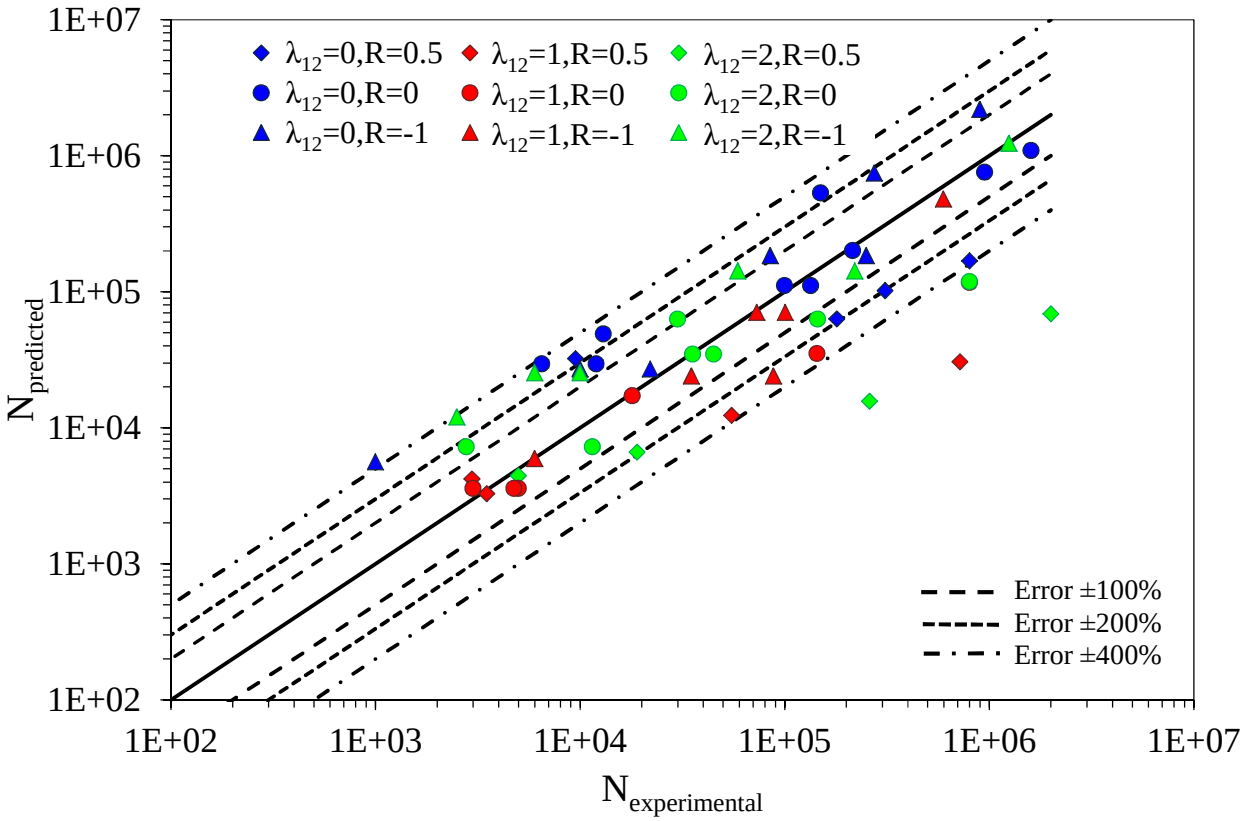

Figure 6.56 – $N_{predicted}$ vs $N_{experimental}$ for modified Petermann and Plumtree's model ($W_{tot,nt}$ *).

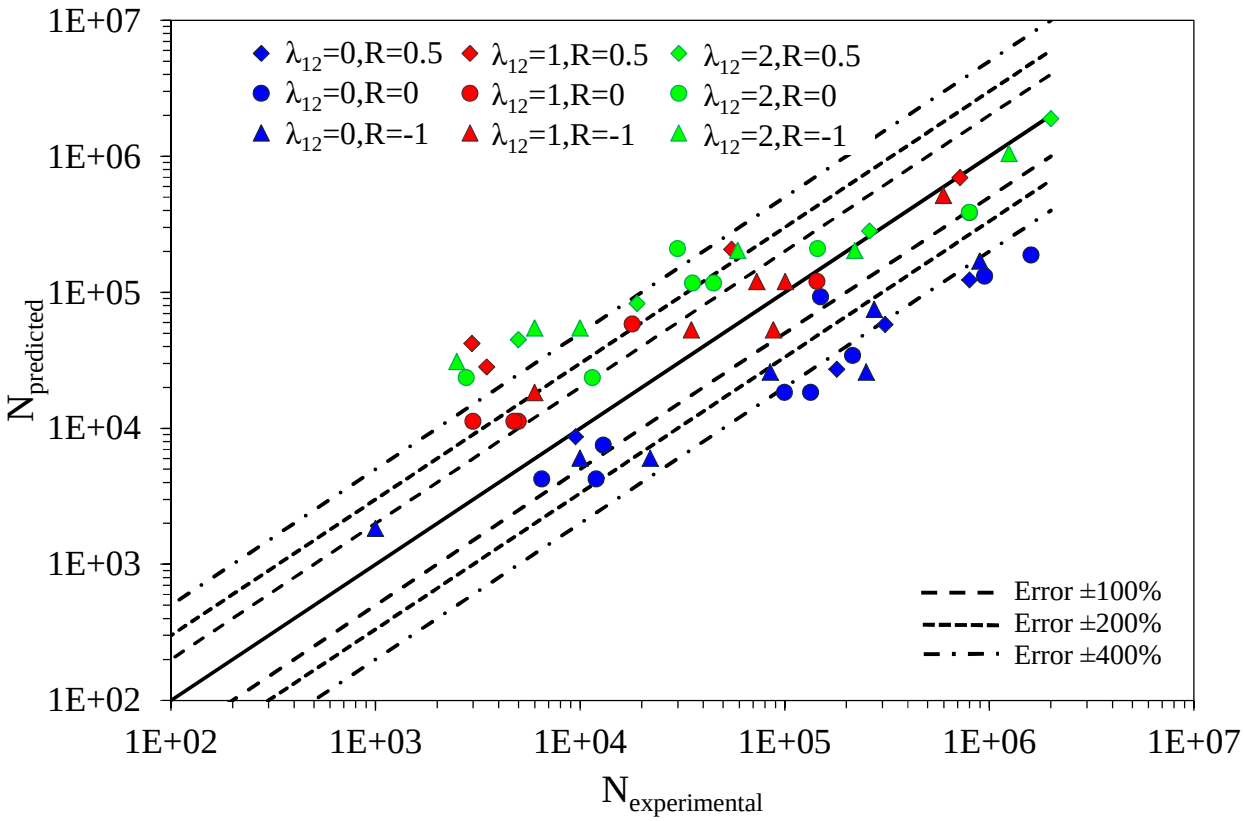

Figure 6.57 – $N_{predicted}$ vs $N_{experimental}$ for Kawai's model (Ψ_K).

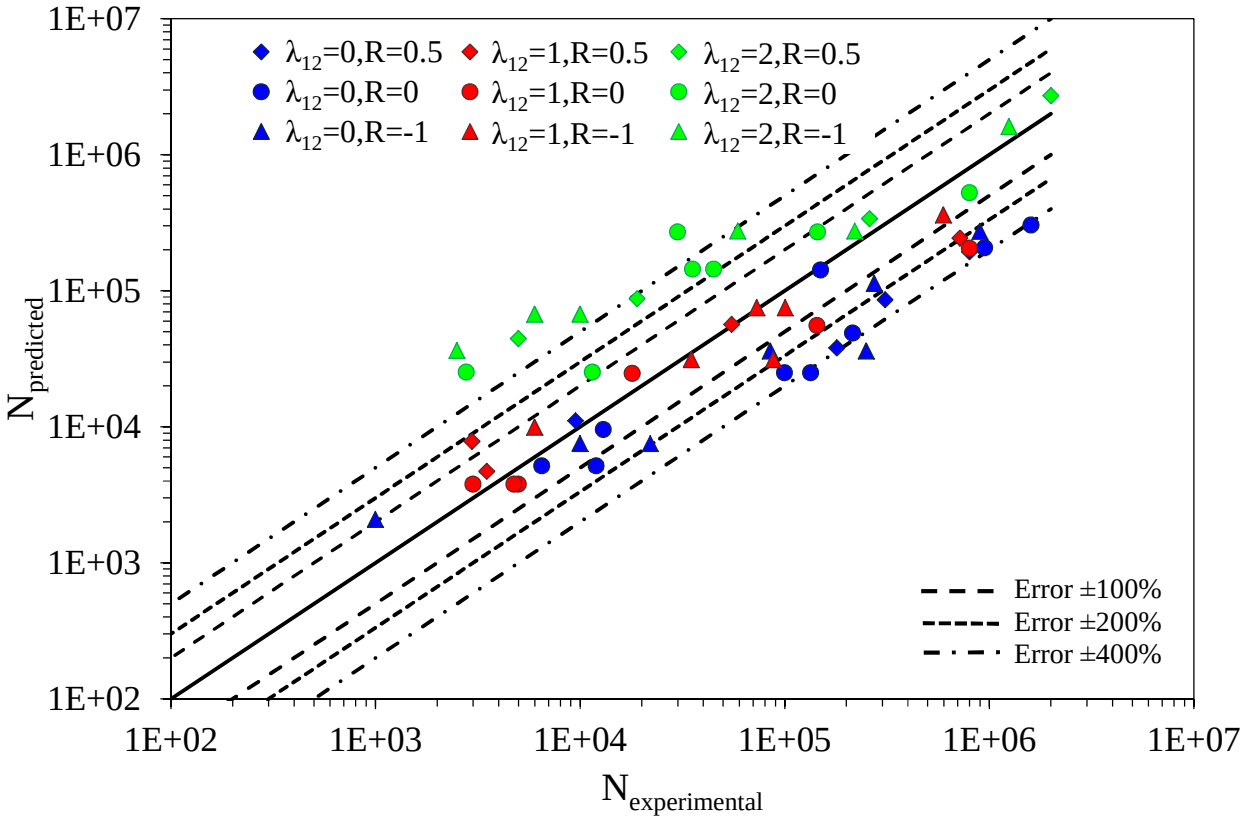

Figure 6.58 – $N_{predicted}$ vs $N_{experimental}$ for Kawai's model (Σ^*).

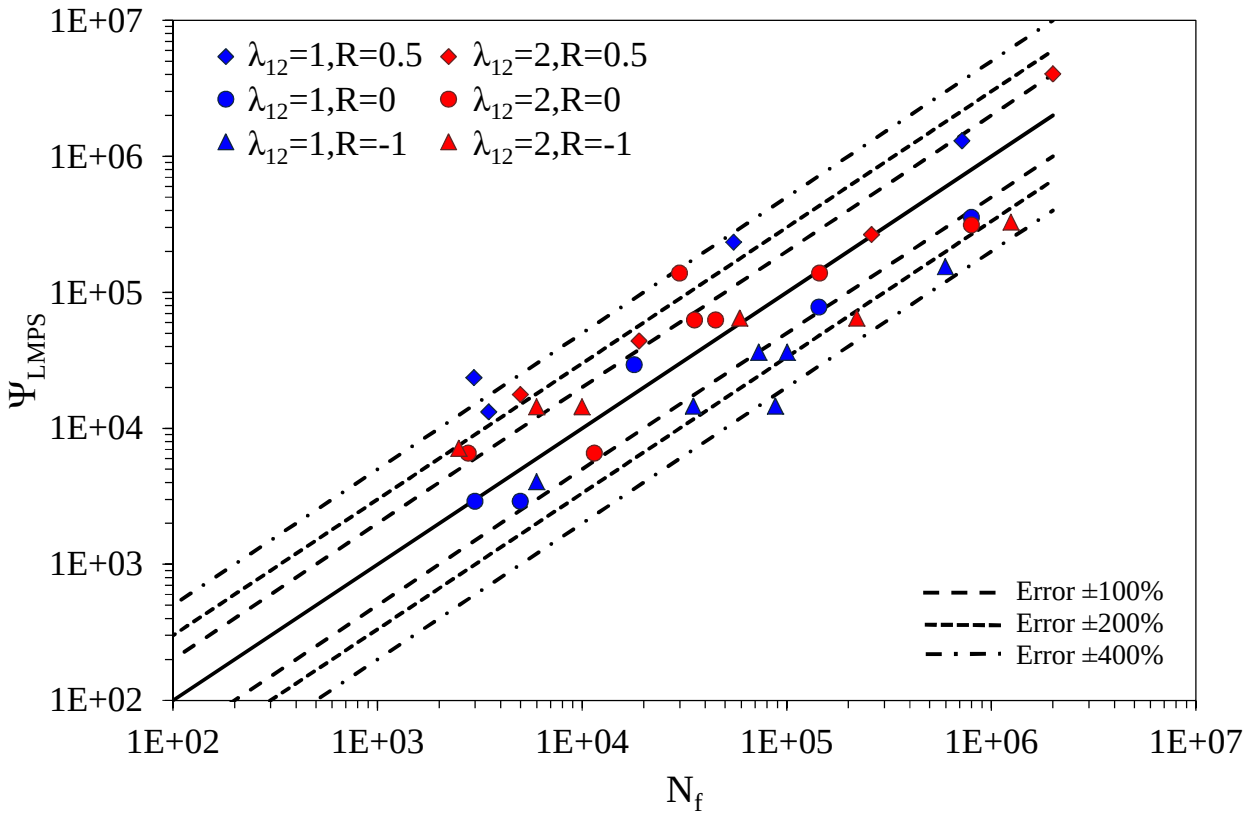

Figure 6.59 – $N_{predicted}$ vs $N_{experimental}$ for the new model (Ψ_{LMPS}).

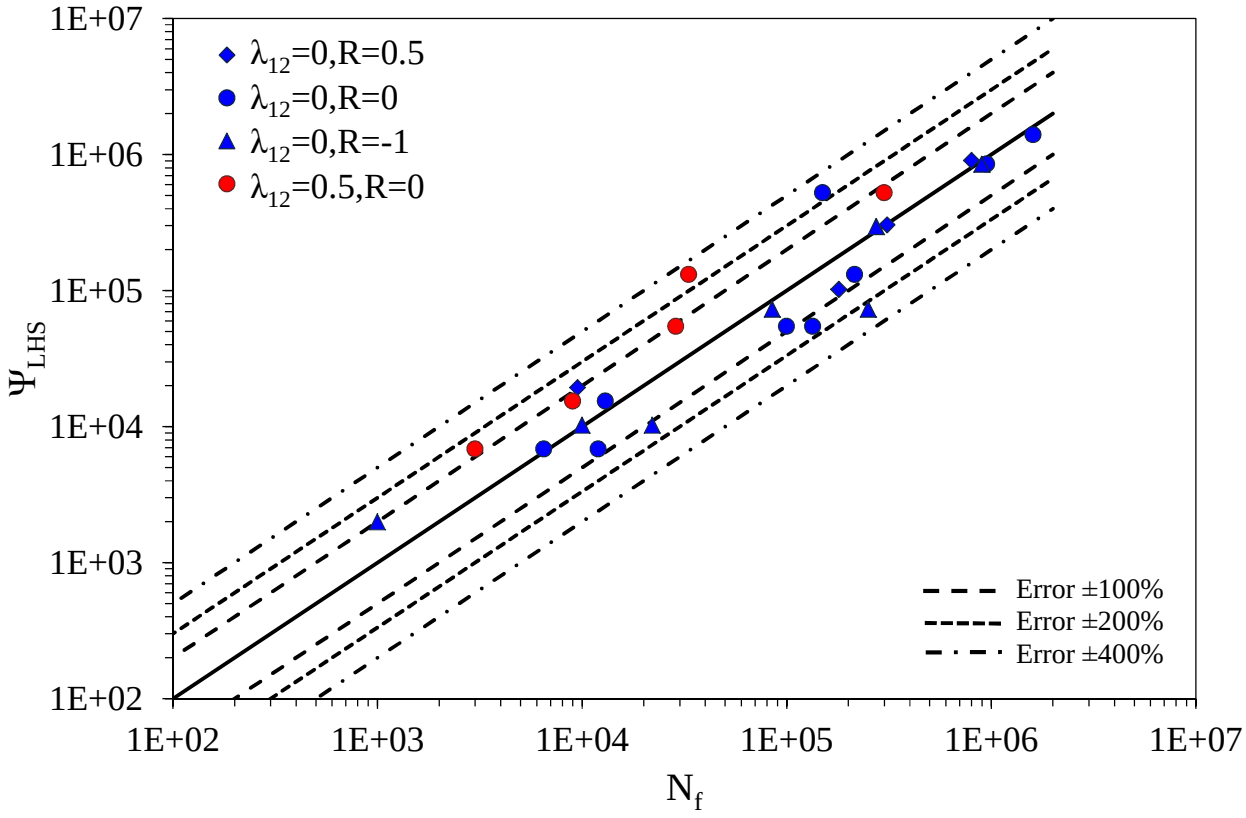

Figure 6.60 – $N_{predicted}$ vs $N_{experimental}$ for the new model (Ψ_{LHS}).

Chapter 7

Conclusions

A study on the influence of the stress ratio on the matrix-dominated fatigue behavior of composite materials was carried out in the present work, by means of an extensive experimental campaign and the analysis of several fatigue life-predicting models that take it into account.

For what concerns crack initiation, it was found that lower values of R lead to lower fatigue curves. The fact that fatigue curves are also steeper for lower R indicates that the effect of this parameter on crack initiation is larger at smaller stresses. The influence of R does not seem to vary sensibly under different multiaxiality conditions. A higher biaxiality ratio causes the fatigue curves to be lower, but it doesn't seem to have any effect on the slope of the curves.

The crack propagation is found to be faster for R = -1 and slower for larger values of R. The Paris-like curves are steeper for smaller R, indicating that the effect of this parameter on crack propagation is larger for smaller values of G_{tot}. The presence of a compressive stress seems to have a greater influence for larger values of the biaxiality ratio λ_{12}. The addition of shear causes the Paris-like curves to be shifted towards smaller values of CGR (for the same value of G_{tot}), and this is due to the presence of fibers that prevent the cracks to deviate, as they would do in presence of shear stress.

It is possible to observe from fractographic examinations that the damage mechanism appears to be the same for all values of R when $\lambda_{12} = 0$. In presence of shear stress instead the damage mode seems to remain the same for R = 0 and R = 0.5, whereas it is hard to draw conclusion for R = -1 because of the unclear separation surface that this loading condition leads to.

Different life-predicting models have been tested on the present experimental data, and evaluated by means T_σ. Of all the models found in literature, Kawai's one resulted to be the one that could collapse better all the data in a narrow band, well describing both the effect of the stress ratio and of the multiaxiality conditions. Smaller T_σ are reached with the modifications proposed to El Kadi and Ellyin's, Plumtree and Cheng's and Petermann and Plumtree's models, but the even better results are reached by the proposed new model based on the one that is being development by the Department of Management and Engineering of the University of Padova, that presents also the

advantage of having a higher reliability and generality, given the fact that it is based on damage mechanisms.

7.1 – Future developments

Possible future work in the in the analysis of the effect of the stress ratio on the multiaxial fatigue behavior of composite materials could be focused on the following topics:

1) Understand the damage mechanism in presence of a negative stress ratio, that is not clear from SEM images. This would be important for a fatigue life predicting model based on damage mechanisms.

2) Develop a model for the propagation of the cracks, in order for the damage evolution description to be more complete.

3) Find a way to express the passage from a loading condition governed by LMPS to one governed by LHS, in order to model loading conditions close to the transition.

4) Analyze the fiber dominated behavior, that is related to the final separation of a composite laminate.

Appendix

Implementation in a Matlab® code of a stiffness degradation model for cracked multidirectional laminates

The department of Managment and Engineering of the University of Padova is working on an analytical model that could relate the stiffness degradation in a composite laminate to the crack density in each layer. Given the difficulties in solving analytically the passages described in [22] the passages have been implemented in a Matlab® code, whose description follows. The full scripts can be given by the author upon request.

The program analyzes half of a symmetric laminate that can be composed by any number of layers (i.e. if the laminate is made of 7 layers, the program analyzes 4 of them, the last one having half of the thickness of the 4^{th} layer of the original laminate). In order to run this program, it is required to have Matlab® installed on the computer. An attempt to make a standalone application (i.e. an executable file, format .exe) was made, but some essential commands used in the program are not compiled by the Matlab® compiler (as all the functions of the Symbolic toolbox), therefore this option was not available. Nonetheless, a graphical user interface (GUI) was developed in order for the code to be more user-friendly and easy to use.

The version of Matlab® used for writing the code is R2010a. Tests with R2009b version showed that it works with this version as well, but no tests were made with previous versions, meaning that the compatibility with them is not guaranteed.

A.1.1 – Main window

The main window that is opened as the graphical user interface is run is shown in Figure A.1. It is possible to choose to input the data manually or from an Excel file (see paragraph A.1.2 for specifications about data input).

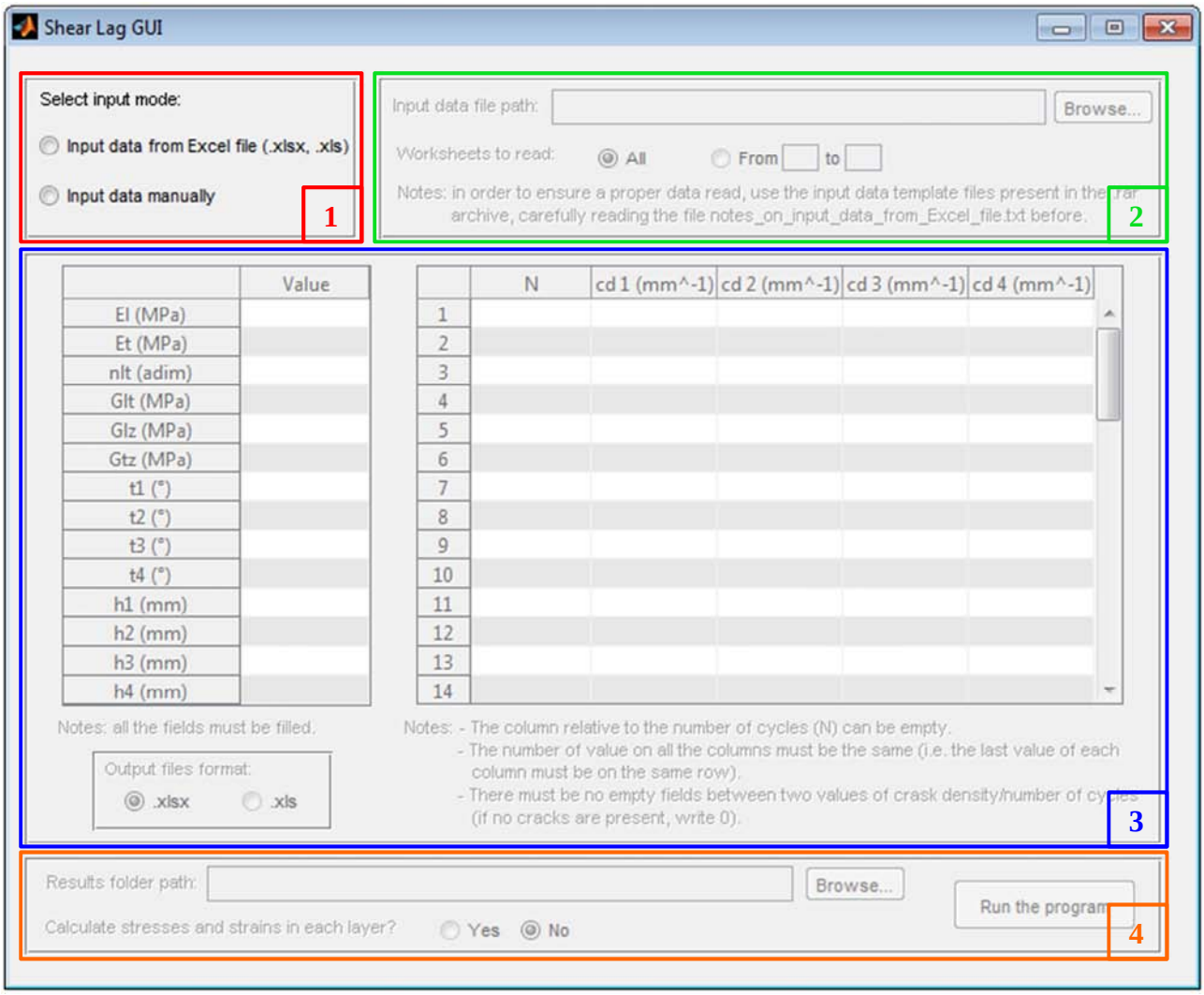

Figure A.1 – Main window as the GUI is run.

The following panels are present in the window (Figure A.1):

1– Input mode panel
2– Input from Excel file panel
3– Manual input panel
4– General settings panel

At first, the only panel enabled is the Input mode panel (1); all the others are "grey" and clicking on them has no effect. Depending on the option selected in the Input mode panel (1), the Input from Excel file panel (2) or the Manual input panel (3) becomes enabled. The General settings panel (4) becomes enabled in both cases. Figures A.2, A.3 and A.4 describes the objects present in these panels.

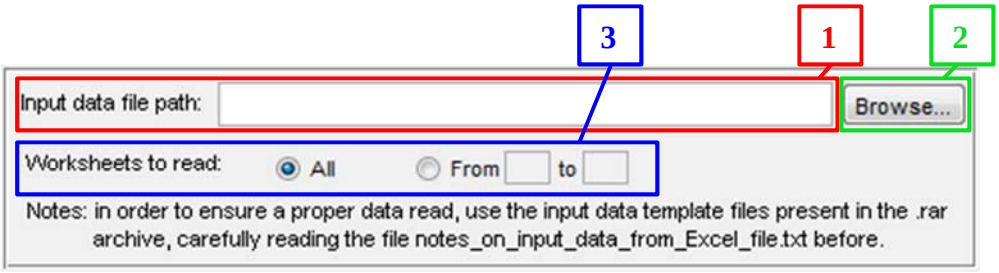

Figure A.2 – Input from Excelpanel.

The objects present in the Input data from Excel file panel are (see Figure A.2):

1 – Input data file path

2 – Browse button

3 – Worksheets to read options

In the Input data from Excel file panel, the user must indicate the path to the input file (**1**). The Browse button (**2**) allows to directly research the file. The program includes the possibility to choose between reading all the worksheets of the source file and reading only an interval of them (**3**).

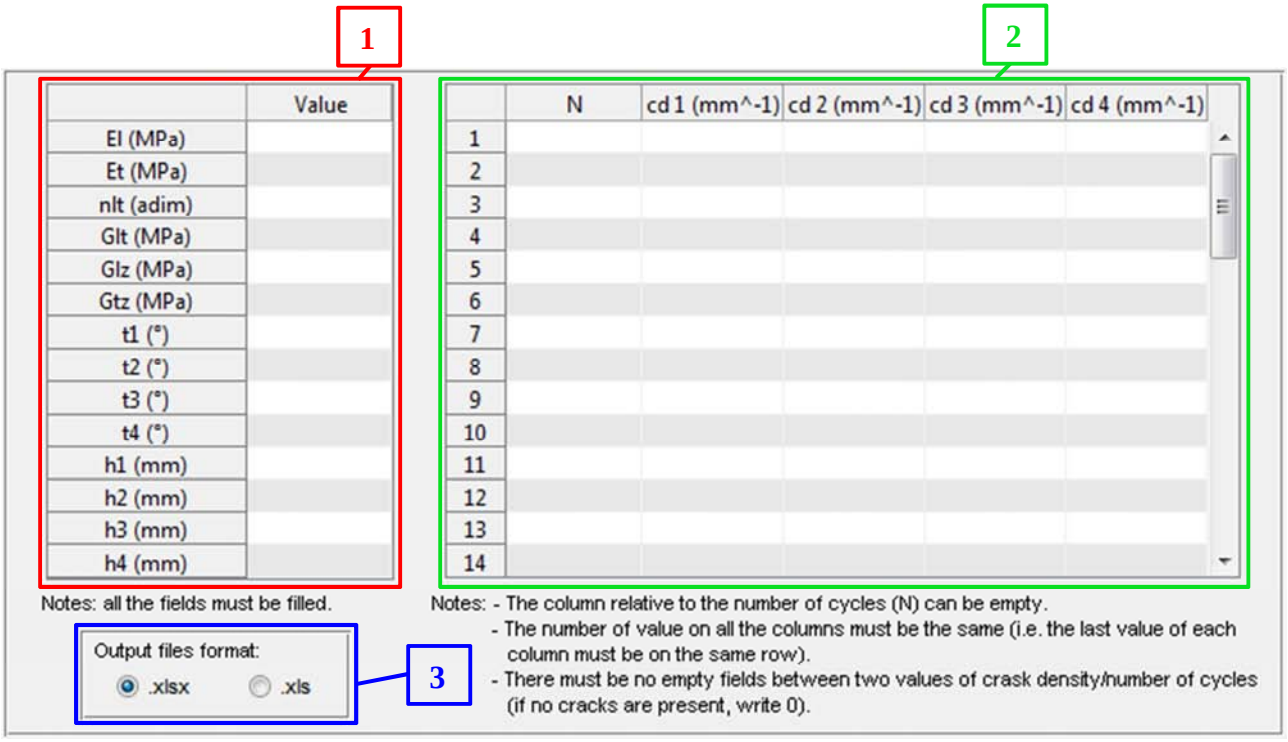

Figure A.3 – Manual input panel.

The following objects are present in the Manual input data panel (see Figure A.3):

1 – Laminate properties table

2 – Number of cycles and crack densities table

3 – Output file format options

If the manual input mode is selected, the user writes the data directly in the main window (**1** and **2**). It is possible to choose the format of the output files between .xlsx and .xls (**3**).

The objects present in the General settings panel are (see Figure A.4):

1 – Results folder path

2 – Browse button

3 – Calculate stresses and strains options

4 – Run the program button

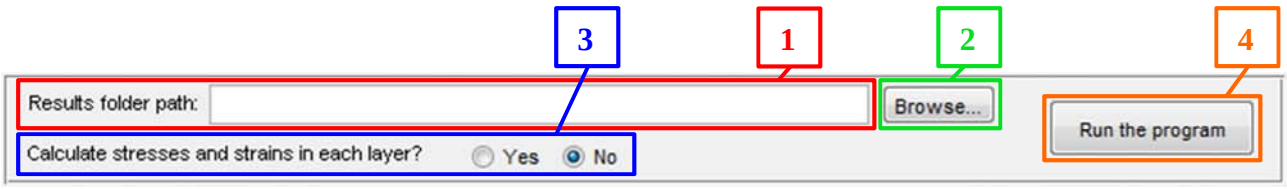

Figure A.4 – General settings panel.

The user must indicate the path to the folder in which results files and figures will be created (**1**). The Browse button (**2**) allows to directly research the folder. The user can choose if having the program calculate the stresses and strains present in each of the four layer of the laminate, relative to all the crack densities in input (**3**). These calculation sensibly heighten the time needed for the program to finish. The Run the program button (**4**), as the name suggest, launches the code that makes all the calculations.

A.1.2 – Data input

As stated in the previous paragraph, the program allows the possibility to input the needed data in two ways: by inputting them manually at the moment the program GUI is run or by directly reading an already existing Excel file.

The input data to be declared are the following:

- Elastic properties of the laminate (elastic moduli and longitudinal-transverse Possion's ratio)

- Geometrical properties of the laminate (off-axis angles and thicknesses for all the layers)
- Crack densities on each layer
- Number of cycles corresponding to the crack densities (optional)

The point corresponding to N = 0, in which all the cd are equal to zero and all the elastic properties of the laminate are equal to its nominal ones, is automatically added by the program in the outputs (even in the case that N data are not given in input), therefore there is no need to write data relative to this condition in input.

A.1.2.1 – Input data from Excel file

A template is given in order for the data to be read correctly by the program, which is reported in Figure A.5.

ELASTIC AND GEOMETRICAL PROPERTIES

	Property	Value
	El (MPa)	
	Et (MPa)	
	nlt (adim)	
	Glt (MPa)	
	Glz (MPa)	
	Gtz (MPa)	
	off-axis angle (°)	thickness (mm)
layer 1		
layer 2		
layer 3		
layer 4		
layer 5		
layer 6		
layer 7		
layer 8		
layer 9		
layer 10		
...		

NUMBER OF CYCLES (N) AND CRACK DENSITIES (cd)

N	cd 1 (mm^-1)	cd 2 (mm^-1)	cd 3 (mm^-1)	cd 4 (mm^-1)	cd 5 (mm^-1)	cd 6 (mm^-1)	cd 7 (m

Figure A.5 – Excel file template for data input.

The following notes are to be respected in using the input data template:

- All the laminate properties must be assigned a value.
- The columns relative to the number of cycles (N) and to the crack densities (cd) can include any number of values.
- The column relative to the number of cycles can be left empty.
- The number of values in the crack densities columns and in the number of cycles column (if it's not empty) must be the same (i.e. the last values of these columns must be in the same row).
- There must be no empty fields between two values of crack density or number of cycles.

(if no cracks are present, assign cd = 0).

Values of crack density equal to 0 will be automatically changed by the program to 0.001, in order to avoid the presence of singular matrices during the calculations.

A.1.2.2 – Manual input data

If it is chosen to input the data manually, the fields to be filled are present in the GUI main window (Figure A.3). The notes to be followed in inputting the data are the same as the input from Excel file (even the one concerning cd = 0), with the following differences:

- It is possible to analyze only a symmetric laminate made of seven layers (configuration found in many works in literature)
- A maximum of 50 values of number of cycles and crack densities is allowed.

A.1.3 – Program progress window

When launched, the program creates a window in which its progress state is displayed, which is shown in Figure A.6. It was chosen to create this window because the program may take a considerable time before finishing, and in this way the user can check what the program is doing. The steps shown in this window are:

- The combination of cracked layer, external stress state ({100}, {010} or {001}) and crack density that is being analyzed.
- The saving of the figures of *elastic properties* vs *crack density* to the chosen folder.
- The saving of the figures of *stresses and strains* vs *length between two cracks* to the chosen folder (if the option for their calculation was selected)
- The printing of the elastic properties results to the relative output Excel file.
- The printing of the stresses and strains results to the relative output Excel file.
- The termination of the program.

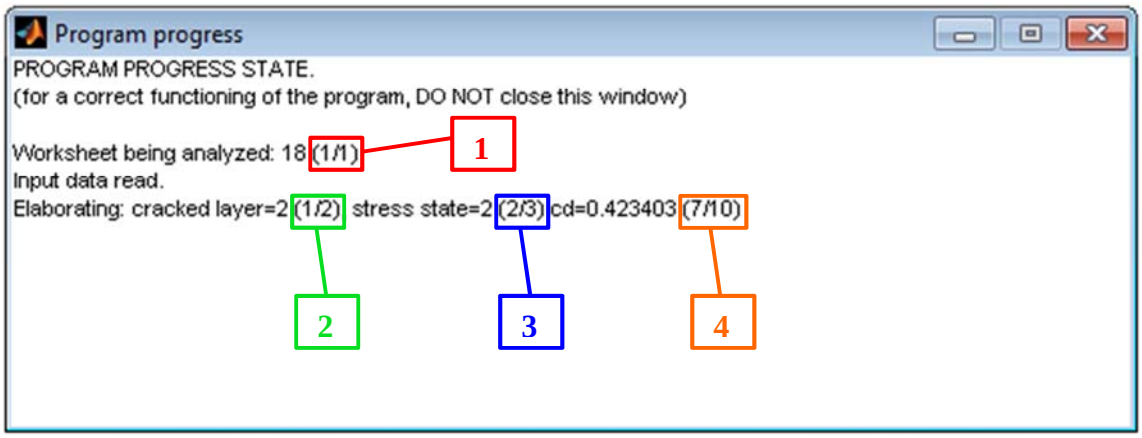

Figure A.6 – Program progress window.

When the program is displaying the combination of cracked layer, external stress state and crack density that is being analyzed, is also shows how many combinations are left, to help the user understand at what point the program is and so as he/she can be sure that the program is running: referring to Figure A.6, the numbers are to be read in the following way:

1– number of the worksheet being analyzed on total number of worksheet to be analyzed (it remains also when the other steps listed above are displayed)
2 – number of cracked layer being analyzed on total number of cracked layers to be analyzed in that worksheet.
3 – number of external stress state (1, 2 and 3 stands respectively for {100}, {010}, {001}).
4 – number of crack density being analyzed on total number of crack densities to be analyzed in that worksheet.

When the calculations of stresses and strains option is selected, it is displayed the number of the last figure saved on the total number of figures to elaborate.
When the progress window is displayed, it disable clicking on other Matlab® windows. In order to avoid this, it is sufficient to press ctrl+c. The same shortcut, pressed on the Matlab® command window, interrupt the execution of the program.

A.1.4 – Output files

The following files are written in output by the program. They are all saved to the selected results folder.

A.1.4.1 – results_elpropr_(inputfilename)

results_elpropr_(inputfilename) is an Excel file containing the calculated elastic properties of the laminate as a function of the number of cycles (N) or – in case no number of cycles is inputted – as a function of the crack density of the first cracked layer. In the case that the data were inputted manually, the "input file name" will be "Manual input".

The properties calculated are normalized respect to their value with no cracks present, with the exception of the normal stress – shear stress coupling coefficients, in order not to obtain infinite values of these parameters in the case that their initial value is zero (i.e the properties displayed are E_x/E_{xi}, E_y/E_{yi}, G_{xy}/G_{xyi}, ν_{xy}/ν_{xyi}, ν_{yx}/ν_{yxi}, $s_{x\text{-}xy}$, $s_{y\text{-}xy}$).

The properties are calculated separately for each cracked layer, and also considering the simultaneous presence of all the cracked layers, both with and without taking into account the interactions between cracks present on different layers.

The worksheet in which the elastic properties results are written is the same as the one read by the program for data input. Note that it is possible, in this way, to make the calculation, for example, for the first three worksheets of an Excel file, close Matlab®, and when the program is run again for the remaining worksheets, the results can be added to the same results_elpropr_(inputfilename) file already existing. Moreover, since the name of this output file depends on the name of the data input file, it is possible to save in the same folder the results of different input files without any overwriting. If data are inputted manually, the results will be written on the first worksheet of this file, and the "inputfilename" will be "manual input".

The format of this output file can be .xlsx or .xls. In case that the data is inputted from an Excel file, the format is the same as the input file. In case of manual data input, the user can choose if create this file in .xlsx or .xlsformat from the Main window. Figure A.7 shows part of a worksheet of the output file results_elpropr_(inputfilename).

Cracked layer: 4							
N	Ex/Exi	Ey/Eyi	Gxy/Gxyi	nxy/nxyi	nyx/nyxi	sx-xy	sy-xy
0	1	1	1	1	1	-2.7E-20	-2.4E-19
1400	0.971058	0.983861	0.986217	0.99922	0.983707	5.79E-07	1.26E-06
11700	0.944752	0.970738	0.973062	0.999827	0.968641	1.08E-06	2.48E-06
23700	0.936856	0.967649	0.968963	1.000812	0.964177	1.21E-06	2.86E-06
34200	0.936856	0.967649	0.968963	1.000812	0.964177	1.21E-06	2.86E-06
79200	0.936856	0.967649	0.968963	1.000812	0.964177	1.21E-06	2.86E-06
109200	0.936856	0.967649	0.968963	1.000812	0.964177	1.21E-06	2.86E-06
199200	0.936856	0.967649	0.968963	1.000812	0.964177	1.21E-06	2.86E-06
304200	0.92945	0.965252	0.965056	1.002229	0.960053	1.31E-06	3.21E-06
401700	0.922547	0.963503	0.961354	1.004033	0.95627	1.39E-06	3.55E-06
491700	0.922547	0.963503	0.961354	1.004033	0.95627	1.39E-06	3.55E-06

Cracks on layers: 2 4														
N	Ex/Exi no	Ex/Exi wit	Ey/Eyi no	Ey/Eyi wit	Gxy/Gxyi	Gxy/Gxyi	nxy/nxyi r	nxy/nxyi	nyx/nyxi r	nyx/nyxi	sx-xy no i	sx-xy with	sy-xy no i	sy-xy with interaction
0	1	1	1	1	1	1	1	1	1	1	-2.7E-20	-2.7E-20	-2.4E-19	-2.4E-19
1400	0.971058	0.971058	0.986217	0.986217	0.983707	0.983707	0.986987	0.983861	0.986987	0.99922	5.79E-07	5.79E-07	1.26E-06	1.26E-06
11700	0.944752	0.944752	0.973062	0.973062	0.968641	0.968641	0.97323	0.970738	0.97323	0.999827	1.08E-06	1.08E-06	2.48E-06	2.48E-06
23700	0.920601	0.921102	0.961053	0.96126	0.954781	0.95506	0.961095	0.964168	0.961095	1.000614	8.8E-07	9.89E-07	2.13E-06	2.12E-06
34200	0.904927	0.906601	0.953352	0.953996	0.945716	0.946611	0.953913	0.956555	0.953913	1.000475	5.62E-07	6.19E-07	1.42E-06	1.42E-06
79200	0.899852	0.90185	0.950867	0.951653	0.942828	0.943929	0.951423	0.954078	0.951423	1.000638	4.62E-07	4.95E-07	1.19E-06	1.19E-06
109200	0.889971	0.892512	0.946047	0.947108	0.937309	0.938808	0.946252	0.949423	0.946252	1.001361	2.73E-07	2.57E-07	7.46E-07	7.5E-07
199200	0.88052	0.883478	0.941441	0.942755	0.932158	0.934033	0.940806	0.945337	0.940806	1.002634	1.05E-07	3.75E-08	3.23E-07	3.34E-07
304200	0.873115	0.876495	0.937534	0.939044	0.928034	0.930176	0.935539	0.942996	0.935539	1.004287	2.07E-07	1.59E-07	6.8E-07	6.88E-07
401700	0.861678	0.865627	0.931613	0.933461	0.921819	0.924432	0.927299	0.939314	0.927299	1.007239	2.11E-07	1.57E-07	8.12E-07	8.22E-07
491700	0.857287	0.861422	0.929447	0.931443	0.919485	0.92231	0.924414	0.937617	0.924414	1.00827	1.43E-07	6.33E-08	6.15E-07	6.29E-07

Figure A.7– Part of a worksheet of a typical output file results_elpropr_(inputfilename).

A.1.4.2 – results_ss_(worksheetname)

If the option to calculate stresses and strains is selected (Figure A.4, object number 3), the program calculates the stresses and strains in each layer as a function of cracked layer, external stress state ({100}, {010} or {001}), crack density of the cracked layer, and the coordinate x2 normal to the fibers of the cracked layer.

Given the great quantity of stresses and strains ("ss" denotes stresses and strains) data that are calculated, the program creates for them to be written a separate Excel file for each worksheet read as input. The name of each of these output files contains the name of the relative input worksheet, in order for them to be easily identified. If data were inputted manually, the "worksheet name" will be "manual input".

In each file, a worksheet is created for any combination of cracked layer, external stress state and layer in which the stresses and strains have been calculated. In each worksheet, the values of the stresses and strains are calculated as a function of the coordinate x2 for each value of crack density of that certain cracked layer. The simultaneous presence of cracks on more than one layer is not considered for this analysis.

The format of this output file can be .xlsx or .xls, as explained above for the file output_elpropr_(inputfilename). In Figure A.8 is reported part of the output file results_ss_(worksheetname). Each x2 column is to be paired with the column at its right

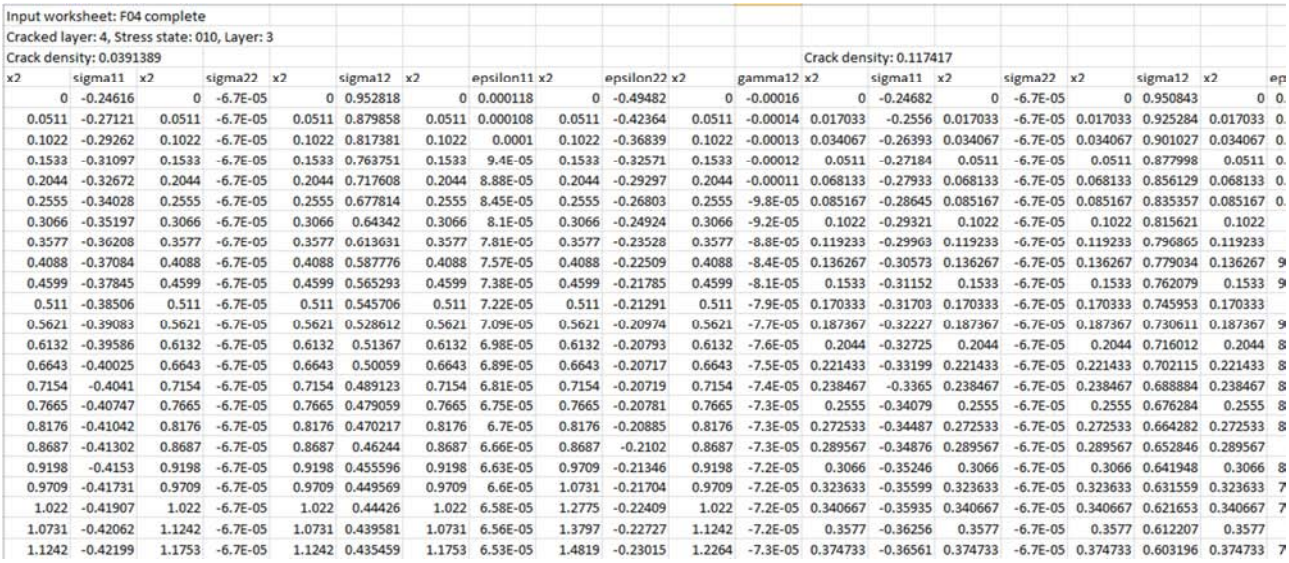

Input worksheet: F04 complete																			
Cracked layer: 4, Stress state: 010, Layer: 3																			
Crack density: 0.0391389												Crack density: 0.117417							
x2	sigma11	x2	sigma22	x2	sigma12	x2	epsilon11	x2	epsilon22	x2	0	gamma12	x2	0	sigma11	x2	0	sigma22	x2	0	sigma12	x2	0	ep
0	-0.24616	0	-6.7E-05	0	0.952818	0	0.000118	0	-0.49482	0	-0.00016	0	-0.24682	0	-6.7E-05	0	0.950843	0	0.
0.0511	-0.27121	0.0511	-6.7E-05	0.0511	0.879858	0.0511	0.000108	0.0511	-0.42364	0.0511	-0.00014	0.017033	-0.2556	0.017033	-6.7E-05	0.017033	0.925284	0.017033	0.
0.1022	-0.29262	0.1022	-6.7E-05	0.1022	0.817381	0.1022	0.0001	0.1022	-0.36839	0.1022	-0.00013	0.034067	-0.26393	0.034067	-6.7E-05	0.034067	0.901027	0.034067	0.
0.1533	-0.31097	0.1533	-6.7E-05	0.1533	0.763751	0.1533	9.4E-05	0.1533	-0.32571	0.1533	-0.00012	0.0511	-0.27184	0.0511	-6.7E-05	0.0511	0.877998	0.0511	0.
0.2044	-0.32672	0.2044	-6.7E-05	0.2044	0.717608	0.2044	8.88E-05	0.2044	-0.29297	0.2044	-0.00011	0.068133	-0.27933	0.068133	-6.7E-05	0.068133	0.856129	0.068133	0.
0.2555	-0.34028	0.2555	-6.7E-05	0.2555	0.677814	0.2555	8.45E-05	0.2555	-0.26803	0.2555	-9.8E-05	0.085167	-0.28645	0.085167	-6.7E-05	0.085167	0.835357	0.085167	0.
0.3066	-0.35197	0.3066	-6.7E-05	0.3066	0.64342	0.3066	8.1E-05	0.3066	-0.24924	0.3066	-9.2E-05	0.1022	-0.29321	0.1022	-6.7E-05	0.1022	0.815621	0.1022	
0.3577	-0.36208	0.3577	-6.7E-05	0.3577	0.613631	0.3577	7.81E-05	0.3577	-0.23528	0.3577	-8.8E-05	0.119233	-0.29963	0.119233	-6.7E-05	0.119233	0.796865	0.119233	
0.4088	-0.37084	0.4088	-6.7E-05	0.4088	0.587776	0.4088	7.57E-05	0.4088	-0.22509	0.4088	-8.4E-05	0.136267	-0.30573	0.136267	-6.7E-05	0.136267	0.779034	0.136267	9
0.4599	-0.37845	0.4599	-6.7E-05	0.4599	0.565293	0.4599	7.38E-05	0.4599	-0.21785	0.4599	-8.1E-05	0.1533	-0.31152	0.1533	-6.7E-05	0.1533	0.762079	0.1533	9
0.511	-0.38506	0.511	-6.7E-05	0.511	0.545706	0.511	7.22E-05	0.511	-0.21291	0.511	-7.9E-05	0.170333	-0.31703	0.170333	-6.7E-05	0.170333	0.745953	0.170333	
0.5621	-0.39083	0.5621	-6.7E-05	0.5621	0.528612	0.5621	7.09E-05	0.5621	-0.20974	0.5621	-7.7E-05	0.187367	-0.32227	0.187367	-6.7E-05	0.187367	0.730611	0.187367	9
0.6132	-0.39586	0.6132	-6.7E-05	0.6132	0.51367	0.6132	6.98E-05	0.6132	-0.20793	0.6132	-7.6E-05	0.2044	-0.32725	0.2044	-6.7E-05	0.2044	0.716012	0.2044	8
0.6643	-0.40025	0.6643	-6.7E-05	0.6643	0.50059	0.6643	6.89E-05	0.6643	-0.20717	0.6643	-7.5E-05	0.221433	-0.33199	0.221433	-6.7E-05	0.221433	0.702115	0.221433	8
0.7154	-0.4041	0.7154	-6.7E-05	0.7154	0.489123	0.7154	6.81E-05	0.7154	-0.20719	0.7154	-7.4E-05	0.238467	-0.3365	0.238467	-6.7E-05	0.238467	0.688884	0.238467	8
0.7665	-0.40747	0.7665	-6.7E-05	0.7665	0.479059	0.7665	6.75E-05	0.7665	-0.20781	0.7665	-7.3E-05	0.2555	-0.34079	0.2555	-6.7E-05	0.2555	0.676284	0.2555	8
0.8176	-0.41042	0.8176	-6.7E-05	0.8176	0.470217	0.8176	6.7E-05	0.8176	-0.20885	0.8176	-7.3E-05	0.272533	-0.34487	0.272533	-6.7E-05	0.272533	0.664282	0.272533	8
0.8687	-0.41302	0.8687	-6.7E-05	0.8687	0.46244	0.8687	6.66E-05	0.8687	-0.2102	0.8687	-7.3E-05	0.289567	-0.34876	0.289567	-6.7E-05	0.289567	0.652846	0.289567	
0.9198	-0.4153	0.9198	-6.7E-05	0.9198	0.455596	0.9198	6.63E-05	0.9709	-0.21346	0.9198	-7.2E-05	0.3066	-0.35246	0.3066	-6.7E-05	0.3066	0.641948	0.3066	8
0.9709	-0.41731	0.9709	-6.7E-05	0.9709	0.449569	0.9709	6.6E-05	1.0731	-0.21704	0.9709	-7.2E-05	0.323633	-0.35599	0.323633	-6.7E-05	0.323633	0.631559	0.323633	7
1.022	-0.41907	1.022	-6.7E-05	1.022	0.44426	1.022	6.58E-05	1.2775	-0.22409	1.022	-7.2E-05	0.340667	-0.35935	0.340667	-6.7E-05	0.340667	0.621653	0.340667	7
1.0731	-0.42062	1.1242	-6.7E-05	1.0731	0.439581	1.0731	6.56E-05	1.3797	-0.22727	1.1242	-7.2E-05	0.3577	-0.36256	0.3577	-6.7E-05	0.3577	0.612207	0.3577	
1.1242	-0.42199	1.1753	-6.7E-05	1.1242	0.435459	1.1753	6.53E-05	1.4819	-0.23015	1.2264	-7.3E-05	0.374733	-0.36561	0.374733	-6.7E-05	0.374733	0.603196	0.374733	7

Figure A.8– Part of a worksheet of a typical output file results_ss_(worksheetname).

A.1.4.3 – Output figures

Several figures are elaborated by the program, both for elastic properties and for the stresses and strains. The name assigned to these figures allows a quick identification of the data they contain. An explanation of how the figure name has to be read follows:

- Elastic properties figures:

Figure name example: F04 complete_elpropr_vs_cd_cl2.fig

1 – worksheet name ("Manual input" in case of data inputted manually).

2 – denotes elastic properties against crack density.

3 – number correspondent to the cracked layer ("cl"). When multiple cracked layer are considered simultaneously, all the cracked layers are included in the figure file name (ex: (…)_cl24.fig if cracks are present on layers 2 and 4).

4 – figure extension (.fig is the standard format for Matlab® figures).

Figure A.9 and A.10 show examples of the elastic properties figures elaborated by the program. In order not to leave doubt in the interpretation of the symbols, they are all described in Table A.1. The coefficient sy-xy is not reported in the figures in order to have a better readability of the other – plotted – parameters. Its values are anyway calculated by the program, and written in the output file results_elprpor_(inputfilename) (see paragraph A.1.4.1). These output figures include the calculated points (circles) and, in the case that the number of cycles (N) is not given in input, also a regression polynomial of fifth grade. It was decided not to calculate this polynomial when the number of

cycles are inputted because in this case it does not always manage to acceptably describe the trend of the calculated points.

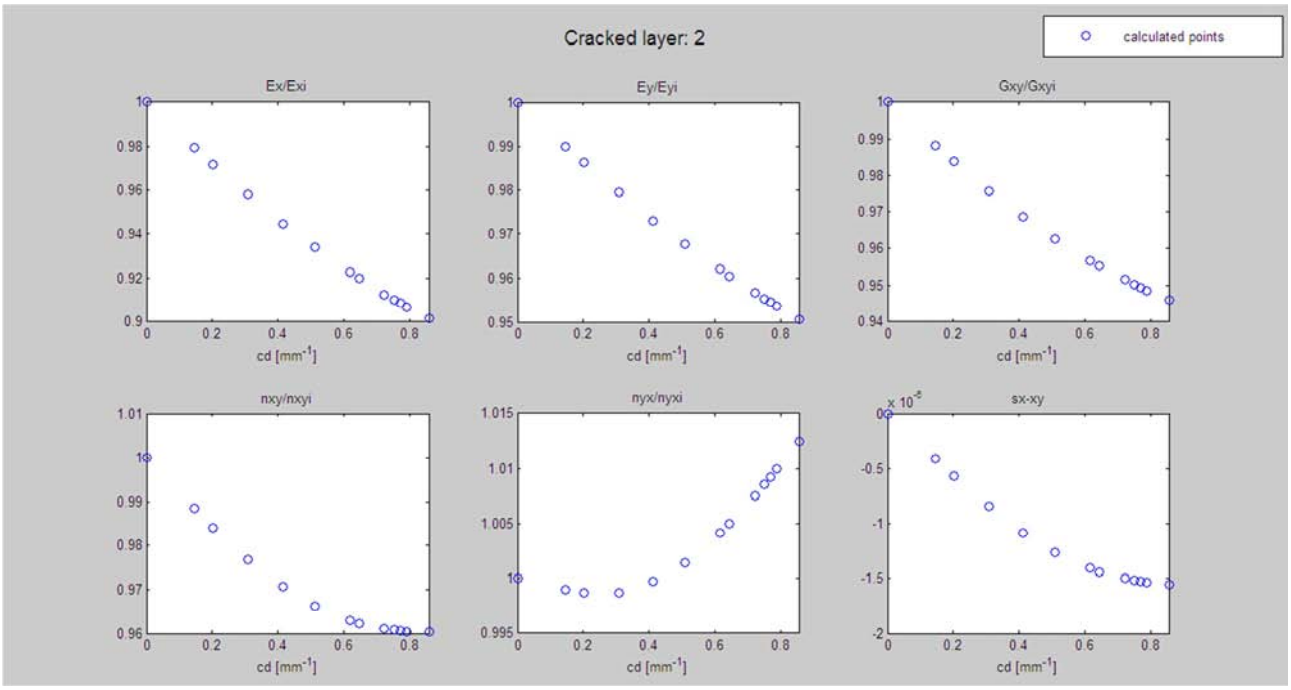

Figure A.9 – Example of elastic properties output figure for one cracked layer.

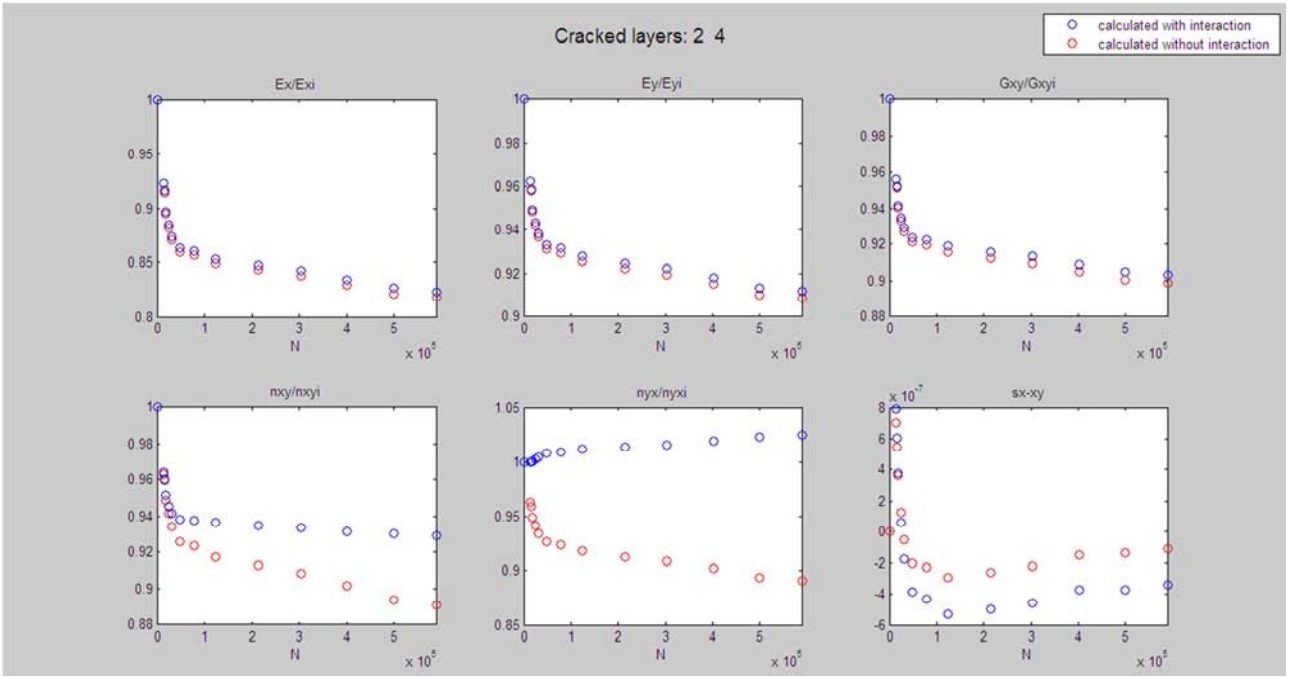

Figure A.10 – Example of elastic properties output figure for multiple cracked layers.

Symbol	Meaning
Ex	Young's modulus in the direction of the applied load.
Ey	Young's modulus in the transverse direction respect to the applied load, in the laminate's plane.
Gxy	In-plane shear modulus.
nxy	Poisson's x-y coefficient.
nyx	Poisson's y-x coefficient.
sx-xy	Normal stress in x-direction – in plane shear stress coupling coefficient.
cd	Crack density in the cracked layer reported on the top of the figure.
The letter i in the figure denotes the initial properties of the laminate, when no cracks are present.	

Table A.1 – Meaning of the symbols present in the elastic properties figures.

- Stresses and strains figures:

Figure name example: F04 complete_ss_vs_x2_cl4_010_layer3.fig

1 – worksheet name ("Manual input" in case of data inputted manually).

2 – denotes stresses and strains against coordinate x2.

3 – number correspondent to the cracked layer ("cl").

4 – external stress state (ex: 010 corresponds to {010})

5 – number of layer in which stresses and strains are calculated

6 – figure format (.fig is the standard format for Matlab® figures)

Figure A.11 shows a typical stresses and strains output figure. In the legend are reported the values of the crack densities and the correspondent value of length between two crack (l = 1/cd). In the plots, the curves are all normalized respect to l, which means that the real value of x2 relative to a certain stress or strain level cannot be directly read. Anyway, all the point calculated by the program in order to draw the curves present in the figures are reported in the output file results_ss_(worksheetname) (see paragraph A.1.4.2).

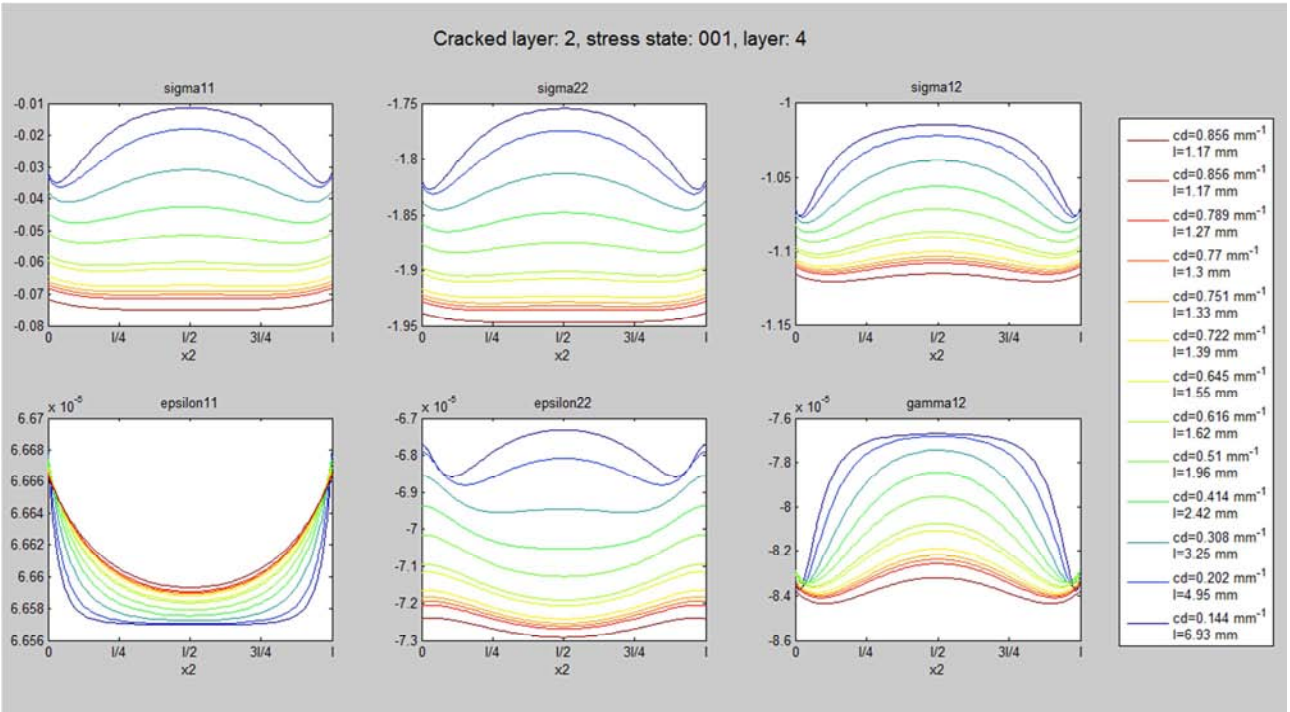

Figure A.11 – Example of stresses and strains output figure.

A.1.5 – Output window

When the program finishes its calculations all the output files and figures are written, an output window is opened, shown in Figure A.12. The function of this window is to allow an easy finding of the desired results figure avoiding the manual search by name among all the created figures.

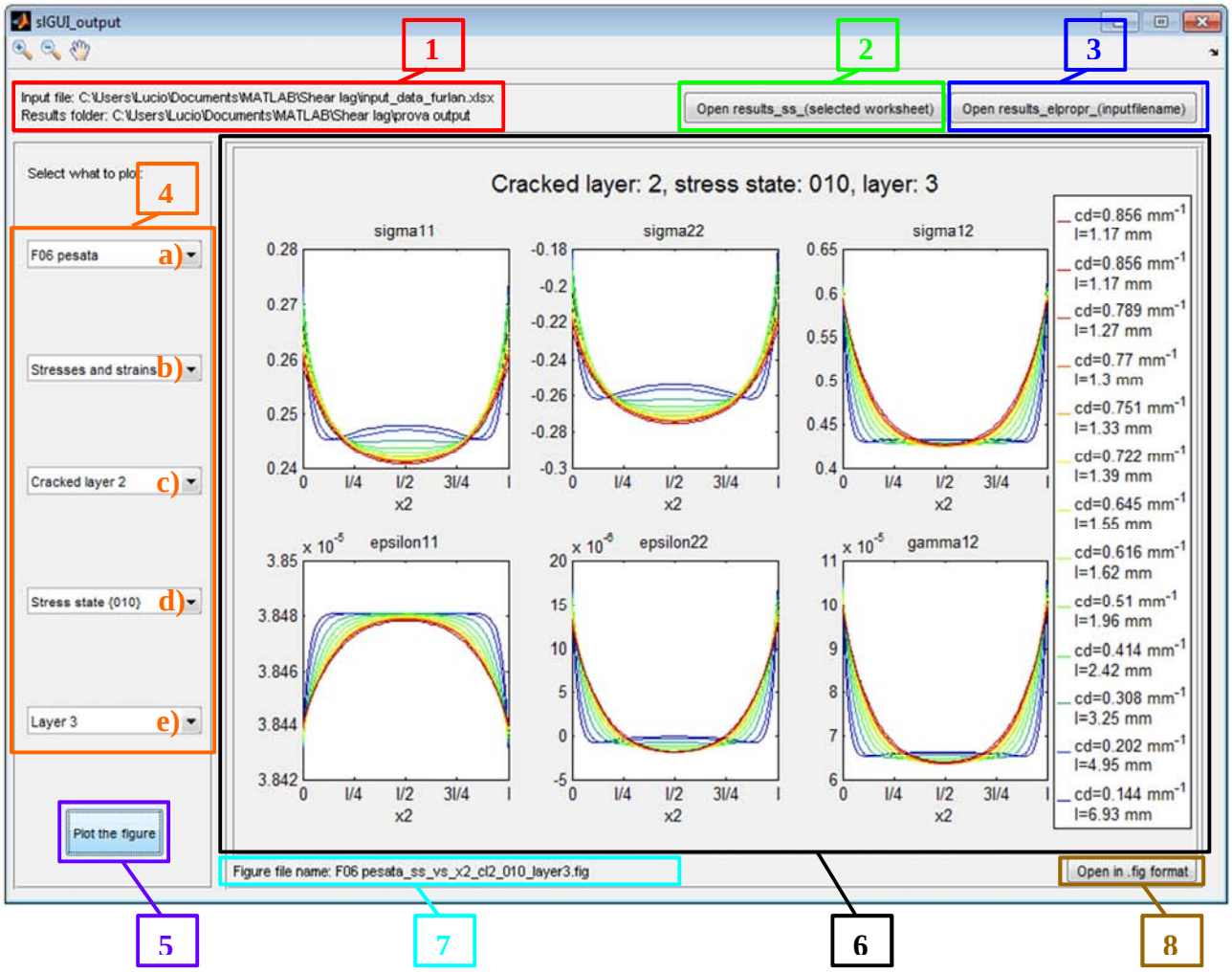

Figure A.12 – Output window.

The objects present in this window are:

1 – path of the input file and path of the results folder

2 – button for opening directly the output file fileresults_ss_(selectedworksheet) from the results folder. The "selected worksheet" is the one choosen from the first popup-menu (see object 4). This button is present only if the option for calculating stresses and strains was selected in the Main window.

3 – button for directly opening the output file fileresults_elpropr_(inputfilename) from the results folder.

4 – popup-menus to select which of the several created figures is to plot:

a) selection between worksheets read in input.

b) selection between elastic properties figures and stresses and strains figures.

c) selection of the cracked layer (if elastic properties was selected in **b)**, there is also the option "all cracked layers").

d) selection between external stress states (enabled only if stresses and strains option is selected in 4b).

e) selection between layers (enabled only if stresses and strains option is selected in **b)**.

5 – pushbutton that plots the selected figure in the figure area (**6**).

6 – figure area.

7 – figure file name.

8 – pushbutton for opening the selected figure in another window, in .fig format.

In the menu-bar of this window, tools for zooming in and out and for moving in the plotted figures can be found.

It is strongly recommended to close this window before running the program another time, in order to avoid superposition between the results obtained before and the new results.

A.1.6 – Analysis of results window

In addition to the Output window (paragraph A.1.5), another tool was developed in order to help the figure search, that is the Analysis of results window (Figure A.13). For the Analysis of results window to be opened it is not needed to open or run any other GUI. It offers the possibility to search between results obtained any time before and not only between the results obtained the last time the main program is launched from the Main window. For example, if only a certain number of worksheets is made read by the program once, and successively the program is run again to elaborate the remaining worksheets, the final Output window will enable to display the figures relative only to the worksheets read the last time, whereas the Analysis of results window allow to search among all the figures relative to that file, at the condition that they are all saved in the same folder. This window cannot analyze data previously obtained with manual data input.

The difference respect to the Output window is only in the panel at the top, zoomed in Figure A.13. The objects present in this panel are:

1 – path of the input file used to generate the results that are wanted to be analyzed (the “Browse” button allows a direct search).

2 – path of the folder in which the results have been saved (the “Browse” button allows a direct search).

3 – button for enabling figure plotting (it enables the popup-menu on the left).

4 – button for directly opening the output file results_elpropr_(inputfilename).

5– button for directly opening the output fileresults_ss_(selectedworksheet) (it gets enabled when a worksheet is selected in the popup menu on the left).

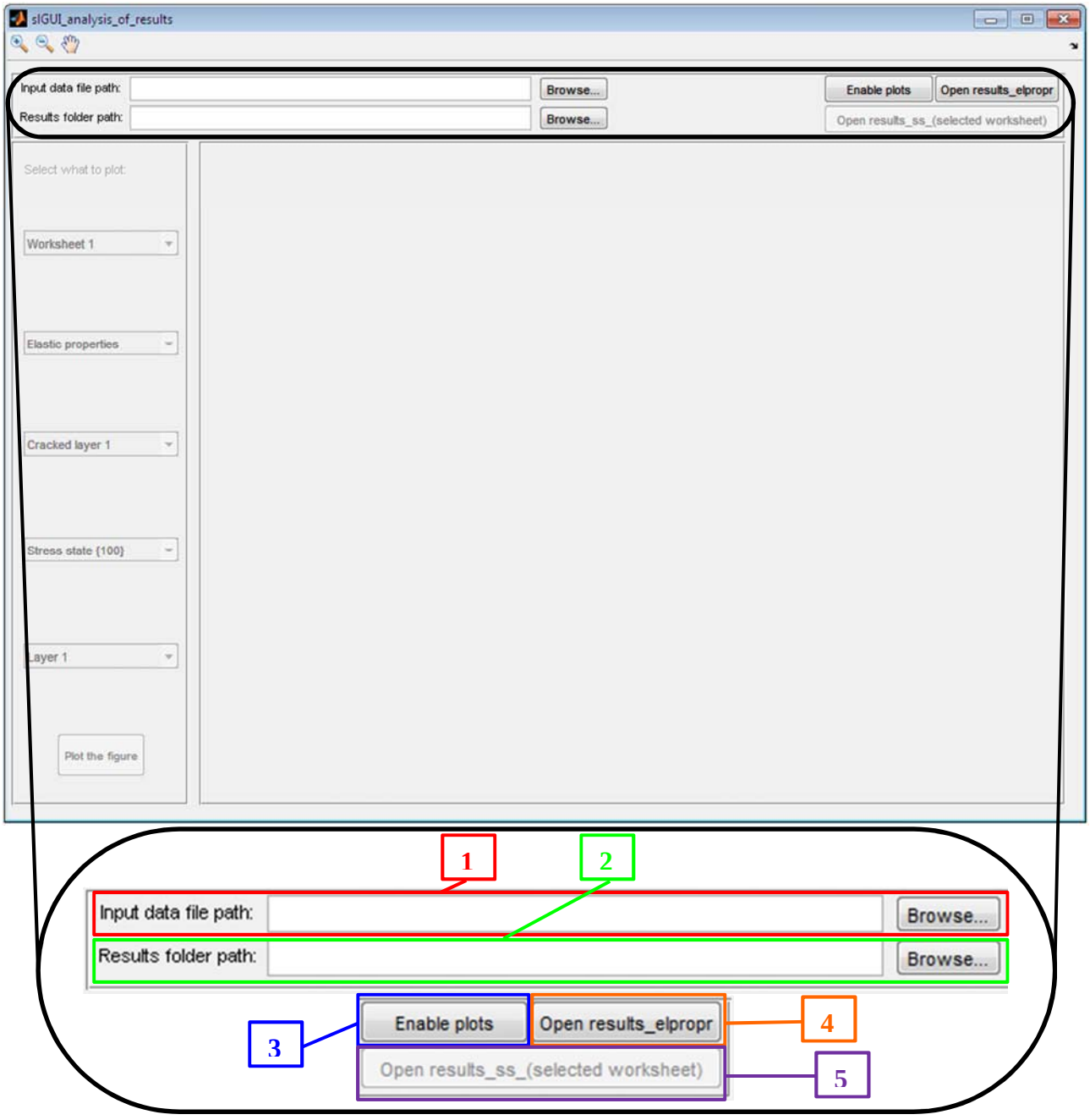

Figure A.13 – Analysis of results window and zoom on the Top panel.

In the first popup-menu on the left panel, all the worksheets of the input file are selectable, even if some of them have not been analyzed yet, so care must be taken in this selection. The second popup-menu allows to select between elastic properties figures and stresses and strains figure, even if the latters were never calculated, so care has to be taken in this selection as well. If, for any

reason, the output files or output figures to be opened or displayed are not found (for example because they have been deleted or moved or renamed), an error window will open (see next paragraph).

A.1.7 – Error windows

In order to help the user to easily understand his/her eventual errors in the input of the needed data, or in the results display by means of the output window, several different error dialog windows are provided by the program, that clearly explains the errors and avoid their display onto the Matlab® command window, where they are hard to be understood for anyone that does not deeply know how the program was written. Here follows a list of the predicted possible errors:

- Input data from file Excel
  - The input data file path does not exist or is left empty.
  - The format of the input data file is not .xlsx or .xls.
  - It is selected to read a certain interval of worksheets, but the any of the worksheet fields are left empty, or they are non-numeric.
  - The last worksheet selected to be read is higher than the first.
  - Any selected-to-read worksheet does not exist in the input data file.
  - In any of the worksheet-to-read of the file, there are some missing value of the mechanical and geometrical properties of the laminate, or some fields are non-numeric.
  - In any of the worksheet-to-read of the file, there are some missing value of the number of cycles (if not entirely empty) or crack densities, or some fields are non-numeric.
  - Last values of number of cycles (if not entirely empty) and crack densities are not in the same row.

- Manual input data
  - There are some missing value of the mechanical and geometrical properties of the laminate, or some fields are non-numeric.
  - There are some missing value of the number of cycles (if not entirely empty) or crack densities, or some fields are non-numeric.
  - Last values of number of cycles (if not entirely empty) and crack densities are not in the same row.

- Run program panel
  - The selected results folder path does not exist, or the field is left empty.

- Output window
  - The file containing the elastic properties results is not found (possible causes: the file has been deleted, moved or re-named).
  - The (eventual) file containing the stresses and strains results is not found (possible causes: the file has been deleted, moved or re-named).
  - The figure to plot in the output window is not found (possible causes: the figure has been deleted, moved or re-named).

- Figure analysis window
  - The field for the input data file or the results folder (or both) are left empty while attempting enabling plots.
  - The file containing the elastic properties results is not found (possible causes: the file has been deleted, moved or re-named).
  - The file containing the stresses and strains results is not found (possible causes: the file has been deleted, moved or re-named).
  - The figure to plot is not found (possible causes: the figure has been deleted, moved or re-named).

In addition to this possible errors, there are some warning message that can be displayed on Matlab® command window. It was decided not to avoid these displaying because they could be important. Three typical warning messages are the following:

- *Warning: Matrix is close to singular or badly scaled.*
  Results may be inaccurate. RCOND = 4.524646e-020.

It is possible that, for small values of crack density (typically <0.1) some matrix in the calculation of the elastic properties of the laminate is close to singular. Several attempts to avoid this have been made, but the problem remains. Anyway, the value of RCOND, which is related to how much the singularity-closeness influences the results, are usually very small.

- *Warning: Matrix is singular, close to singular or badly scaled.*
  Results may be inaccurate. RCOND = NaN.

This message can be displayed during the calculation of the elastic properties of the laminate, if the value of crack density is very close to 0. In this case, since the elastic properties of the laminate will be very similar to the ones when no cracks are present, and given the fact that they cannot be calculated by the program, their values will be considered *exactly* equal to the ones without cracks.

- *Warning: Added specified worksheet.*

When a new worksheet is added to a .xlsx/.xls file (in the present case, the output files), Matlab® displays a warning message. This message does not influence the program calculations and results.

A.1.8 – Program files

A very brief description of the files needed for the execution of the program follows, in alphabetical order, in order for the user to understand at least what is the role of each of them.

- extrcoeff.m

this function extracts the coefficients of a linear symbolic system constituted by any number of equations (even a single equation) in any number of variables.

- HKFcalcfunction.m

this function calculates the H, K and F coefficients of equations (17) to (19) in [22]

- input_data_template.xls

template for data input in .xls format (see paragraph A.1.2.1)

- input_data_template.xlsx

template for data input in .xlsx format (see paragraph A.1.2.1)

- mappacolorilucio.m

color map created for the plotting of the stresses and strains figures.

- notes_on_input_data_from_Excel_file.txt

text file containing the instructions for a correct reading of the data from Excel file.

- readme.txt

file containing a list of the created file and what file is to run to open the Main window (Figure A.1).

- regrpoli_constr_1pt.m

this function calculates in symbolic form the regression polynomial of the selected grade, imposing the passage through one fixed point.

- shear_lag_GUI_function.m

it is the core function, the one that makes all the calculations to find the elastic properties of the laminate and (eventually) stresses and strains in each layer.

- SLfunction_parte1.m, SLfunction_parte2.m

These functions calculates the strains in the global frame of reference in the non-cracked layers. It is part of the shear_lag_GUI_function.m above. It is divided in two parts in order to decrease the time needed for the program to complete its calculations.

- slGUI.fig

Main window figure (Figure A.1).

- slGUI.m

script relative to the Main window, that contains all the functions associated with each object. This is the file to run in order to start the data analysis.

- slGUI_analysis_of_results.fig

Analysis of results window figure (Figure A.13).

- slGUI_analysys_of_results.m

script relative to the Analysis of results window, that contains all the functions associated with each object. This is the file to run in order to start the analysis of results obtained in previous sessions.

- slGUI_output.fig

Output window figure (Figure A.12).

- slGUI_output.m

script relative to the Output window, that contains all the functions associated with each object.

Acknowledgments

I would like to thank Professor Quaresimin for the opportunity to work on such interesting topics, and for the support and consideration he showed to me.

Thank you Gioia and Mauro for having been and being great parents, and for making me become who I am. I love you and I hope I'll be able to pay you back for everything.

Thank you Sergio and Lorenzo for not hating me too much despite my being a psychopath sometimes. Maybe more than sometimes.

Thank you Mirko, it doesn't matter how far we are and what we do, you have been and will be my best friend, it's great to have you by my side. Sakuta turto.

Thank you Giordano and Tito – my Ghetto brothers – and Francesco. We spent together a time of my life that I will always remember. I am glad that I met you and now that we are not together anymore, I'll do my best to keep in touch with you. Sdraiate un saluto.

Thank you Cristiana and Giulia for being such amazing friends. I am sorry I do not hang out with you as much as I should, I'll try to make up for it. A big, big hug to you.

Thank you Paolo, not only for being a great supervisor – and a genius – but also for becoming a friend. I'll be ready for the jokes in the next two years. I hope.

Thank you Davide, Paolo, Chiara, Enrica, Filippo and Massimo for making the Californian experience what it has been. I hope that it was just the beginning of a great friendship. An advice: don't go Asian or you'll never go back (yes, also for you girls).

Thank you Bodyrock, I never enjoyed bboying so much as I did with you. I had so much fun and I feel like I owe you all something. Come visit me. Sorry for all those crashes at SFF.

Thank you Lorenzo, Ferro, Pingu, Bisca and Volpe for making me feel at home the times I came home. Count on me for anything. No, not for one more round of Tamango.

Thank you Nicola, Niccolò, Chiara, Enrico, Luca and Elena, for making Formula SAE one of the best things I've ever done in my life. I spent a great time with you. Let's reunite once in a while.

Thank you Anna for being the nicest person and a confidant. But please stop asking those uncomfortable questions.

Thank you Cecilia, for having been such a great part of my life. We shared a lot and you did a lot for me. Two lines are just not enough to express how I feel towards you. I sincerely hope you'll find the happiness you deserve.